Jet Initiation of Deflagration and Detonation

Thesis by

J. Christopher Krok

In Partial Fulfillment of the Requirements
for the Degree of

Doctor of Philosophy

California Institute of Technology
Pasadena, California
14 May 1997

To the memory of my father,
James Charles Krok,
who looked forward to my doctorate even more than I did.

Acknowledgements

I would like to thank the United States Nuclear Regulatory Comission for funding this research, first at Rennselaer Polytechnic Institute, and continuing at the California Institute of Technology. The research presented in this thesis was funded at Caltech by contract number NRC-04-94-044. I would also like to thank the National Science Foundation for awarding me a graduate fellowship covering the first three years of my graduate work, allowing me to concentrate on research.

I would also like to thank the following individuals:

Joe Shepherd, my advisor, for finding diverse and interesting topics, assisting my literature search, and leaving me some spare time to build car parts instead of experiments;

Hans Hornung, G. Ravichandran, Dan Meiron and Joe Kirschvink, for agreeing to serve on my committee and remaining patient through several date, time and venue changes;

My family and friends, for support over the past n years;

Raza Akbar, for providing information and insights related to my research, as well as a few good laughs (Does this mean that Ann-Margaret won't be coming?);

Sensei Tetsuyasu Uekema and my fellow kenshi in Shorinji Kempo, for an awesome budo experience;

Michael Kaneshige, for solving many a Unix problem;

Jamie Guthrie, for administrative and feeding assistance;

Georgia Frueh, for thoughtful insights unrelated to my research;

Karen Cheetham, Katie Gross, Carol Irwin and Jeri Chittum, for their help on administrative matters;

Joe Haggerty, Phil Wood, Larry Fraizer, and Ali Kiani, of the Aero Machine Shop, for free machine shop instruction (free save for the semiannual case of beer);

Pavel Svitek, for mechanical assistance;

Jerry Landry, for the same plus letting me use the wood shop to furnish my apartment;

Ron Kibbe and Bob King, of Engineering and Estimating, for their assistance in the design and construction of the laboratory;

Mike Gerfen, of Central Engineering, for work on parts of the facility;

Dave Evans, James Spotila, Liz and John Holt, Donovan Stevens and my other friends in the GPS division for making my Geology minor an enjoyable experience;

Last, but not least, I would like to thank Mr. Van Norman, for innumerable hours of tireless service during the construction of the HYJET facility.

Abstract

We have constructed a facility for the study of jet-initiated deflagration and detonation in hydrogen-air-steam mixtures. The facility is built around two pressure vessels. Mixtures of hydrogen, oxygen and nitrogen are spark-ignited in the driver vessel, generating a hot mixture of combustion products. The pressure rise ruptures a diaphragm, venting the products into the receiver vessel through nozzles of 12.7–92 mm diameter. The receiver is filled with hydrogen-air and hydrogen-oxygen mixtures diluted with either nitrogen or steam.

The deflagration tests studied the lean and maximum-dilution limits of hydrogen-air mixtures ignited by a hydrogen-steam jet. The lean limit of 6% hydrogen was comparable to other studies. The maximum dilution limit for steam was 60%. This is higher than the limit found in spark/glow plug ignition experiments. Shock oscillations in the receiver increased with nozzle size.

Further tests studied the initiation of detonation in both hydrogen-air and stoichiometric hydrogen-oxygen-diluent mixtures. In terms of jet diameter, D, and receiver detonation cell size, λ, we found initiation limits of $2<D/\lambda<7$, where other experiments required a D/λ of 11 or more. We propose that the D/λ model does not adequately characterize jet initiation, as it does not reflect the conditions in the driver.

The tests indicated that shock focusing plays an important role, promoting strong secondary explosions with or without prompt initiation of detonation. Mixtures with steam dilution were prone to DDT near the detonation limit, as the slower flame speed allows shock reflection and pressurization to occur before the reactants are consumed. Tests with nitrogen dilution had no DDT regime. Because of DDT and shock focusing, peak pressures were highest in mixtures that were slightly less sensitive than the detonation threshold. Schlieren movies confirmed the formation of a detonation near the nozzle exit.

Contents

List of Figures

List of Tables

Chapter 1

Introduction

1.1 The Hydrogen Problem in Severe Accidents

In the event of a severe loss-of-coolant accident (LOCA) in a nuclear power plant, hydrogen gas can be generated by oxidation of the zircalloy cladding on the fuel rods. Figure 1.1 shows the layout of a typical pressurized water reactor (PWR). The LOCA may be the result of a broken pipe, jammed valve, or other related event. As water drains from the reactor cooling system (RCS), steam will fill the open regions. With sufficient loss of coolant, the core may be partially uncovered and the surface temperature can rise enough to start an oxidation reaction between the steam and the zircalloy cladding. The steel vessel lining and core support structure may also oxidize, but the zirconium reaction is considered to be the main source of hydrogen. The amount of hydrogen generated depends on the specific accident, and how much of the cladding is involved. If all of the available zirconium reacts, a pressurized water reactor (PWR) could produce 1000 kg of H_2, and a boiling water reactor (BWR) could produce 2000 kg (Camp et al. 1983). As the hydrogen is generated, a hydrogen/steam mixture fills the open portions of the RCS. Hydrogen dissolved in the liquid water is not a problem; under normal operation, a certain amount of dissolved hydrogen is maintained in the RCS to scavenge oxygen and reduce corrosion in the system.

If the RCS continues to leak, the H_2-H_2O mixture can enter the containment dome, creating a potentially flammable mixture. If the mixture is ignited, the mode of combustion (deflagration or detonation) will depend on several factors. These include hydrogen concentration, temperature, dilution, ignition source strength, and size of the confined area.

1.2 Combustion Modes

The mixture will not sustain a deflagration unless the hydrogen concentration is above a certain limit, typically taken as 4% (Coward and Jones 1952). Near this lean limit, these flames burn incompletely and only propagate upward. The temperature of the products creates a buoyant flow, which the flame speed can not overcome. For a hydrogen

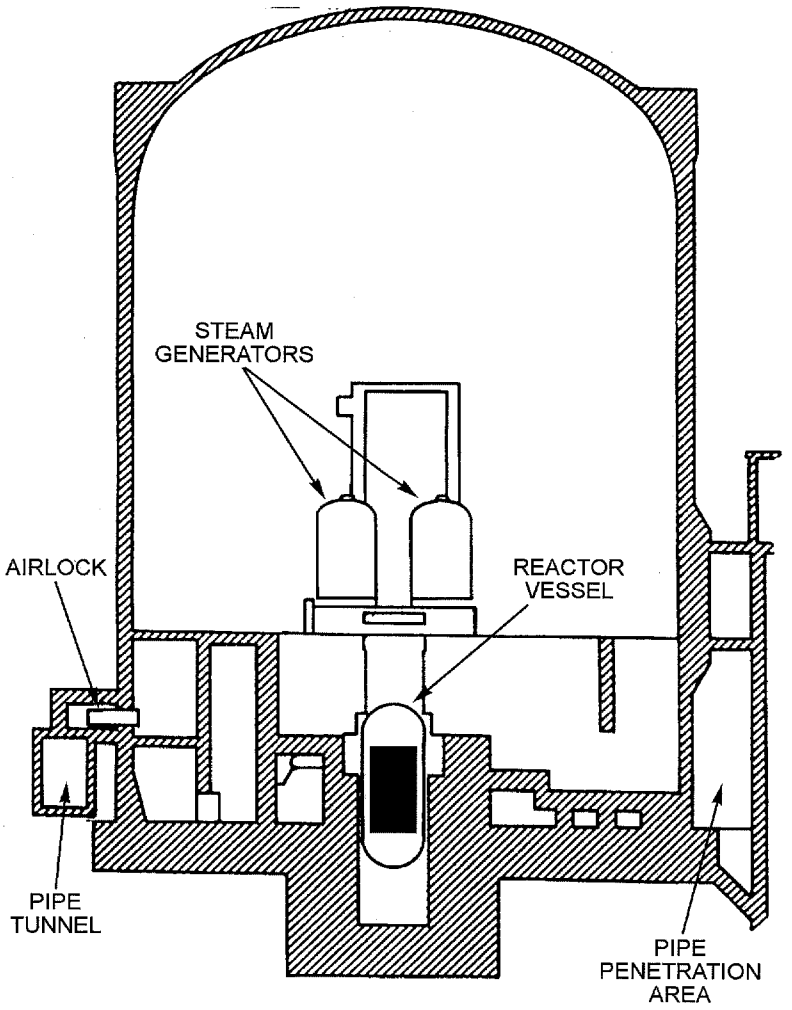

Figure 1.1: Layout of a typical PWR containment (Camp et al. 1983).

concentration of 8–10%, the flame will burn completely and propagate in all directions (including downward). These flames are expected to place minimal thermal and pressure loads on the containment and equipment. Such a burn took place during the Three Mile Island Unit-2 event in 1979. At 9 hours and 50 minutes into the incident, a 28 psig (1.9 bar) pressure spike was recorded in the containment. For hydrogen concentrations above 10–11%, there can be fast flames and deflagration to detonation transition (DDT). Fast flames can do nearly as much damage as a DDT, due to pre-pressurization by the lead shock, and subsequent shock reflection and focusing.

For a detonation to occur, additional criteria must be satisfied. For a detonation to be "directly initiated," a strong (i.e., explosive) ignition source is required. A strong, impulsive jet of hot gas can also directly initiate a detonation. A detonation can also be the result of flame acceleration. If a flame propagates over obstacles and/or in a confined

space, turbulence and shock reflection will accelerate the flame, possibly resulting in a DDT. In addition, detonations will not propagate in a mixture unless it occupies a large enough volume. The less sensitive a mixture is, the larger the volume must be. This means that research can not be scaled-down to a convenient size. The initiation energy must also be increased for less-sensitive mixtures.

There are methods for mitigating a hydrogen release. Hydrogen recombiners are located in the containment, to re-oxidize hydrogen generated by radiolysis of water in the RCS. While these are not designed to handle a large release, efforts are being made to develop large-scale units for this purpose. Water can also be sprayed into the containment; in addition to cooling the reactor components, the evaporated water will increase the steam fraction in the atmosphere and help inert the mixture. If the mixture is flammable, it can be deliberately ignited by glow plugs placed throughout the containment. In the event of an accident, the glow plugs are left on continuously, so the hydrogen will be ignited as soon as it reaches flammable levels. Small containments are inerted with nitrogen, although this can complicate repair efforts in an emergency. All containments in the United States are either inerted or use deliberate ignition as a mitigation method.

1.3 Jet Initiation

In a flammable mixture, the strength of the ignition source can determine the mode of combustion. In most cases, the source will be fairly weak, such as an electrical spark, or deliberate ignition by glow plugs. In the worst case, the reactor core can melt through its vessel, venting a hot jet of hydrogen, steam and molten core particles into the containment atmosphere through pipe and instrument penetrations. This is known as direct containment heating, or DCH. This will heat and pressurize the containment, and can serve as an ignition source. Three possible combustion regimes are shown in Figures 1.2 through 1.4, in order of increasing strength.

If the hydrogen concentration in the containment is too low to support a deflagration, the jet can burn as a diffusion flame. This is shown in Figure 1.2. The jet must be ignited near the release point, before the jet gas is diluted and cooled by entrainment of the containment atmosphere. The hydrogen release must also be sufficiently rapid. If ignition occurs, the resulting plume of combustion products will heat and pressurize the containment. The diffusion flame can also be stabilized and enhanced by entrainment of hydrogen in the containment atmosphere.

If the hydrogen concentration in the containment is above the lean limit, a deflagration can be initiated (Figure 1.3). The lean limit will also be affected by the amount of steam in the containment. If the H_2 concentration is sufficiently high, and the H_2O concentration sufficiently low, flame acceleration and DDT may occur. Diffusion flames and lean-limit ignition were studied previously in a facility at Rensselaer Polytechnic Institute (RPI) (Krok 1992; Ross 1994).

The third and highest-order mode of combustion is a detonation, as in Figure 1.4. In this case, turbulence and heat supplied by the jet cause a local explosion in the contain-

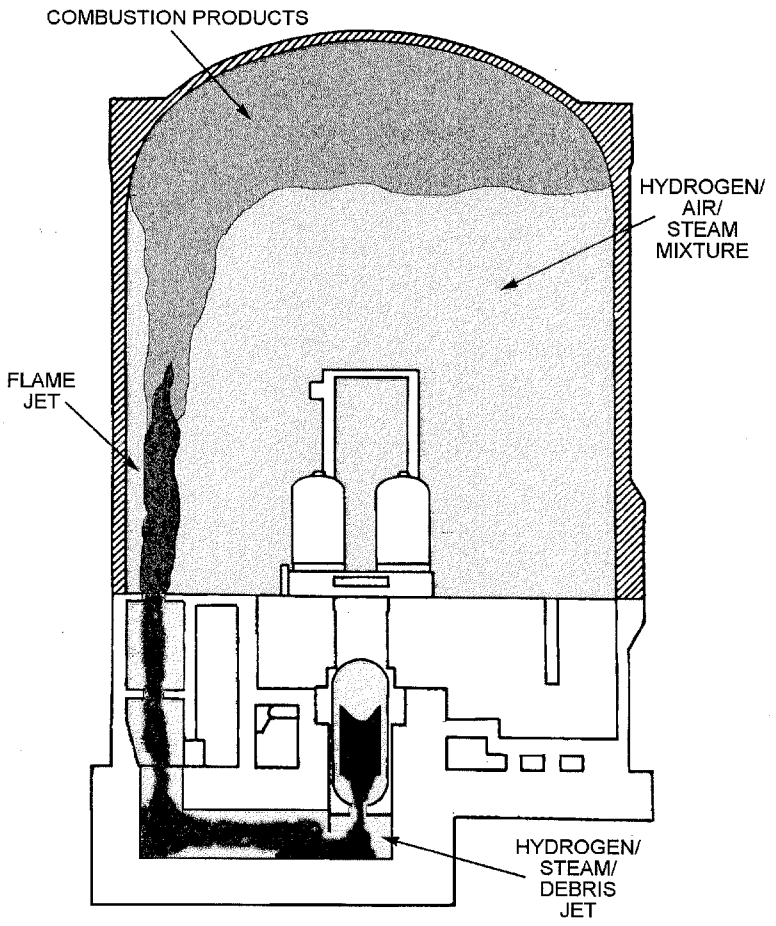

Figure 1.2: Jet diffusion flame resulting from DCH.

ment mixture, which propagates as a detonation wave. The strength of the detonation can be amplified by reflection off of objects and containment surfaces, and through focusing mechanisms.

An in-depth discussion of detonation physics is beyond the scope of this work, but can be found elsewhere (Fickett and Davis 1979; Nettleton 1987). A basic treatment will be provided to lay groundwork for later discussions of results. Briefly, a detonation is a supersonic combustion wave, comprised of a shock and an exothermic chemical reaction. The shock increases the temperature and pressure of the reactants, and after a suitable induction time, the reaction occurs. Energy released by the reaction drives the shock. Thus, the shock and reaction are coupled. While the thickness of a shock is typically a few mean free paths, the finite rate of chemical reaction increases the thickness of a detonation. A detonation can be as much as a centimeter thick, depending on the sensitivity of the mixture. The detonation process is similar in both gaseous fuel-oxidizer mixtures and solid explosives. Chapman and Jouguet independently determined that

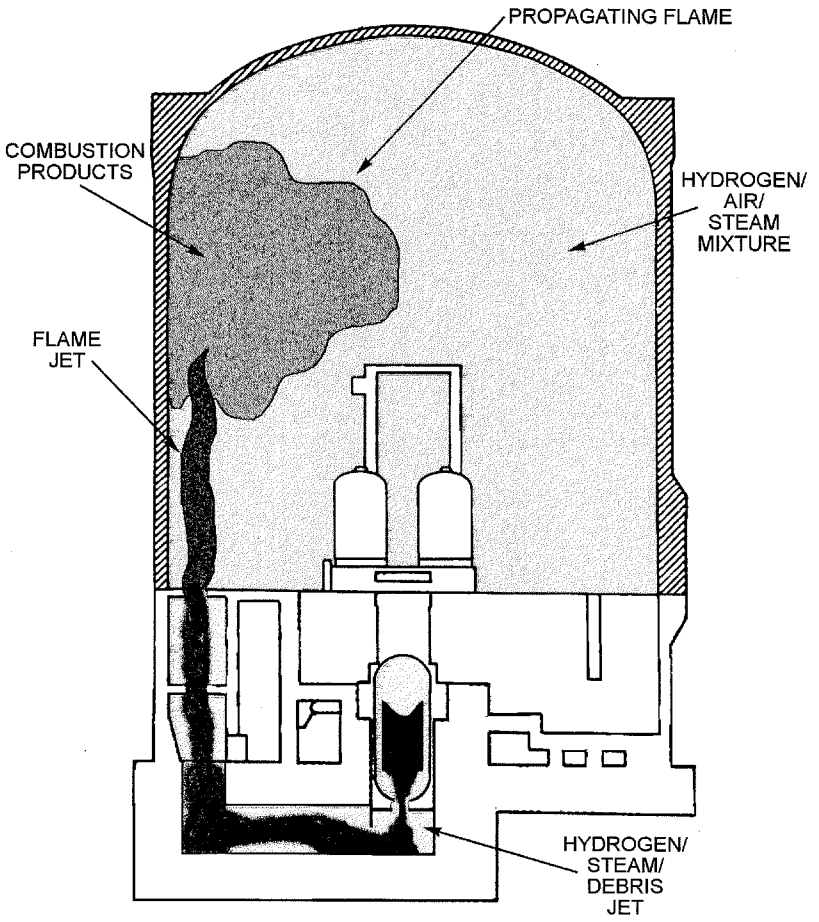

Figure 1.3: Initiation of deflagration in containment atmosphere.

flow out of a steady-state detonation is sonic relative to the shock. This sonic condition is required to match the steady-state detonation with the unsteady Taylor expansion behind it. Also, the sonic condition corresponds to the point of minimum entropy in the reaction products (Thompson 1972). Other properties related to a steady detonation are the Chapman-Jouguet velocity, V_{CJ}, and the CJ pressure, P_{CJ}. As the CJ conditions are independent of the internal structure, P_{CJ}, V_{CJ} and other state variables can be evaluated with chemical equilibrium codes, such as STANJAN (Reynolds 1986). The structure of the detonation wave was first modeled by Zel'dovich, von Neumann and Doring, each independently, in the early 1940's. Their model is collectively referred to as the ZND model, and consists of a planar shock followed by a reaction zone.

The one-dimensional, steady detonation model was widely accepted, as the CJ theory predicted velocities fairly accurately. Analytic studies in the 1950's found that the wave structure was not stable, however. The first experimental proof of three-dimensional structure was given by White (1961). Later studies found that the detonation wave

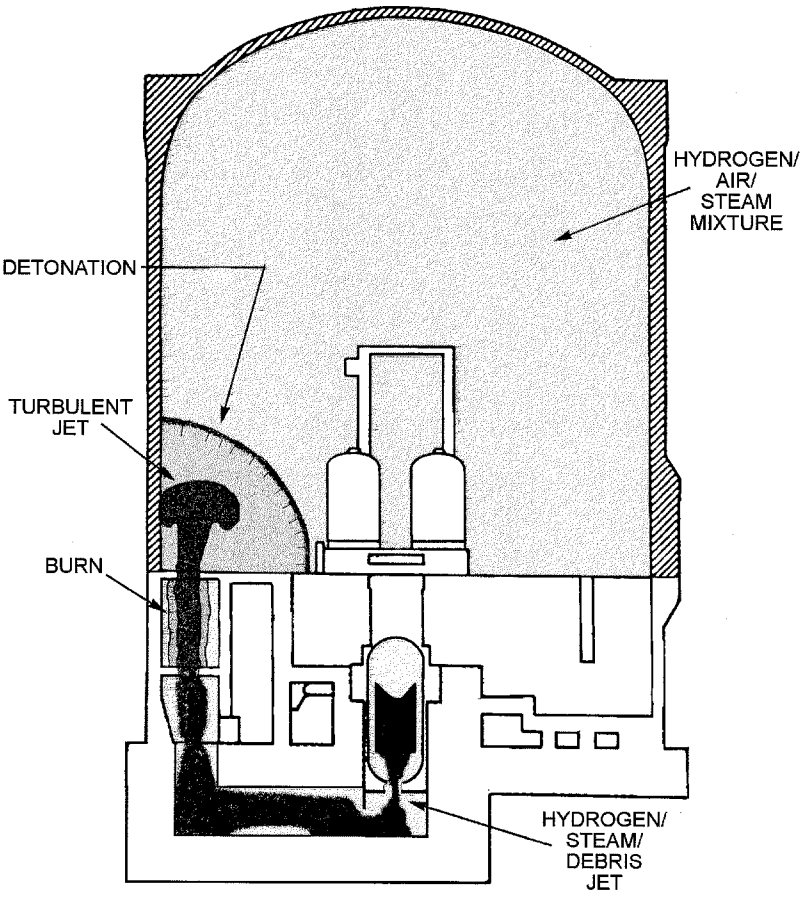

Figure 1.4: Initiation of detonation in containment atmosphere.

contained transverse compression waves. Figure 1.5 shows the transverse wave structure. As the detonation propagates, the transverse waves run back and forth across the incident wave, generating Mach stems when they collide. The junction of the incident wave, transverse wave, and Mach stem is called the triple point. The paths of the triple points can be recorded by running a detonation over a soot-covered metal sheet, called a "soot foil" or "smoked foil." The triple points will remove soot from the sheet, tracing their paths (Figure 1.6). The tracks form irregular parallelograms, called cells. Detonations are thus said to have a cellular structure. The cells are characterized by their width, denoted by λ.

Cell size indicates the sensitivity of a mixture to detonation. As the cells get smaller, the mixture becomes more sensitive. Cell size depends on several parameters of the reactants, including temperature, pressure, stoichiometry, and dilution (both diluent and concentration). Cell size is commonly used to correlate properties of detonations, and to compare different fuel-oxidizer systems. For example, critical initiation energy scales

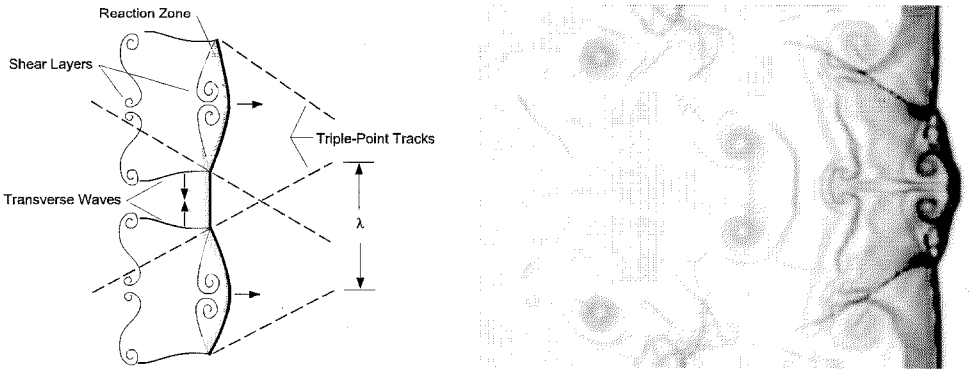

Figure 1.5: Schematic of detonation cell components, showing wave structures. Cell width is the distance between triple point tracks, measured parallel to wave front. Compare to pseudo-schlieren image of cell generated by numerical simulation (Quirk 1996).

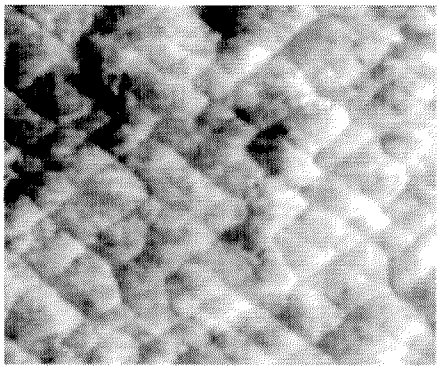

Figure 1.6: Detonation cells imprinted on soot foil.

with λ^3 ($E_C \propto \lambda^3$). Another important property is the critical diameter, d_C, which is used in detonation diffraction studies. For a detonation to exit a tube (or orifice) and successfully re-establish itself in an open area, the tube diameter must be greater than d_C. Studies have found that $d_C \approx 13\lambda$. This correlation has been carried over to jet initiation experiments, where early studies have found that a jet diameter, D, of 13λ was required for direct initiation of detonation. The use of D/λ will be examined further in Chapters 5 and 6. Much work has been done to measure cell size, but the results are not fully reliable. Within a single detonation, cells recorded on soot foils can have a range of sizes, and their measurement is subjective. Measurements by different members of the same research group can have ranges of $\pm 100\%$ (Tieszen et al. 1986). The particular diluent also affects the regularity of the cellular structure. Mixtures with N_2 dilution have very irregular cells, while Ar dilution results in a more regular pattern.

Attempts have also been made to correlate measured cell size against reaction zone lengths computed with the ZND model. It was first suggested by Shchelkin and Troshin (1965) that λ is proportional to reaction zone length, Δ: $\lambda \propto \Delta$, or $\lambda = A\Delta$. The value of

A is determined by comparison to experimental data, and varies from system to system. Detailed reaction mechanisms are now available for hydrogen-air mixtures with various diluents (e.g., Shepherd (1986)), making computation of Δ quite easy. Several criteria are used to locate the end of the reaction zone; I will use the point of maximum energy release. (Other criteria are M=0.9, M=0.75 or maximum $\partial T/\partial x$.)

1.4 Research Overview

Much work has been done in these areas, but some gaps still exist, primarily in detonation of H_2-air-H_2O mixtures. Recent examples of small-scale jet initiation research include Carnasciali et al. (1991) and Bezmelnitsin et al. (1997). Large scale tests have been performed by Dorofeev et al. (1995) and Dorofeev et al. (1993). While these tests were mostly unconfined, they did indicate the significance of confinement in initiation of a local explosion. Our goal is to expand the database of these tests by studying a moderate size scale with confinement effects. To that end, we have constructed the Hydrogen Jet Facility, or HYJET. This facility consists of two connected vessels, separated by a diaphragm, and is described in the next chapter.

The first HYJET test series (COMP) revisited the RPI experiments on the effect of igniter strength on the lean flammability limit of diluted hydrogen-air mixtures. These were then expanded (S series) to study the difference in suppression abilities of nitrogen and steam. These tests are described in Chapter 3. Chapter 4 describes the SA test series, which examines jet ignition of constant-stoichiometry H_2-air mixtures with steam dilution. Examination of jet-initiated detonations begins with the NITRO series in Chapter 5, which studies the effect of driver composition on detonation of H_2-air mixtures. Chapter 6 covers the BETA series, which fixes the driver composition and determines dilution limits for detonation initiation in stoichiometric H_2-O_2 mixtures.

Chapter 2

HYJET Experimental Facility

The HYJET facility is located in the GALCIT Explosion Dynamics Laboratory, in the basement of the Guggenheim building. It is built around two pressure vessels, representing the reactor vessel and containment in a nuclear power plant. This is the second-generation redesign of a facility built at Rensselaer Polytechnic Institute in Troy, NY (Krok 1992). A schematic of the HYJET facility is shown in Figure 2.1. As this facility was built in the United States, the majority of its components and support equipment have nominal dimensions given in English units. In the interest of correctness and accuracy, the facility will be described in English units, with conversions where appropriate. In subsequent chapters, information will be given in metric units only.

A copy of the GALCIT Safety Assessment (GSA) for HYJET is provided in Appendix A. The GSA contains an in-depth discussion of the HYJET design considerations, as well as hazards typical of such facilities, and the steps taken to mitigate them. That material will be touched on briefly here.

2.1 Pressure Vessels

The driver vessel, representing the reactor, was constructed at Caltech by the Aeronautics and Central Engineering machine shops. It is shown in Figures 2.2 and 2.3. It is made from 6" OD by 0.5" wall (152×12.7 mm) seamless 316SS tubing, with stainless steel flanges welded to both ends. Attached to one end is one half of the hydraulic closure mechanism and an extension which brings the overall length of the driver to 92" (2.3 m). The closure and extension create an annular channel near the middle of the driver, which may enhance flame acceleration through generation of turbulence (see Figure 5.2, p. 43). The opposite end of the driver is capped by a blind flange containing instrumentation ports. The volume of the driver is 1 ft^3 (0.028 m^3). The full assembly was hydrotested in situ to a pressure of 1500 psi (103 bar). Interchangeable nozzles mate to the end of the driver extension. The nozzle retains the diaphragm and incorporates O-rings to seal to the receiver socket. Three nozzles are available with diameters of 1.5", 2.5" and 3.625" (38, 64, and 92 mm, respectively). A fourth unit has a threaded hole that accepts nozzle inserts of 0.25", 0.5" and 1" diameter (6.4, 12.7 and 25 mm), and is equipped with a

cruciform diaphragm cutter. Figure 2.4 shows the 3.625" nozzle and threaded nozzle adapter. A threaded plug is also available for the adapter, so either vessel can be used as a constant volume chamber. The diaphragms used in these experiments are 0.005" (0.13-mm) Mylar. Mylar was chosen over aluminum because it was much easier to handle and less expensive. Because of clogging problems, a piece of cellophane tape is used as a diaphragm with the 0.25" nozzle. This works remarkably well, as long as the pressure differential favors the tape during filling.

The receiver is an ASME section VIII pressure vessel built by R. L. Morton Welding, Inc. It is rated for 750 psi at 250 °F (52 bar at 395 K), and carries the ASME U stamp. The vessel is 36" (0.91 m) in outside diameter, and 64" (1.6 m) across the seams, with a total volume of 42 ft^3 (1.19 m^3). It has a number of through-holes for access and instrumentation. These include: One 10" flange on one end for connection to the driver; one 6" flange on the other end for instrumentation; two 12" flanges for interior access; seven 1" NPT ports along the top for gas and instrumentation connections; two 2" NPT ports for vacuum and mixing; two 1/2" NPT drains; and two Caltech-designed window retainers which hold three windows each. Attached to the 10" flange is the other half of the hydraulic closure, as well as a socket that extends inside the vessel (described below).

Both vessels are mounted on linear bearings and steel rails, allowing them to be moved back and forth. The driver must be moved in order to replace diaphragms. Movement of the receiver allows different window stations to be placed in the path of the schlieren system, illuminating different parts of the jet. The interior walls enclosing the vessels have 0.125" (3.2 mm) steel armor to help contain blown transducers or failed schlieren windows. The exterior walls are concrete foundation and need no additional protection.

2.2 Hydraulic Closure

A hydraulic closure mechanism is used to connect the vessels and seal the diaphragm. This is a modified version of a Caltech-designed closure, used on the GALCIT 6" shock tube. A cross section of the closure is shown in Figure 2.5. (Individual drawings are in Appendix B.) The extensions are designed to align the nozzle exit with the edge of the first schlieren window. The removable ring clamp is the key fastener in the system. It can be seen in Figure 2.3, suspended by counterweights above the juncture point. Figure 2.3 also shows the driver (inner) extension and the two halves of the closure. The diaphragm is placed between the inner extension and nozzle, and the nozzle is secured by two cap screws. The screws are used only to hold the nozzle and diaphragm in place until pressurization. The closure halves are brought together by rolling the driver into the receiver, seating the inner extension in the receiver socket (outer extension). The ring clamp is brought down and latched around the closure flanges. An air-powered hydraulic pump pressurizes the fluid space (Figure 2.5) to 2500 psi (170 bar). Pressure on the annular piston drives the inner extension against the bottom of the socket with a force of over 120 thousand pounds (530 kN). This force is used to crimp the diaphragm and seat the O-rings, which seal all face junctions. The driver, attached to the piston, rolls forward slightly during pressurization. The ring clamp takes the full closure force,

keeping the halves from separating. When the system is depressurized, a set of springs (not shown) drive the piston rearward.

2.3 Gas Handling System

Figure 2.6 is a schematic of the gas handling system inside the laboratory. Bottled gases used in the facility are stored in an outdoor bottle farm, while compressed air is plant-supplied. The gases are stored outside as a seismic safety precaution. Supply pressure is controlled by two-stage regulators at the farm, so gas pressures do not exceed 15 psig (1 bar) inside the building. The feed lines are 0.5" x 0.049" seamless SS connected by Swagelok fittings. Special precautions are taken for hydrogen, as it is highly flammable at a wide range of concentrations. The hydrogen line is controlled by a spring-return electropneumatic ball valve, also at the bottle farm. To open this valve, a "dead-man's" switch on the gas handling panel (in the control room) must be held down. This prevents the operator from leaving the panel while hydrogen is flowing, and overfilling the vessel with flammable gas. The spring-return actuator will close the valve if either power or air pressure is lost, blocking the flow of hydrogen in an earthquake or other accident.

Gas handling panels are used to fill the vessels with the desired mixtures. The vessels are filled using the method of partial pressures, via the Heise gauge and metering valves on each panel. All valves at the vessels are Whitey ball valves with electropneumatic actuators. They are controlled from a mimic panel in the control room. Limit switches on the valves activate lights on the mimic panel, showing all valve positions. The switches also signal a logic circuit which only sends power to the firing circuits when all valves are closed.

Gases in the driver vessel are mixed by recirculation with a Senior Flexonics MB-302 bellows pump. In the receiver, gases are mixed by a 12" diameter propeller. The propeller is driven by a Parr Instruments A1180HC magnetically-coupled rotary feedthrough. This feedthrough uses magnets to transfer power from the outer housing to the inner shaft, so there is no need for dynamic shaft seals. It is designed to stir reactants in caloric bomb reactors, so it can withstand high pressures. The feedthrough is cooled by a water jacket at its base. The feedthrough is belt-driven by a universal motor with a variable-speed control.

When steam is used in a mixture, it is supplied by a steam generator (see "Heating System," below). Flow is metered by a preset needle valve. Flow into the receiver is controlled by an electropneumatic ball valve. The system also contains a purge valve, for draining condensate and heating the lines before filling the vessel. Both the purge and fill valves are operated from the control room.

Main vacuum is supplied by a Kinney KTC-112 compound vacuum pump located in the sub-basement Detonation Physics Laboratory. This pump has a free air displacement of 107 cfm, and can pump the facility down to 100 millitorr within 20 minutes under good conditions. This pump has a gas ballast system, enabling it to handle moderate amounts of volatiles, like water vapor. When large amounts of water vapor are present, either from heating or combustion, the Kinney MLR-30 is used for the initial pump-down. This

pump displaces gas via an impeller-driven ring of water. It is limited to a minimum pressure of about 150 mbar, but can handle liquid water through the inlet.

2.4 Control Systems

The control and experimental rooms are separated by an armored wall of heavy construction. Once the vessels are joined and the closure pressurized, the experiment is run from the control room. Figure 2.7 shows the layout of the controls. The gas fill panels are on the left. To the right are the mimic panel, heater controls and firing system. The small panel above these is an auxiliary panel with controls for the steam valves, a manifold vacuum gauge, and hydraulic closure indicator. On the far right is the controller for the Cordin camera, and a remote switch for the MLR-30 vacuum pump. Below is the Macintosh IIfx computer, which has since been replaced by a Gateway for data acquisition.

2.5 Firing System

Each vessel has independent primary and secondary ignition systems. The primary system consists of an NGK four-electrode automotive spark plug in a Teflon insulator, mounted in the instrumentation flange. Spark energy is supplied by an EG&G TM-11A high voltage trigger module, which generates a 30 kV pulse. The driver firing button controls a trigger fanout box which distributes signals to the data acquisition boards, video timer, and BNC 7010 delay timer. The delay timer controls the Cordin camera and the driver TM-11A, giving the camera shutter time to open before firing the TM-11A (or, delaying the shutter for slower-burning mixtures). On the receiver, the TM-11A is controlled directly by the firing button. The logic circuit on the mimic panel blocks power to the trigger modules until all valves are closed and the closure is pressurized. In addition, the modules have been modified to include an arming switch, preventing firing by spurious signals.

The secondary system on each vessel consists of a Delco 9G glow plug mounted in the instrumentation flange. These are powered by a Kepco ATE 15-50 power supply, and are used to burn off flammable gas mixtures if the primary system fails.

2.6 Schlieren System

The schlieren system is mounted in two towers straddling the receiver vessel, as shown in Figures 2.8 and 2.9. The sending tower uses a 150 W xenon arc lamp in an Ealing housing, and a 1 mm aperture to provide a point source of light. This is collimated by a 100 mm dia. by 1 m f.l. mirror, and a turning mirror directs the light through the receiver windows. Three window stations are available, for imaging different regions downstream of the nozzle exit. The window ports are 4.6" (117 mm) in diameter, and are bored on 6.125" (156 mm) centers. The windows are made of BK7 glass, and are

150 mm in diameter by 25 mm thick. Windows are only used in one station at a time; the others are filled with steel blanks. One of the window retainers is shown in Figure 2.10, with a light/dust boot on the active window station.

The receiving tower directs the light towards another 100 mm x 1 m mirror, which focuses it on a knife edge. The wood skin on the towers responds to atmospheric changes, and tends to move the focal point off of the knife edge. To compensate for this, lateral motion of the knife edge is controlled by an electric motor and gear drive, which is powered from the control room. The operator can adjust the position of the knife edge until the schlieren image is satisfactory. After passing the knife edge, the light goes through an auxiliary lens, is redirected by a turning mirror, and goes through a second auxiliary lens. These lenses are needed to provide proper image size in the Cordin camera. The light then passes through a Pyrex beamsplitter plate, with approximately 5% of the light going to a Pullnix CCD video camera, and the other 95% going to a Cordin 350-M rotating-drum framing camera.

The CCD camera is used for recording slower burns, and some of the weaker jets. The video system is also used to check system alignment and knife edge position as described above. The Cordin 350-M is a rotating drum camera that uses 35mm film, exposing 224 frames at speeds up to 35,000 frames per second. It is used to film jet startup, rapid deflagrations, and detonations. Camera speed is controlled by a Drive Control Systems MicroSpeed 196 feedback controller. Drive power is supplied by a Kepco ATE 100-10M DC power supply.

2.7 Heating System

The receiver vessel can be heated to a maximum temperature of 383 K, allowing use of water vapor for mixture dilution. Initial heating is provided by a Chromalox CES-48A steam generator. This generator draws 46 kW of electrical power, and can supply up to 139 pounds (63 kg) of steam per hour. Live steam enters the receiver through the steam heating valve (Figure 2.6), heating the vessel walls by condensation. When the receiver reaches the desired temperature, the steam heating valve is closed, and the condensate is pressure-drained through the drain valve. Temperature maintenance is provided by electrical heating pads and tapes affixed to the surface of the vessel. The electrical heaters supply 7.6 kW of heating, split into two zones. Each zone is controlled by an Omega Engineering CN6071A feedback controller, using an SCR73-Z power controller to control 208V, three-phase power. The vessel is insulated by a 2" thick fiberglass blanket, with a Teflon-coated outer surface.

2.8 Data Acquisition System

The data acquisition system used for the first 205 runs was based on a Macintosh IIfx computer. The data acquisition boards and software were manufactured by National Instruments. The boards used were the MIO-16XL-18, the A2000, and the DMA-2800.

The MIO-16 contains 16 single-ended analog input channels, and has an 18 μs conversion time. The A-2000 has four channels that are sampled simultaneously, with a 1 μs conversion time. The DMA-2800 allows data to be written directly to memory as it is acquired, and also contains a GPIB interface. LabView software was used to acquire the data.

For runs 206 and on, the data acquisition system was updated by replacing the Macintosh with a Gateway2000 P5-133 PC-compatible. This computer was equipped with two National Instruments 16-channel acquisition boards, an AT-MIO-16E-1 and AT-MIO-16E-10. The 16E-1 board can acquire data up to 1 MHz, and is used for high-speed acquisition from piezoelectric pressure transducers during detonation tests. The 16E-10 board can acquire data at rates up to 500 kHz, and is used for the remaining pressure transducers and thermocouples in deflagration tests. The data from the two boards are displayed on the screen and saved to the hard disk.

Temperature instrumentation consists of a number of type K thermocouples. The driver contains one heavy-duty thermocouple. This does not respond quickly enough to indicate the peak temperature during the driver burn, but does provide initial mixture temperature data. The receiver contains two probes, used primarily for initial mixture temperature, and a rake of seven smaller thermocouples. These are distributed vertically from one of the top instrumentation ports.

To record pressure, both the driver and receiver are equiped with Kulite strain-gauge pressure transducers. The driver uses a model XTC-190-300A, while the receiver uses a XTME-190-250A. The latter model is temperature compensated to 450 °F (500 K), allowing for vessel heating. To protect the diaphragms from combustion temperatures, sintered metal frits are mounted inside the vessels, covering the pressure ports. The frits are 1" in diameter by 0.125" thick. The outer fritt has a pore size of 40 microns, with 20 microns for the inner frit. These serve to quench combustion and absorb heat from the products before they reach the transducers. The Kulites are powered by Dynamics 7600A excitation amplifiers. For faster pressure measurements taken during detonation experiments, the receiver is outfitted with two PCB model 1125A26 piezoelectric transducers. One of these is located in the last instrumentation port on the top of the receiver, and one is in the 6" end flange. The driver also contains a PCB transducer, mounted in the end flange. The PCB transducers are powered by a PCB power supply, and the output is fed through the Trig-Tek amplifiers before being connected to the A-2000 acquisition board. The Trig-Tek amplifiers can be run in attenuating mode for high-pressure tests.

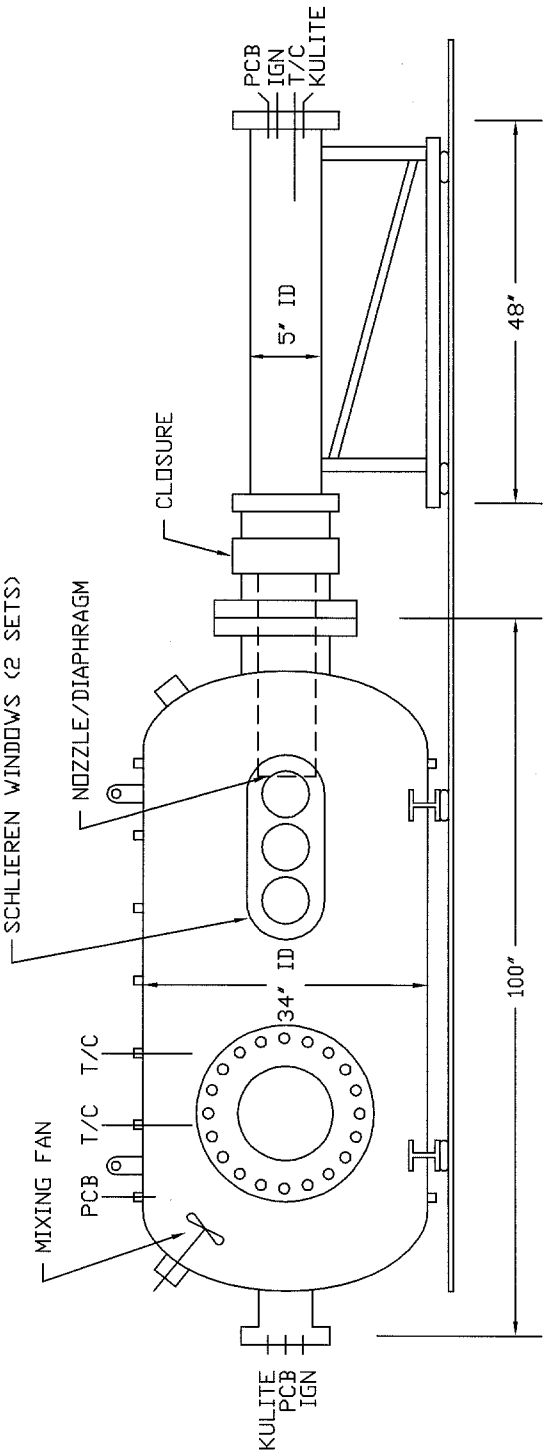

Figure 2.1: Overall schematic of HYJET facility showing instrumentation locations.

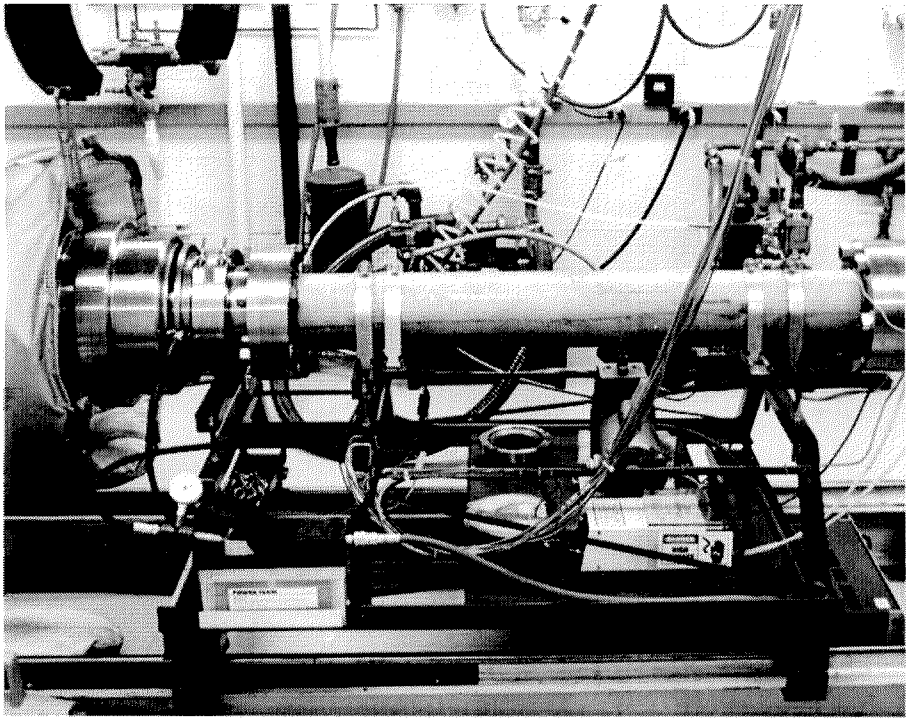

Figure 2.2: Photo of driver vessel mated to receiver. Pneumatic hydraulic pump, TM-11A trigger module and mixing pump are visible on support rack. Support rails can be seen at bottom of photo.

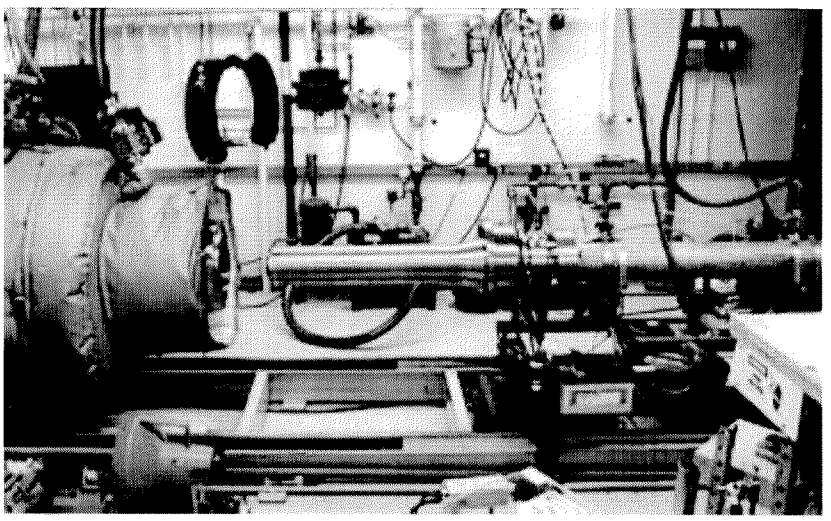

Figure 2.3: Photo of driver separated from receiver, showing driver extension. Cordin high-speed camera is visible in lower left. Clamp ring and counterweight are hanging over juncture point.

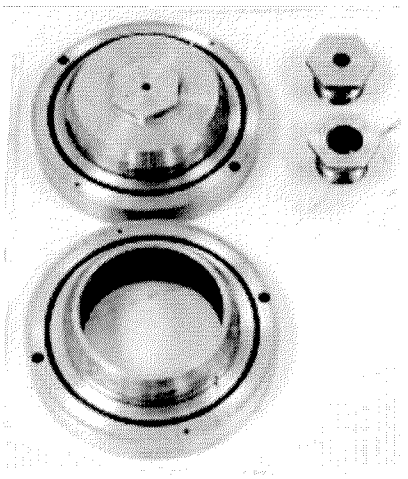

Figure 2.4: Threaded nozzle adapter with nozzles, and 3.625" (92-mm) nozzle.

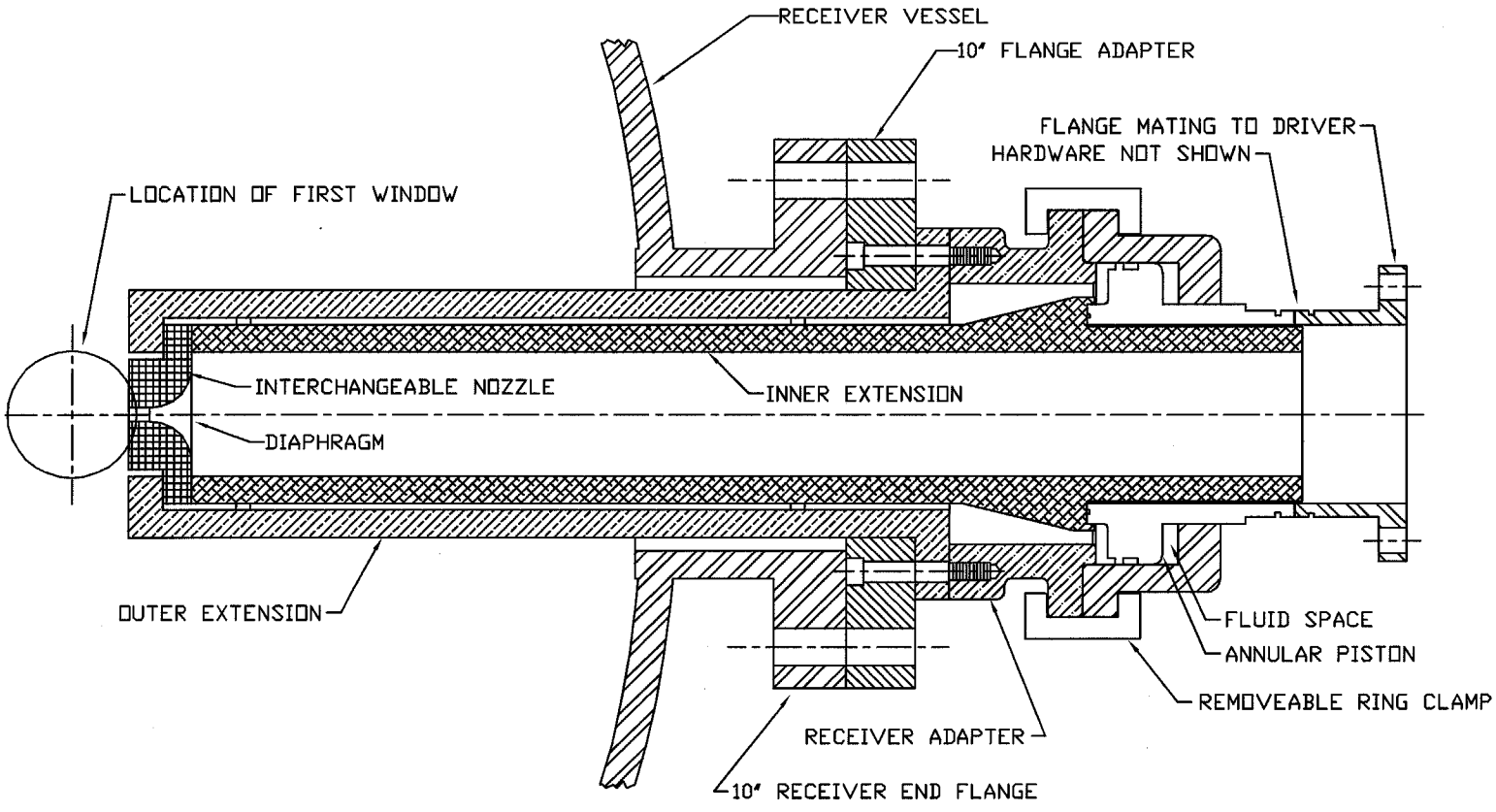

Figure 2.5: Cross section of hydraulic closure; receiver on left, driver on right.

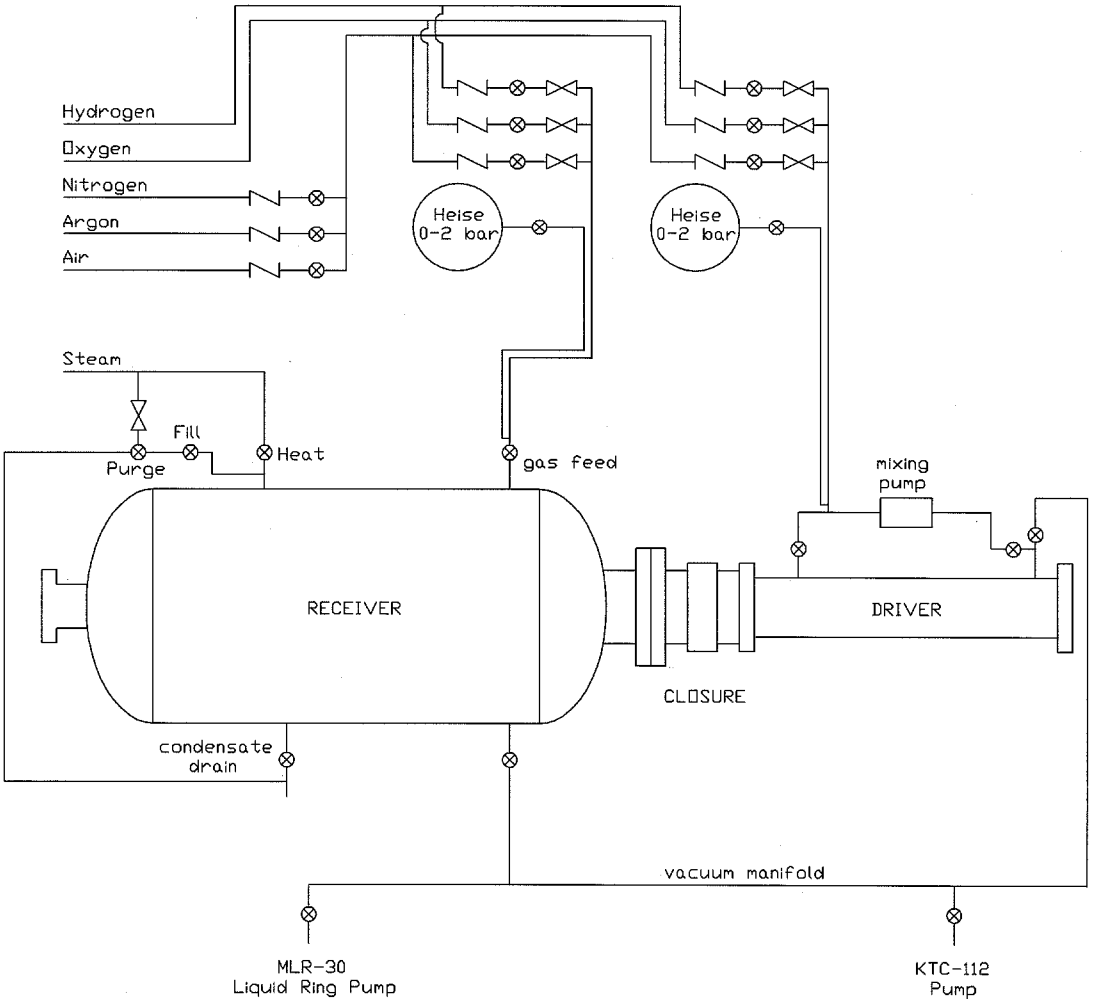

Figure 2.6: Schematic of gas handling system.

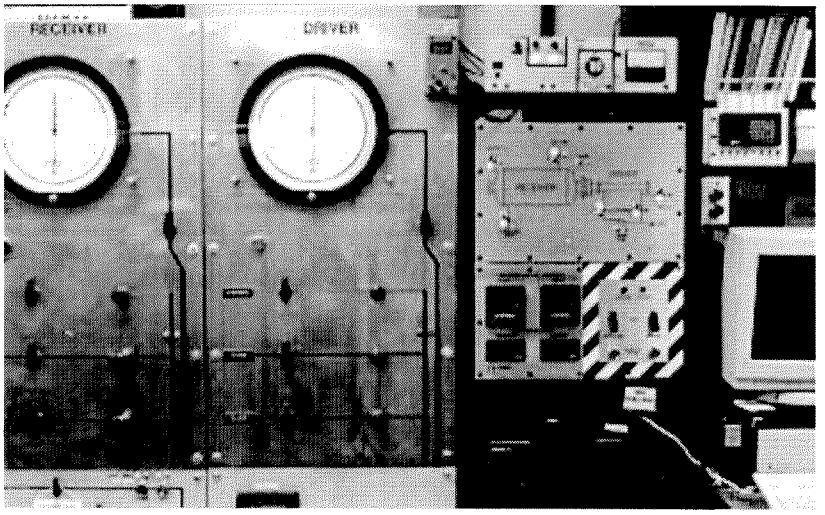

Figure 2.7: HYJET control system, showing gas filling panels, mimic panel, heating and firing controls, camera controller and acquisition computer.

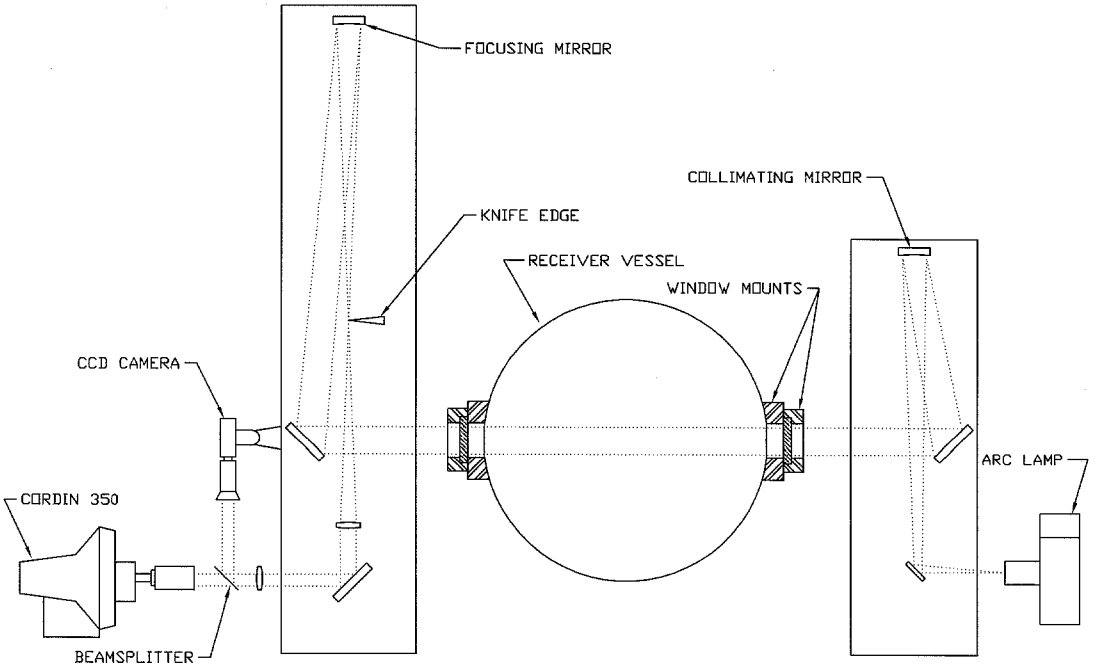

Figure 2.8: Cross-sectional view of schlieren system. Cameras and light source are rotated for clarity.

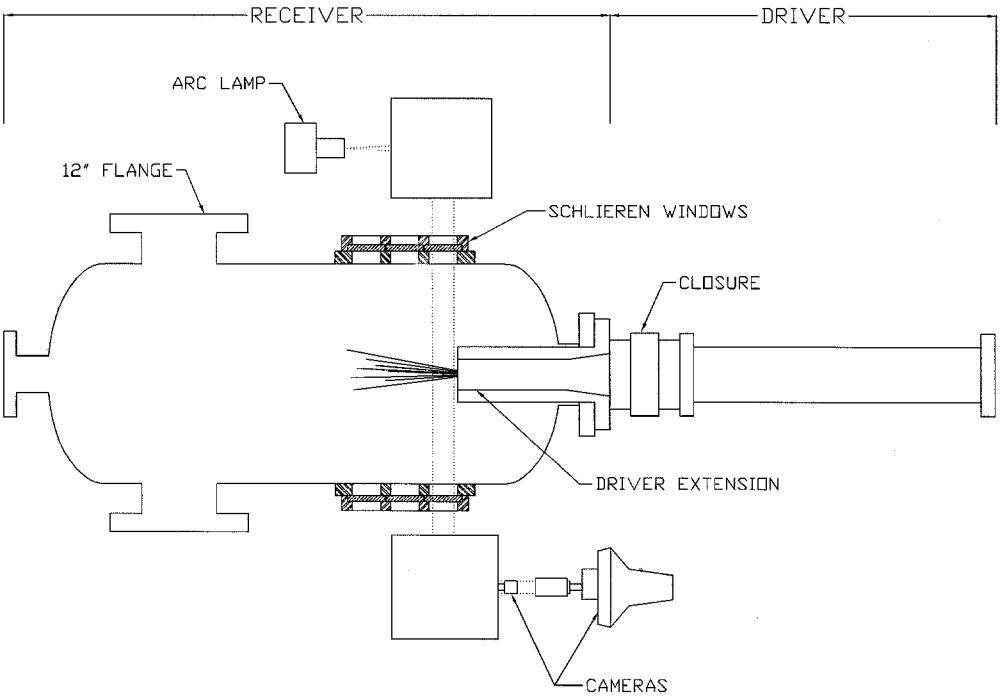

Figure 2.9: Top view of schlieren system.

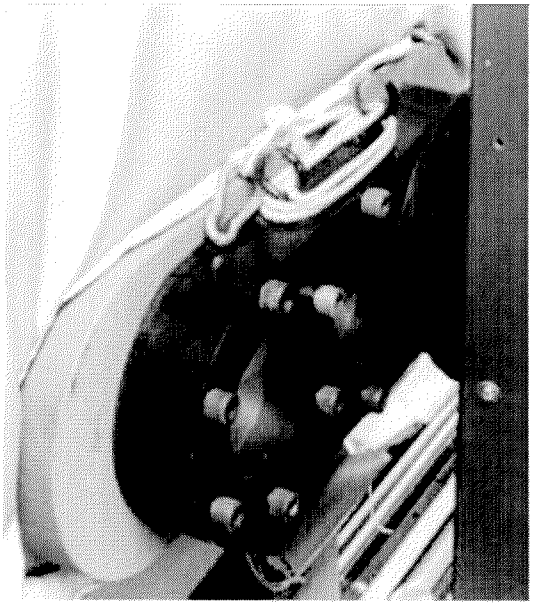

Figure 2.10: Window retainer and light/dust boot.

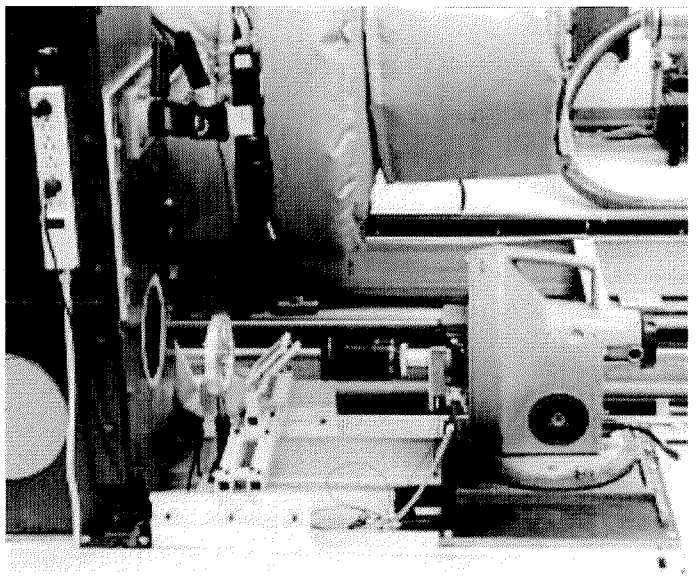

Figure 2.11: Exit end of schlieren system, showing auxiliary lens, beamsplitter, and cameras.

Chapter 3

COMP and S Series

3.1 Introduction and Background

The purpose of the COMP test series was to compare the CIT HYJET facility to the original facility at RPI. These tests duplicated the RPI lean limit deflagration tests (Krok 1992). In these tests, the driver mixture was 80% H_2-20% O_2 at 1 bar. When ignited, this vents a mixture of 50% H_2-50% H_2O into the receiver, simulating a DCH jet in a reactor containment. The receiver mixtures contained air and nitrogen in a 1:1 ratio, with 0-10% hydrogen at 1 bar (addition of an inert gas to a flammable mixture is known as "partial preinerting"). Both vessels had an initial temperature of approximately 298 K. The tests used the 12.7 and 25-mm nozzles. It may be argued that diluting the air with nitrogen will raise the lean limit by displacing oxygen. Previous studies have shown that the lean limit in this system is unaffected with up to 70% N_2 in the overall mixture (Kuchta 1985).

In typical flammability limit tests, the gas mixture is ignited by a strong spark at the bottom of an open, vertical tube. These tests have found a lower flammability limit of 4% H_2 in air (Coward and Jones 1952). At these concentrations, however, the flames burn incompletely, and are driven by their own buoyancy. To obtain a deflagration that can propagate in all directions, 9% H_2 is needed for weak ignition sources (Krok 1992). In the COMP series of tests, ignition was supplied by a jet of combustion products. In addition to supplying heat and turbulence to the receiver gas, the jet may burn as a diffusion flame, providing additional energy.

The S series repeated some of the COMP tests using water vapor as a diluent, at 373 K. In this series, only the 12.7-mm nozzle was used. These tests compared the effectiveness of steam and nitrogen as diluents.

3.2 Results and Discussion

The COMP series test matrix is shown in Table 3.1. Figure 3.1 summarizes the results and compares them to those from RPI. The solid points represent tests run at RPI, while the open points are from the CIT COMP tests. The reference line is the adiabatic, isochoric complete combustion pressure (P_{AICC}) calculated by STANJAN (Reynolds 1986).

The tests showed that a hot jet of H_2 and water vapor could ignite a deflagration in mixtures containing at least 6% H_2. The combustion at this concentration was incomplete, however. The hydrogen concentration had to be increased to 8% for complete combustion to occur. Tests in the RPI facility using a glow plug for ignition found that 9% hydrogen was required for any kind of combustion to occur. Glow plug tests were not run in the HYJET facility, but the results should be similar.

Similar results for H_2-air mixtures were found by Benedick et al. (1984) and Marshall (1986), using spark and glow plugs for ignition. These igniters could initiate weak, upward-propagating flames in mixtures with at least 5% H_2, but 8% H_2 was required for complete combustion. The use of mixing fans during combustion was found to increase the degree of completion in the lower concentrations. The tests by Benedick also included 30% N_2 preinerting (30% N_2-70% air); these showed similar results, although some of the tests with 6 and 7% H_2 failed to ignite.

Völkl and Schlamp (1996) studied ignition of H_2-air mixtures with a hot jet of air, heated by a reflected shock. For a jet temperature of 2550 K, they required a minimum of 10% H_2 to initiate a deflagration in their test chamber. The jet temperature in HYJET has not been measured, but the 12.7-mm jet temperature was measured at RPI (Krok 1992) and estimated to be 1200 K. The jet temperature may be slightly higher in HYJET, owing to differences in the facility design. The combustion-generated jet injects radicals into the receiver, making up for the lower temperature. Also, since the jet contains excess hydrogen, it has the potential to re-ignite as it enters the receiver. The jet can thus maintain temperature as it entrains the cooler receiver gasses.

In the RPI facility, both vessels were of identical size (0.43 m^3). Because of the 1:1 volume ratio, the tests were dominated by jet combustion and pressurization. In addition to the influx of mass, the receiver pressure was increased by combustion of hydrogen in the jet. The work by Ross (1994) determined that both the 12.7 and 25-mm jets could produce stable diffusion flames as they vented into the receiver. Thus, as nozzle size is increased, more mass enters the receiver, and more hydrogen burns in the diffusion flame. The 12.7-mm nozzle was small enough to minimize these effects, giving a clear deflagration limit seen in Figure 3.1. The peak pressures remain fairly level until they jump at 6% hydrogen, indicating a deflagration. (This is a marginal case, as evidenced by both high and low points at this concentration.) With the 25-mm nozzle, the receiver pressure repeatedly exceeds the AICC value. The slope in peak pressure is higher between 4 and 6% hydrogen than between the other points, but this would be hard to justify as a deflagration limit without the information from the 12.7-mm nozzle.

In the CIT HYJET facility, receiver pressurization is much less significant. This is illustrated in Figure 3.2, which compares the receiver pressure traces for the 12.7 and 25-mm nozzles venting into 50% air-50% N_2. With the 12.7-mm nozzle, the RPI receiver sees a peak pressure of over 2.5 bar, but the CIT receiver reaches only 1.1 bar. Pressurization is even more pronounced for the 25-mm nozzle, for which the peak pressures reach 3.75 and 1.25 bar, respectively. The lower jet pressurization in HYJET makes deflagrations much easier to detect.

With this in mind, we can examine the full pressure traces from the RPI tests with

Table 3.1: COMP series receiver mixtures.

Case	% Hydrogen	% Nitrogen	% Air
COMPAIR	0	0	100
COMPN2	0	100	0
COMP0	0	50	50
COMP2	2	49	49
COMP4	4	48	48
COMP6	6	47	47
COMP8	8	46	46
COMP10	10	45	45

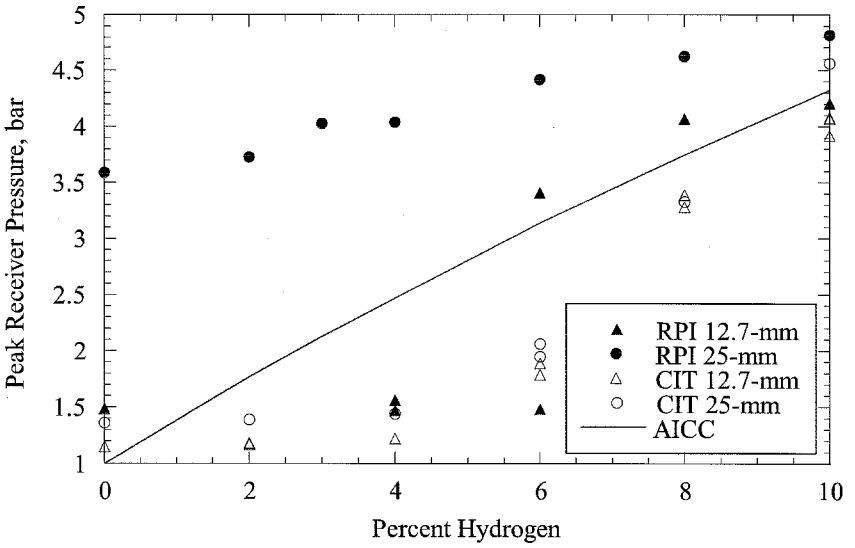

Figure 3.1: Comparison of RPI and CIT facilities: 0-10% hydrogen in 1:1 air:nitrogen.

the 25-mm nozzle, shown in Figure 3.3 (taken from Ross (1994)). As the hydrogen concentration is increased, the peak pressure continuously rises, with no large jump between 4 and 6%.

By comparison, the onset of deflagration is much clearer in the HYJET facility. In Figure 3.1, the peak pressures for both nozzles are nearly constant for 0-4% hydrogen. At 6%, there is a small but distinct jump. The transition is clearly visible in the full pressure traces, shown in Figures 3.4 and 3.5. With both the 12.7 and 25-mm nozzles, the trace for 6% H_2 climbs well above those for lower concentrations. The slow pressure rise compared to the higher concentrations shows the lower speed of the burn. Also, note that there is a delay in ignition, particularly for the 25-mm nozzle. This may be caused by reverse flow through the nozzle, as shown in Figures 3.6 and 3.7. The driver mixture burns in 4–5 ms, generating hot hydrogen and water vapor as products. The products cool quickly because of the driver's cold walls and large surface to volume ratio, condensing the water.

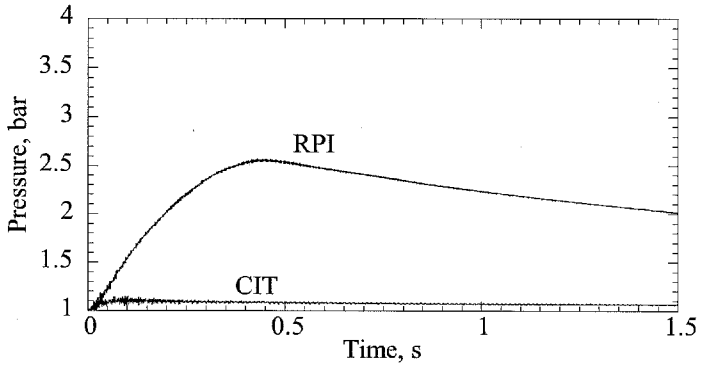

a: 12.7-mm nozzle

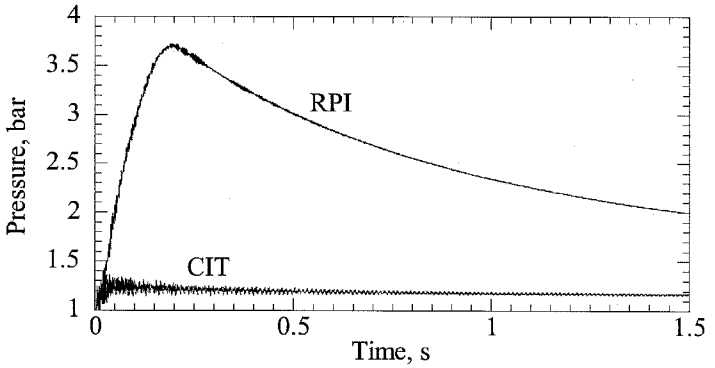

b: 25-mm nozzle

Figure 3.2: Comparison of RPI and CIT receiver pressurization, driver venting into 1:1 air:nitrogen.

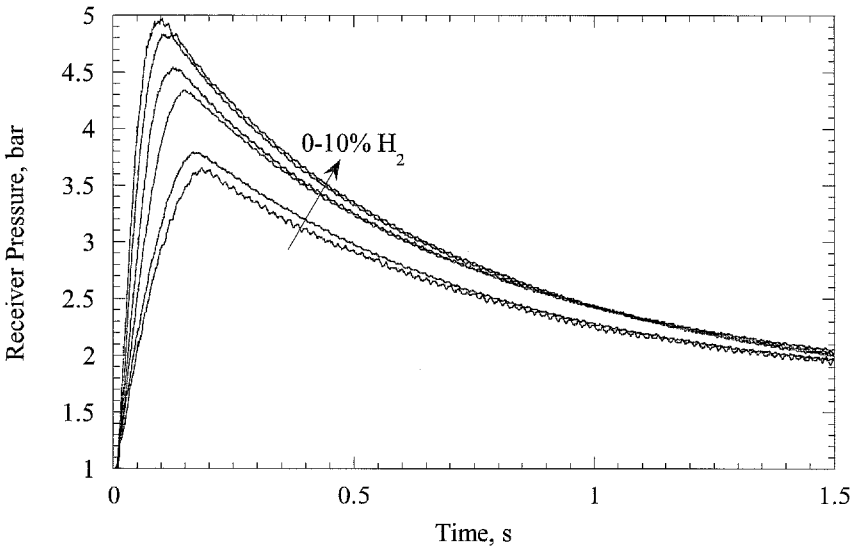

Figure 3.3: Receiver pressure traces for the original COMP-type tests in RPI facility, venting through 25-mm nozzle.

This rapidly drops the pressure to below 1 bar. Now, the pressure drop across the nozzle is reversed, and flow through the nozzle is reversed until the pressures equilibrate. The reverse flow period is shorter with larger nozzles. Figure 3.6 shows pressures for the 12.7-mm nozzle. The traces in Figure 3.6a are from an inert receiver (which is a close approximation to the 6% H_2 case). We see that reverse flow occurs from $0<t<1.1$ s. Figure 3.6b shows a case with a deflagration in the receiver (10% H_2). The increased pressure in the receiver extends the reverse flow period to almost $t=1.4$ s. Figure 3.7 shows the same cases for the 25-mm nozzle, and we see that the driver response is much quicker, shortening the reverse flow period. In terms of weak receiver deflagrations, the flame might not be able to outrun this reverse flow, although it does not get extinguished. In Figure 3.7a, we see that the reverse flow ends at about $t=0.25$ s. The 6% deflagration in Figure 3.5 doesn't show a pressure increase until $t=0.45$ s, so it must take some time for the flame kernel to re-establish itself. The 12.7-mm restricts the reverse flow, so the 6% deflagration in Figure 3.4 proceeds immediately. This reverse flow will again be significant in the next chapter (SA test series).

Although the receiver pressure traces indicate when a deflagration occurs, they do not indicate the completeness of combustion. At 10% H_2, combustion should be complete, but may not be for the 8 and 6% mixtures. A simple analysis (Krok 1992) can give a rough idea of the degree of combustion. First, the two vessels are combined into one control volume. Then, the reaction balance is written, weighting the mole (partial pressure) fractions with the vessel volumes. For example, the 6% H_2 mixture gives us:

$$28(0.8H_2 + 0.2O_2) + 1180(0.6H_2 + 0.47N_2 + 0.47(0.79N_2 + 0.21O_2)) \longrightarrow$$
$$93.2H_2O + 991.2N_2 + 75.8O_2$$

When the vessel cools after combustion, we assume that all of the water condenses to

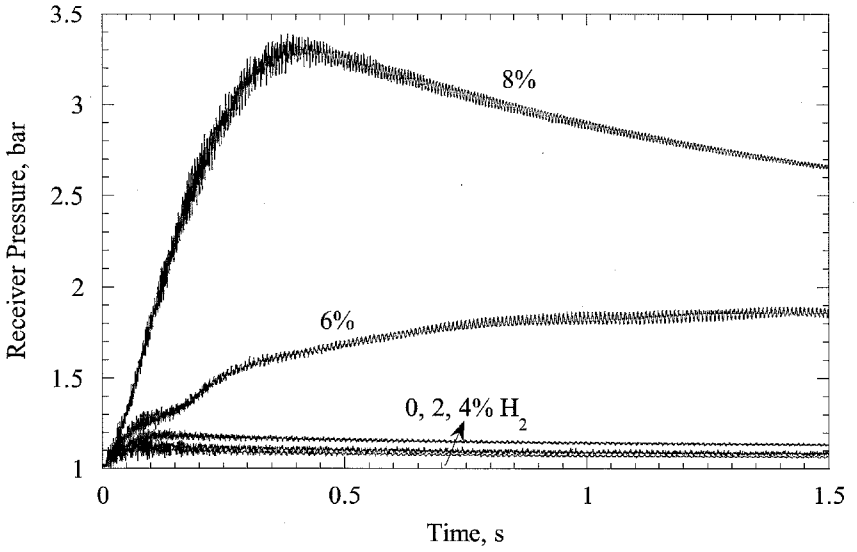

Figure 3.4: Receiver pressure traces from COMP series in HYJET facility, venting through 12.7-mm nozzle.

Table 3.2: Comparison of measured and calculated final pressures.

% H_2	P_f, calculated	P_f, 12.7-mm	P_f, 25-mm
2	0.985	0.988	0.981
4	0.956	0.988	0.984
6	0.926	0.954	0.952
8	0.897	0.901	0.904
10	0.868	0.872	0.868

liquid, and makes no contribution to the pressure. Using the ideal gas law, $PV{=}nRT$, we note that $P/n{=}RT/V$, which is constant (we are bringing T back to the initial value). The result is that $P_f{=}(n_f/n_i)P_i$, or the final pressure is the original pressure multiplied by the mole ratio across the reaction. In addition to the condensed water, this accounts for mole reduction in combustion. For the 6% H_2 case, this gives us $P_f = 1.0(991.2{+}75.8)/(93.2{+}122.4{+}991.2) = 0.884$ bar. Finally, we account for the condensed water by adding its vapor pressure. The tank is cooled to about 303 K when the final pressure is measured; the corresponding vapor pressure is 0.042 bar. The expected value of P_f for complete combustion of the 6% H_2 mixture is thus 0.926 bar. These final pressures are tabulated in Table 3.2, and compared to representative values from the experiments.

In the real system, not all of the driver hydrogen burns, resulting in higher final pressures. Also, variations in measurement temperature will affect the results. For cases with no deflagration in the receiver, the final pressure is recorded at only 293 K or so. Also, there may not be enough water present to make up the 0.042 bar stated as the vapor

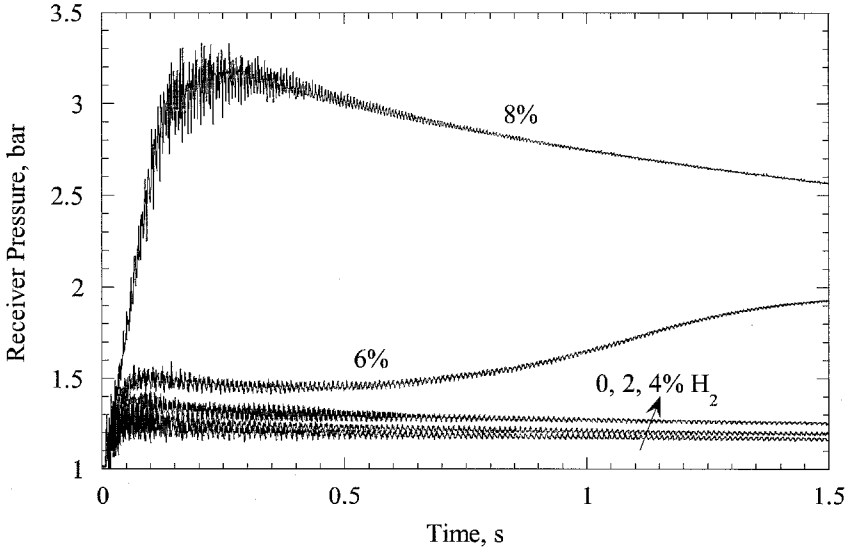

Figure 3.5: Receiver pressure traces from COMP series in HYJET facility, venting through 25-mm nozzle.

pressure. For 2 and 4% H_2, we see that the final system pressure is fairly constant for the two nozzles. It is slightly lower for the 25-mm nozzle, probably because the larger nozzle vents more H_2 into the receiver where it burns as a diffusion flame. At 6% hydrogen, there is a definite drop in P_f, but it is not as low as expected. The conclusion is that combustion was not complete. In the 8 and 10% mixtures, we get final pressures that are very close to the calculated value, indicating complete combustion. Even though we found a deflagration limit at 6% hydrogen, combustion was not complete until 8%. These results agree with those of Benedick et al. (1984) and Marshall (1986), where gas chromatography was used to analyze the post-burn mixtures. Marshall found a combustion fraction of 90% for 6% H_2, although both experimenters experienced difficulties with the chromatograph equipment. Thus, their estimates of burn completion were given for reference only.

The S series of tests duplicated the COMP series, but replaced the nitrogen in the receiver with water vapor. The starting temperature of these runs was approximately 373 K. Only the 12.7-mm nozzle was used in these tests. The results are shown in Figure 3.8. With water vapor, we needed at least 8% H_2 in the receiver to get a deflagration, compared to 6% for N_2 dilution. Water vapor is a more effective diluent than nitrogen, as it has a higher heat capacity (C_v=0.74 and 1.41 kJ/kg-K for N_2 and H_2O, respectively, at 300 K). Figure 3.9 directly compares the receiver pressure traces for the COMP8 and S8 tests with a 12.7-mm jet. The nitrogen mixture burns much quicker, giving a sharp peak pressure. The water vapor mixture has a low, broad peak pressure. The presence of water vapor in this mixture reduces the flame speed (Liu and MacFarlane 1983; Liu et al. 1980), allowing heat transfer to occur during the burn, and reducing the peak pressure. The peak pressure seen in the plot is about 2 bar, while P_{AICC}=2.92 bar for this mixture. The increase in initial temperature also reduces the peak pressure, but

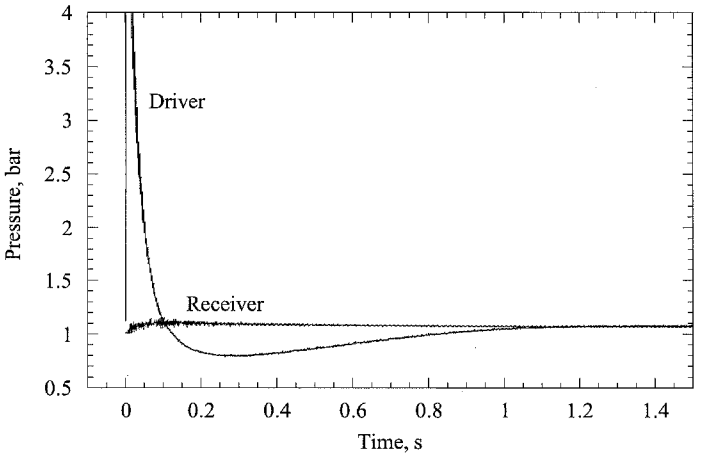

a: 1:1 air:N_2 receiver, no H_2.

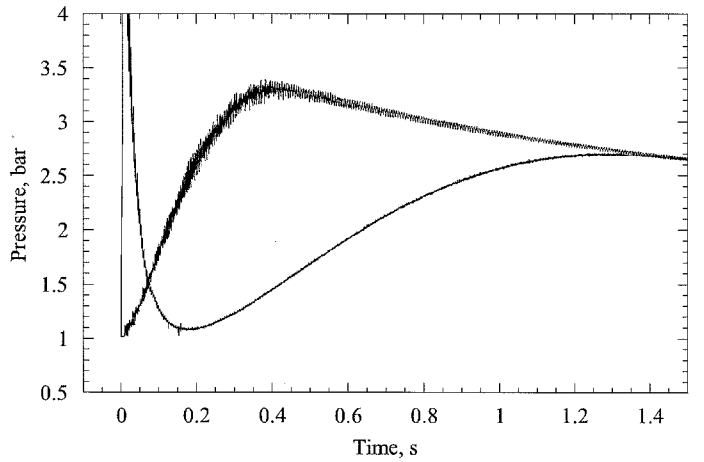

b: 8% H_2 in 1:1 air:N_2 receiver.

Figure 3.6: Pressure traces for 12.7-mm nozzle venting into nonflammable and flammable receivers.

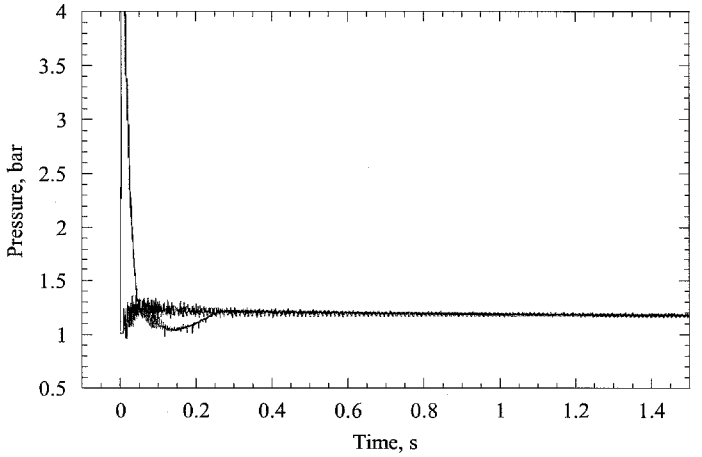

a: 1:1 air:N_2 receiver, no H_2.

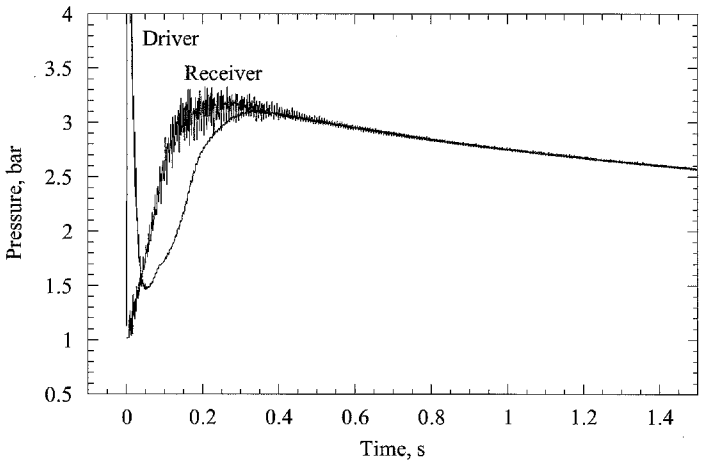

b: 8%H_2 in 1:1 air:N_2 receiver.

Figure 3.7: Pressure traces for 25-mm nozzle venting into nonflammable and flammable receivers.

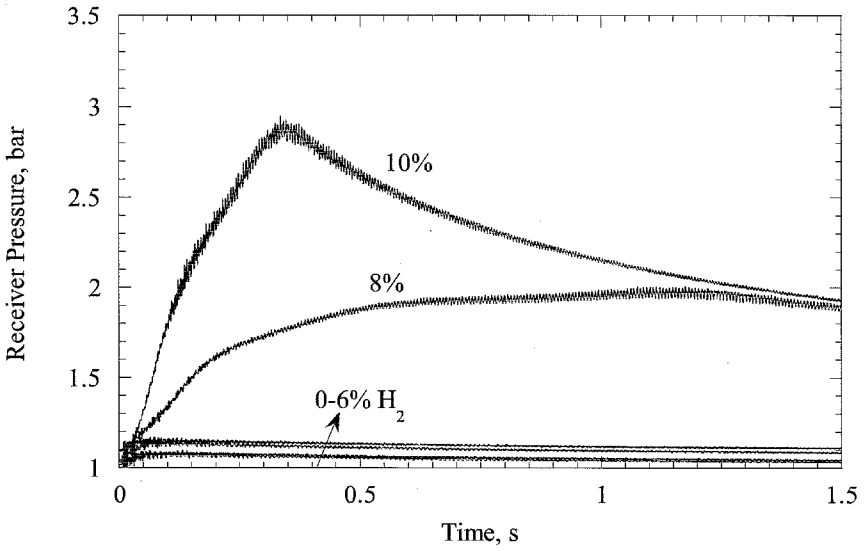

Figure 3.8: Receiver pressure traces from S series in HYJET facility, using 12.7-mm nozzle.

not to this degree. At the higher temperature, the gas mixture is less dense, reducing the energy density and total energy in the vessel. From STANJAN calculations, P_{AICC} for the COMP8 receiver at an initial temperature of 300 K is 3.75 bar. This drops to 3.17 bar for an initial temperature of 373 K. Marshall (1986) also found that combustion times were increased with the addition of water vapor.

The mole-balance test for complete combustion can not be used for the S series, due to the high water fraction in the receiver and difference in vessel temperatures. Although the receiver is heated, the driver is left at room temperature. As water vapor condenses in the driver (from the initial combustion event), the pressure drops to subatmospheric (see reverse flow discussion on page 27). The reverse flow drives more hot water vapor into the driver, which continues to condense. The result is a constant flow of vapor into the driver, and a buildup of liquid water. With the difference in vessel temperatures, there is some ambiguity in the amounts of condensed and gaseous water. Also, the driver is not equipped with a condensate drain, so cleanup is difficult. As a result, in these experiments, the vessels are evacuated using the liquid ring pump as soon as the system pressure drops below 1 bar. Liu et al. (1980), however, found that there is no significant difference in the degree of combustion between wet and dry mixtures of the same H_2 concentration.

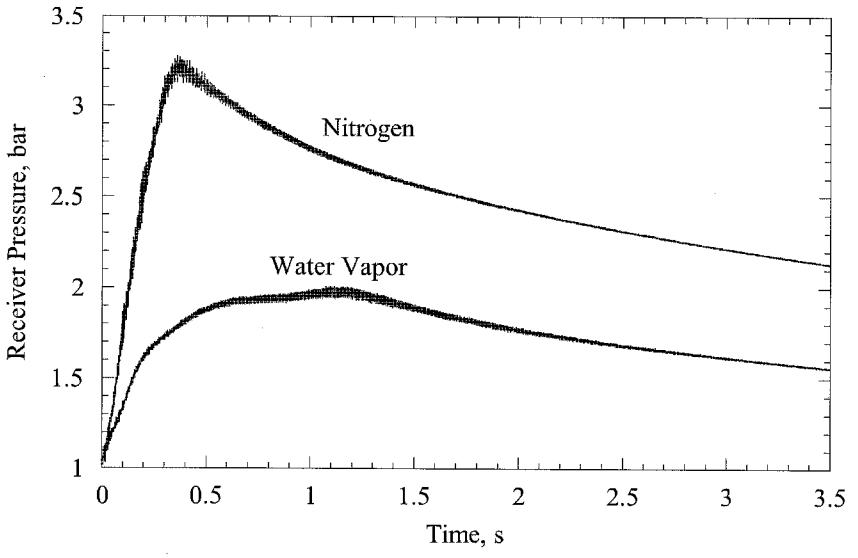

Figure 3.9: Receiver pressure traces showing effectiveness of water vapor as diluent. Mixtures are 8% H_2 in 1:1 air:diluent, with T=300 K for N_2 and 373 K for H_2O.

Chapter 4

SA Series

4.1 Introduction and Background

The SA series of tests examines the effect of ignition source strength on the flammability of H_2-air mixtures with steam dilution. In this series, the hydrogen:air ratio was kept constant at 1:4, or 20% H_2 in air (dry). This mixture was then diluted with 0–60% water vapor. The mixtures are listed in Table 4.1. The initial receiver temperature was approximately 373 K. The driver contained 80% hydrogen and 20% oxygen at 1 bar and 293 K. The 12.7, 25 and 92-mm nozzles were used for receiver ignition.

4.2 Results and Discussion

Figure 4.1 summarizes the results of the SA-series tests by comparing the peak receiver pressures to P_{AICC} for the full range of vapor concentrations. As the vapor concentration is decreased from 60 to 50%, the peak pressures rise to the AICC line. From 40% to zero, the peaks for the 12.7 and 25-mm nozzles plot right along the line. (At elevated receiver temperatures, condensation of products at the walls is slower, and the reaction can reach the theoretical peak pressure.) The peak pressures from the 92-mm nozzle lie above the

Table 4.1: SA series receiver mixtures.

Case	% Water Vapor	% Hydrogen	% Air
SA0	0	20	80
SA10	10	18	72
SA20	20	16	64
SA30	30	14	56
SA40	40	12	48
SA50	50	10	40
SA55	55	9	36
SA60	60	8	32

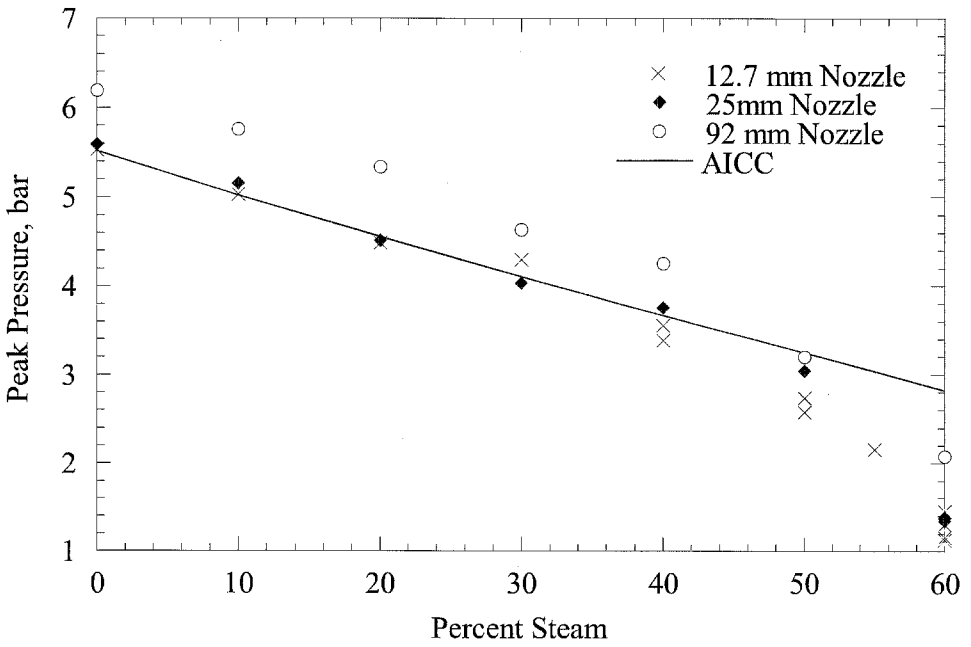

Figure 4.1: Summary of peak receiver pressures for SA-series tests.

AICC line. This is probably due to dynamic effects, such as pre-pressurization of the receiver mixture by the jet startup shock.

Previous experiments by Marshall (1986) used similar mixtures in a condensing-steam environment, with glow plug ignition. The dilution limit was found to be 50% in those tests. Other work cited in that report found maximum limits of 55% H_2O. Djebaili et al. (1994) used a hot jet of 60% H_2-40% Ar to ignite 18% H_2-82% air mixtures with water vapor dilution. With a jet temperature of 2550 K (generated by shock reflection), they found a dilution limit of 48% H_2O. In the present experiments, the 12.7-mm jet was able to initiate a deflagration in a 60% H_2O mixture. Despite the lower temperature (Chapter 3), the radicals in the combustion-generated jet make it a more effective initiator.

The individual tests are illustrated in Figures 4.2–4.4. Figure 4.2 shows the receiver pressure traces for the 12.7-mm nozzle, with vapor concentrations from 0 to 60%. The lowest trace on the plot (from run 68) corresponds to 60% water vapor. A deflagration is seen in this case, but the pressure does not begin to rise until nearly one second after driver ignition. This deflagration takes a long time to ignite, but still progresses. This was also seen in the video recording from the schlieren system. Typically, when a deflagration is initiated in the receiver, it starts when the jet enters the receiver and proceeds down the vessel. In run 68, however, the jet from the driver starts and finishes before any deflagration is seen. At 0.68 seconds after driver ignition, a flame front is seen moving back into the field of view, traveling in the upstream direction. This indicates that the slug of products from the driver ignited the receiver mixture somewhere downstream. Perhaps the mixture was ignited immediately, but the flame speed was so slow that the ignition kernel was convected downstream with the jet gas. Two other tests were run

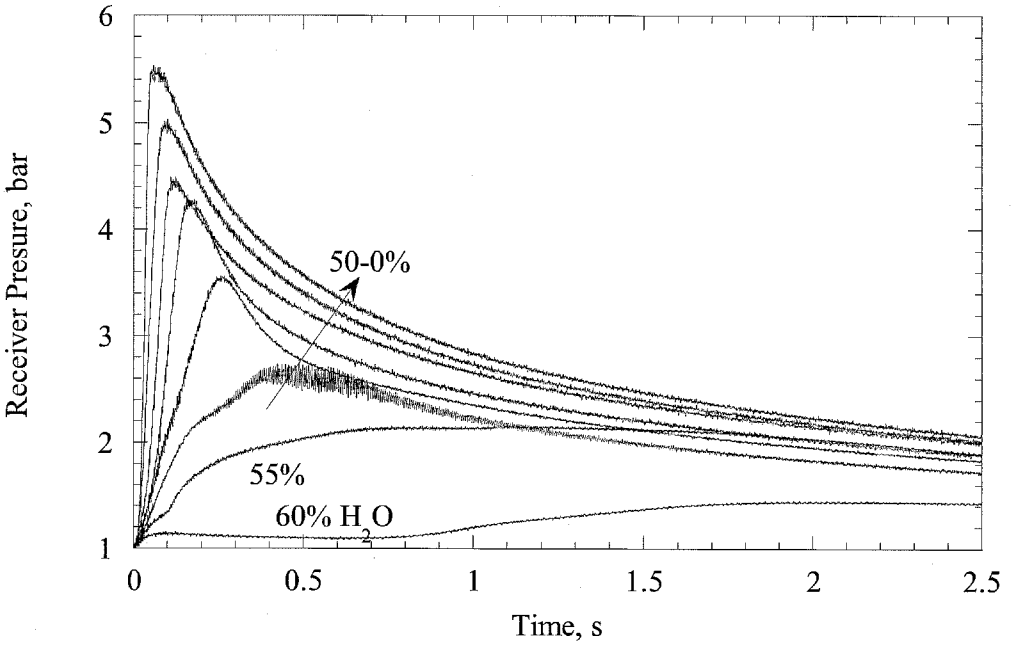

Figure 4.2: Receiver pressure traces from SA-series tests, 80:20 driver venting through 12.7-mm nozzle.

with this mixture, one producing a burn, and the other failing to ignite. Clearly this is a marginal case, and small differences in the water vapor fraction and quality can affect the results.

Figure 4.3 shows the pressure traces for the 25-mm nozzle. Despite two tests with 60% water vapor (SA60), the 25-mm nozzle was unable to ignite a deflagration at this dilution. We saw from Figure 4.2 that the successful deflagration in the SA60 mixture was very slow, comparable to the 6% H_2 mixture in the COMP tests. In those tests, we speculated that the reverse flow after jet depletion was inhibiting propagation of the flame. In the current tests, the strength of the reverse flow with the 25-mm nozzle may be extinguishing the flame kernel before it can propagate. The tighter obstruction provided by the 12.7-mm nozzle constricts the reverse flow and allows the flame to persist. Also during the 25-mm SA60 tests, condensation was seen forming on the schlieren windows (the windows can not be insulated). Problems with condensation in the steam supply may have created a condensing atmosphere, affecting the results.

Pressure traces from the 92-mm nozzle are shown in Figure 4.4. A 5-point average has been used to reduce the oscillations on these traces. With this nozzle, driver effects dominate the receiver pressure. There is a large jump from 60 to 50% water vapor, so it does not appear that a deflagration occurs at 60%. However, the trace for 60% is above that for 100% air. Also, the 60% trace has a blunt peak, offset from the y-axis, that is indicative of weak combustion (vs. the sharp peak close to the axis for a shock alone). In Figure 4.5, we will see that the long-term pressure trace for 60% H_2O coalesces with that for the 12.7-mm nozzle (see below).

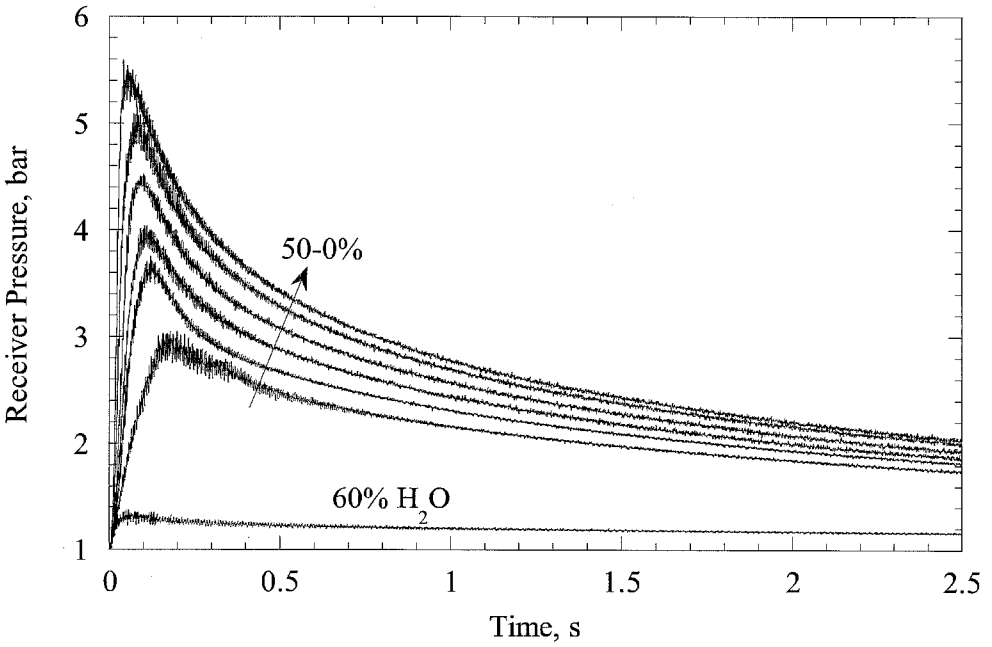

Figure 4.3: Receiver pressure traces from SA-series tests, 80:20 driver venting through 25-mm nozzle.

Figure 4.5 shows receiver pressure traces for the three nozzles used in this series, with 60% water vapor in the receiver. The trace from the 12.7-mm nozzle shows the initial pressurization, followed by a shallow decay as gas flows back into the driver. At t=1 s, the pressure increases again as the deflagration proceeds. The pressure peaks between 3 and 3.5 s, and then decays as the products cool. With the 25-mm nozzle, there is a higher initial peak, but the pressure then decays with no rebound. The higher initial pressure is due to an increased amount of mass venting from the driver before the flow reversal, as well as combustion of hydrogen in the jet. With the 92-mm nozzle, there is a much higher initial pressure. Much of this is from the startup shock. This masks the early stages of the deflagration, but it is evident where the pressure trace joins that from the 12.7-mm nozzle at t=3 s. Also, note the increase in oscillations with nozzle size. This is particularly evident with the 92-mm nozzle. The oscillations are the result of shocks reverberating in the vessel. The soundspeed of the burned SA60 mixture is 740 m/s (STANJAN). The vessel is approximately 2 m long, so an acoustic wave takes 5 ms to make a round trip. The corresponding frequency is 185 Hz, low enough to be resolved by the Kulite sampling at 1 kHz. Expanding the trace for the 92-mm nozzle revealed that the oscillation period was 6 ms, in close agreement with the predicted time. As the mixture cools, the soundspeed decreases, increasing the period. The trace for the 12.7-mm nozzle is smooth in comparison to the other two.

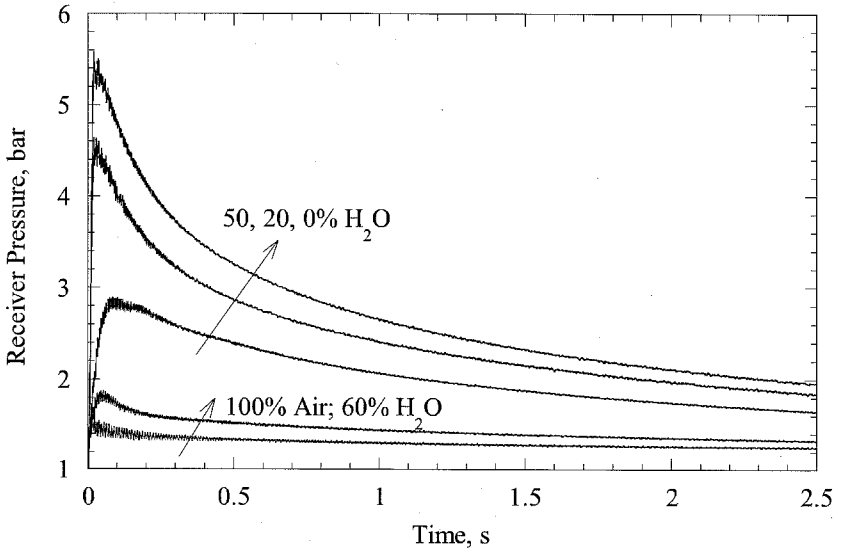

Figure 4.4: Receiver pressure traces from SA-series tests, 80:20 driver venting through 92-mm nozzle. Shock oscillations smoothed by a 5-point average (see Figure 4.5 and discussion).

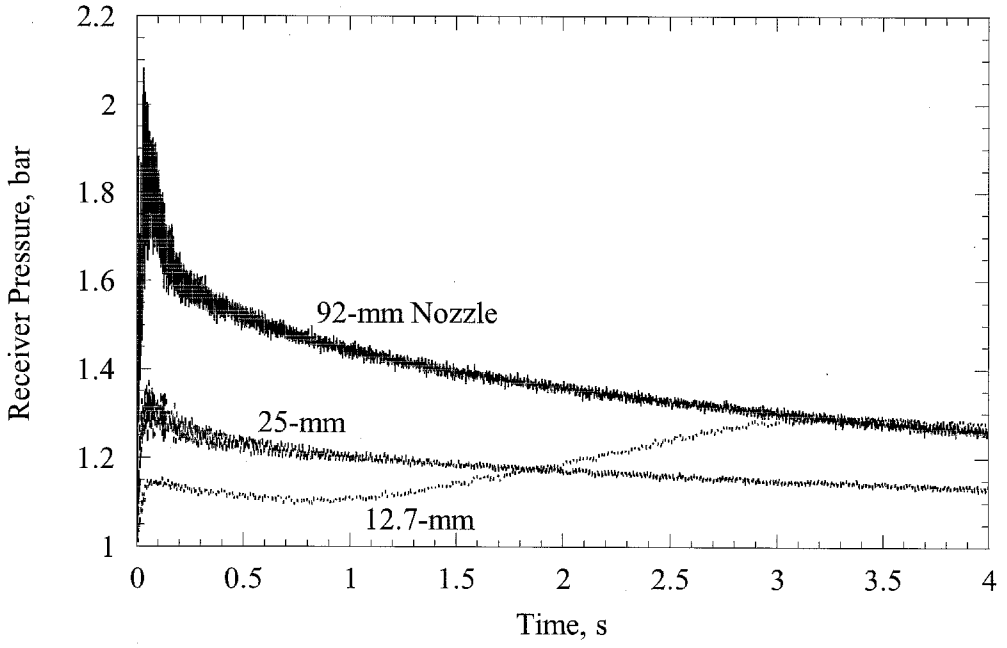

Figure 4.5: Receiver pressure traces for SA60 mixture, showing effect of nozzle size. Note increase in peak pressure and increase in oscillations as nozzle size is increased.

Chapter 5

NITRO Series

5.1 Introduction and Background

This series of tests began our study of jet initiation of detonation. The work by Knystautas et al. (1979) showed that turbulent mixing of reactants and hot combustion products could initiate a detonation. Those experiments focused on DDT of a flame front venting through an orifice. Two directly connected vessels (with no diaphragm separation) were uniformly filled with an oxy-acetylene mixture. Orifice plates with various hole configurations were mounted in the connection between the vessels. The mixture was spark ignited in one chamber, and vented into the other through the orifice plate. With the proper arrangement of holes, the flame would transition into a detonation shortly after passing through the plate. The best arrangement was found to be an array of holes with a spacing large enough to prevent recombination of the small jets into one large jet. In addition to the orifice plates, wire screens could be installed to generate fine scale turbulence. The results indicated that transition was aided by both large and small scales of turbulence. Large eddies serve to entrain fresh reactants into the hot jet gas, while the fine scales mix the gases together. The use of screens alone would not cause DDT, as there were no large-scale structures to create entrainment. With an orifice plate alone, the detonation appeared to begin in a localized explosion on the surface of the jet. With the addition of the screen, the entire surface of the jet transitioned at once, at a shorter distance from the exit. Finally, if a particular orifice plate could not cause transition, addition of the screen would not help. It is important to note that entrainment has two counteracting effects: While entrainment and mixing heats the receiver mixture, it also dilutes and cools the jet gas, reducing its effectiveness. Ignition occurs when a balance is reached between these two processes.

Other research (Moen et al. 1985; MacKay et al. 1988; Moen et al. 1989) expanded these results to larger scales and less-sensitive mixtures, but in all cases the "driver" and "receiver" chambers were continuously connected, making it difficult to quantify the jet at the time of start-up. (The aim of these experiments was to study DDT in a fuel-oxidizer cloud containing obstacles, possible in an industrial accident, so attempts were not made to quantify the jet.) The first work to separate the vessels with a diaphragm was

that of Carnasciali et al. (1991), followed by Dorofeev et al. (1993), Bezmelnitsyn et al. (1995), Dorofeev et al. (1995) and Bezmelnitsin et al. (1997). The work of Carnasciali et al. (1991) and Bezmelnitsin et al. (1997) will be further addressed in the next chapter, which describes the BETA test series. The work by Dorofeev has some connection to the present NITRO series, as their driver and receiver chambers used hydrogen-air mixtures. In many works, what we refer to as the "driver" is named the "jet" or "flame" chamber. Likewise, the receiver is named the "detonation" or "explosion" chamber. I will use the "driver" and "receiver" terms throughout for clarity.

5.2 Results and Discussion

The present NITRO test series began with a driver mixture of 80% H_2-20% O_2, and went on to study the effect of a slower driver flame speed. The flame speed was reduced (see Figure 5.3) by diluting the H_2-O_2 mixture with nitrogen, to a maximum of 50%. Since the diluent displaces reactants, it also reduces the peak driver pressure. To correct for this, the initial driver pressure was increased with the amount of dilution, in a way that would keep the peak pressure constant (9.7 bar, corresponding to no N_2). The required initial pressures were calculated with STANJAN. The resulting driver mixtures are shown in Table 5.1. Unforeseen dynamic effects raised the peak pressures, however (discussion below).

Table 5.1: NITRO Series driver mixtures.

Driver	% Nitrogen	% Hydrogen	% Oxygen	P_i, mbar
0N	0	80	20	1000
5N	5	76	19	1018
10N	10	72	18	1036
15N	15	68	17	1057
20N	20	64	16	1083
25N	25	60	15	1114
30N	30	56	14	1152
35N	35	52	13	1198
40N	40	48	12	1254
45N	45	44	11	1322
50N	50	40	10	1405
55N	55	36	9	1506

All of the tests used the 92-mm nozzle. The receiver mixtures consisted of 0-30% hydrogen in air at one bar and room temperature. The objective of the tests was to determine the lean limit of receiver detonation initiation for each driver dilution. We did not expect direct initiation of detonation in the receiver; previous tests have indicated (Dorofeev et al. 1993) that a minimum jet diameter of 13λ is required to directly initiate a

detonation via a turbulent jet. Cell-size measurements for stoichiometric (30%) hydrogen-air range from 11 mm (Bull et al. 1982; Stamps and Tieszen 1991) to 15 mm (Guirao et al. 1982). Based on these values, the 92-mm nozzle in HYJET has a D/λ ratio of only 6.1–8.4 for this mixture. However, the tests showed that we were able to initiate detonations in mixtures with as little as 24% hydrogen, or D/λ=4.3 (Guirao et al. 1982). The current experiments used the PCB transducers mounted on the end flange (reflected pressure) and the last top port of the receiver vessel (static pressure). These are the E and T3 locations shown in Figure 6.2 on page 62. Data was acquired at 250 kHz for 32 ms.

The results were surprising. Some of the tests showed high pressure peaks after the initial shock wave, even with no detonation evident. In order to better separate the results, we use a criteria called "prompt" initiation. Initiation is prompt when both the static and reflected pressure traces show the passage of a detonation. Figure 5.1a shows a prompt detonation. Both of the pressure traces show the sharp rise in pressure and peak values characteristic of a detonation. Figure 5.1b shows a trace from a failed initiation. The lead wave on both transducers is small, but strong secondary explosions are evident shortly after passage of the lead wave. The secondary explosions in Figure 5.1b probably occur in the precompressed mixture at the end of the vessel. We later determined that this was the result of shock focusing (described below).

Due to the D/λ limitations of our driver, we originally thought that the "prompt" cases were the result of a DDT occurring between the jet exit and the T3 transducer. However, the results of the BETA test series (in the next chapter) showed that the detonations were directly initiated by the jet. It appears that the D/λ criteria is not appropriate for this type of experiment, as it does not reflect the driver composition or exit geometry. The initiation process is probably similar to that described by Knystautas: Large eddies from the jet entrain reactants and small-scale turbulence mixes them with the hot products. The startup structure of impulsively generated jets (i.e., from diaphragm rupture) was photographically studied by Lacerda (1986). Photographs show that the jets have a large head, enclosing a vortex ring. The jet head is preceded by a bow shock. Both the shock and the jet head travel downstream, and the jet assumes a quasi-steady structure at the nozzle exit. Photographic tests in the RPI facility (Appendix D) showed the jet head to be highly turbulent, a result of the violent rupture process. In the current initiation experiments, the bow shock will sensitize the reactants before they are entrained by the vortex ring. Once entrained, small-scale turbulence in the head mixes the reactants with the hot jet gas. After a suitable induction time, one or more local explosions will occur, initiating the detonation. Typically, jet initiation is attributed to the SWACER mechanism (shock wave amplification by coherent energy release), first proposed by Lee et al. (1978). This requires an induction time gradient in the reactants, which is provided by turbulent diffusion at the reactant-jet boundary in the large eddies. (If the induction time is uniform, the whole body explodes simultaneously, only reaching the constant-volume pressure. The gradient allows pressure waves to build into a detonation.) Additional vortex combustion studies include Chan et al. (1990), Yip et al. (1985) and McCormack et al. (1972).

The results of the NITRO tests are summarized in Table 5.2. The undiluted driver was able to initiate a detonation in 26% hydrogen, and we expected the diluted drivers to require higher hydrogen concentrations. This was not the case. Drivers with 30% or more N_2 were unable to initiate detonations in any H_2-air mixture. All drivers with 25% and less N_2 initiated detonations in H_2-air mixtures with at least 26% H_2. The "25N" mixture was the most effective, giving a prompt initiation in only 24% hydrogen. Despite the small difference in hydrogen concentrations, the results were repeatable.

Table 5.2: Results of NITRO tests.

% N_2	Minimum % H_2 for Detonation	% N_2	Minimum % H_2 for Detonation
0	26	25	24
10	25	30	No detonation
20	26		

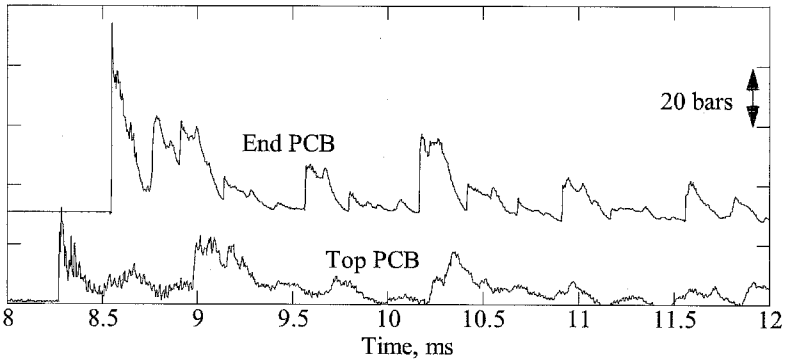

a: "Prompt" initiation.

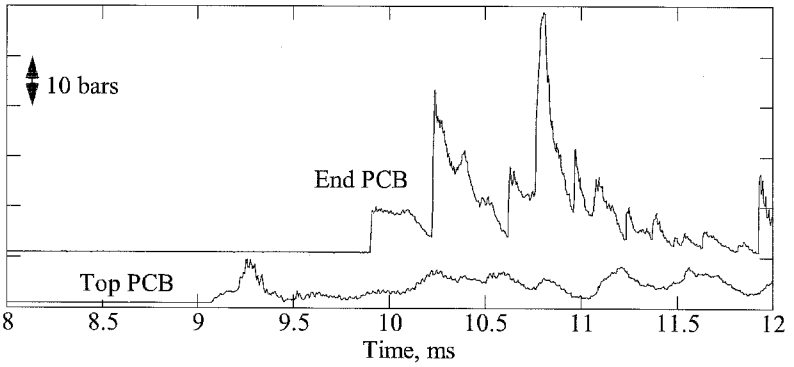

b: Prompt initiation failure with secondary explosion.

Figure 5.1: Examples of prompt initiation and secondary explosion in receiver.

The first step was to determine why the 25% nitrogen driver was more effective than the others. Using the nozzle plug, I ran a series of constant-volume driver tests with the

full range of dilutions. The results, shown in Figure 5.3, indicated that the peak pressures in the driver were not constant as planned. While the flame speed did go down (represented by the burn time, from ignition to peak pressure), the peak pressure increased to a broad plateau of nearly 13 bar. This can only be a dynamic effect of the confinement geometry. When P_{AICC} is calculated by STANJAN, it is strictly an equilibrium calculation. The reactants immediately turn to products, with no consideration for dynamic effects. This is best approximated by rapidly-burning mixtures in a spherical vessel with central ignition. In our case, the vessel is a long tube ignited at one end. Shock waves, such as the one generated at ignition, have time to run to the end and reflect back, compressing the reactants. Furthermore, turbulence can be generated by the annular channel at the driver-extension junction (Figure 5.2), promoting flame acceleration. This would generate further waves and precompression. Also, as the initial pressure is increased, the effects of the shock will multiply. As the N_2 fraction is increased beyond 30%, the decrease in flame speed overcomes these effects, and the peak pressure is reduced by heat transfer during the burn.

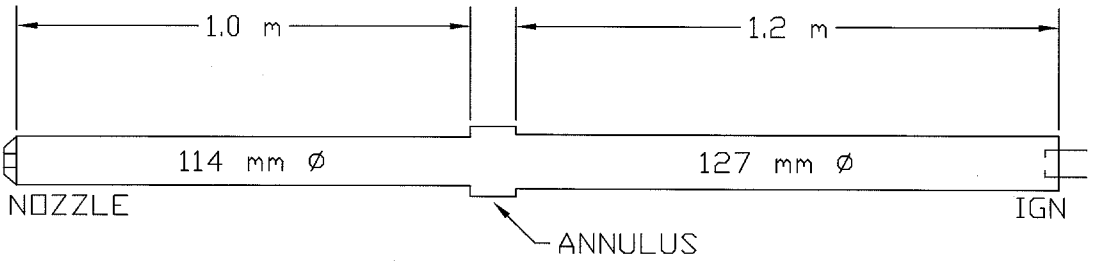

Figure 5.2: Internal geometry of driver vessel. Annular channel (166 mm dia. by 102 mm long) is formed by the hydraulic closure and extension.

The idea of driver enhancement by dilution is not unheard of. In Carnasciali et al. (1991), a driver with stoichiometric H_2-O_2 and 46% N_2 was more effective than one with only 12% N_2. This was attributed to increased radical concentration in the jet with less dilution. They argued that the response time of the receiver mixture must be short enough (i.e., more sensitive) to accept the higher concentration of radicals.

To study the possibility of transition in the driver, I installed a PCB transducer in the instrumentation flange, next to the spark plug. In this location, the transducer can not record the actions near the diaphragm. However, shock waves reflected from the diaphragm or generated by local explosions at the end of the driver can be seen. The reflected pressure ratio is much higher for shocks than for detonations (approx. 7 vs. 2.5, see p. 73), so the shock reflections seen here over-represent the conditions in the driver. The pressure traces from two drivers, with zero and 25% N_2 dilution, are shown in Figure 5.4 (P_{CJ}=18.22 and 18.58 bar, respectively). The 0N driver shows a peak of 15 bar, while the 25N reaches nearly 25 bar. The higher pressure in the 25N driver is a result of the lower flame speed. In this case, there is time for shock reflection and flame acceleration to induce transition to detonation. Without dilution, most of the reactants are consumed before transition can occur. From the pressure traces, it is likely that

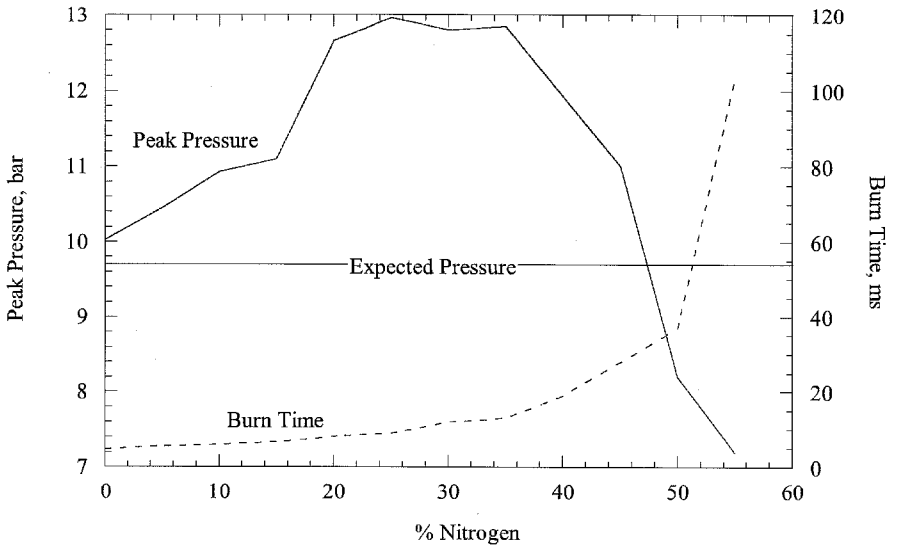

Figure 5.3: Peak pressures and burn times (time to peak pressure) for nitrogen dilution mixtures burned in plugged driver. The peak pressures were expected to fall around 9.7 bar, as calculated with STANJAN.

detonation occurred in the 25N driver, but not in the 0N driver, as the peak reflected pressure in that case is below even P_{CJ}.

If a detonation does occur, our problem becomes one of a stronger impulsive jet, or of detonation transmission and direct initiation. The effect of detonation in the driver can be evaluated with an appropriate wave analysis. Figure 5.5 shows a wave diagram for this system. If a detonation occurs in the driver, it will generate reflected and transmitted waves at the mixture interface (i.e., the diaphragm). Wether the reflection is a shock or an expansion depends on the detonation conditions and the properties of the receiver mixture. When the diaphragm ruptures, it is replaced by a contact surface between the two gases. The pressure and velocity must be matched across this surface (i.e., P_2=P_3, u_2=u_3). The conditions in region 1 are the CJ detonation conditions, and can be computed with an equilibrium code such as STANJAN. The conditions in regions 2 and 3 are computed by shock and expansion relations that calculate pressure change as a function of velocity change across the wave. Typically, ΔP is calculated for a range of Δu across the waves (i.e., the shock Hugoniot), and the matching condition is found graphically. The equations can be found on page 417 of Thompson (1972).

The results of the wave calculations are shown in Figure 5.6. The reflected wave conditions are plotted for both drivers. For the receiver Hugoniot, a representative mixture of 25% H_2-air was chosen. In the figure, the solid lines on the reflected wave indicate a reflected shock, and the dashed lines indicate a reflected expansion. The CJ points are also shown on both curves. If the receiver mixture is tailored, its Hugoniot will pass through the CJ point, and a shock will be transmitted with no reflected wave in the driver. In our case, we see how the character of the reflected wave is affected by the

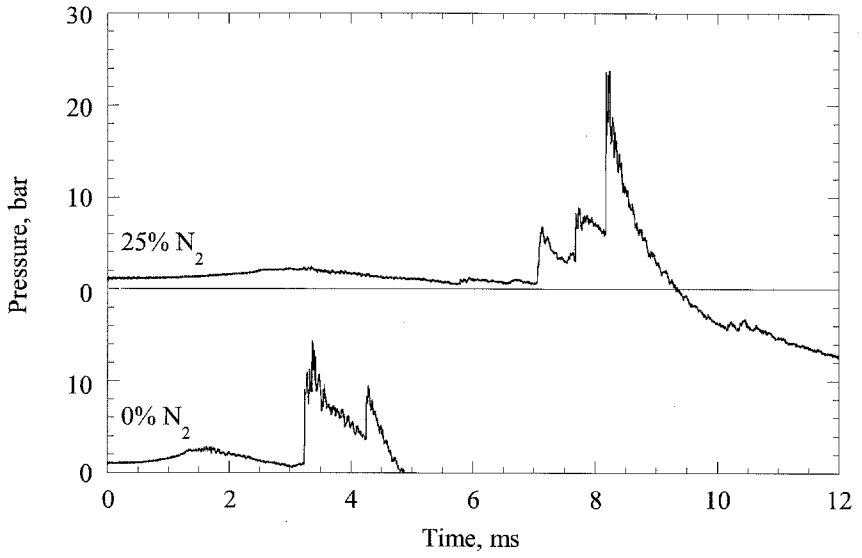

Figure 5.4: PCB traces from NITRO drivers, venting into air. 25N driver shows stronger reflected shock. PCB is located at ignition end of driver.

driver mixture. The high H_2 fraction in the 0N driver results in a high soundspeed, CJ velocity, and gas velocity following the detonation. The receiver mixture is much denser than the combustion products in the driver, and a reflected shock is the result. This drives a stronger shock into the receiver than the 25N driver, where increased driver density allows a reflected expansion to occur.

The Mach numbers of the shocks in the receiver can be determined from the Hugoniot matching conditions. For the 0N driver, the receiver shock has M=4.31, and a post-shock temperature of 1242 K. The 25N driver generates a M=3.98 shock, with a corresponding temperature of 1107 K. To determine the consequences of these shocks, we need to determine the induction time of the shocked mixture. This can be estimated by calculations with thermodynamic data and kinetic mechanisms. I calculated the induction times with a constant-volume combustion program ("CV"), that uses thermodynamic data and chemical kinetics to determine temperature and pressure profiles over time. For the M=4.31 shock (0N driver), the induction time is 27 μs. In this time, the shock moves 45 mm. A typical detonation is less than 1 cm thick, so it is unlikely that a detonation in the 0N driver would directly initiate the 25% H_2-air receiver mixture. In addition, the PCB pressure traces indicated that a detonation was unlikely in this driver, so this shock process may not apply.

The M=3.98 shock generated by the 25N driver leads to an induction time of 0.457 ms, much longer than with the 0N driver. In this time, the shock moves 0.7 m, which would clearly decouple it from the reaction zone. As these shocks leave the nozzle exit, they diffract into the larger receiver vessel, rapidly reducing their strength. Thus, we conclude that neither driver is creating direct initiation conditions.

We will now examine the combustion events in the receiver. In many cases, even with

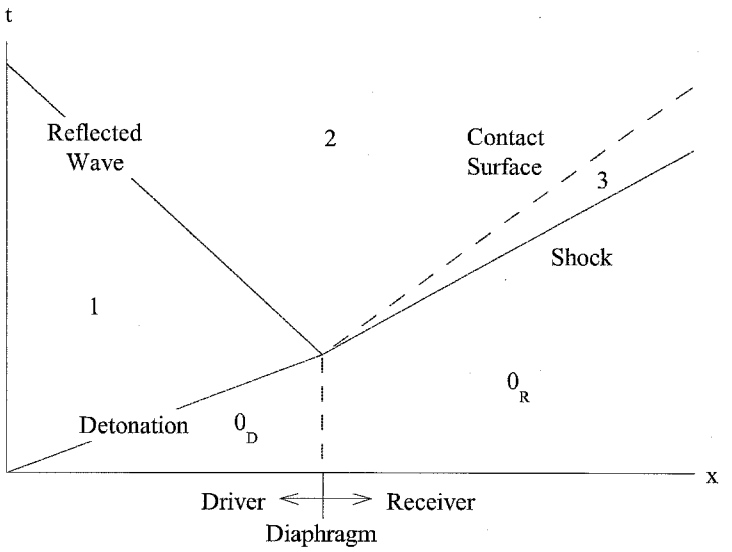

Figure 5.5: Wave diagram for reflection of detonation at end of driver.

prompt initiation, the highest peak pressure did not occur at the lead wave, but some time later. Some of these were very strong. Two of the 25N tests had late peak reflected pressures of just over 100 bar, despite receiver hydrogen fractions of only 22 and 23%. A repeat of the 23% H_2 case obtained a peak pressure of 50 bar, which is half the previous value but still more than the reflected CJ pressure of 33 bar. Clearly, the geometry and dynamics of a confined system is important in any type of combustion analysis. In an attempt to analyze these results, Figure 5.7 plots the highest peak pressure in each test versus the delay time from the initial wave (excluding 8 points with delays over 3 ms). Some of the points fall along $t = 0$, showing that the lead shock or detonation was the strongest wave in the train. Many of the tests, however, had a highest peak near 0.3 ms, as shown by the points clustered around the reference line. This indicated a regular wave phenomena, later determined to be shock focusing.

To summarize the results for the various driver dilutions, Figures 5.8 through 5.12 plot the initial and peak wave pressures (recorded at the end of the vessel) against receiver hydrogen percentage. In all cases, the solid points indicate prompt initiation, and the open points represent all other cases. As these values are taken from the end-mounted transducer, where reflection occurs, only the reflected CJ pressure is shown for comparison. The 25% dilution case (Figure 5.11) has the most data points, and its description can be applied to the other cases. At low H_2 concentrations, <10%, we see that both the lead and delayed-peak waves are small. In the 15–20% range, we begin to see significant secondary explosions, approaching 20 bar. Above 20%, the secondary explosions get quite strong. In these cases, even though the mixture is not sensitive enough to detonate promptly, it is sensitive enough to undergo a local explosion or DDT after it has been sensitized by the lead shock. As we pass the initiation threshold, the peak pressures are relieved to some degree, because the detonation is proceeding into

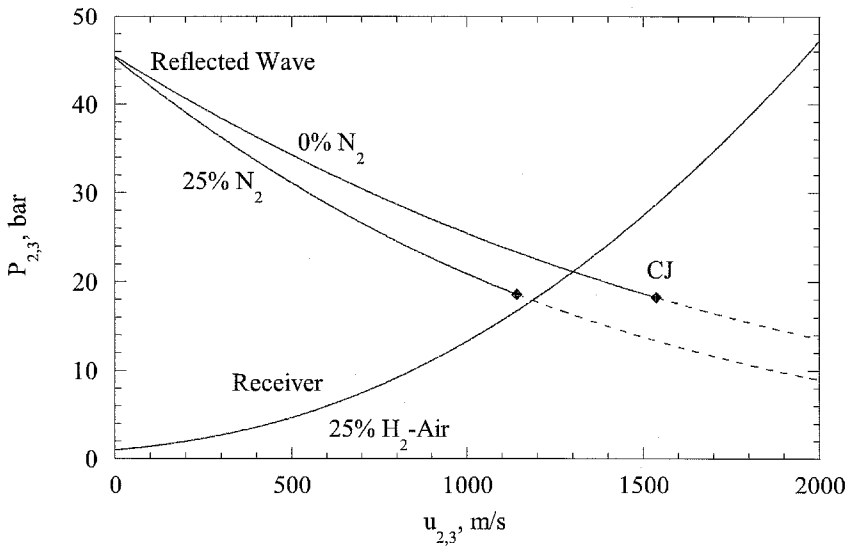

Figure 5.6: Hugoniot plots for reflected wave in driver and shock in receiver. On reflected wave Hugoniot, solid line indicates reflected shock; dashed line indicates reflected expansion.

undisturbed reactants. In terms of industrial or reactor scenarios, this means that the greatest potential for damage may be found in mixtures below the detonation threshold.

To study the shock focusing problem, the E transducer was mounted on a sting penetrating the end flange, aligned with the axis of the vessel. A series of tests were run using a stoichiometric H_2-air driver to generate a shock in the receiver, which was filled with air. One run was made with the sting at each of 16 positions, ranging from 100 to 475 mm from the end of the vessel, in 25 mm increments. The results are shown in Figure 5.13, as a sort of x-t diagram. To account for variations in diaphragm rupture time, each trace was time-adjusted to make the lead shock correspond to a shock of M=1.09 running along the sting. This Mach number was selected based on the lead shock reflected pressure of 1.33 bar. While Figure 5.13 does show focused waves, with peak pressures reaching 2.5 bar and more, no distinct structure is seen. The curved line connects small waves that have a pattern consistent with the results of the ray tracing simulation (described below). Based on calculations of round-trip times, the first large shock after the lead (labeled "initial focus") is not the reflection from the end flange. At the 100-mm station, the delay between the initial shock and this initial focus shock is 0.3 ms, consistent with the characteristic time found in Figure 5.7. This is the focus responsible for secondary explosions, which we will try to model below.

In addition to the timing problems, it seemed remarkable that the lead shock could be amplified to this degree. I wondered if the small shock was not from the diaphragm rupture, but an artifact of driver combustion. To study this, I ran a test wherein the diaphragm was ruptured by slowly pressurizing the driver with air. The sting was placed at the 250-mm station, where it would be outside the flange pipe. As evident from

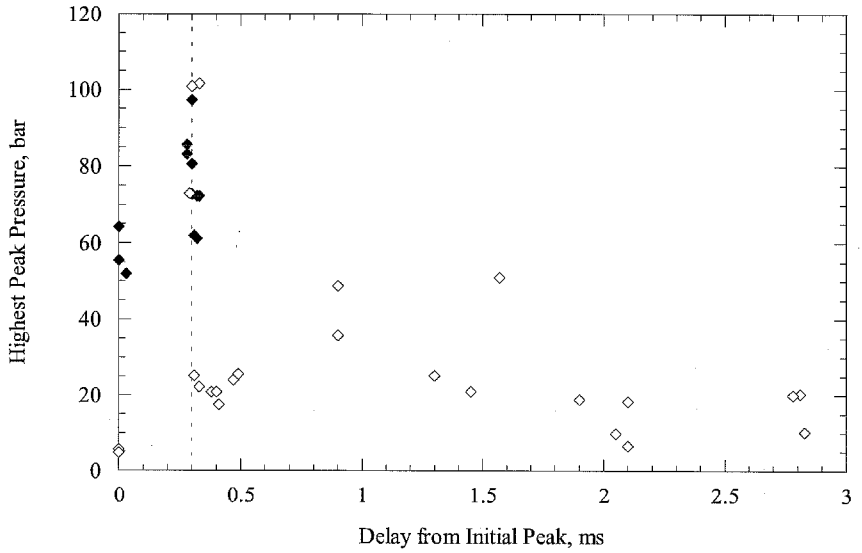

Figure 5.7: Highest peak receiver pressure seen in receiver versus time from lead shock. Note cluster of points around t=0.3 ms.

Figures 5.14 and 5.15, the lead and focused shocks follow the same pattern. Thus, we conclude that the small lead shock is in fact the diaphragm rupture shock, and the following shocks are the result of focusing.

In a final attempt to expose the focusing, an acoustic wave study was performed using a ray tracing program ("raytrace") written by Joe Cates and Danny Howard of GALCIT (Cates and Howard 1993). This program is written in PV-Wave command language, and uses displacement potential functions to track acoustic longitudinal and shear waves. The program can calculate reflections and transmissions at fluid, solid and fluid-solid interfaces.

The ray tracing program uses a unit square as a domain. The inside diameter of the vessel is 0.86 m, so the dimensions were scaled by 1.16. The interior contour of the end flange connection was measured and scaled, and was input with a 4:1 ellipse matching the interior surface of the head. (Previously, the facility has been shown with the receiver on the left and the driver on the right; this has been reversed for simplicity in the calculations.) A curved shock was used as the starting condition, and was generated with 146 rays, each specified by the coordinates of the initial point and the launch angle. The outer ends of the shock start at x=0.05 in model space, and the associated rays were calculated assuming that they radiated from a point source behind the nozzle (see Figure 5.16). The location of this point was chosen so that the rays grazing the edge of the 92-mm nozzle would meet the edge of the elliptical head. The resulting half angle is 14.5°. Rays were launched at 0.2° increments.

The results are shown in Figure 5.17, where t=0 is arbitrarily taken as point of first contact. The extra line segments connecting the waves at t=0.668 ms are artifacts of the program. We clearly see the formation of a focus region at t=1.158 ms, where the

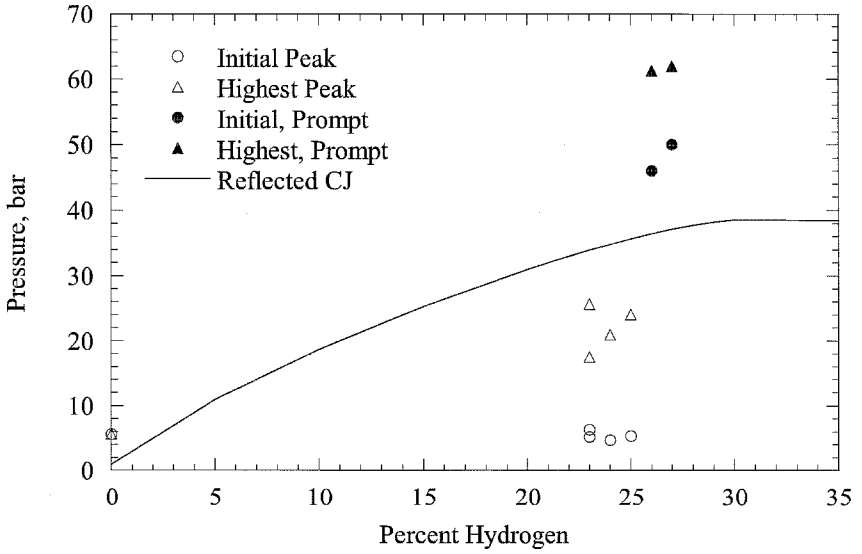

Figure 5.8: Initial and highest peak receiver pressures for undiluted driver.

shock fronts collide and cross over, after reflecting from the end of the tank. The point of collision is about 325 mm from the face of the end flange. The portion of the original shock reflecting from the end flange will also enter this region and shock it further. Local explosions may occur in this region. It has been difficult to reconcile this with the map of pressure traces shown in Figure 5.13, although one similar structure is shown, centered at 280 mm. Nonlinearities in the real system will alter the timing and shape of the wavefronts.

A second attempt was made to find the origin of the first strong focus in Figure 5.13. When the shock reaches the end of the vessel, we expect a reflection from the corners of the flange extension, as shown in Figure 5.18. This may not have been seen in the first ray tracing simulation because the corners were sharp (zero radius). If we modify the surface definition and angle the corners, we see the focus generated in Figure 5.19. This is a rough approximation, as the corners are only modeled with two surfaces. Unfortunately, time constraints prevented me from adding rounded corners to the surface definition. Such a simulation would give results similar to Figure 5.18. At a later time, the parts of the shock reflected from the elliptical head form a second focus, as shown in the first simulation (Figure 5.17). This simulation also explains the nature of the (apparently) erroneous shock fronts shown at t=0.668 ms in the first simulation. These were an attempt by the program to account for the corner, but as it had an infinitesimal radius, a large number of starting rays would have been needed to resolve it.

The existence of focal regions was shown in the experiments of Sturtevant and Kulkarny (1976). In that study, shocks of various strengths ($1.005<M<1.5$) were reflected by different concave forms. The focus region seen in Figure 5.17 is similar to those of weak shocks (M=1.1, 1.2) reflected from parabolic reflectors. Even for weak shocks, nonlinear effects were found to dominate the focal region. Because of these nonlinearities,

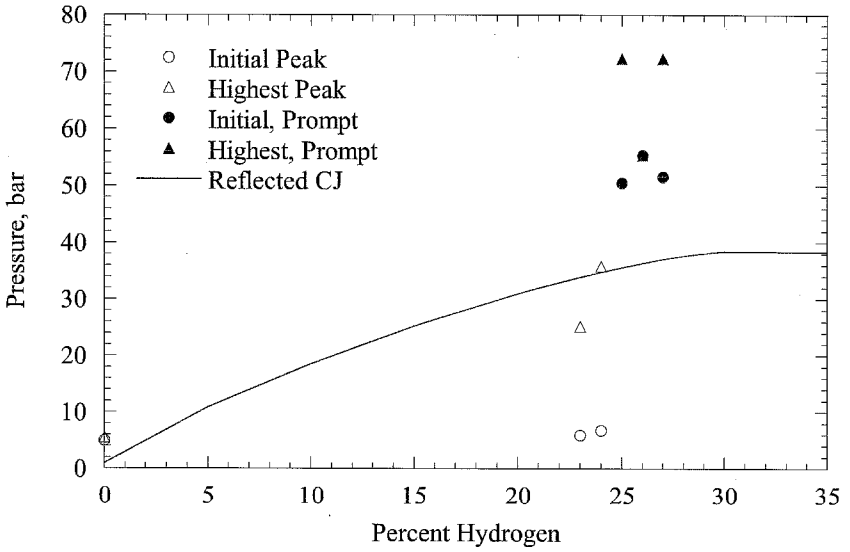

Figure 5.9: Initial and highest peak receiver pressures for driver with 10% N_2 dilution.

the focus problem would be much better modeled by Amrita (Quirk 1996) or a CFD (computational fluid dynamics) code.

In the HYJET receiver, reflected shocks and focal regions can sensitize reactive mixtures, promoting local explosions and DDT (Chan 1995). The result is the presence of strong secondary explosions as seen in Figure 5.1. Strong reflections can occur even when a detonation is initiated promptly.

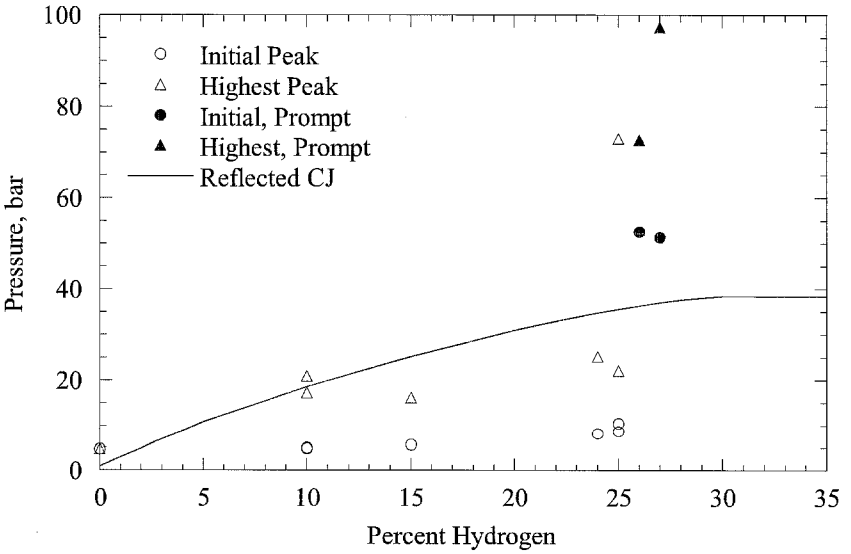

Figure 5.10: Initial and highest peak receiver pressures for driver with 20% N_2 dilution.

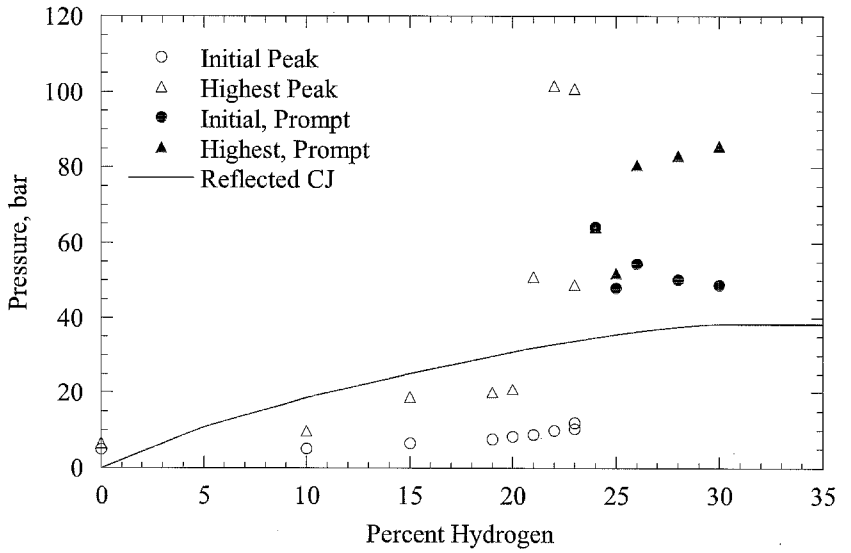

Figure 5.11: Initial and highest peak receiver pressures for driver with 25% N_2 dilution. This was the strongest driver, initiating prompt detonations at 24% H_2 in receiver, and high peak pressures just below that threshold.

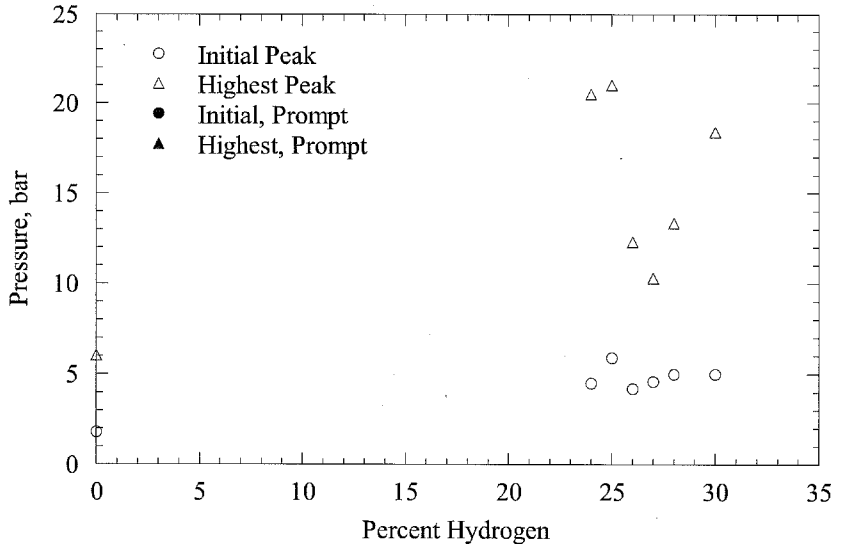

Figure 5.12: Initial and highest peak receiver pressures for driver with 30% N_2 dilution. No prompt detonations were initiated by this mixture. P_{CJ} not shown.

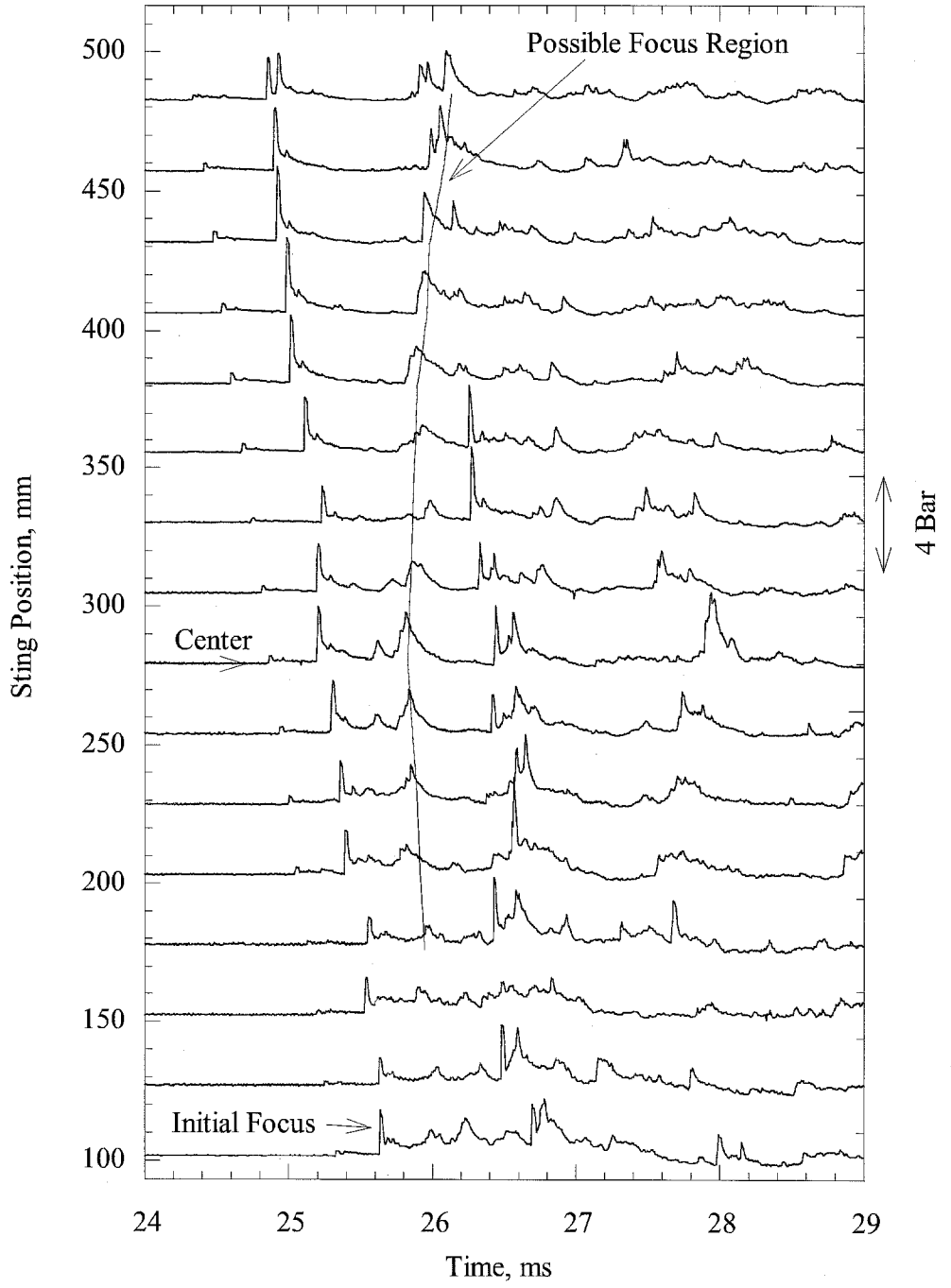

Figure 5.13: Pressure traces from sting-mounted PCB transducer, positioned at 25 mm intervals from 100 to 475 mm from face of end flange. Position of lead shock is adjusted for M =1.09. Driver is 30% H_2-air, receiver is 100% air.

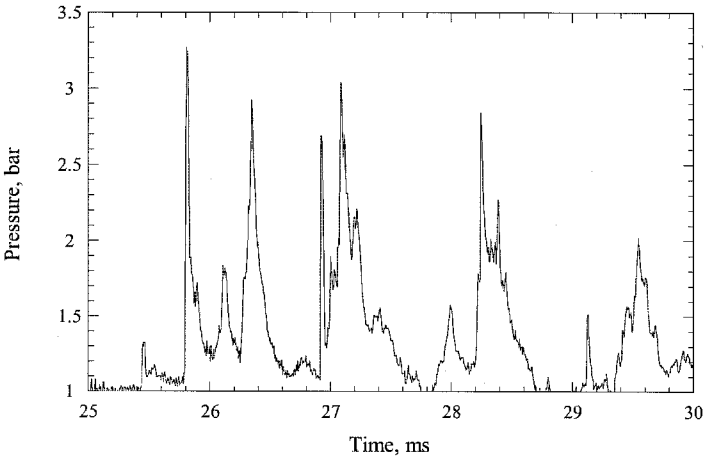

Figure 5.14: Pressure trace with sting at 250-mm station. Driver mixture was stoichiometric hydrogen in air, and gave a peak pressure of 6.14 bar. Receiver is filled with air.

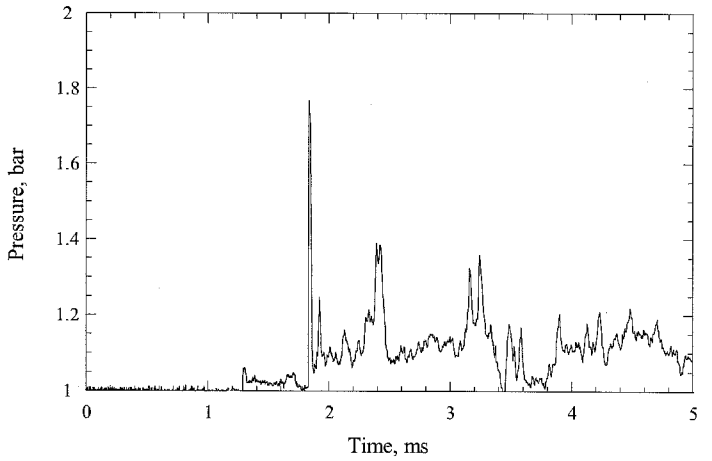

Figure 5.15: Pressure trace with sting at 250-mm station. Diaphragm was ruptured by quasi-static driver pressurization. Rupture occurred at 6.78 bar. Receiver is filled with air.

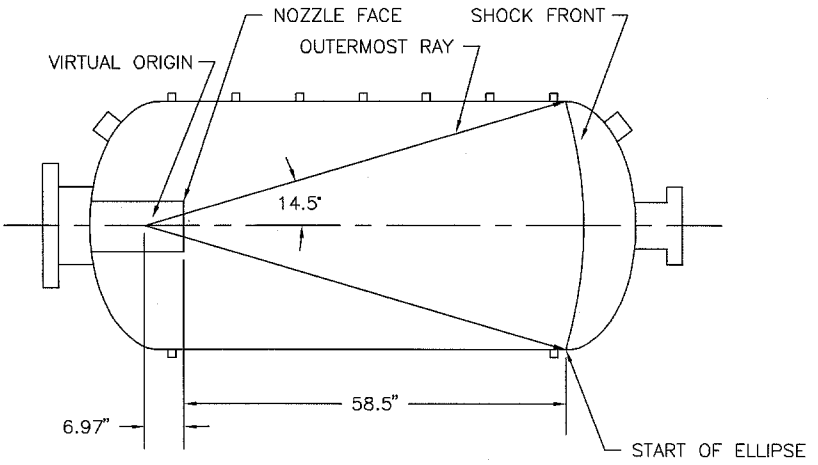

Figure 5.16: Geometry of initial shock for ray tracing simulation.

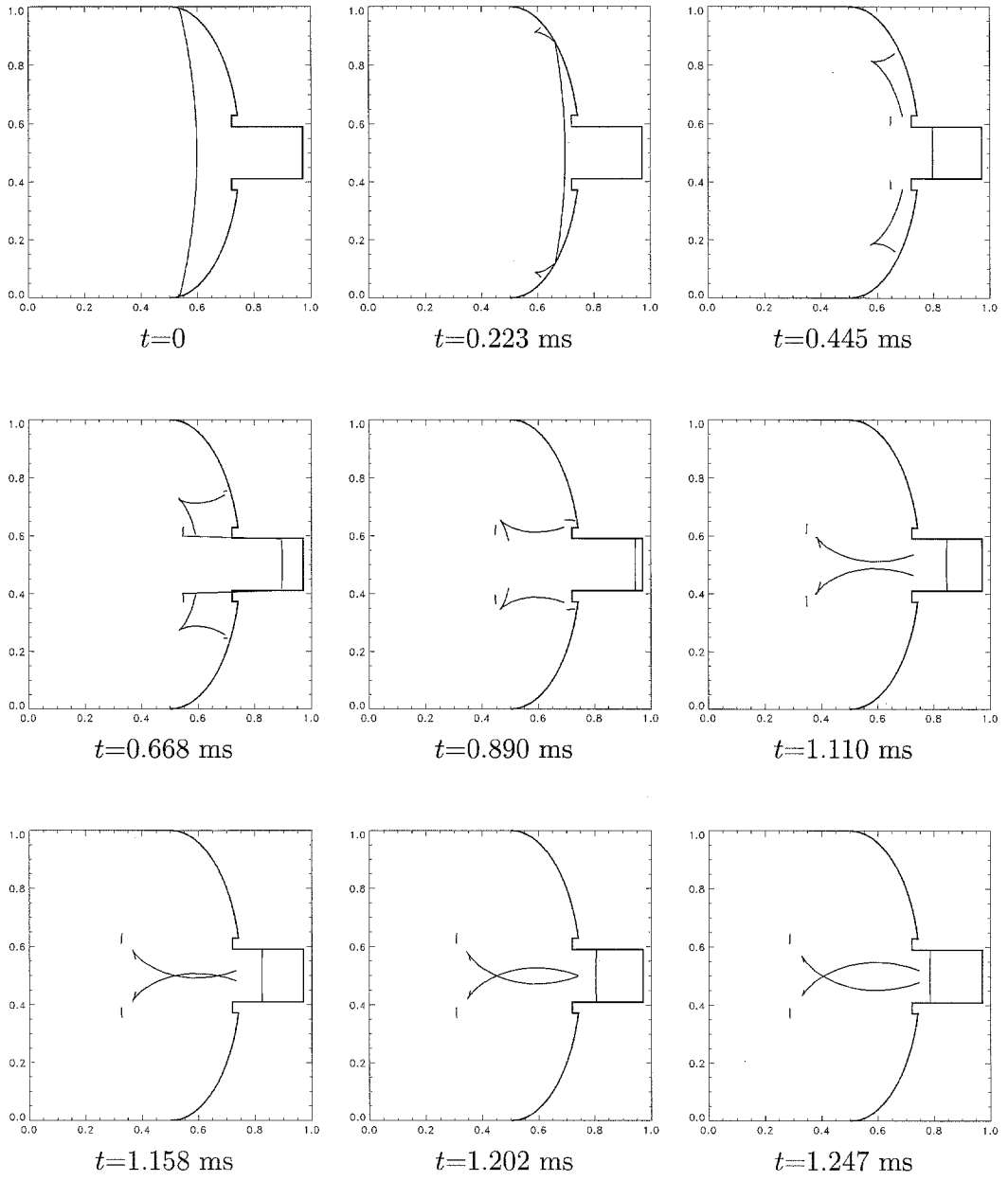

Figure 5.17: Results from ray tracing simulation, showing development of focus region at far end of receiver vessel.

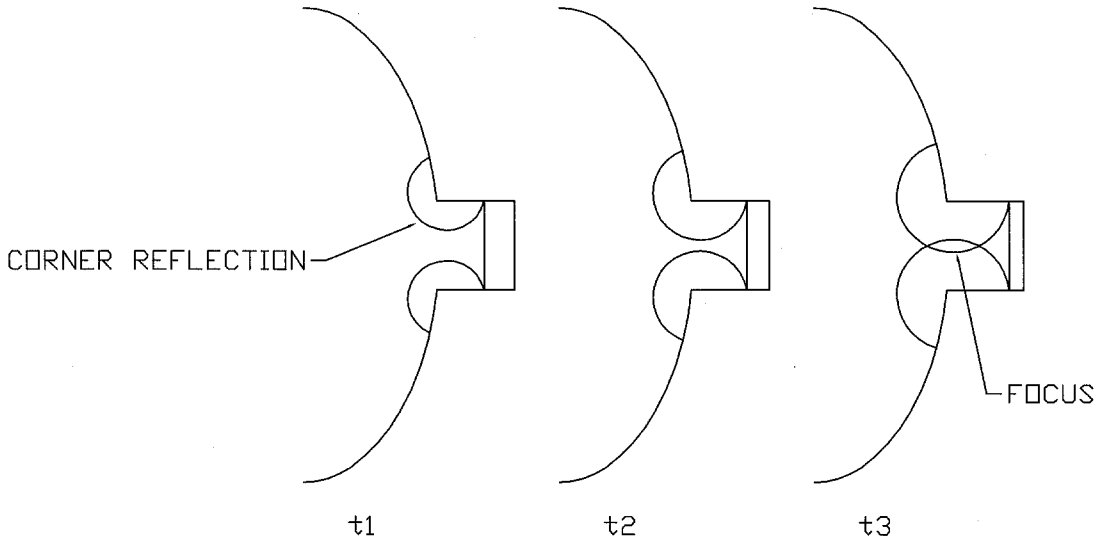

Figure 5.18: Shock reflections expected from corners of flange extension. The reflections coalesce to create a focus region near the face of the flange.

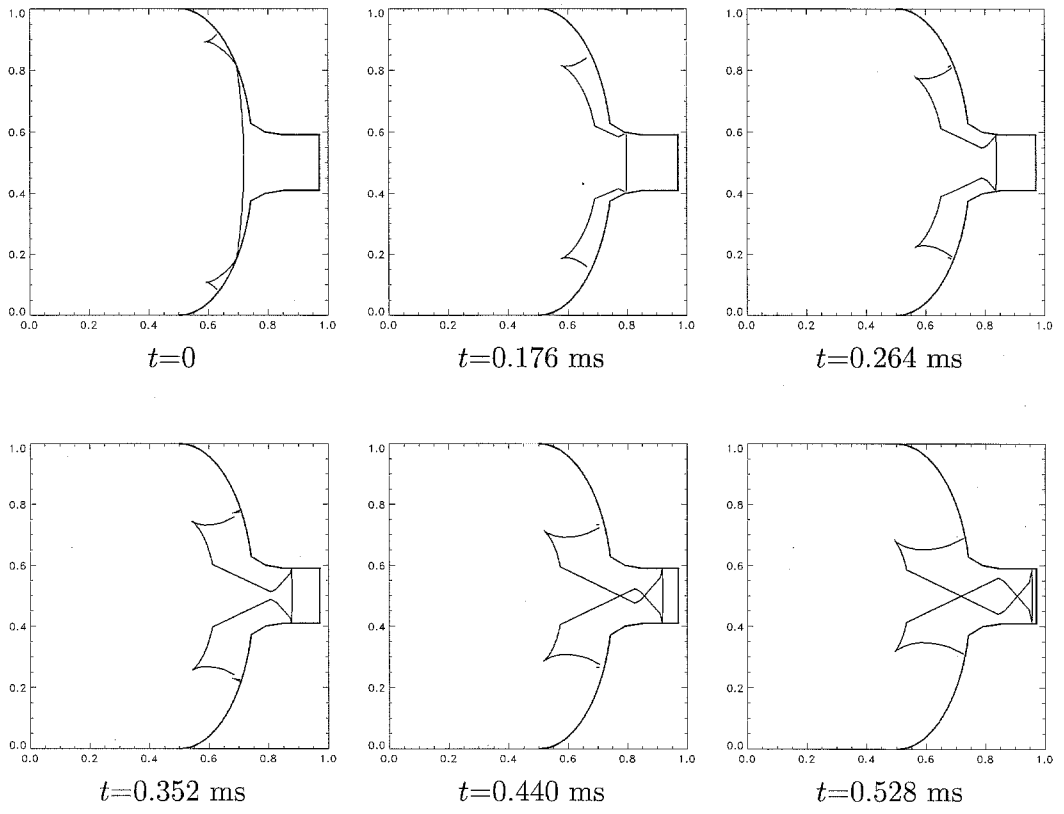

Figure 5.19: Results from second ray tracing simulation, showing reflections from (truncated) corners. If corners were modeled with a radius, results would be similar to Figure 5.18.

Chapter 6

BETA Series

6.1 Introduction and Background

The purpose of this test series was to study jet initiation of detonation in comparison with previous experiments (Carnasciali et al. 1991; Bezmelnitsin et al. 1997). Those experiments used stoichiometric mixtures of the form $H_2 + 0.5(O_2 + \beta N_2)$. The degree of dilution is represented by β, the ratio of diluent to oxygen. The objective is to find the maximum value of β (β_{CRIT}) for which a detonation can be initiated in the receiver vessel. The present experiments differ from the previous ones mainly in facility size and location of the jet with respect to the receiver gas. A comparison of the three facilities is given in Table 6.1. In addition to the listed differences, the previous facilities used eight spark plugs distributed throughout the driver for a rapid pressure rise and consistent peak pressure. The HYJET facility has only one spark plug at the end of the driver. The peak pressures remain fairly consistent, however. An analysis of 14 runs used for photographic shots gave an average peak pressure of 13.84 bar, with a standard deviation of 0.26. The time from ignition to peak pressure was 11.23 ms on average, with a deviation of 0.15. (The driver Kulite pressure was recorded at 4 kHz, so the peak time has an accuracy of ± 0.13 ms.) A sample driver pressure plot is shown in Figure 6.1. These peak pressures are for the 25-mm nozzle; pressures are similar for the 38-mm nozzle. The 64 and 92-mm nozzles have peak pressures of 10–11 bar, due to the increased venting area. The peak pressure recorded with the 25-mm nozzle is much higher than the P_{AICC} of 8.62 bar, and is fairly close to the CJ pressure of 16.8 bar. A PCB transducer was later installed in the driver, and the pressure signals indicated that the driver mixture was transitioning to detonation somewhere down the tube. An analysis (described below) showed that a detonation in the driver is not adequate to directly initiate a detonation in the receiver, but our jet is better described as strongly impulsive, vs. a jet generated by constant-volume combustion. The jets in the previous facilities entered flush with the end of the receiver vessel. In the present facility, the driver vessel extends into the receiver by about 0.5 m. The effect of this extension has not been determined.

The first reported data was from Carnasciali, where the effect of diaphragm material and driver composition were also studied. These tests used glass diaphragms for clean

Table 6.1: Comparison of jet-initiation facilities.

	Carnasciali	Bezmelnitsin	Krok
Driver diameter, m	0.2	0.2	0.13
Driver length, m	0.66	0.66	2.36
Driver volume, ℓ	21	21	28
Receiver diameter, m	0.48	0.52	0.86
Receiver length, m	0.78	0.72	1.98
Receiver volume, ℓ	141	154	1180
Receiver/driver volume ratio	6.8	7.3	42
Orifice diameter, mm	76, 102, 119	120	25, 38, 64, 92

rupture and consistent peak pressure. They found an optimum driver mixture of β=2.6, proposing that this created the ideal radical concentration. This mixture was used in the HYJET experiments. Carnasciali also found little dependence on orifice diameter, using ethylene as a fuel and orifice diameters of 76, 100 and 120 mm.

The experiments of Bezmelnitsin et al. sought to duplicate Carnasciali's experiments, and then relate them to initiation in unconfined mixtures. To do this, the driver vessel was attached to a polyethylene bag 1.5 m in diameter by 3.5 m long. The bag was hung vertically to avoid any surface reflections from ground contact. As they expected, confinement played a strong role in detonation initiation. Unfortunately, a table in Carnasciali et al. (1991) contained a typo, stating that the optimum driver β was 7.6, instead of the 2.6 quoted in the body of the text. J. Shepherd discovered the typo after we were unable to rupture our mylar diaphragm with the β=7.6 mixture. Bezmelnitsin had occasional diaphragm rupture problems (with copper diaphragms), but was able to complete the tests. They found a maximum dilution of β=2.1 for detonation in confinement, and β=1.5 for the unconfined case. They were able to show that confinement plays a strong role in the initiation of detonation. However, the effect of their weak driver mixture is unclear. From pressure traces, they determined that initiation was due to interaction of the jet's bow shock with the vessel wall, thus relying on confinement. In the HYJET facility, photographic evidence shows the detonation propagating directly from the jet, initiating within 100–150 mm of the jet exit. Furthermore, the receiver vessel diameter is larger in HYJET, requiring a longer time for the rupture shock to reflect and return to the jet region.

The present experiments first duplicated the mixtures of Carnasciali and Bezmelnitsin, to compare the effect of HYJET's geometry to the other facilities. With nitrogen dilution as a reference, the experimental series was then expanded to include N_2 and H_2O dilution at 373 K. In addition, nozzle sizes of 25, 38 and 64-mm were used to study the effect of jet diameter. The PCB transducer configuration is shown in Figure 6.2. The early tests with nitrogen (runs 312 through 318) used only the E and T3 transducers, as in the NITRO series. For the remainder of the tests, two more transducers were installed at the T1 and T2 stations. The four transducers are spaced at 0.51 m intervals.

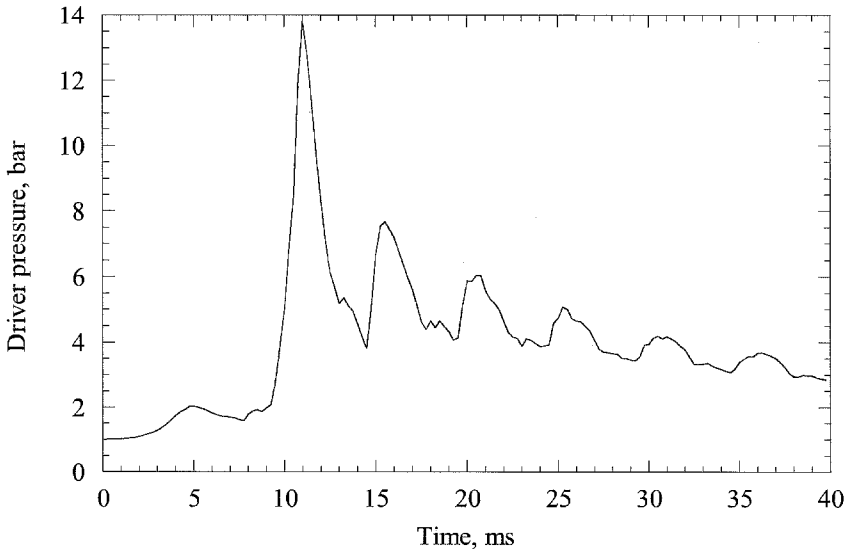

Figure 6.1: Sample driver pressure trace (25-mm nozzle), from Kulite (slow) transducer. Run 406.

The variety of phenomena observed in this series requires use of terminology similar to that in the NITRO series. A "prompt" initiation is one in which a detonation is initiated in the region of the nozzle exit. A DDT occurs when there is evidence of a slow pressure rise followed by detonation-like waves, or when shock waves traveling down the vessel build into a detonation. A "secondary" explosion occurs shortly after the primary wave train has passed. These are typically found in the end of the vessel, where focusing occurs, but have been seen elsewhere. A related phenomena is a "late" explosion, which occurs some time after the lead waves have passed, and is usually localized to a single transducer. Finally, any weaker combustion event will be termed a deflagration. A deflagration will show no significant wave action on the PCB transducers. The Kulite transducer was used to record deflagration pressure rises, but the data are not presented here. Two Kulites were destroyed during tests with H_2O; after the second one was destroyed, it was not replaced. In jet initiation terminology, only a prompt initiation is considered a "GO." All other cases are "NO-GOs." The broader terminology is used here as a reminder that significant events can occur, even when a detonation is not initiated.

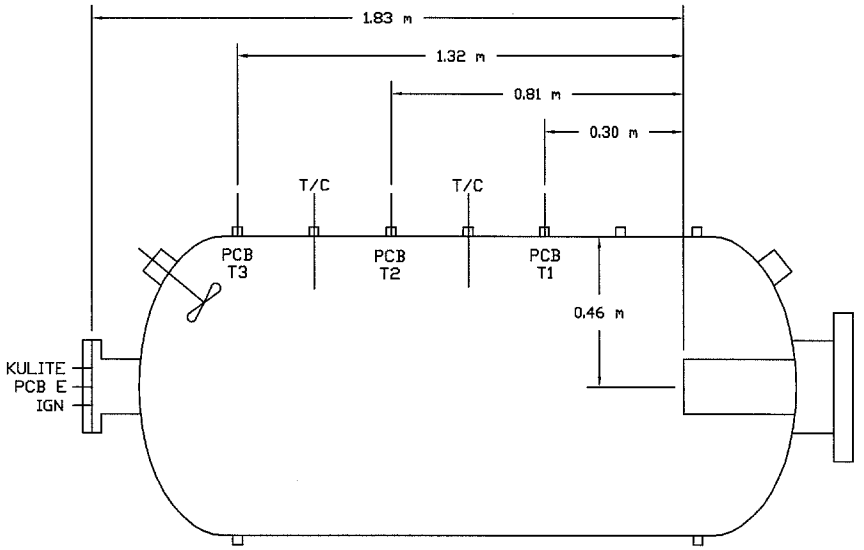

Figure 6.2: Locations of PCB transducers in beta dilution test series.

Table 6.2: Mixture compositions for representative values of β in the system $H_2 + 0.5(O_2 + \beta X)$.

β	$\%X$	$\%O_2$	$\%H_2$	β	$\%X$	$\%O_2$	$\%H_2$
1.0	25.0	25.0	50.0	3.6	54.5	15.2	30.3
1.2	28.6	23.8	47.6	3.8	55.9	14.7	29.4
1.4	31.8	22.7	45.5	4.0	57.1	14.3	28.6
1.6	34.8	21.7	43.5	4.2	58.3	13.9	27.8
1.8	37.5	20.8	41.7	4.4	59.5	13.5	27.0
2.0	40.0	20.0	40.0	4.6	60.5	13.2	26.3
2.2	42.3	19.2	38.5	4.8	61.5	12.8	25.6
2.4	44.4	18.5	37.0	5.0	62.5	12.5	25.0
2.6	46.4	17.9	35.7	5.2	63.4	12.3	24.7
2.8	48.3	17.2	34.5	5.4	64.3	11.9	23.8
3.0	50.0	16.7	33.3	5.6	65.1	11.6	23.3
3.2	51.6	16.1	32.3	5.8	65.9	11.4	22.7
3.4	53.1	15.6	31.3	6.0	66.7	11.1	22.2

6.2 Results and Discussion

6.2.1 Driver Conditions

With driver pressures of 14 bar indicated by the Kulite transducer, a PCB was installed in the driver to record shock wave data, as in the NITRO series. The receiver was filled with air, and the driver was vented through the 25 and 92-mm nozzles. The pressure traces are shown in Figure 6.3. As the transducer is at the ignition end of the vessel, it can not directly detect events near the nozzle. We can only see reflected shocks that result from local explosions or detonation there. With the 92-mm nozzle, we see a peak pressure well below that for a reflected detonation. The 25-mm trace shows a much higher peak, which is likely the result of a detonation reflecting off of the nozzle adapter. Thus, local explosions appear with the increased confinement of the smaller nozzles. We will still do the detonation transmission analysis for all cases.

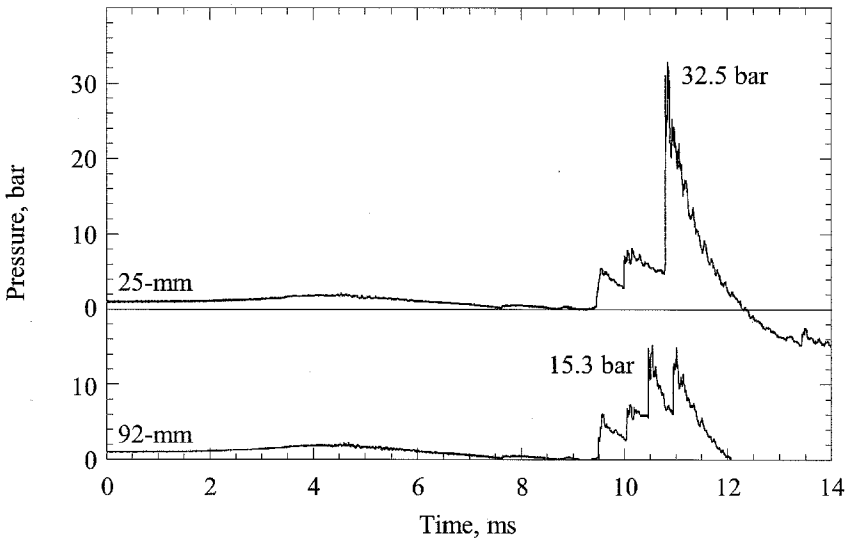

Figure 6.3: PCB traces from driver venting into air. Transducer located on instrumentation flange, adjacent to spark plug.

The procedure for generating a shock Hugoniot and matching the reflected detonation was given in the NITRO analysis (page 44), and will not be repeated here. In the BETA series, we have one driver mixture, and a number of receiver mixtures. The resulting Hugoniots are plotted in Figure 6.4. The intersection of the Hugoniots for the receiver and the reflected driver wave indicates both the pressure/velocity jump across the shock in the receiver, and the nature of the reflected wave in the driver. In the BETA tests, all of the receiver mixtures result in a reflected expansion in the driver. With the shock conditions for the receiver determined, we can again calculate the shock temperatures and induction times. The results are tabulated in Table 6.3.

From Table 6.3, we see that none of the receiver mixtures are subject to direct initiation. The 373 K N_2-dilution mixture has the shortest induction time, at 0.27 ms. In this

Table 6.3: Results of analysis on transmitted shock in receiver, initiated by detonation in driver.

Diluent	T_R, K	β	M_{CJ}	M_S	P_S, bar	T_S, K	t_{IND}, ms
N_2	298	4.3	4.90	3.62	14.7	971	11.8
N_2	298	3.0	5.05	3.58	14.4	958	15.0
N_2	298	2.6	5.10	3.56	14.2	951	17.2
N_2	373	5.2	4.17	3.38	13.5	1130	0.27
H_2O	373	1.1	4.45	3.10	11.3	972	13.1
H_2O	373	0.55	4.56	3.06	11.0	973	10.9

time, the shock will move 0.4 m, so there is no chance of shock-reaction coupling. All of the other induction times are on the order of 20 ms, which is enough time for the receiver to deflagrate from jet ignition before spontaneous explosion would occur. So, while our driver does not directly initiate detonation, it does provide a stronger impulse than the Carnasciali (constant-volume combustion) driver. Previous research (Inada et al. 1992) has further indicated that interaction of a detonation with a diaphragm will destroy the cellular structure. The volume of the HYJET driver is 30% larger than the others, and has a total energy equivalent of approximately 9 g Tetryl. This energy is not released instantaneously, but over 1 ms or so. The HYJET driver also has a much larger aspect ratio (length divided by diameter) than the others (18 vs. 3). This increases the acoustic resonance time and the "piston" effect of work done on the receiver gas. In the future, we will minimize the potential for transition by moving the spark plug to the midpoint of the driver (Üngüt and Shuff 1989) or by adding more spark plugs, distributed throughout the driver.

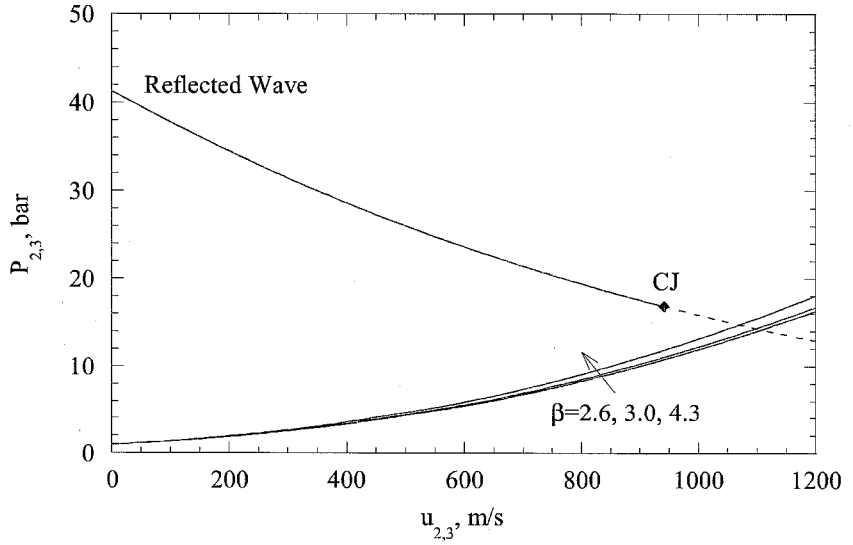

a: Receiver at 298 K

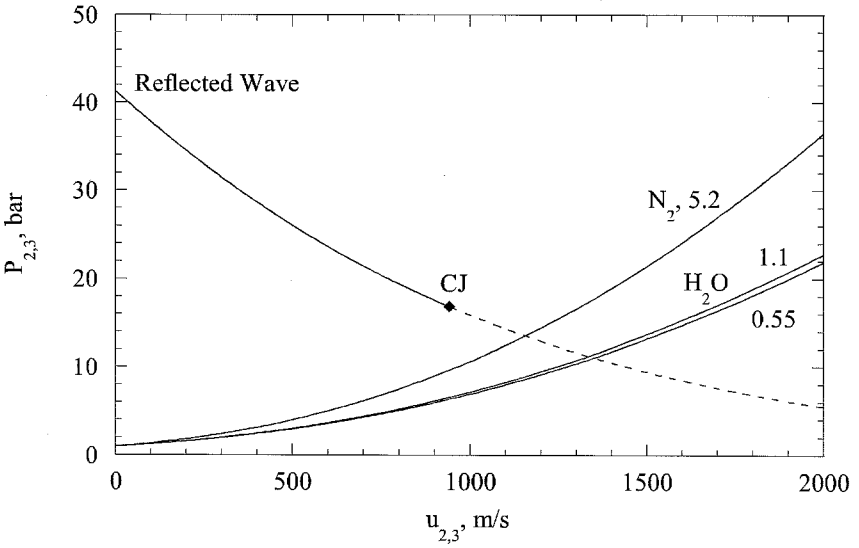

b: Receiver at 373 K

Figure 6.4: Shock Hugoniots for BETA receiver mixtures, with reflected driver wave Hugoniot. Upper plot is for mixtures at 298 K, lower plot for mixtures at 373 K. For reflected wave Hugoniot, solid line indicates reflected shock; dashed line indicates reflected expansion.

Table 6.4: Comparison of detonation initiation results.

	Maximum β for detonation		
Receiver	Carnasciali	Bezmelnitsin	Krok
N_2, 298 K	2.6	2.1	4.3
N_2, 373 K			5.2
H_2O, 373 K			1.0

6.2.2 Critical Dilutions

In the HYJET experiments, β_{CRIT} was determined to a resolution of 0.1, with the exception of the steam runs. At higher values of β (above, say, 3.76, the value for air), this means a difference of only one half of one percent in diluent, and less in the reactants. This approaches the accuracy of the pressure gauges used to fill the vessels, resulting in a "fuzzy" (i.e., uncertain) determination of β_{CRIT} in some cases. For example, in the series of shots with N_2 at 298 K, one run with β=4.4 was a prompt initiation, but subsequent runs were not. The reverse occurred with nitrogen at 373 K, where one of the runs with β=5.2 failed to initiate; when the others were prompt.

Note that the initial temperatures of 298 K and 373 K are "nominal;" they represent the average/typical receiver temperature of the series. In the tests at 298 K, the true initial temperatures ranged from 294 to 304 K. In the N_2-dilution tests at 373 K, the temperature range was from 372 to 378 K. In the H_2O tests at 373 K, the temperature range was from 374 to 378 K. The initial conditions for each run are listed in Appendix C. The digital thermometers used to measure temperature have an accuracy of $\pm$0.5 K.

After the β_{CRIT} tests were completed, a few tests were done without a diaphragm separating the two chambers, using the 92 and 25-mm nozzles. These runs were done as a link to the work by Knystautas et al. (1979). The plumbing system was rerouted to allow circulation between the two vessels.

The results with the 92-mm nozzle are summarized in Table 6.4, to provide a quick comparison with the other facilities. The BETA tests in the HYJET facility found considerably higher values of β_{CRIT} than the previous studies. This will be examined in more detail below.

In jet initiation experiments, results are typically presented as the ratio of jet diameter to detonation cell size in the receiver mixture, or D/λ. In the present experiments, the detonation only takes place in the receiver mixture. Since the driver composition is not reflected in λ, the D/λ criterion may not be applicable here. Carnasciali did a brief study of the effects of driver composition. For a driver with β=2.6, they obtained receiver initiation at $D/\lambda \approx 11.7$ (β_{CRIT}=2.6). For a driver with β=0.4, they found $D/\lambda \approx 59$ (β_{CRIT}=0.4). (The critical receiver dilutions for H_2 matched the driver dilutions. This was not true for other fuels.) A smaller effect of driver composition was seen in the H_2-air system in the NITRO series, as well as in the work of Dorofeev et al. (1993).

Regardless, D/λ will be presented here for completeness and comparison to other work. Cell sizes are thus needed for the values of β_{CRIT} found for each nozzle and dilu-

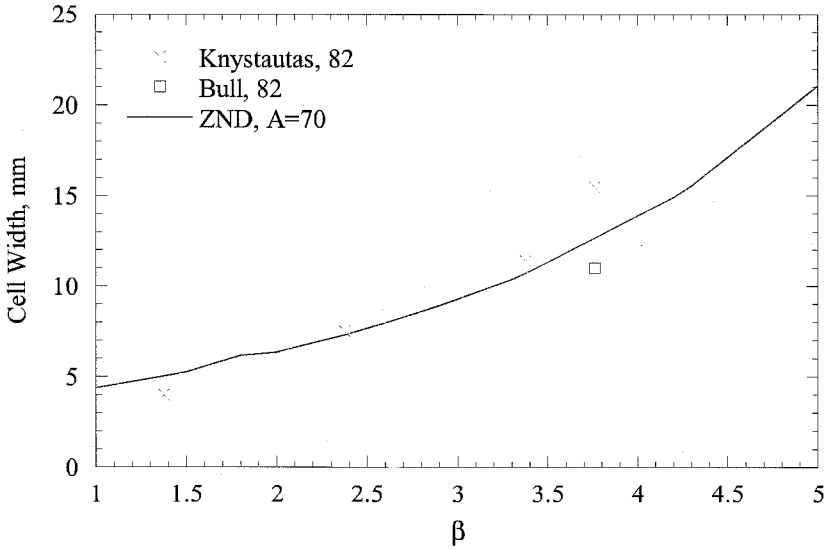

Figure 6.5: ZND estimation of cell sizes for N_2 dilution at 298 K (A=70). Data points are from Knystautas et al. (1982) and Bull et al. (1982).

ent. The cell sizes can be estimated from computed reaction zone lengths, as described in Chapter 1. For the BETA mixtures, Δ was calculated for each β_{CRIT} using the program "ZND" (Shepherd 1986). Typically, the correlation is $\lambda = A\Delta$, where A is assumed constant for a given system and determined by comparison to experimental data. Data for stoichiometric H_2-O_2 with N_2-dilution is available from Knystautas et al. (1982) and Bull et al. (1982), and is plotted in Figure 6.5 against the ZND computation for A=70. No previous studies have been done on the H_2-O_2-H_2O system, but data for H_2-air-H_2O is available from Stamps et al. (1991) and Ciccarelli et al. (1994). The effect of the N_2 is unclear, but the data is plotted in Figure 6.6 against the ZND curve for A=30.

We see from Figures 6.5 and 6.6 that a constant A does not accurately reflect the measured values of λ, particularly at high and low values of β (Figure 6.5) and low steam concentrations (Figure 6.6). To overcome this, and better adapt the steam data to mixtures without nitrogen, a different correlation can be used. Recently, Shepherd and Kaneshige (unpublished) have found that a power-law correlation can be used to account for the change in A. In Figure 6.7, the data from the previous figures are plotted as $\log \lambda$ versus $\log \Delta$. The data can be correlated by the relation $\lambda = 39\Delta^{0.68}$ (fitted by least squares). Unfortunately, this relation is not dimensionally meaningful, but this form has proven useful in several fuel-oxidizer systems. The data show increased scatter for some of the Knystautas N_2 data; this is considered acceptable, as cell irregularities can lead to measurement uncertainties. The power-law correlation was used to calculate the required values of λ.

The results are listed in Table 6.5, and plotted in Figure 6.8. With the exception of one case, the values fall roughly within the range $2 < D/\lambda < 7$, well below the previously quoted value of 13. The exception is the 92-mm nozzle with N_2 and no diaphragm

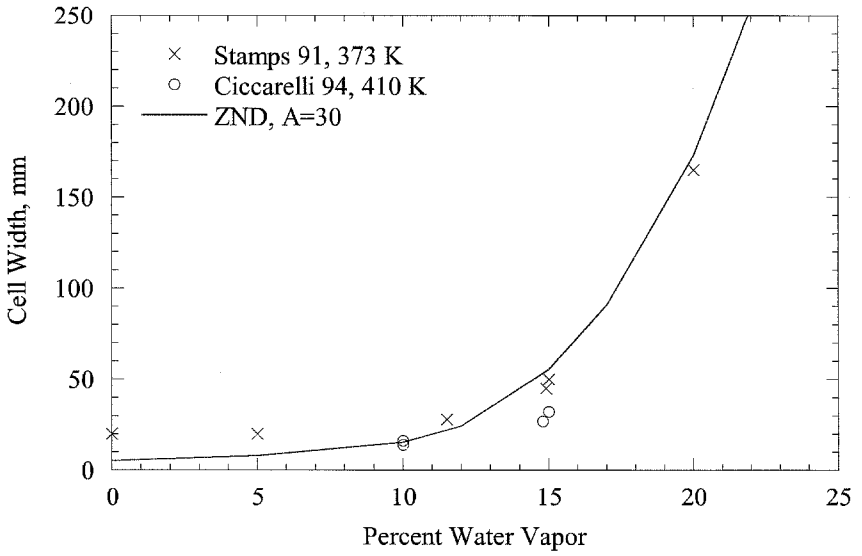

Figure 6.6: ZND estimation of cell sizes for stoichiometric H_2 in air with steam dilution at 373 K (A=30). Data points are from Stamps et al. (1991) and Ciccarelli et al. (1994).

(D/λ=10.7). The tests with no diaphragm are not directly comparable to the other tests, though.

In the similar work by Knystautas et al. (1979), D/λ was not computed for the mixtures, as the geometry of the orifice between the vessels was the main factor. (Degree of turbulence was also found to be important by MacKay et al. (1988) and Moen et al. (1989).) Knystautas proposed that the minimum size of the large eddies must be at least of the order of the detonation kernel, or λ, for initiation to occur. This means that, with the right exit conditions, initiation could be seen in mixtures with $D/\lambda \rightarrow 1$. Carnasciali et al. (1991) suggested that minimum kernel size could be defined by the critical tube diameter, $d_c \approx 13\lambda$, but the BETA results indicate that a smaller kernel is possible. Again, we see that the D/λ criterion is not well-suited to jet initiation experiments, even when the same mixture is used in both vessels.

As shown in Figure 6.9, the results correlate much better when plotted as β_{CRIT} vs. nozzle area. First, we see that the points for nitrogen dilution at 298 K fall on a regular trend. With the two largest nozzles, the curve seems to be approaching an asymptote, which represents a physical limitation of the driver. Perhaps increasing the driver volume (length or diameter) would shift the asymptote upward. The size of the receiver vessel may also play a role in these experiments. While larger jets can initiate more dilute mixtures, these mixtures have longer induction times, leading to delayed initiation. A strong jet, entraining reactants, may reach the end of the vessel before initiation can occur. As nozzle size decreases, the curve must have a very sharp drop-off, as a nozzle with zero area can not initiate combustion. Thus, it would be possible to find a nozzle area for which even straight H_2-O_2 could not be promptly initiated. Unfortunately, lack of time prevented using the 12.7 and 6.4-mm nozzles in the HYJET tests. Instead of

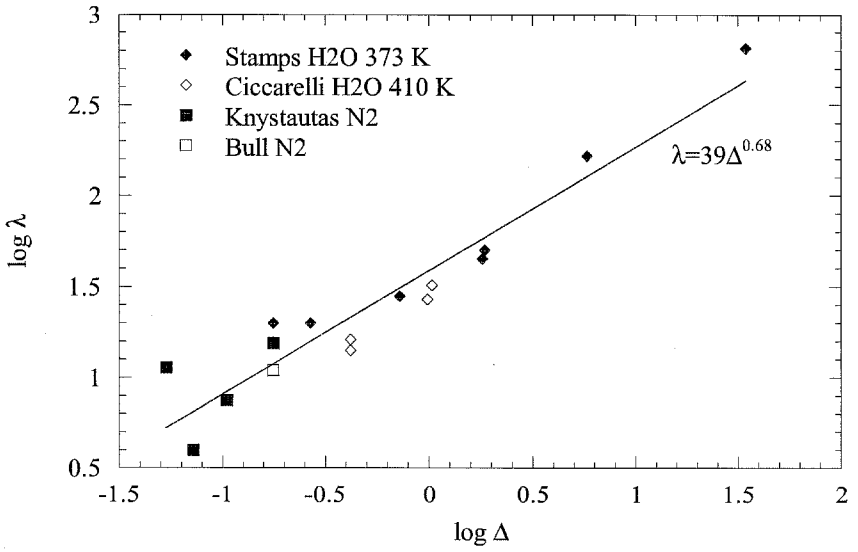

Figure 6.7: Plot of $\log \lambda$ vs. $\log \Delta$, with power law correlation.

using D/λ, perhaps it would be better to model the driver as an initiation energy (which scales with λ^3). The problem is to determine the key parameters. Figure 6.9 indicates that D^2 would be useful. Other possibilities would be the peak pressure, P_P, and energy density of the driver mixture. For exit geometries other than a circular nozzle, a factor would be needed to reflect turbulence generation, as shown by Knystautas et al. (1979).

A critical energy approach was taken by Üngüt and Shuff (1989) in their experiments on jet-initiated DDT. As their experiments used a uniform mixture in both vessels, they found that D/λ still represented the normalized energy release of the jet. They also used the Damköhler number, τ, defined in this case as the ratio of vortex entrainment time to reaction induction time. If τ is large, the reaction will go to completion before the entrainment process is complete (and initiate a deflagration). The results indicated that D/λ must be greater than 5 for initiation to occur, and that if τ was above a critical value, initiation would not occur for any D/λ. Üngüt and Shuff related this to a minimum jet velocity requirement. Urtiew and Tarver (1979) studied the transmission of a detonation from a tube to a hemisphere and modeled the process in terms of work done by the driver on the receiver gas. In the future, we will examine and combine ideas from both analyses to generate a model for our case, where different mixtures are used in the vessels.

The work of Knystautas et al. (1979) showed that obstructions in the jet enhance turbulence and can aid in transition. To see if increased turbulence would affect the HYJET results, β_{CRIT} was determined for the 25-mm nozzle with the diaphragm cutter installed. As shown in the plot, this raised β_{CRIT} by a small but significant amount. I expected that the cutter would develop only small-scale turbulence, as it is upstream of the nozzle exit, and the four quadrants of the jet can easily recombine. However, the results of Knystautas et al. (1979) (discussed in Chapter 5) found that addition of small-scale turbulence would not help a particular orifice initiate a detonation when it could

Table 6.5: Summary of D/λ results. (w/c, with cutter; ND, no diaphragm.)

D, mm	Diluent	T	β_{CRIT}	ZND Δ, mm	D/λ
92	N_2	298 K	4.3	0.222	6.6
64	N_2	298 K	4.2	0.213	4.7
38	N_2	298 K	3.0	0.133	3.8
25	N_2	298 K	2.6	0.114	2.8
25, w/c	N_2	298 K	2.9	0.128	2.6
92, ND	N_2	298 K	3.3	0.149	10.7
25, w/c, ND	N_2	298 K	1.8	0.088	3.3
92	N_2	373 K	5.2	0.293	5.4
92	H_2O	373 K	1.1	0.479	3.9
38	H_2O	373 K	0.55	0.114	4.3

not before. The diaphragm cutter must be adding some amount of large-scale turbulence.

Other comparisons can be made from Figure 6.9. One set of runs was done with nitrogen dilution at 373 K and the 92-mm nozzle to provide a link between the nitrogen and steam runs. Higher temperatures increase a mixture's sensitivity to detonation, and we see from the figure that β_{CRIT} follows this trend. We also see the effectiveness of steam as a detonation supressant. The points for steam dilution lie well below those for nitrogen. Below β=1, the resolution of the tests was increased to 0.05 to keep the change in diluent near 1%. In a few of the tests, the vessel was overfilled with steam because of condensation problems in the supply. This resulted in an initial pressure error of +3% or so, but β was recalculated so it would be correct. The excess of vapor in these tests placed them outside of the area of β_{CRIT}, so they did not affect the limit determinations.

In the tests with no diaphragm, the mixture had to be much more sensitive for prompt initiation to occur. Without a diaphragm, the driver continuously vents reactants ahead of the flame front, lowering the peak pressure. The resulting flow field in the receiver may reduce the strength of the jet head vortex when the flame front reaches the nozzle and products are vented. High-speed photography (discussed below) of detonation initiation with the 25-mm nozzle showed no evidence of pre-flow leading the jet into the receiver, so these mixtures had probably detonated before reaching the nozzle. However, β_{CRIT} for this system gives D/λ=3.3. Critical tube diameter experiments have shown a fairly reliable correlation of d_C=13λ, so there is virtually no chance of detonation transmission through this nozzle. With the 92-mm nozzle, β_{CRIT}=3.3, with D/λ=10.7. This is much closer to d_C, but in this case the nozzle diameter is nearly the diameter of the driver, so only a small surface is available for shock reflection. While flame acceleration will still occur, transition to detonation in the driver is unlikely. These tests were only done to a resolution of β=0.25 or so, to roughly characterize the results with respect to the other tests.

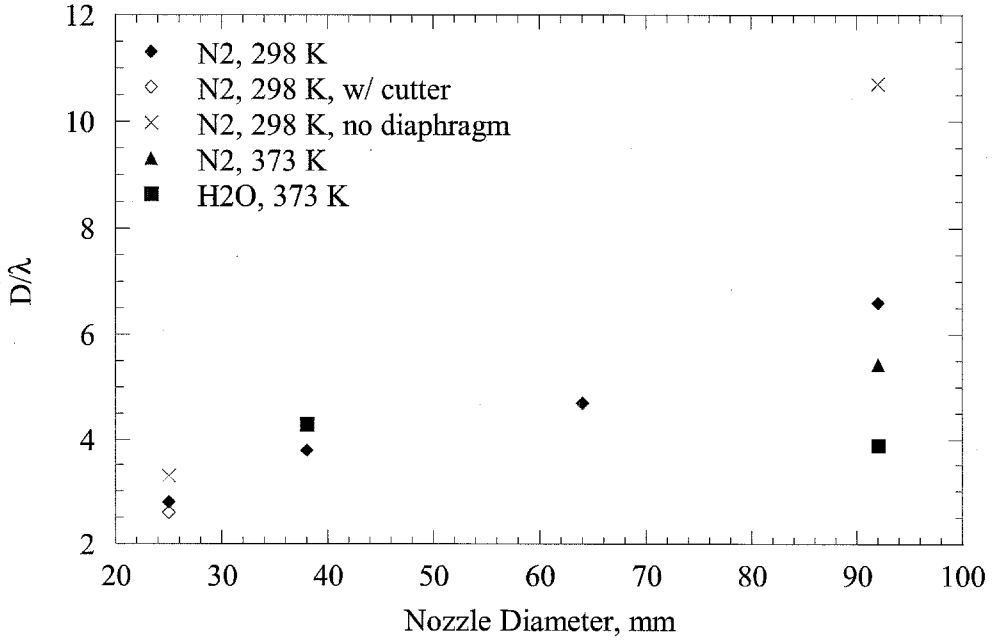

Figure 6.8: Plot of initiation results as D/λ.

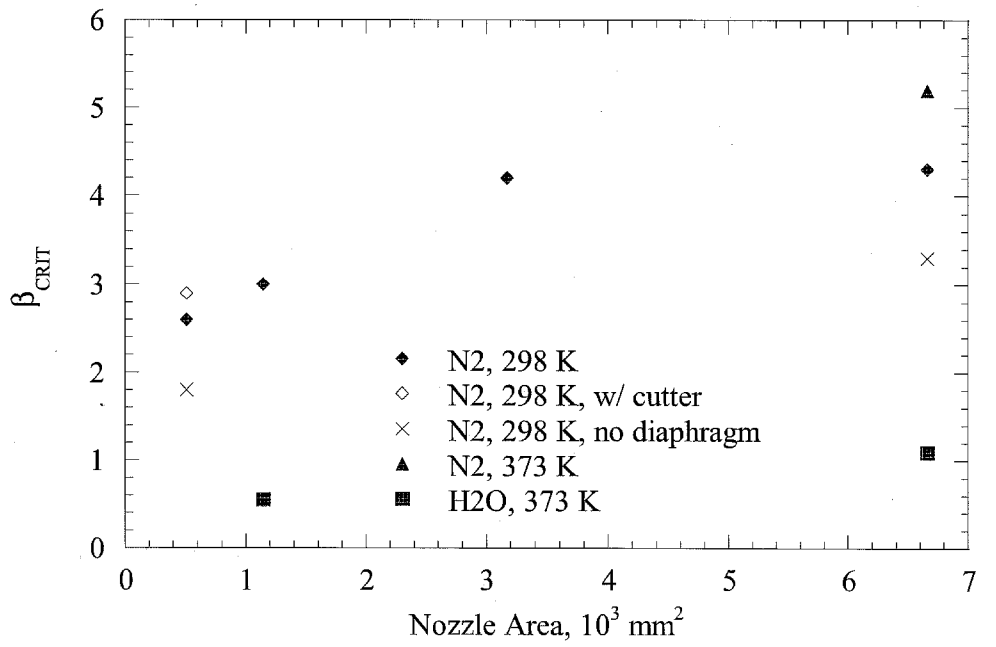

Figure 6.9: Summary of critical beta values.

6.2.3 Sample Pressure Traces

Pressure traces from selected runs are shown in Figures 6.11 through 6.21, representing borderline values of β. Typical examples are shown of prompt initiation, secondary and late explosions, and deflagration. Examples are given of both the 92 and 25-mm nozzles, to show the weaker shocks of the small nozzles in deflagrations. These shocks decay by the end of the vessel.

Interestingly, the tests with nitrogen showed no DDTs, although there were some secondary and late explosions. This result led me to reassess the NITRO experiments. In the NITRO tests, I originally thought that the detonations we saw at the end of the vessel were the result of DDT, because of our low D/λ in those tests (see Chapter 5). The additional instrumentation in the BETA tests showed that all of the mixtures with N_2-dilution are either promptly initiated or do not detonate. Thus, I concluded that the detonations in the NITRO tests were the result of prompt initiation. (The receiver mixtures in the NITRO series are very close to the BETA mixtures with β=3.76.) DDT *was* seen in the tests without diaphragms, although these are not directly comparable. The DDTs may result from the pre-existing, turbulent flow field generated by driver venting, before the flame reached the nozzle.

In contrast, the water vapor tests had a region of DDTs between deflagration (β=2.0) and prompt detonation (β=1.1). The presence of water vapor reduces the flame speed (Liu et al. 1980; Liu and MacFarlane 1983). This may allow shock reflection and focusing to occur before all of the reactants are consumed. With only nitrogen, the flame burns fast enough to consume the reactants before the onset of DDT.

In some cases, noise is evident on one or more of the transducers. The PCB transducers use Microdot connectors, which are prone to loosening under vibration. Since the transducers run on constant current, a break in the circuit results in a (theoretically) infinite voltage from the power supply, causing a spike in the data. Attempts were made to minimize this, but the problem can only be resolved by removing the transducers from their mounts and tightening the connections. This required a tool that was not always available. Fortunately, the lead wave is always clean, and the noise only occurs after a strong wave passes.

In the early runs, the T-station transducers were mounted in pipe plugs that thread into fittings along the top of the vessel. I did not realize that this left a long cavity between the transducer and the vessel, about 25 mm in diameter and 50 mm deep. For runs 354 and on, new mounts were installed that brought the transducers to the inner surface of the receiver. Fortunately, the results indicate that the antechamber had little effect on the pressure traces, other than adding some noise from shock reflections. This is shown in Figure 6.10, with recessed transducers in run 353, and flush-mounted units in run 356.

Figures 6.11 through 6.13 represent runs with nitrogen dilution at 298 K. Figure 6.11, β=4.3, is a typical rendition of prompt initiation in this facility. No shock waves appear before the detonation. The small amount of noise immediately preceding the detonation, particularly on T3, is believed to be stress waves traveling through the vessel. This has also been seen in the GALCIT 11-inch Detonation Tube. Immediately behind the

reflected detonation on the E transducer, there is a three-pronged peak as strong as the detonation (this form is seen often). I believe this is the result of focusing at the end of the vessel, as described in Chapter 5. In this case, the second peak follows the detonation by 0.28 ms, which agrees with the 0.3 ms characteristic time of the focusing process. The traces show a pressure pulse traveling back up the vessel from this explosion. Reflected detonations have recently been studied by Shepherd et al. (1991). When a detonation undergoes normal reflection, the pressure is approximately $2.5P_{CJ}$. For the BETA mixtures, $M_{CJ}\approx 5$. By comparison, a $M=5$ shock in air has a reflected pressure of nearly seven times its incident pressure. The complex geometry of HYJET will yield different reflection traces than those from a simple tube, but the basic pattern is the same. Figure 6.12, $\beta=4.4$, shows a failure to initiate. The deflagration process is much slower than the leading waves, so it does not appear on these traces. There is a significant secondary explosion on T2, near 13.6 ms. The cause of this is unknown, although it is occasionally seen in other runs. It is highly localized; the only corroboration is provided by the shock oscillations on T1. Figure 6.13 shows the same mixture with a secondary explosion at the end of the vessel. This appears to be a DDT, as there are waves building behind the lead shock as it moves down the tank, but the peak pressure delay corresponds to shock focusing.

Figures 6.14 and 6.15 represent runs using the 25-mm nozzle (with cutter) with nitrogen dilution at 298 K. Figure 6.14 is a prompt initiation, similar to that with the 92-mm nozzle. The wave traveling shortly behind the detonation on T1 appears on many prompt initiations. I believe that this may result from detonation of material behind the nozzle exit, and reflection off the upstream head of the vessel. Figure 6.15 is a deflagration with no explosive phenomena. Note that the lead shock is much smaller, and decays to a continuous compression by the end of the vessel.

Figures 6.16 through 6.19 are from runs using H_2O dilution at 373 K, with the 92-mm nozzle. Figure 6.16 is a prompt initiation, with the same structure as the previous examples. Figure 6.17 is the next increment of dilution, $\beta=1.2$. This shows a small shock running down the vessel, with a closely coupled secondary explosion at the end. This appears to act too quickly for shock focusing to occur. A wave then runs back up the vessel. This is probably a detonation, as there would not have been enough time for a deflagration to consume the reactants. Also, the peak pressure and sharpness of the wave are consistent with prompt detonations. Figure 6.18 is for $\beta=1.6$, and shows a "running" transition to detonation. As the lead shock moves down the vessel, a stronger wave builds immediately behind it, and the wave reflects off the end of the vessel as a detonation. This sends another wave back up the vessel. Finally, Figure 6.19 shows initiation of deflagration, with a moderate explosion in the reflection, and a localized late explosion on T1.

Figures 6.20 and 6.21 are from one of the runs with the 25-mm nozzle and no diaphragm, allowing a flow field to be set up before combustion reaches the receiver. This is a classic DDT. Figure 6.20 shows the complete set of traces, while 6.21 is a closeup of the T3 trace, showing the pre-pressurization. We see that the initial wave reaches T3 at 8.5 ms, and gradual pressurization occurs from venting and deflagration. About 4.5 ms

after the initial wave, an explosion occurs near T3. This explosion travels both up and down the vessel as a detonation. This wave is fairly weak at the upper end of the tank (T1 and T2), as some of the reactants have already been consumed in the deflagration.

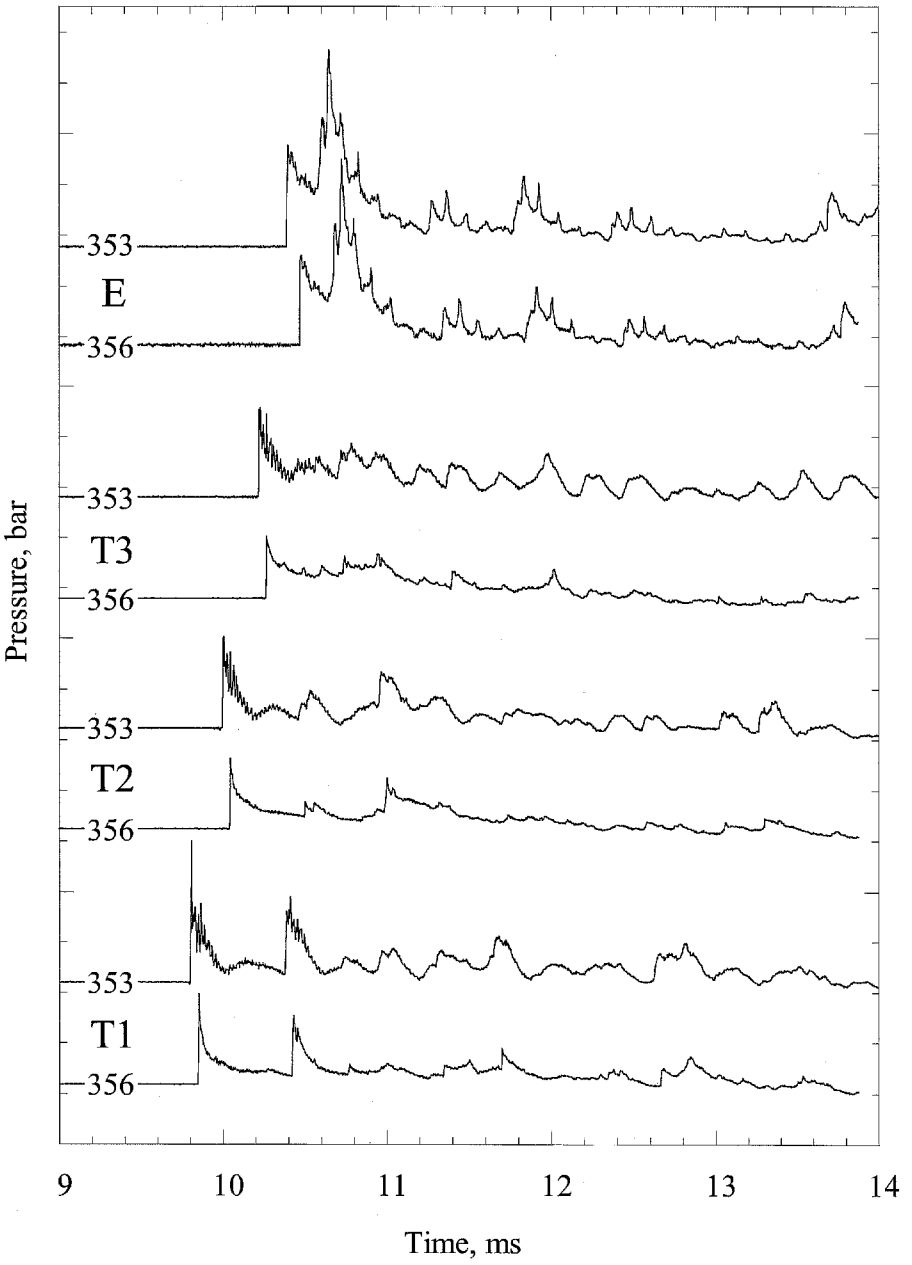

Figure 6.10: Comparison of recessed (run 353) and flush-mount (run 356) transducer signals.

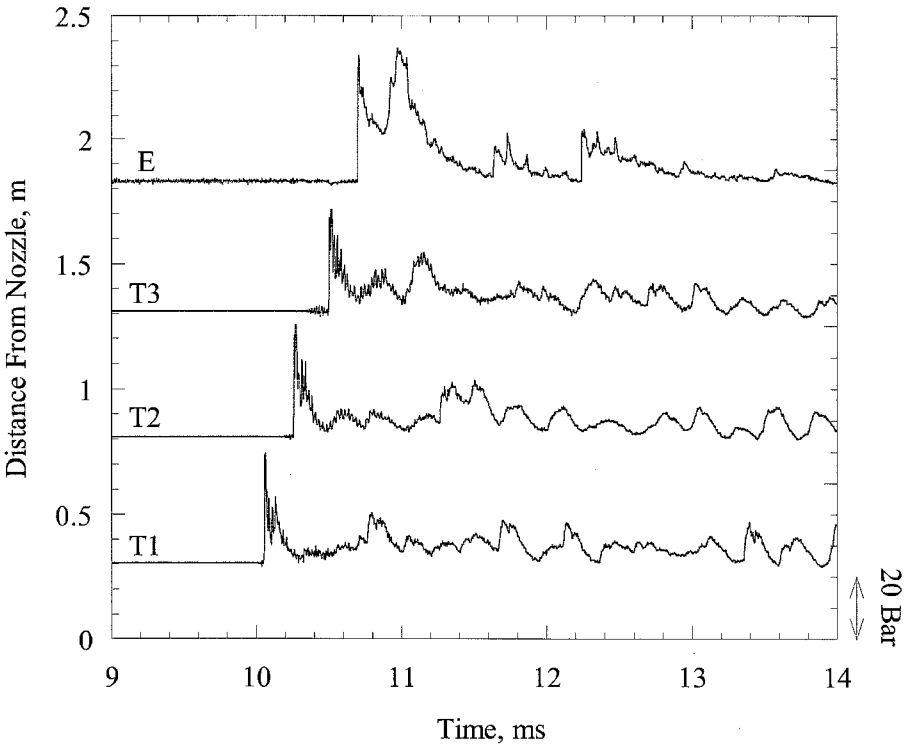

Figure 6.11: Prompt initiation with 92-mm nozzle, N_2 at 298 K, β=4.3. Note upstream propagation of reflection. Run 338.

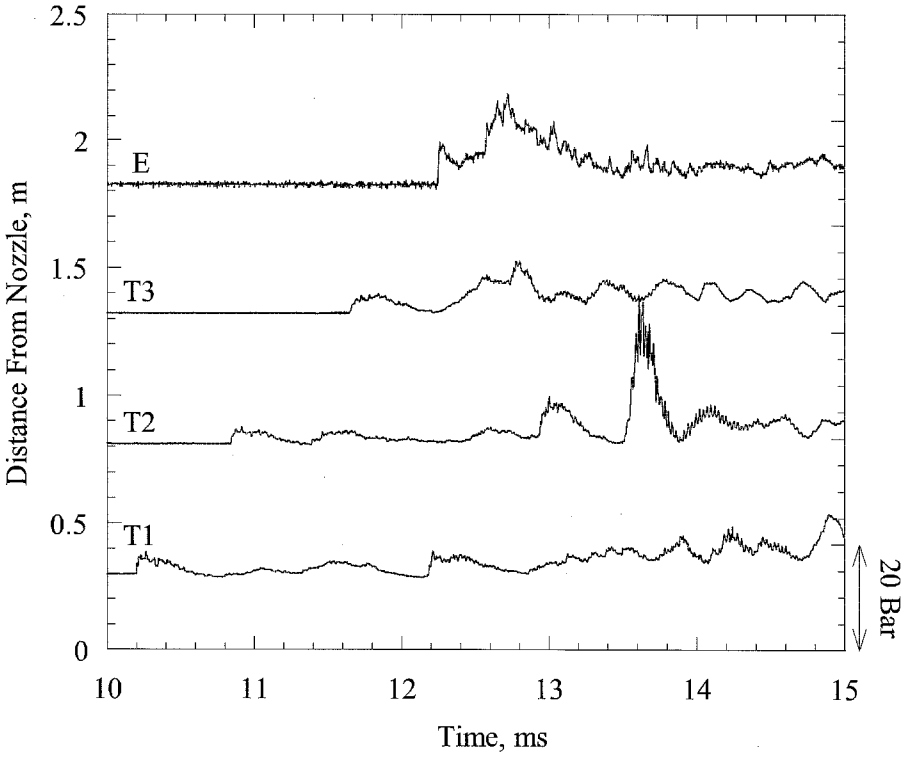

Figure 6.12: Failure to initiate detonation with 92-mm nozzle, N_2 at 298 K, β=4.4. Note late explosion on T2. Run 337.

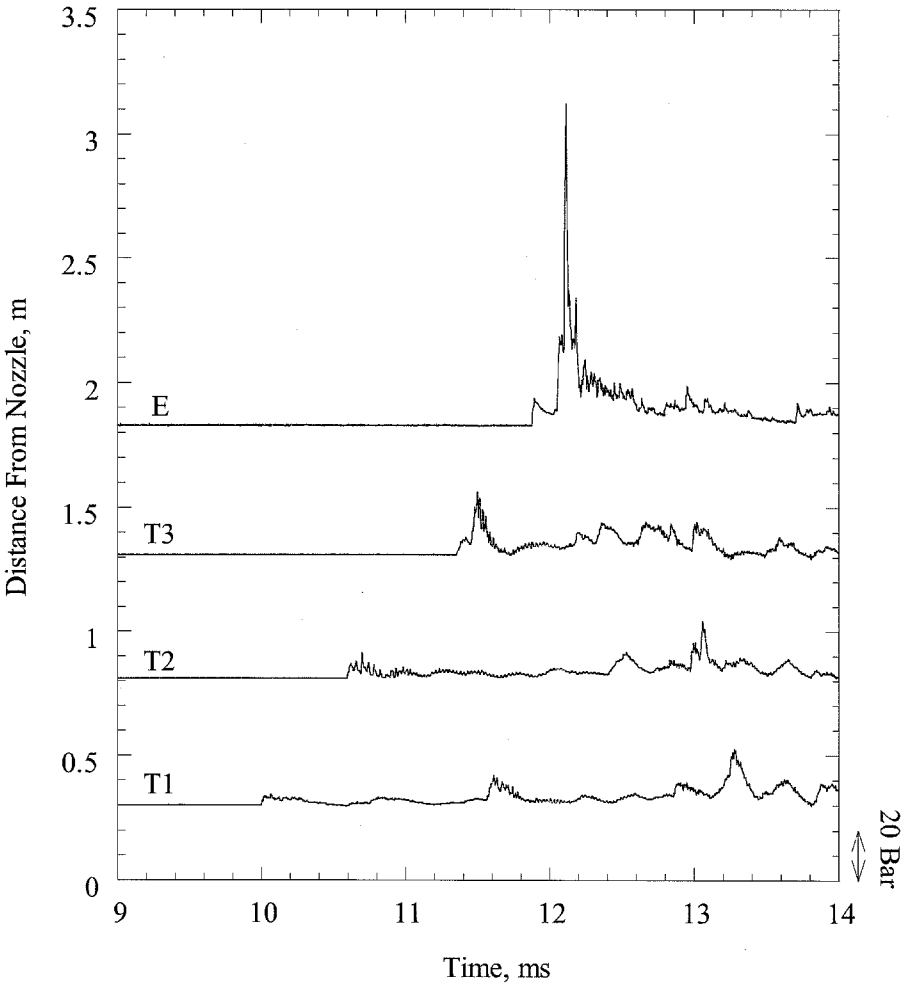

Figure 6.13: Failure to initiate detonation with 92-mm nozzle, N_2 at 298 K, β=4.4. Secondary explosion on E presumed to be in focal region. Run 339.

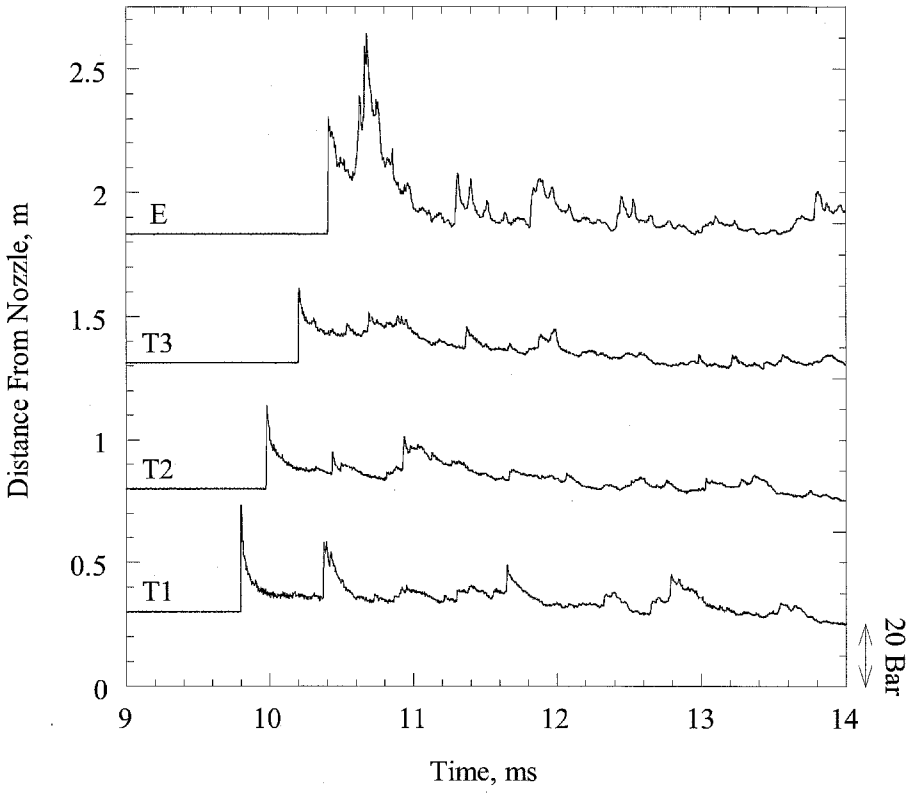

Figure 6.14: Prompt initiation with $\dot{N}_2$ at 298 K, β=2.9, using 25-mm nozzle with cutter. Run 369.

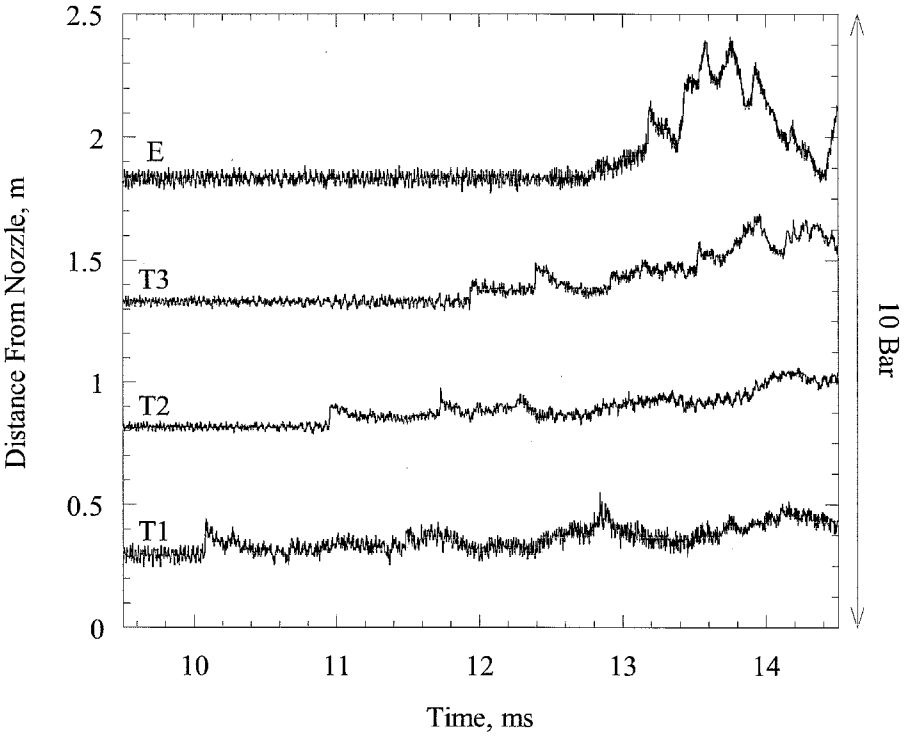

Figure 6.15: Failure to initiate detonation with 25-mm nozzle (with cutter), N_2 at 298 K, β=3.0. Run 368.

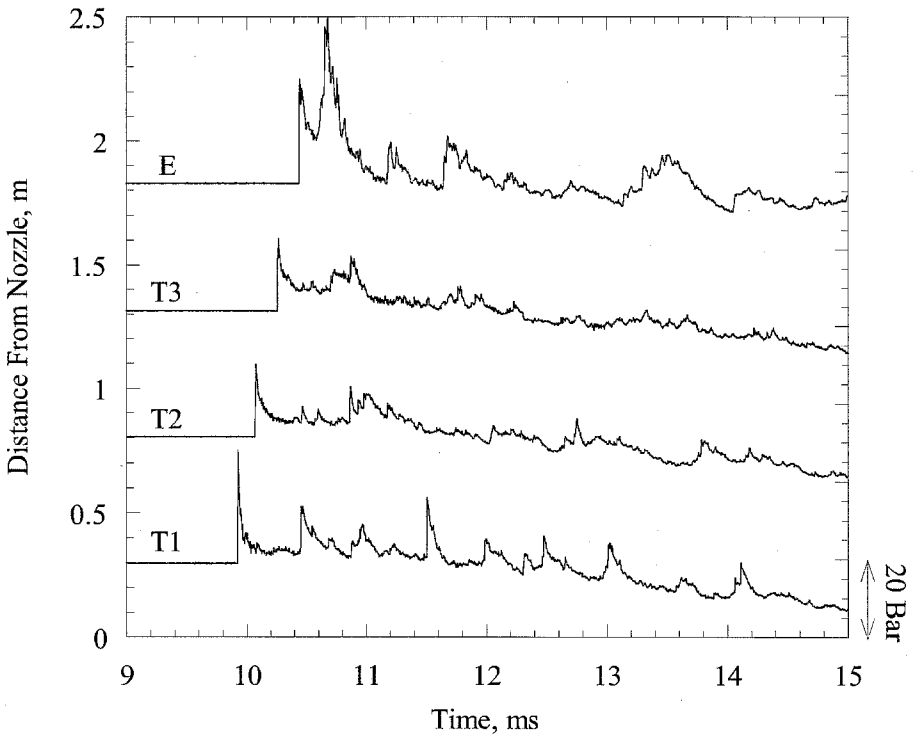

Figure 6.16: Prompt initiation with H_2O at 373 K, β=1.1. Run 380.

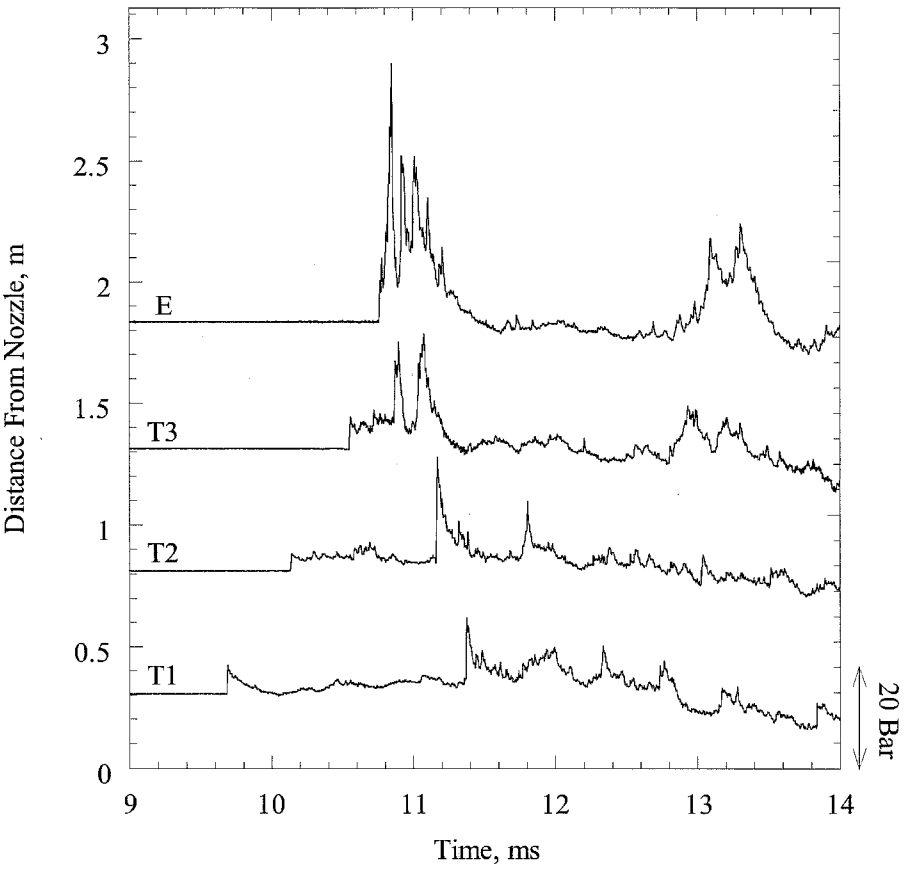

Figure 6.17: DDT at end of vessel, with H_2O at 373 K, β=1.2. Run 382.

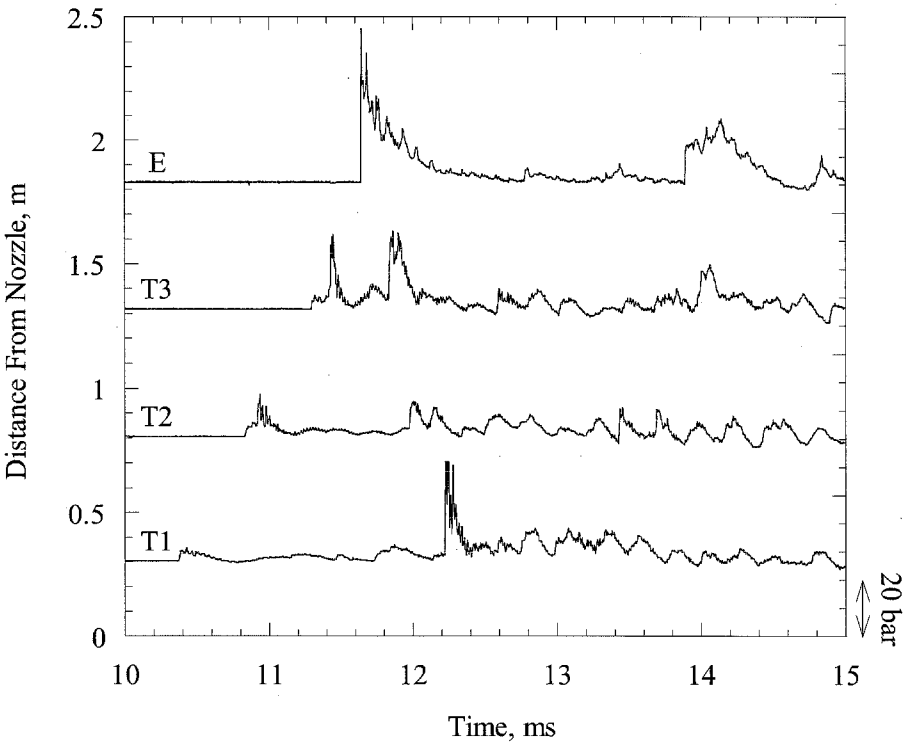

Figure 6.18: Running buildup to DDT, with H_2O at 373 K, β=1.6. Run 351.

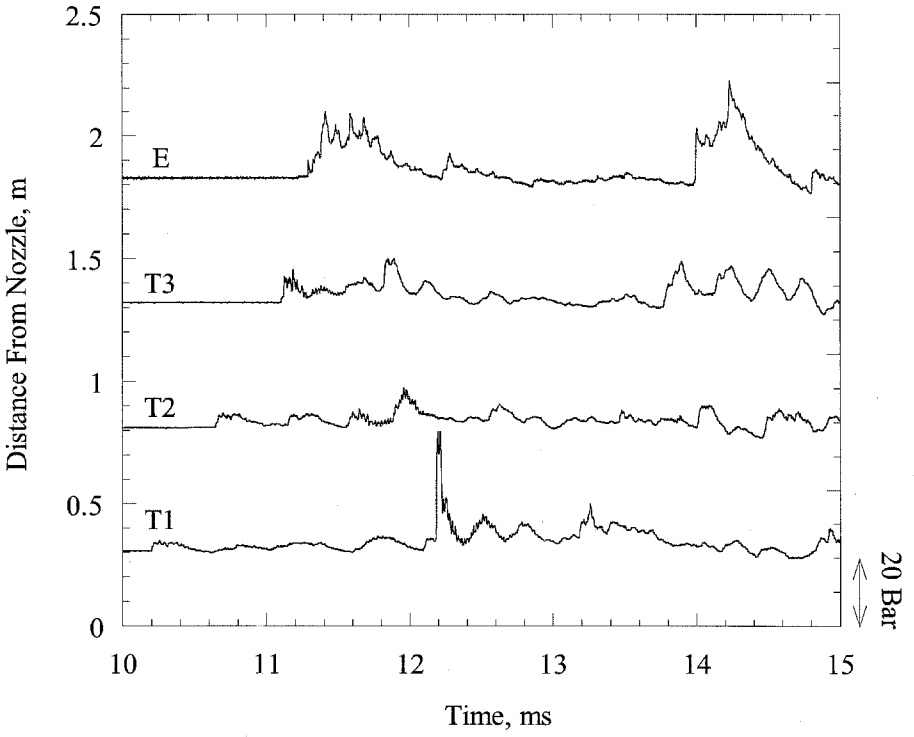

Figure 6.19: Failure to initiate detonation, with H_2O at 373 K, β=2.0. Run 348.

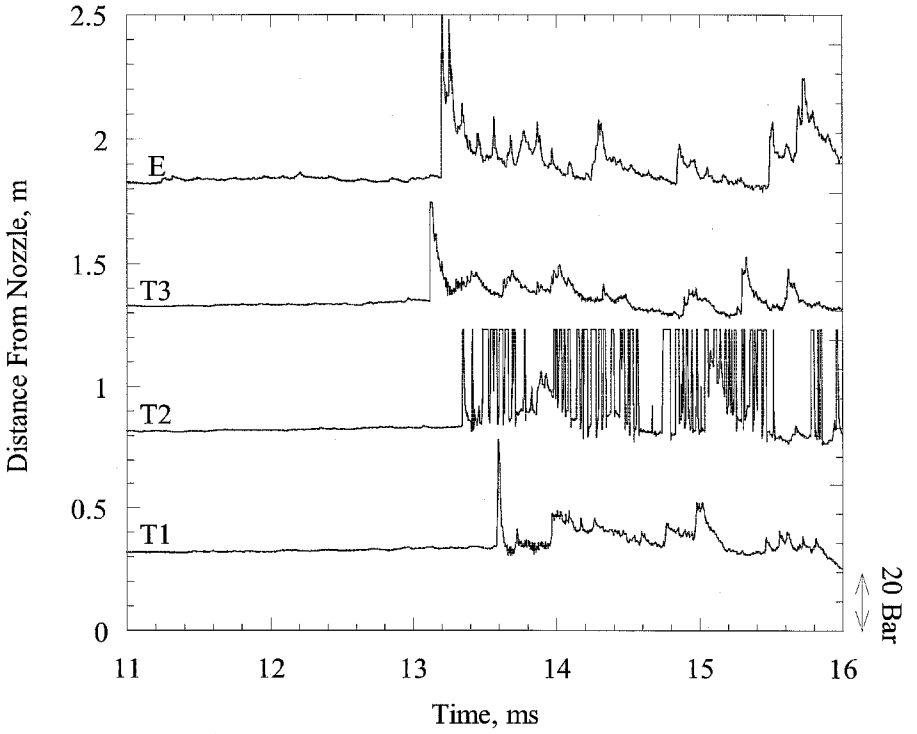

Figure 6.20: DDT near T3, 25-mm nozzle with no diaphragm, with N_2 at 298 K, β=1.8. Run 409.

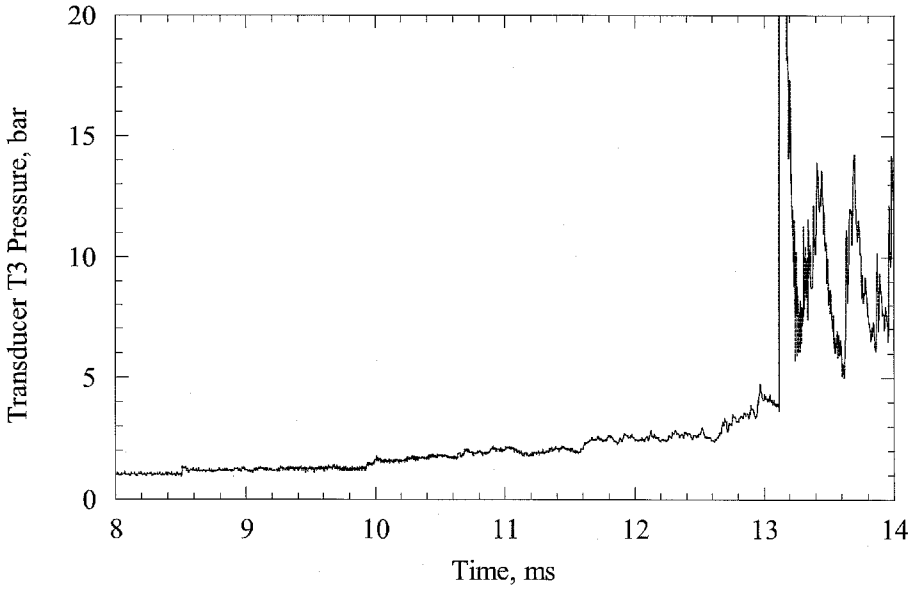

Figure 6.21: Pressure trace from T3 in previous plot, enlarged to show pre-pressurization before detonation.

6.2.4 Lead Wave Pressures

Figures 6.22 through 6.36 are a study of the lead wave pressures at each transducer. Reference pressures on each plot (shock wave, CJ detonation, and reflected detonation) were calculated with STANJAN. The choice of M=1.33 as a shock Mach number is based on two runs (numbers 319 and 320) with an air-filled receiver. The standard (β=2.6) driver mixture was used with the 92-mm nozzle, and the amplifier gains were turned up to minimize noise. The tests showed the lead shock moving at 450 m/s between T2 and T3, with a pressure of 1.8 bar. STANJAN gave the sound speed of the air as 388 m/s, and the pressure from a M=1.33 shock to be 1.82 bar. Although this is only used as a reference in the graphs, it gives good agreement in most of the tests with no prompt initiation. The 92-mm nozzle gives slightly higher pressures when there is hydrogen in the gas mixture.

In all prompt initiation cases, we see a pressure at T1 that is near the reflected CJ pressure. As the wave proceeds down the vessel, the pressure decreases at T2 and T3, but is still above the static CJ pressure. At transducer E, the pressure is again near the reflected CJ value, as expected. The T_i pressures can be explained by Figures 6.24–6.26, which model the detonation growth. In the case of an unconfined spherical detonation, the wave locally becomes flatter as the radius of curvature increases. The initial process in the vessel is similar, with the addition of reflections from the vessel walls. The reflections will not interfere with the detonation as it propagates, but determine the pressure measured at the wall.

In Figure 6.24, the detonation is initiated a short distance from the nozzle exit. It is unlikely that the detonation could be initiated immediately at the exit, as the reactants are being pushed downstream by the jet and time is needed for entrainment and ignition. Using the spherical initiation model, the wave flattens as it proceeds down the vessel. As the wave flattens, the angle between the wave and the wall (θ in Figure 6.25) changes from zero (normal reflection above point of initiation) to the limit of 90° (planar detonation). The change in θ leads to a change in the reflection mode and wall pressure. The two modes of reflection are regular and Mach reflection, and are shown in Figure 6.25. The associated wall pressures are shown in Figure 6.26. The pressures in Figure 6.26 were calculated by Raza Akbar of GALCIT (work in progress) from two- and three-shock theory with heat release. The data presented is not for the BETA mixtures, but illustrates the typical variation of pressure expected for reflected detonations (see also Nettleton (1987)). For θ=0, normal reflection occurs, and the pressure is approximately $2.5P_{CJ}$. When the detonation is planar, θ=90° and there is no reflected wave, yielding a wall pressure of P_{CJ}. A cusp occurs in the region of Mach wave formation. Pressure data from the BETA experiments follows this trend. A similar effect is seen in blast waves generated by explosives detonated above the ground (Glasstone and Dolan 1977).

The 92-mm nozzle (Figures 6.22 and 6.23) tends to give high pressures (reflected detonation) at nearly every transducer in a prompt initiation, with the exception of the runs with no diaphragm. Note that some of these traces were clipped by the acquisition system, so the true peak pressures may be higher. This may indicate that the large nozzle is able to initiate a detonation further into the vessel than the other nozzles. A

second possible reason for these high pressures is the combination of driver mass flow and receiver induction time. The 92-mm nozzle was able to initiate detonation in the least sensitive mixtures, but as a consequence, the induction time (for the receiver mixtures) was the highest. The detonation will be initiated further into the vessel, as the reactants are being driven downstream by the jet flow. In comparison, the T2 and T3 pressures were lower for the tests with β=2.6. This mixture is considerably more sensitive than the other mixtures used ($\beta \geq 3.76$), and the reduced induction time may allow initiation to occur before the reactants are driven far downstream by the jet flow.

Figures 6.27 and 6.28 show the detonation growth for the 64 and 38-mm nozzles. The same trend occurs here as for the 92-mm nozzle, but the results are more pronounced. The pressures at T1 are at or above the reflected CJ value, so the detonation is initiated near that axial location. The pressures drop progressively at T2 and T3, indicating flattening of the wave, and again jump to the reflected CJ value as they reflect off the end of the vessel.

Figures 6.29 and 6.30 show the peak pressures from the 25-mm nozzle, both with and without the diaphragm cutter. The pressures at T1 fall further below the reflected CJ line than those for the larger nozzles, indicating that the detonation is initiated closer to the nozzle. The 25-mm nozzle will have a lower mass flowrate than the other nozzles, so the reactants will not be convected as far downstream before initiation as with the other nozzles. In addition, the mixtures are more sensitive, so the induction time is reduced, bringing initiation closer to the jet exit. The photographic tests support this, showing that detonation was initiated within 100–200 mm of the nozzle exit. The peak pressures follow the decreasing trend at T2 and T3. At the end of the vessel, the pressures approach the reflected CJ value but fall short; the larger nozzles typically met or exceeded this value. The data for the 25-mm nozzle is particularly well clustered; perhaps the increased sensitivity of this mixture provides more repeatable initiation (i.e., initiation across most of the jet head vs. local initiation at the edge of one of the larger jets).

The tests with no diaphragm (and a uniform mixture in both vessels) are represented in Figures 6.31 and 6.32. The 92-mm nozzle gives high pressures at T1, typical of the other cases. The pressures at T2 and T3 follow the usual trend. In the tests using the 92-mm nozzle with diaphragm, the points were often near the reflected CJ line at all three T transducers. The mixtures used in the no-diaphragm tests were more sensitive, however, and the reduced induction time may allow initiation closer to the nozzle exit, as mentioned previously. This is most evident with the 25-mm nozzle, for which the T1 pressures fall far below the reflected CJ pressure. These were the most sensitive mixtures used in the BETA series, and have the shortest induction times.

The lead wave pressures for the N_2-dilution tests at 373 K are shown in Figures 6.33 and 6.34. These tests used the 92-mm nozzle only, and the results are similar to those for the 92-mm tests at 298 K (Figures 6.22 and 6.23). The pressures at the T-transducers are all high near β_{CRIT}, but the T2 and T3 pressures drop as β is decreased. The induction time reasoning applied to the other cases can be used here as well.

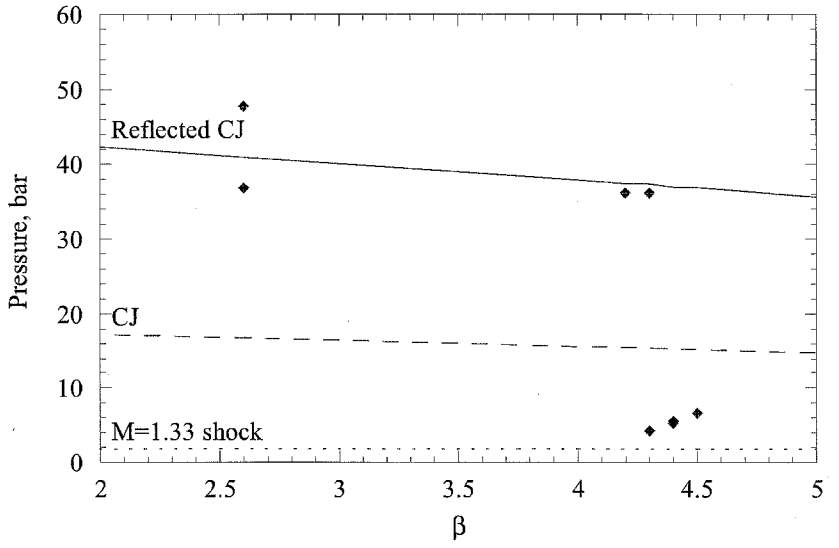

Transducer T1

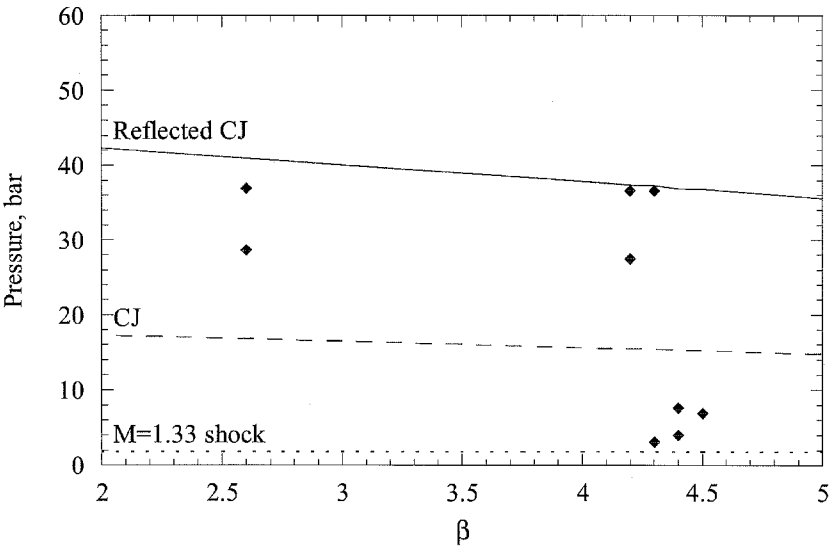

Transducer T2

Figure 6.22: Lead wave pressures for nitrogen-diluted mixtures at 298 K, with 92-mm nozzle. Three points on T1 plot at 36 bar are at the maximum transducer level; true values will be somewhat higher.

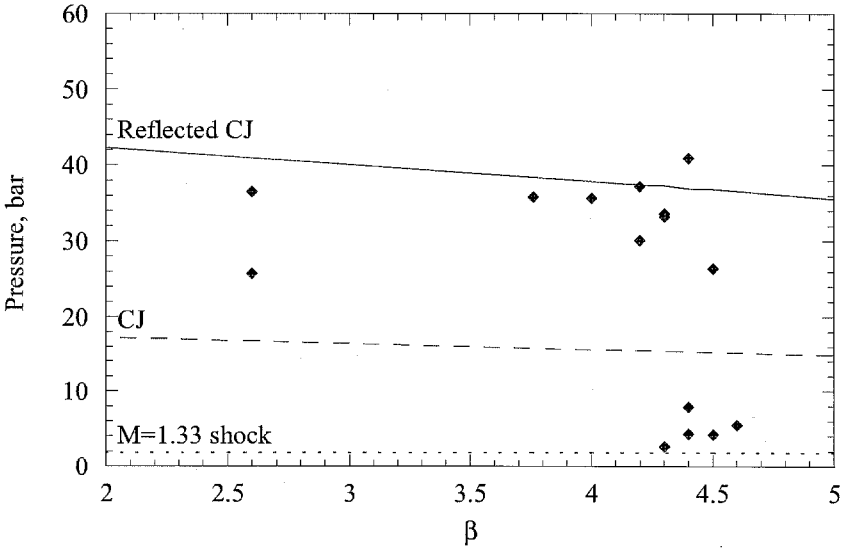

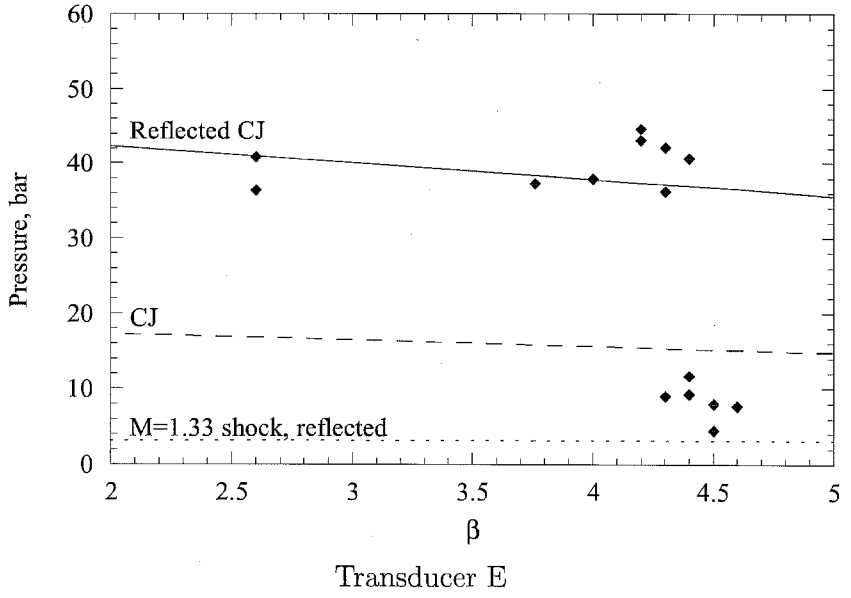

Figure 6.23: Lead wave pressures for nitrogen-diluted mixtures at 298 K, with 92-mm nozzle, continued.

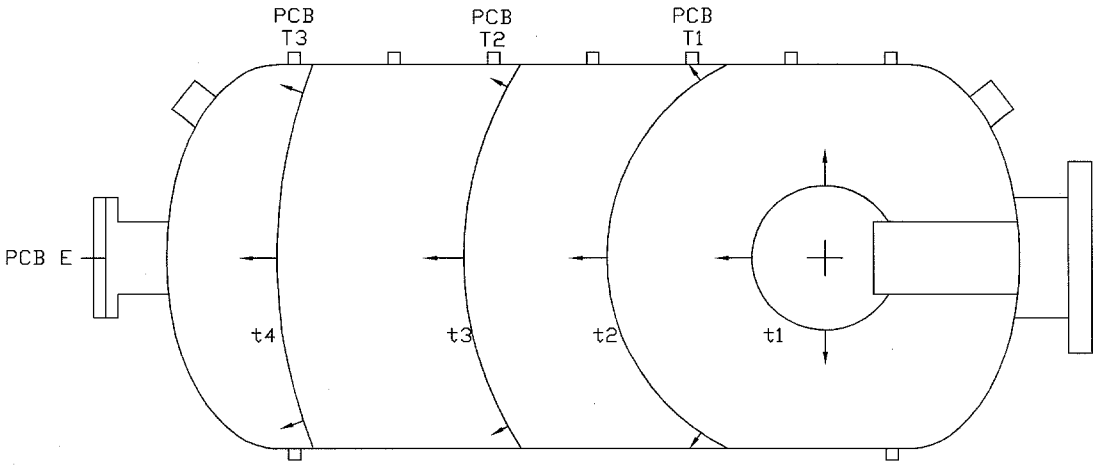

Figure 6.24: Model of detonation growth as sphere. Wave flattens as detonation proceeds down vessel, and angle between detonation and wall approaches 90°.

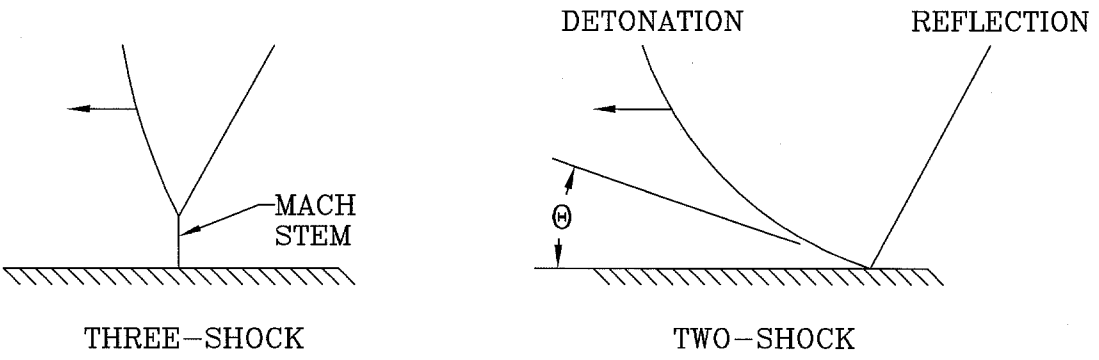

Figure 6.25: Schematics of Mach and regular reflection. If θ is small enough, regular (two-shock) reflection occurs. For θ larger than about 60° (Figure 6.26), a Mach wave is generated to match the flow behind the detonation to the boundary.

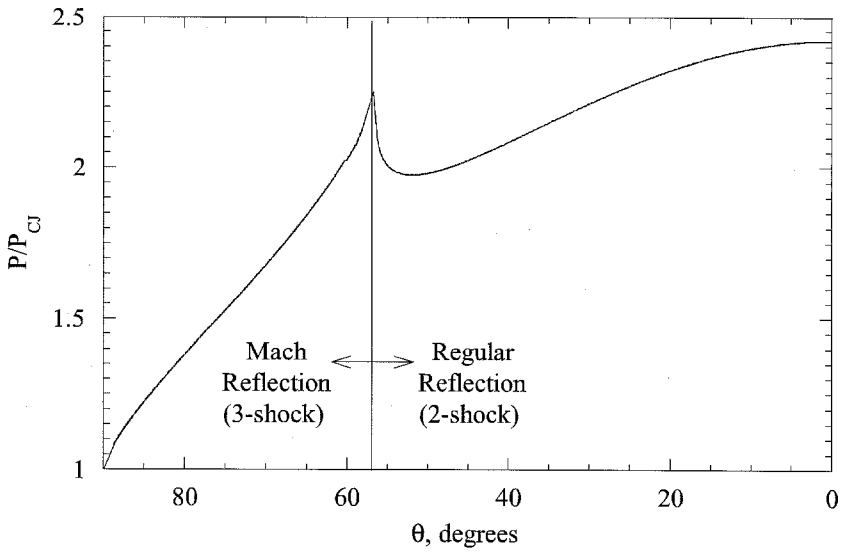

Figure 6.26: Calculated values of wall pressure using two- and three-shock theory with energy release.

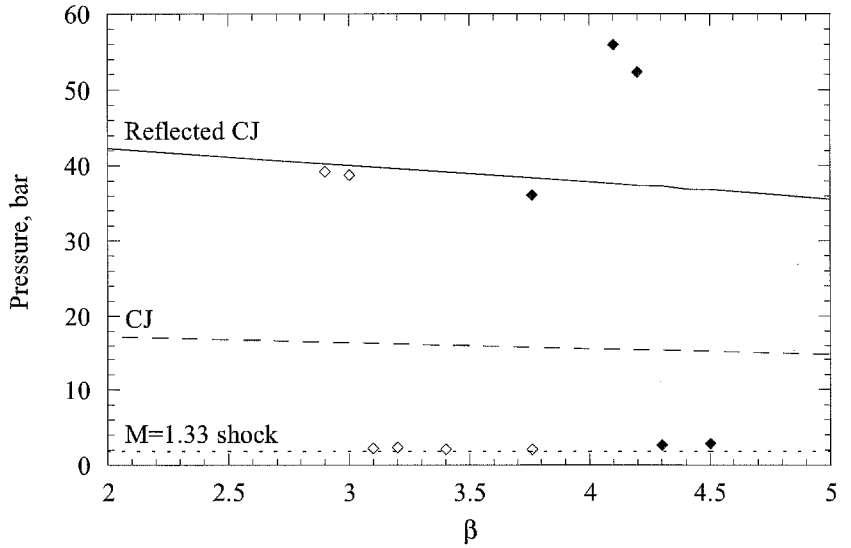

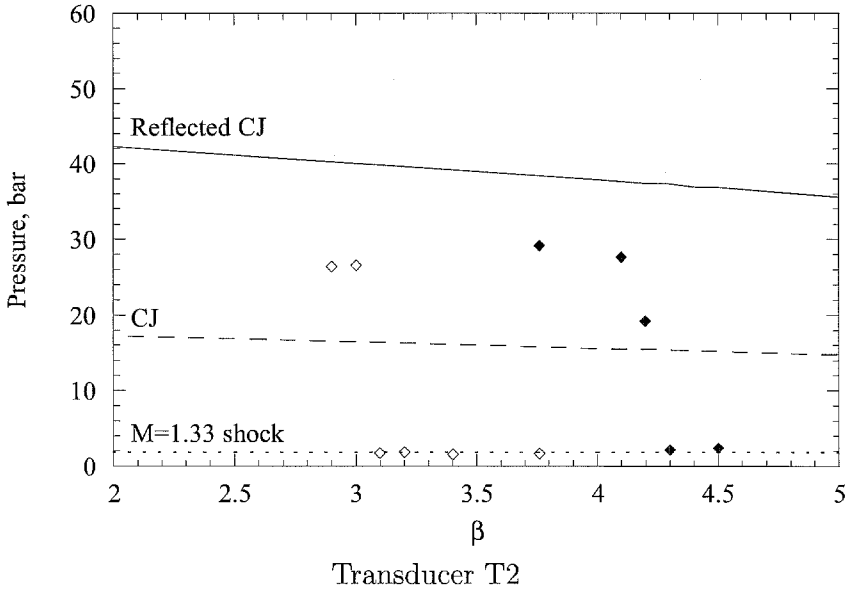

Figure 6.27: Lead wave pressures for nitrogen-diluted mixtures at 298 K, with 64- and 38-mm nozzles. Solid points are for 64-mm nozzle, open points for 38-mm.

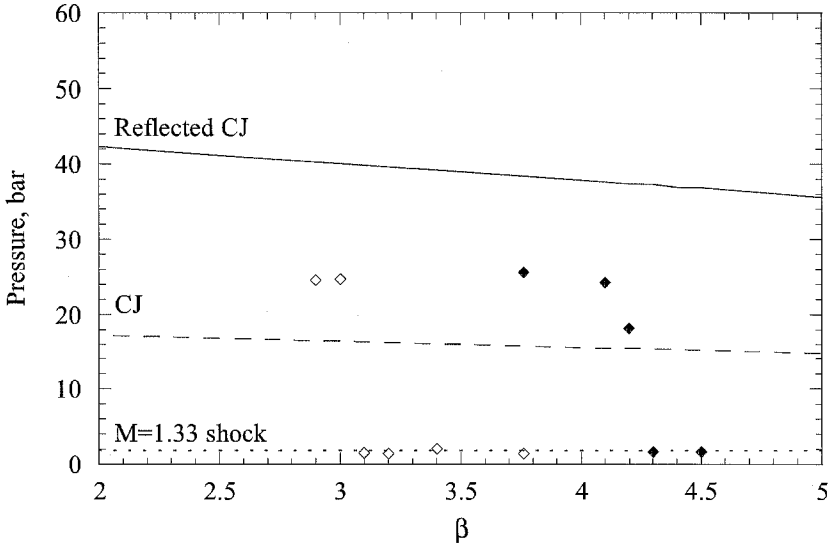

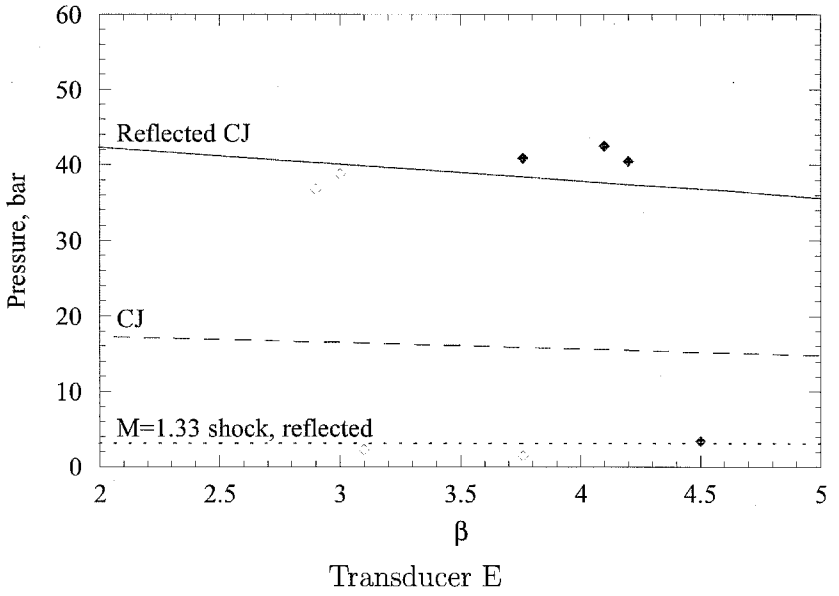

Figure 6.28: Lead wave pressures for nitrogen-diluted mixtures at 298 K, with 64- and 38-mm nozzles, continued. Solid points are for 64-mm nozzle, open points for 38-mm.

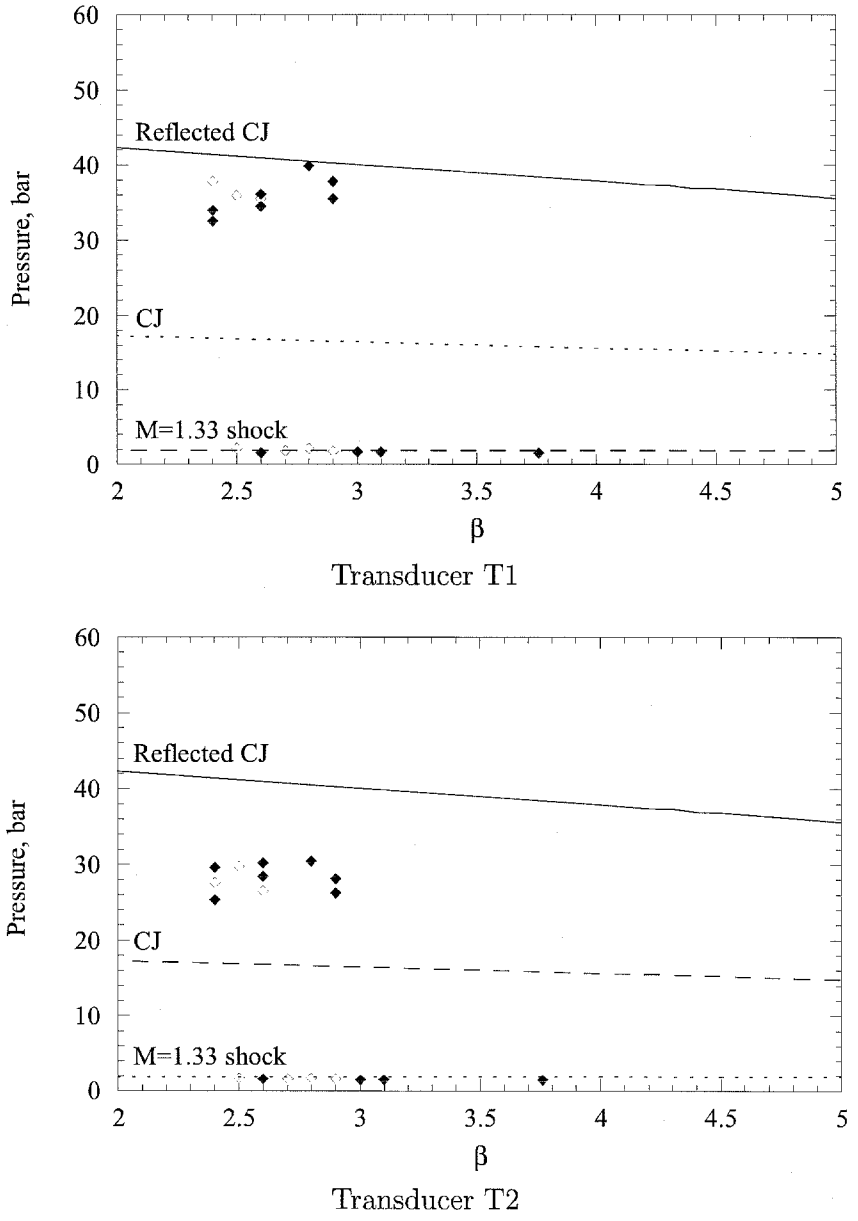

Figure 6.29: Lead wave pressures for nitrogen-diluted mixtures at 298 K, with 25-mm nozzle. Solid points are for nozzle with diaphragm cutter.

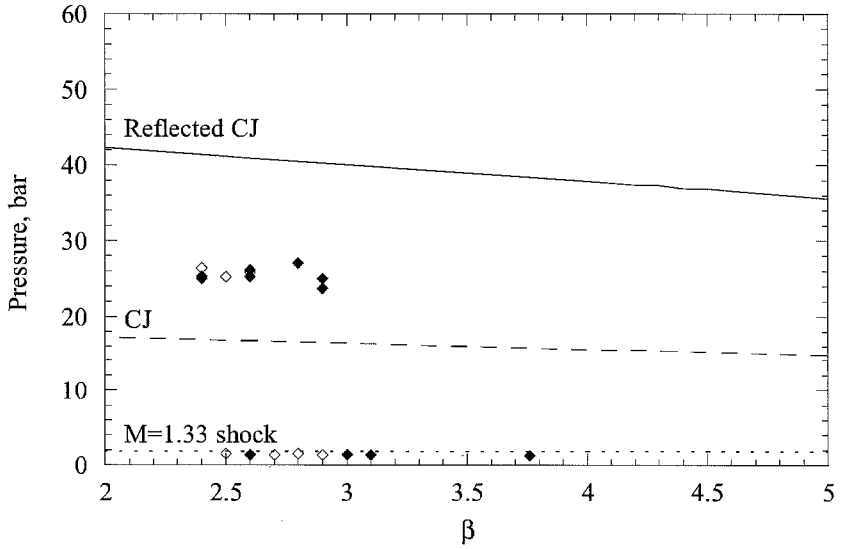

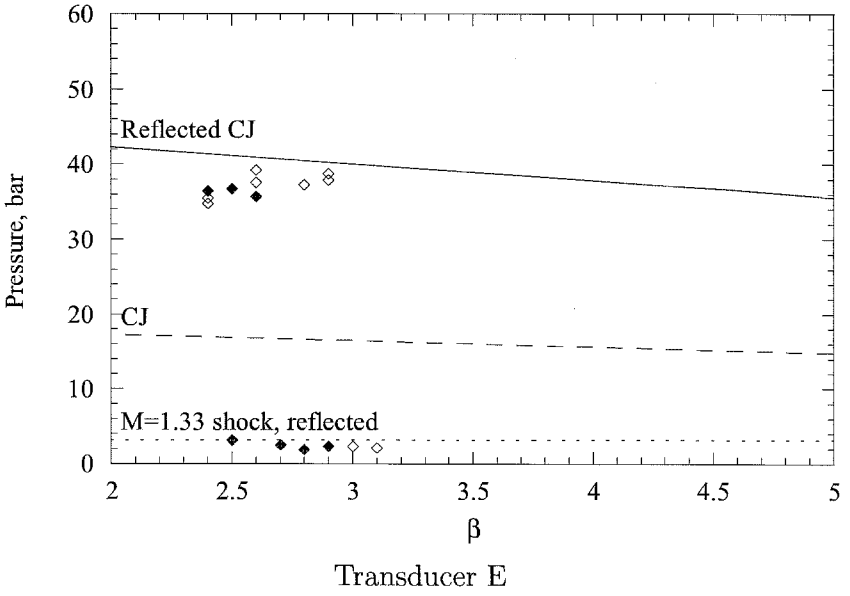

Figure 6.30: Lead wave pressures for nitrogen-diluted mixtures at 298 K, with 25-mm nozzle, continued. Solid points are for nozzle with diaphragm cutter.

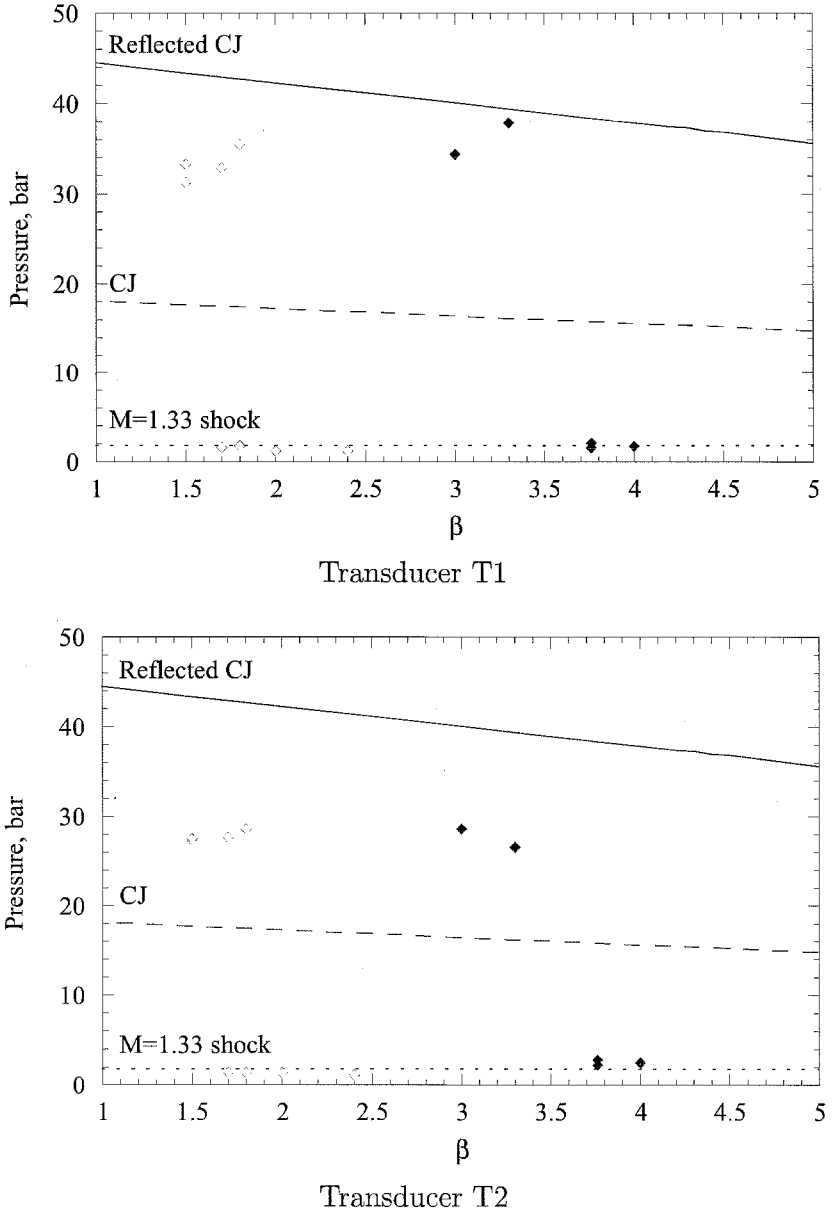

Figure 6.31: Lead wave pressures for nitrogen-diluted mixtures at 298 K, with no diaphragm. Mixture is same in both vessels. Solid points are for 92-mm nozzle, open points for 25-mm nozzle with diaphragm cutter.

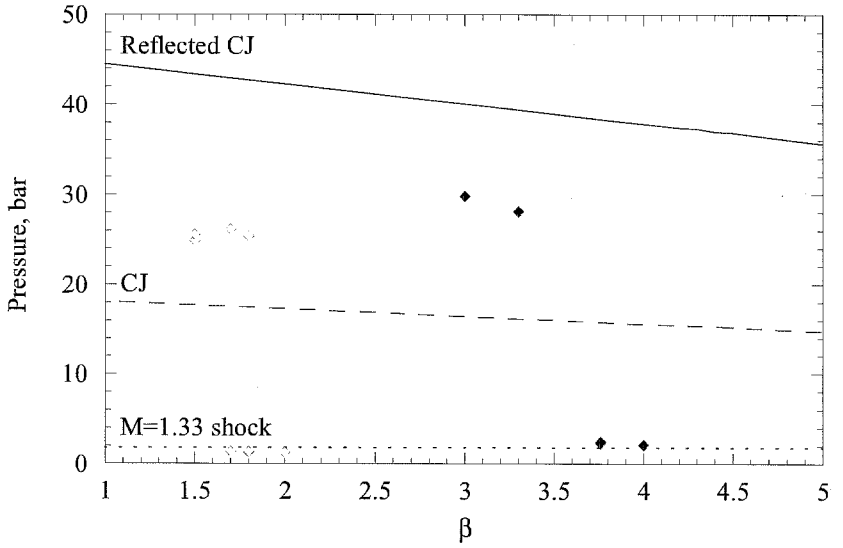

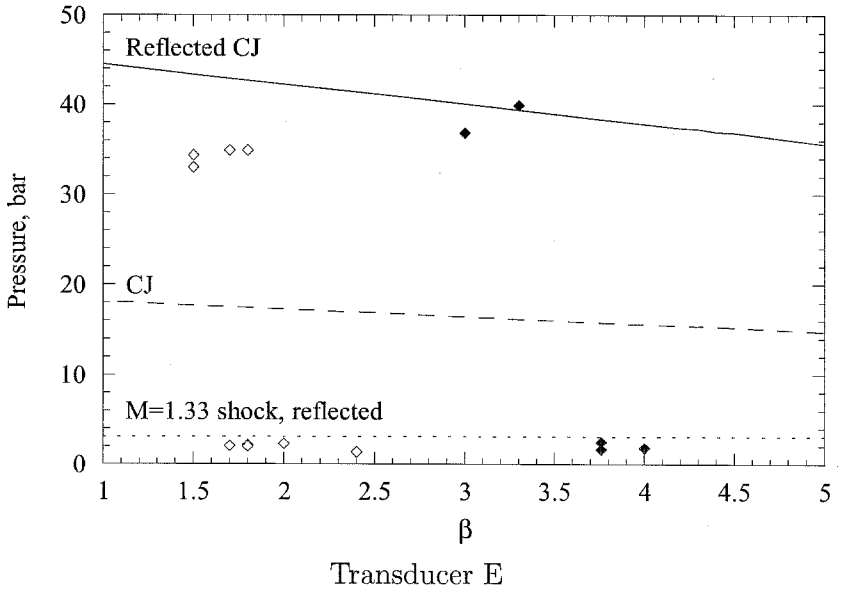

Figure 6.32: Lead wave pressures for nitrogen-diluted mixtures at 298 K, no diaphragm, continued.

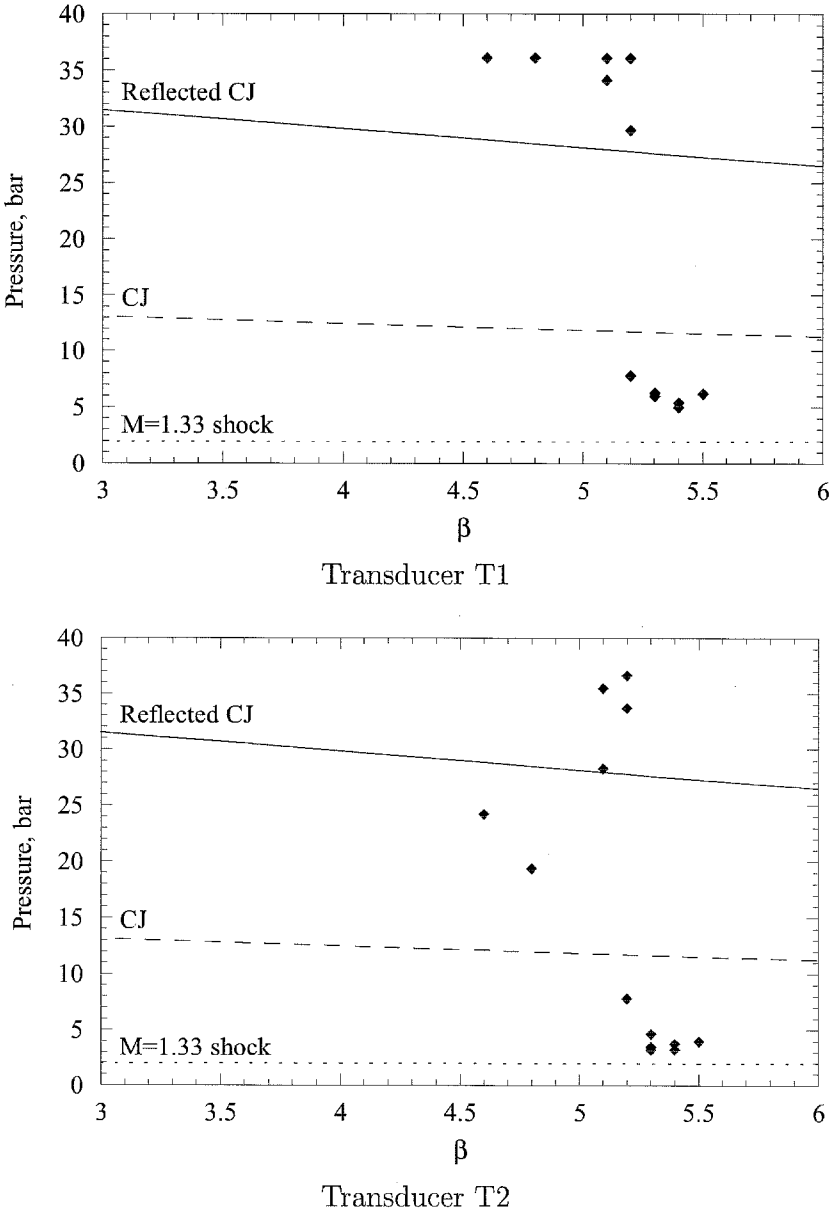

Figure 6.33: Lead wave pressures for nitrogen-diluted mixtures at 373 K, 92-mm nozzle.

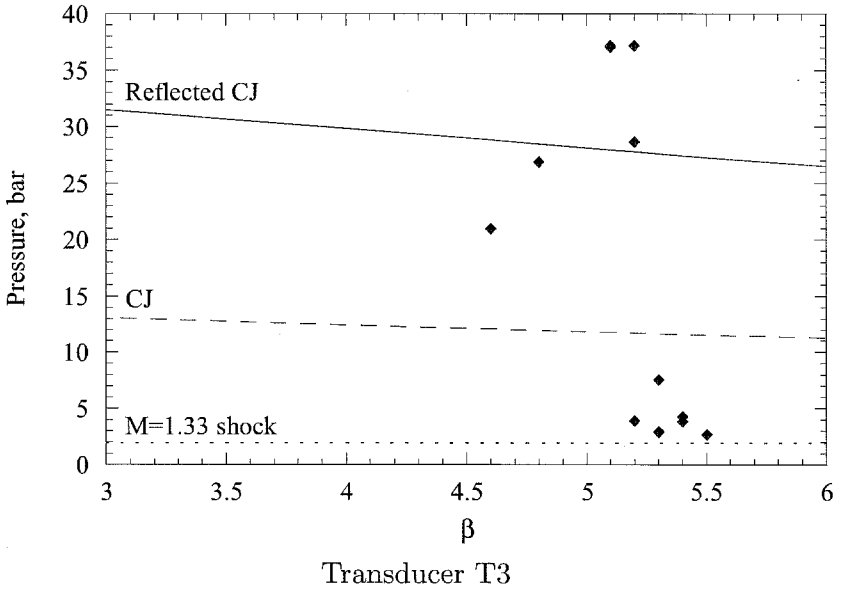

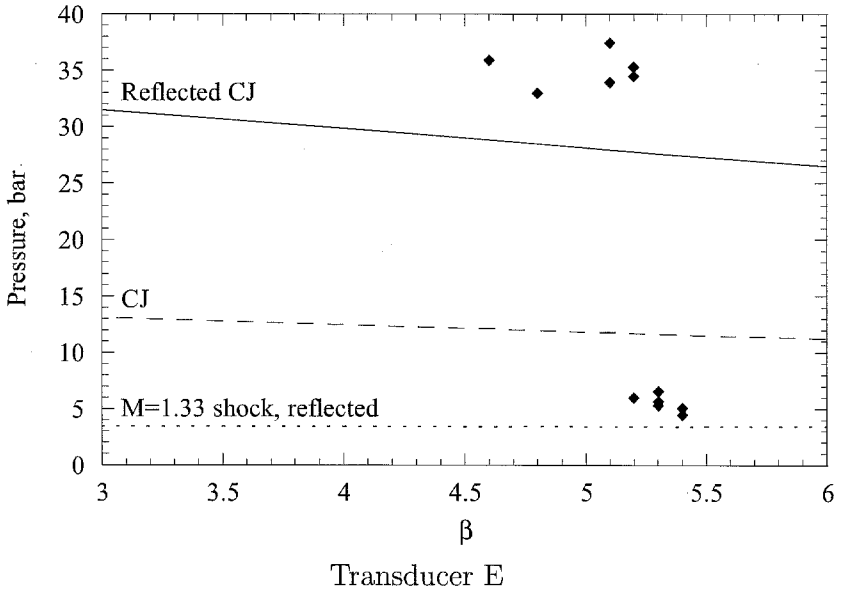

Figure 6.34: Lead wave pressures for nitrogen-diluted mixtures at 373 K, continued.

Figures 6.35 and 6.36 show the process of DDT in the H_2O dilution cases. As β is decreased, the lead wave pressures begin to rise, especially on T3. They finally take a large jump at the transition point. The pressures at the E transducer are especially high in the DDT region. This is to be expected. As β is decreased, the mixture becomes more sensitive, but not enough for prompt initiation. When β is slightly above β_{CRIT}, the mixture is most susceptible to transition. This results in the highest pressures (up to 80 bar in this set of tests), because the mixture is shocked before the transition. Once the prompt limit is reached, the pressures are relaxed, because the detonation is proceeding into unshocked reactants.

Shepherd (1992) studied combustion-generated loading in H_2-air-H_2O mixtures, and found similar results. Severe loadings occurred when slow-burning, lean or dilute mixtures burned almost to completion before transitioning to detonation. The combustion compresses the unburned mixture, leading to hot spots and localized explosions that can coalesce and detonate the remaining reactants. This is analogous to knock in an internal combustion engine. Estimated pressures from this condition reach 165 bar. The worst DDT case occurs under unique conditions, when a detonation forms in shocked reactants very close to a confining surface. If the precursor shock reflects just before the detonation overtakes it, the surface will receive an impulse from both waves (i.e., shock piling). Reflected pressures in this regime were predicted to be in the range of 300–600 bar. However, the conditions and timing required for this scenario are highly improbable.

Combustion modeling by Breitung (1993) predicted peak DDT pressures of over 100 bar in realistic mixtures and conditions. Boyack et al. (1992) determined that detonation focusing by edges and corners created pressures higher than that for normal detonation reflection. Reflected pressures can also be increased if a layer of inert gas lies between the detonation and the surface.

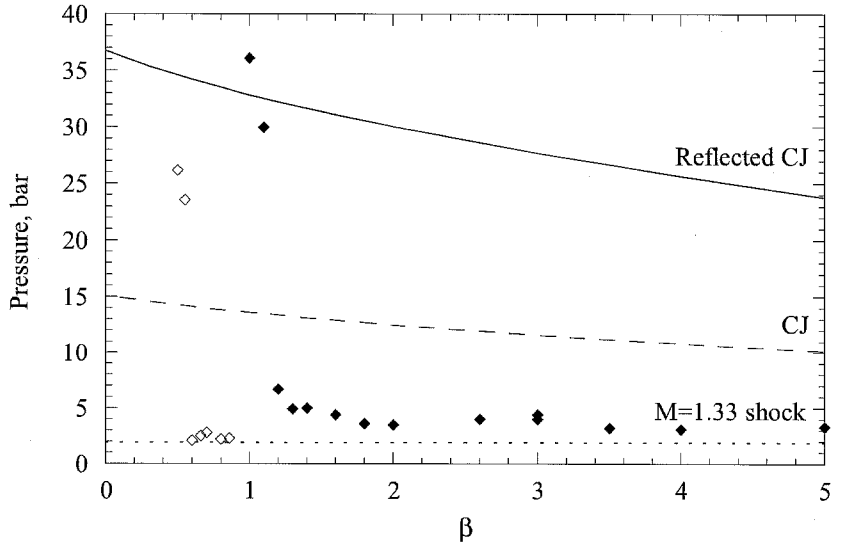

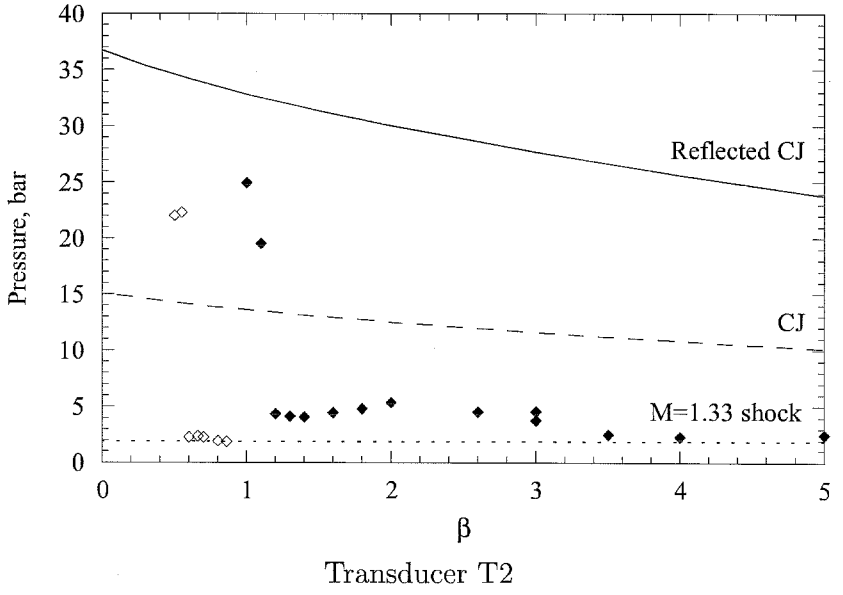

Figure 6.35: Lead wave pressures for steam-diluted mixtures at 373 K. Solid points are for 92-mm nozzle, open points for 38-mm nozzle.

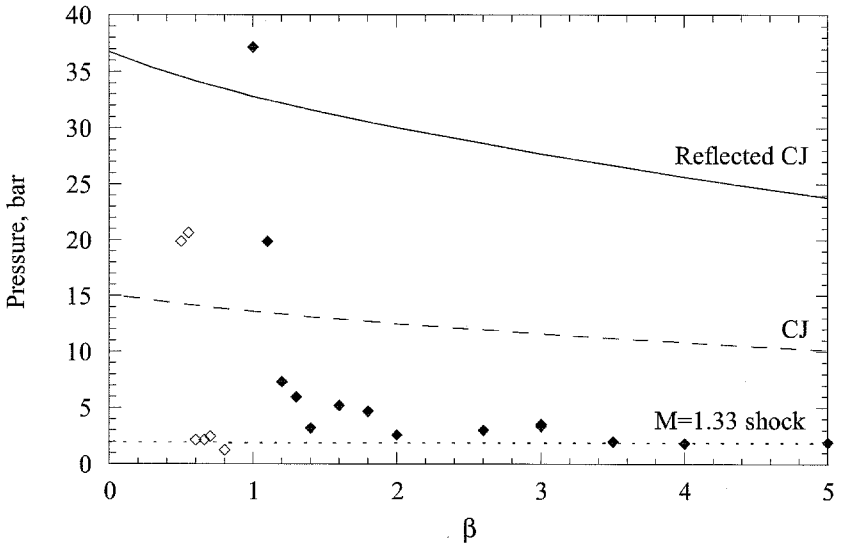

Transducer T3

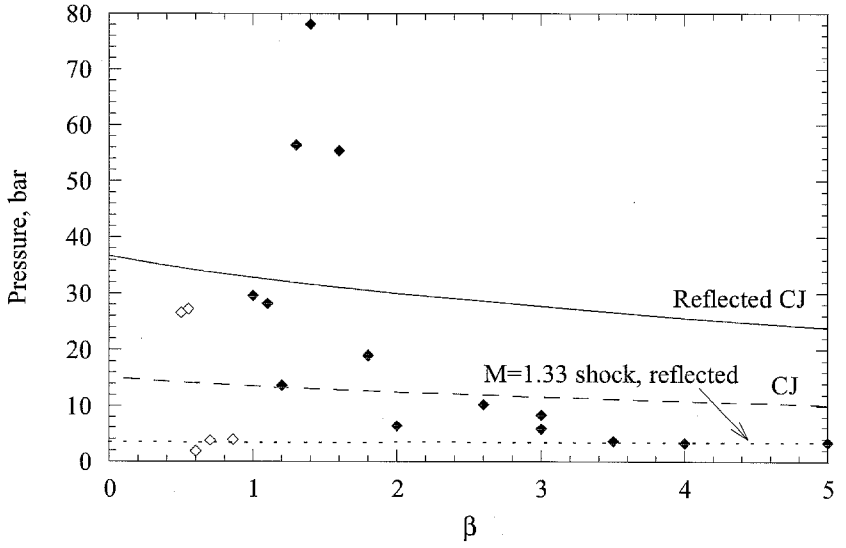

Transducer E

Figure 6.36: Lead wave pressures for steam-diluted mixtures at 373 K, continued.

6.2.5 Lead Wave Velocities

The final study is into the lead wave velocities. The wave arrival times were recorded at each transducer, and the wave speed was calculated between transducers T2 and T3. Between T1 and T2, wave curvature and the startup process will introduce timing differences over and above those due to acceleration or decay. Transducers T3 and E are at different radial locations, so the shape of the wave would affect the apparent velocity. This effect will be used to estimate wave curvature.

The lead wave velocity, V_{2-3}, is shown in Figures 6.37 through 6.39. Transition is clear in the N_2-dilution plots; the points either lie near the shock line, or above the CJ line. The excess velocity of the detonations may be due to overdrive, or may be the result of wave obliquity at the edges of the vessel (Figure 6.24). In the H_2O case (Figure 6.39), the evolution of the lead wave from shock, through DDT to detonation, is evident from β=3 to β_{CRIT}. When detonation occurs, we see that the velocity is a bit higher than the CJ value, for the reasons cited above.

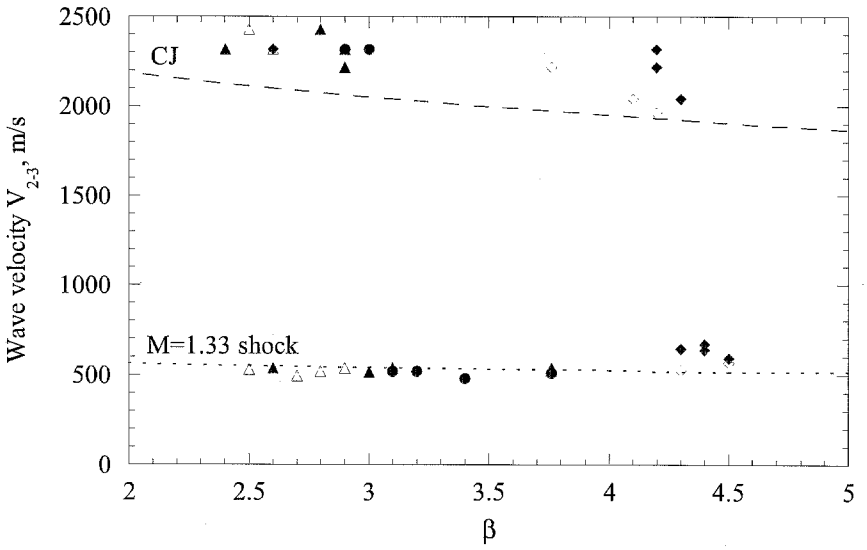

Figure 6.37: Leading wave speed measured between transducers T2 and T3, for N_2-diluted mixtures at 298 K. Diamonds, 92-mm nozzle; squares, 64-mm; circles, 38-mm; triangles, 25-mm; open triangles, 25-mm w/c.

The velocity between the T3 and E transducers can not be measured accurately, because the transducers are at different radial locations, and the wave is bowed. The center of the wave arrives before the edges, and the velocity between T3 and E will appear to be higher. We can, however, measure the amount of lead that the center of the wave has over the edges. Figure 6.40 shows a simplified schematic of the wave, relative to the transducers. If we assume that the wave velocity is constant at V_{2-3}, the lead, L, is equal to the distance between the transducers minus the "apparent" distance traveled. In short, L=0.51 $- V_{2-3}(t_E - t_{T3})$, where t_i is the arrival time at transducer i. The leads

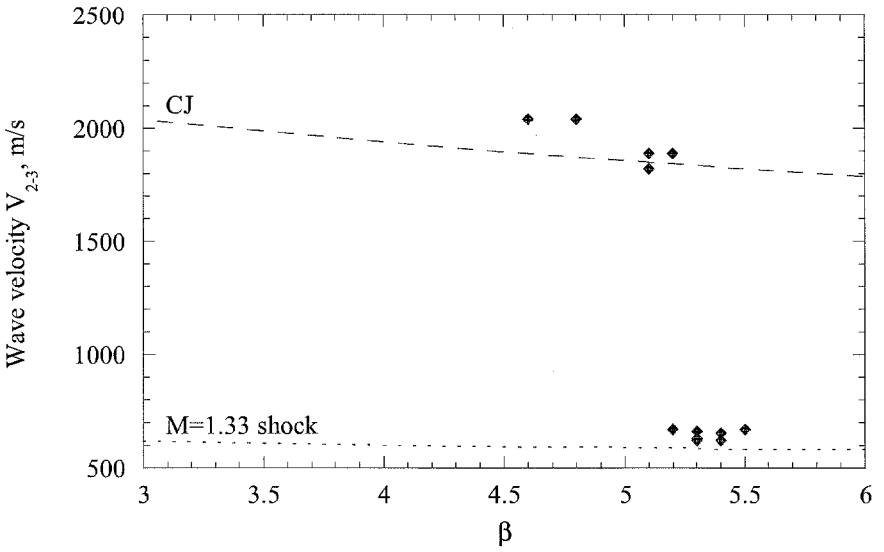

Figure 6.38: Leading wave speed measured between transducers T2 and T3, for N_2-diluted mixtures at 373 K (92-mm nozzle).

calculated from the detonation arrival times varied from 1 to 12 cm, with a few negative values. The negative values indicate that the wave was decelerating between the T3 and E transducers. As shown in Figure 6.37, the detonations are still overdriven at station T3, so deceleration is expected. The lead calculation is only a rough estimate. For comparison, we can look at the ray trace simulation of Chapter 5. In the simulation, the initial wave (Figure 5.16, page 55) had a radius of curvature of 1.72 m. The horizontal distance from the wave origin to the edge of the wave was 1.66 m. This results in a lead of 6 cm, so at least the magnitude is comparable. On the final run of the BETA series, the sting from the shock focusing study (Chapter 5) was installed in the end flange and aligned with T3. A detonation was initiated with the 92-mm nozzle in a mixture of β=2.6 (N_2), and the lead was calculated. The velocity was measured at 2320 m/s. The arrival time difference was 0.04 ms, giving a lead of 9.3 cm. This is considered to be the "correct" measurement.

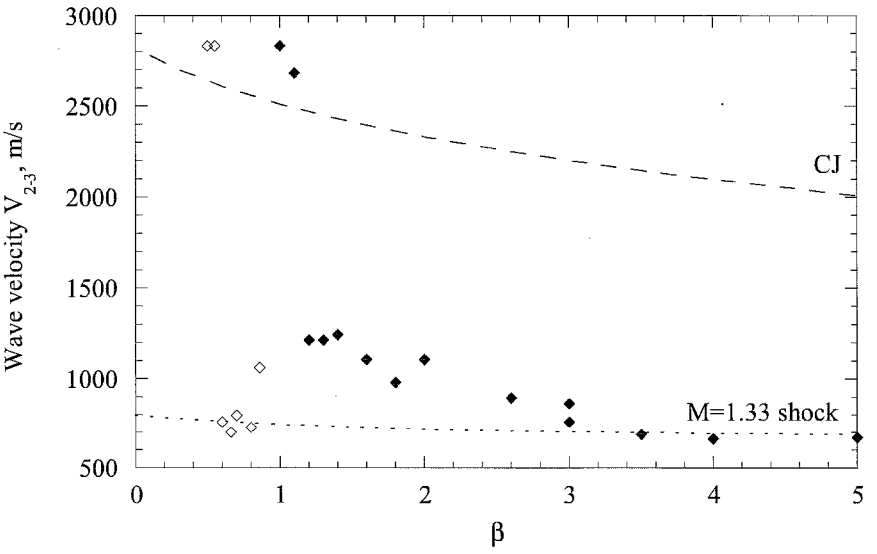

Figure 6.39: Leading wave speed measured between transducers T2 and T3, for H_2O-diluted mixtures at 373 K. Solid points, 92-mm nozzle; open points, 38-mm.

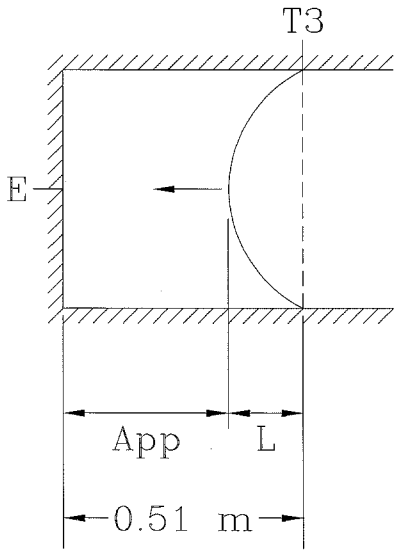

Figure 6.40: Simplified schematic of wave shape relative to transducer positions. Note that as wave travels, center arrives before edges. L is lead distance, App is apparent distance traveled.

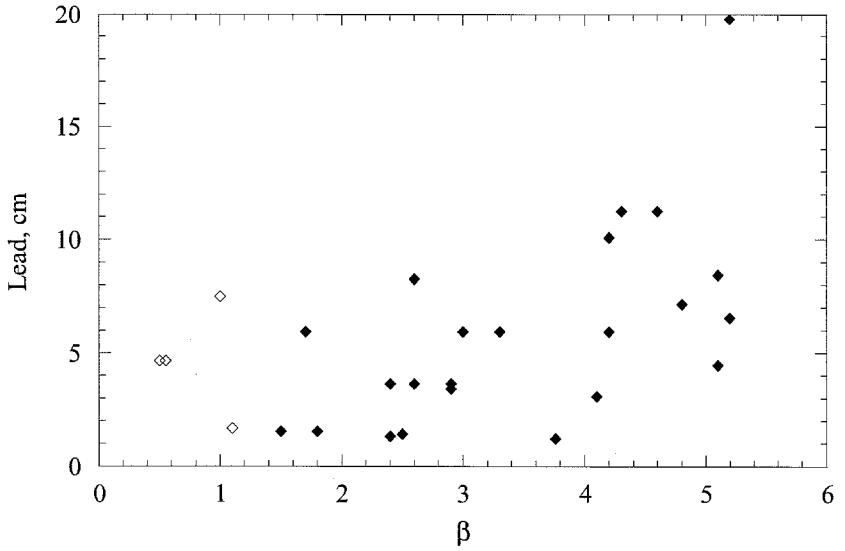

Figure 6.41: Detonation leads computed from V_{2-3} and arrival times at T3 and E. Solid points are for N_2 (298 and 373 K), open points for H_2O (373 K).

6.3 Photographic Tests

In the final set of tests, the schlieren system and Cordin camera were used to film the startup and ignition phenomena. In these runs, the camera was run at 34 kfps using 3200 ASA Kodak T-Max black-and-white film. At this framing rate, the frame-to-frame time is 29.412 μs, and the exposure time for each frame is 3.9 μs. A total of 224 frames is written per run, give or take a few frames lost to capping shutter synchronization. At 34 kfps, this gives a total write time of 6.6 ms. The film was not pushed in developing, but the camera writes in such a way that image on the negative is only 7.6 mm in diameter. (The frames are rectangular, placed two across on 35-mm film. The system was adjusted to get the largest possible circle within that frame size.) This means that the negative must be enlarged by 11x to make a printed image 85 mm in diameter (which fills a standard 4x5-inch print). As a result, the pictures are fairly grainy. The actual diameter of the area imaged is that of the light path, 100 mm. Square tabs are seen at the edges of the field; these are retention brackets from the collimating and focusing mirrors.

The camera speed is more than adequate for a deflagration, but is fairly slow for capturing jet startup and detonations. The images do show some interesting phenomena, however, and indicate that the detonations are initiated by the time they enter the second window station. Good images of jet-initiated detonations, taken at higher speeds, can be found in Inada et al. (1992).

Unfortunately, we have no fiducial reference for the time of diaphragm rupture, or the time delay for shutter opening. As a result, the times shown on the figures are for frame-to-frame reference purposes, and are not tied to the ignition time. Some velocities are calculated from the photos, but the boundaries are not always clear because we are looking at the entire thickness of a 3-dimensional phenomena in 2 dimensions. The wave position measurement is accurate to about $\pm$6 mm (after scaling), which can result in more than 10% error in waves that move 50 cm between measurements. (Detonations and jet heads tend to be visible on only two frames, which generates this amount of error. Slower moving features can be measured over several frames, reducing the relative error.) Also, the detonations move a significant distance during the exposure, so this adds some smear. The reported velocities given in the subsequent discussion should be considered rough estimates.

One run was taken at each of the three window stations for two different regimes: Prompt initiation, and deflagration. In addition, these cases were run both with and without a diaphragm. The 25-mm nozzle was used (with cutter) in all cases, to minimize the radial extent of the jet and keep the phenomena in the field of view. The windows are on 156-mm centers. In the cases with a diaphragm, the driver always uses the standard (β=2.6) mixture. In cases without the diaphragm, the mixture is the same in both vessels. In the deflagration tests, β=3.76 in the receiver. During the detonation tests, a problem was encountered. To minimize the possibility of initiation failure, a receiver mixture of β=2.6 was used in the receiver tests, adequately below the β_{CRIT} of 2.9. In the first two detonation runs, 407 and 408, this mixture underwent prompt initiation as expected. On subsequent runs, the mixture could not be detonated, and β had to be

reduced to 2.4 for prompt initiation to occur. Similarly, the dilution had to be reduced (to β=1.5) for the no-diaphragm runs. After run 414, the hydrogen supply bottles were replaced. While gas contamination seems highly unlikely, this is being investigated, as nothing else seems to be suspect.

6.3.1 Tests With Diaphragm Installed

Figures 6.42 through 6.48 are from runs using a diaphragm. Figure 6.42 shows the jet startup process in an air-filled receiver, as a reference. In frame 1, we see a vortex ring leaving the nozzle, with a faint lead shock moving out ahead of it. In frame 5, another shock is passing through the vortex. This shock was measured at 330 m/s, which is subsonic; the true speed must be a little faster than sonic (340 m/s). The vortex ring is traveling at 40 m/s. It is difficult to directly relate this to the driver pressure trace (Figure 6.1), as the Kulite transducers (with thermal protection) do not respond quickly enough to show shock waves in the driver. However, we can deduce that some event in the driver is pulsing the diaphragm without breaking it, like hitting a drum. This displaces gas that is between the diaphragm and nozzle exit, forming the vortex ring. Other wave actions in the driver will cause the other shock waves. The initial lead shock in frame 1 may be formed when the driver is ignited. Also, the driver inner surface has an annular channel (Figure 5.2, p. 43) where the body of the driver mates to the extension, and this may generate turbulence and flame acceleration. In frame 62, the jet begins to emerge from the nozzle. Note that the vortex ring is just exiting the field of view. The jet head rapidly expands into the driver, at a speed of 1700 m/s. Experiments with the camera run at a slower speed for a longer time show that this jet assumes a quasi-steady structure once the initial expansion head leaves the field of view. In the final experiments of the former RPI facility (Appendix D), startup of a 12.7-mm jet was filmed at 6.72 and 13.44 kfps. The smaller nozzle reduced the radial extent of the flowfield, and a highly turbulent vortex head was visible, leading the flow downstream. Lacerda (1986) did an in-depth photographic study of jet startup, varying the pressure and density ratio across the orifice. In Figure 6.42, gas density is 0.68 kg/m^3 in the driver, and 1.18 kg/m^3 in the receiver. This falls between the $N_2 \longrightarrow N_2$ and $He \longrightarrow N_2$ cases in Lacerda. Lacerda found that lateral expansion was enhanced when a light gas vented into a heavier one (e.g., $Ne \longrightarrow N_2$.).

Initiation of a deflagration is shown in Figures 6.43–6.45, taken from stations 1–3, respectively. In 6.43, we see the jet emerging in frames 1–3. The jet head velocity measured here is 1500 m/s. The vortex ring has already left the field of view. In frame 3 it appears that material is being entrained into the jet from the right. (The face of the inner extension is 230 mm in diameter, more than twice the size of the window, so flow must move radially inward as it is entrained.) In frames 4 and 5, the beginning of a fine flame structure is visible. As the turbulence from the jet subsides, the flame surfaces join and form larger cells (frame 41), but the cells become fine and elongate by frame 51. In frame 61, the cells seem to be hitting the window, which flattens and smoothes them. By frame 91, the flame is fully against the window, with only the two

large structures remaining. The long arc structure that bisects the frame moves to the upper right in later frames, while the other branch disappears. The flame structure again becomes turbulent around frame 120. This alternate smooth and rough structure is seen in many of the deflagration runs. A possible explanation is that jet-induced motion of the receiver atmosphere is convecting the flame fronts to different regions of the vessel. Also, the initial flame front will move downstream with the jet, leaving a volume of unburned gas in the head of the vessel upstream of the nozzle exit. It is important to remember that the schlieren system is looking through the entire width of the vessel, so we may be seeing flame fronts at different depths, while the flames hitting the window have quenched.

In Figure 6.44 we move to station 2. In frames 1–4, we see the vortex ring (moving at 100 m/s) being rapidly overtaken by the bow shock of the jet (740 m/s). Remarkably, the vortex is still visible in frame 4, despite interference from jet gas. By frame 20 the flame structure is visible, and large pieces of the diaphragm are passing in frame 28. In the remaining frames, we see the alternating smooth/rough structure seen in the previous figure.

The deflagration photos from station 3 (Figure 6.45) are very interesting. In the first frame, we see that the lead shock from the jet startup has had time to advance away from the body of jet gas. At the same time, particles from the diaphragm are overtaking the lead shock. The small particle visible in the first few frames is moving at 680 m/s, while the larger ones that come later are moving at 760 m/s. (The sound speed in the receiver gas is 400 m/s). The Mach angle of the small particle was measured at 35°, yielding 700 m/s, in good agreement with the previous value. As the large particles go past, we see that they are acting as flameholders, dragging the flame fronts behind them, in their wakes. By frame 20, this region of the vessel is fully involved in combustion, and at frame 120 we see the flame front hitting the window.

Figures 6.46–6.48 show the jet initiation of detonation, at stations 1–3. The pressure traces from these runs confirm a prompt initiation. At the first station, Figure 6.46, I believe that the regions of self-light in frames 2 and 3 are the initiation region. The head of the jet is moving at 1500 m/s, consistent with previous measurements. In this run, the frames after 5 were obliterated by self-light. For subsequent runs, I added more baffles to the schlieren system, which seemed to solve the self-light problem. We would not expect much of the detonation to be visible at this station, as the reactants are being driven downstream by the jet. Unfortunately, the windows were also "sandblasted" by the detonation. The wave loosened rust particles from the sides of the tank, and drove them into the windows. I was able to clean the windows to some extent, but the surface was still pitted from the impacts. From the damage pattern, it appears that the particles had hit the downstream side of the window port in the vessel wall, and then bounced back into the windows. The mounting pad in the vessel wall for the window retainer is about 60 mm thick, with a 120 mm diameter hole for the light path; see Figure 2.8 for a cross section. For future runs, when I moved the windows to a new station, I sanded and cleaned the inner surface of the port. This greatly reduced the damage in future runs. A separate set of fresh windows was used for deflagration tests, to improve picture quality.

Figure 6.47 shows the detonation passing station 2. Here, the wave is highly curved, and has a measured speed of 1400 m/s. These observations are better correlated to the previous jet heads, but in the original print of frame 3, cellular structure is visible in part of the field. This did not come out in reproduction. In Figure 6.48, however, we see that the detonation has begun to flatten out by station 3. The measured velocity at this station is 1950 m/s, and with the measurement error, this corresponds well to the CJ velocity of 2100 m/s for this mixture. At this velocity, the wave moves about 1 cm during the 3.9 μs frame exposure, adding to the uncertainty. In measuring the photographs, I took the sharpest part of the leading edge as the reference. In frames 2, 3 and 5, cellular structure characteristic of a detonation is visible in the original prints. This did not reproduce well, but is visible in the figure. It is important to not look at the figure too closely, and just try to see the overall texture of the image. The cells are composed of a grid of lines that are nearly orthogonal, rotated about 45° from horizontal. The cell size for this mixture is approximately 8 mm. A few other waves are seen in frames 54 and 55, but since the curvatures are different, they don't seem to be the same waves. Thus, their direction can't be determined.

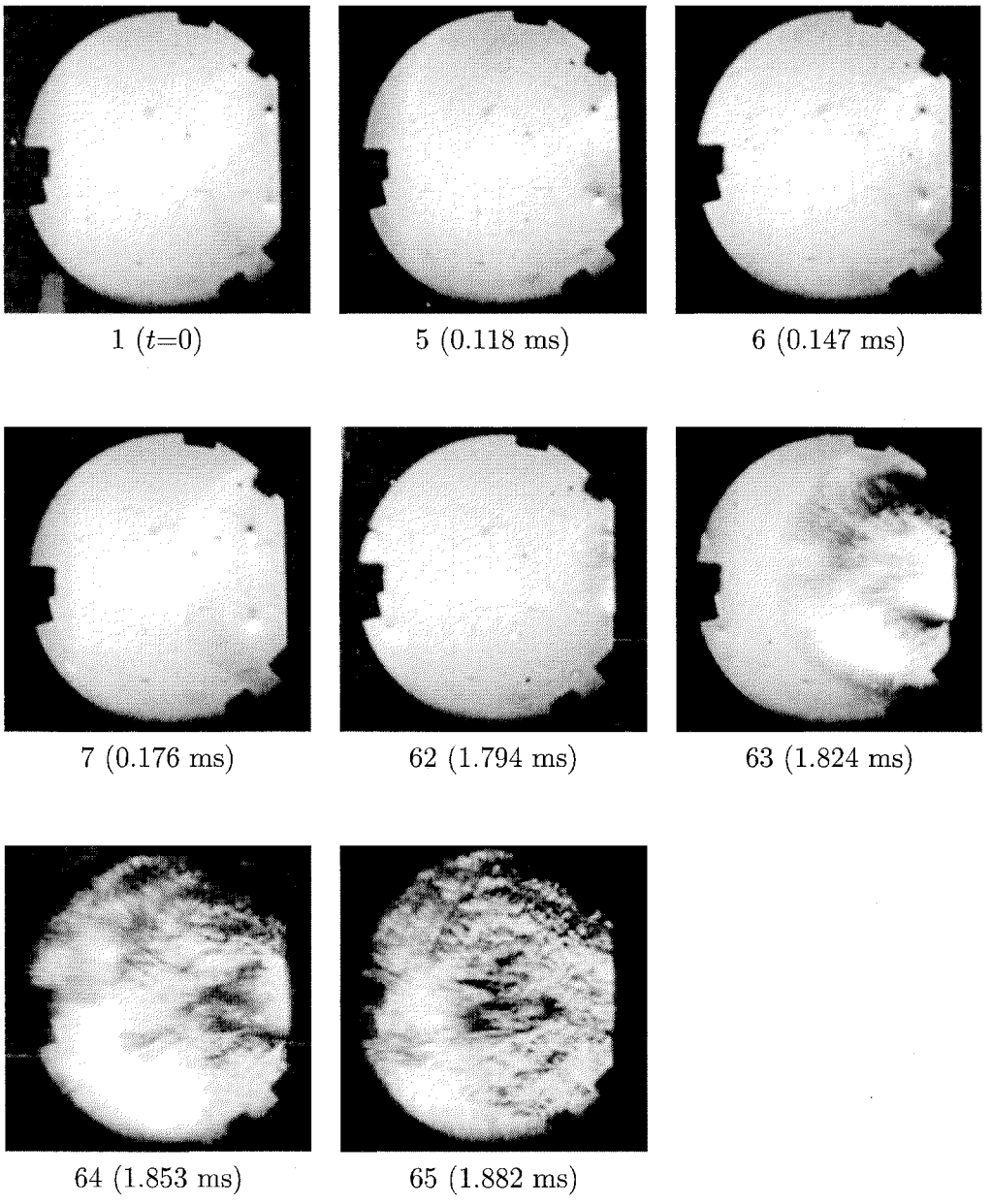

Figure 6.42: Jet startup sequence for standard driver (β=2.6), with 25-mm nozzle. Run 406.

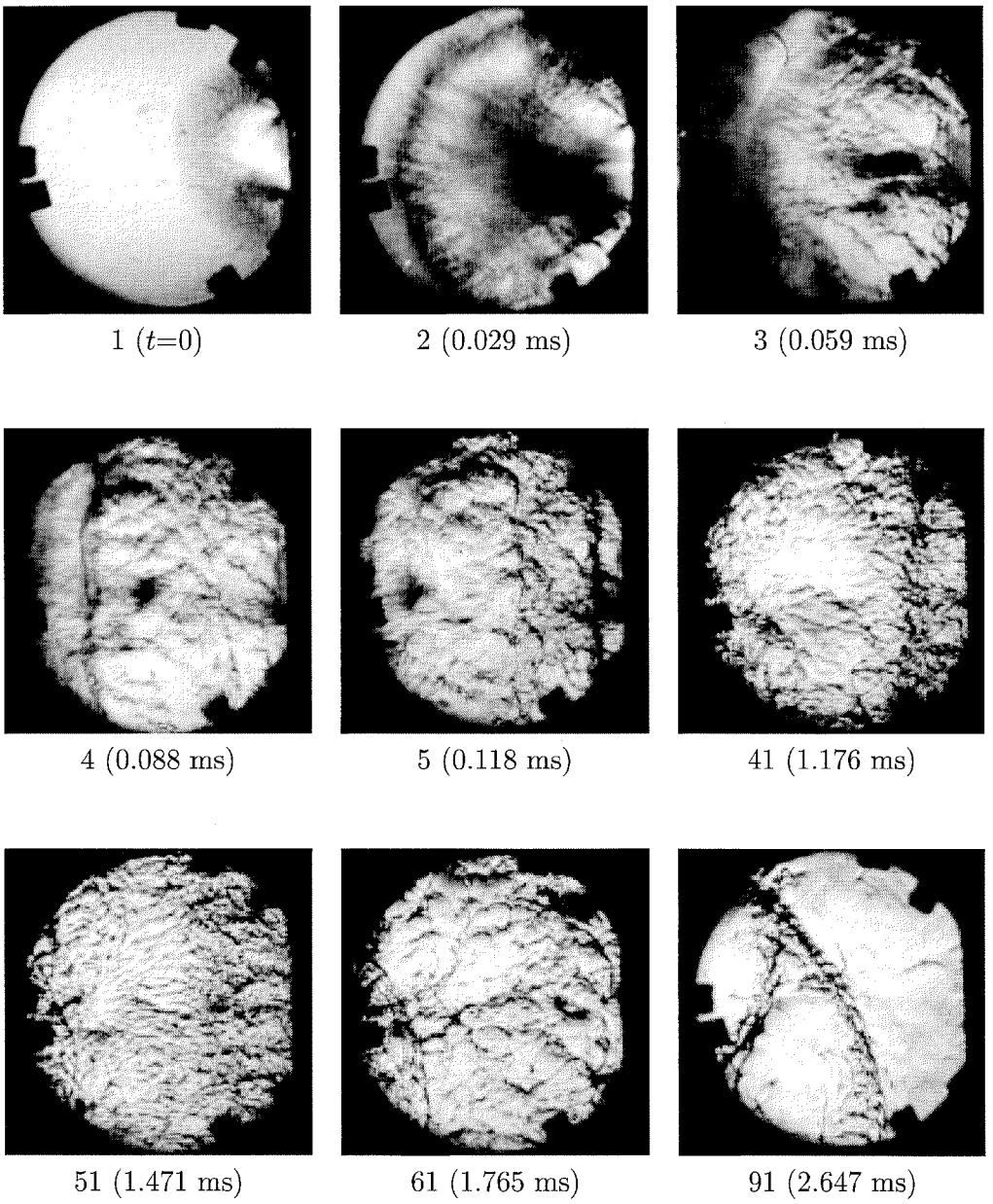

Figure 6.43: Jet initiation of deflagration by 25-mm nozzle, window station 1. Receiver β=3.76. Run 416.

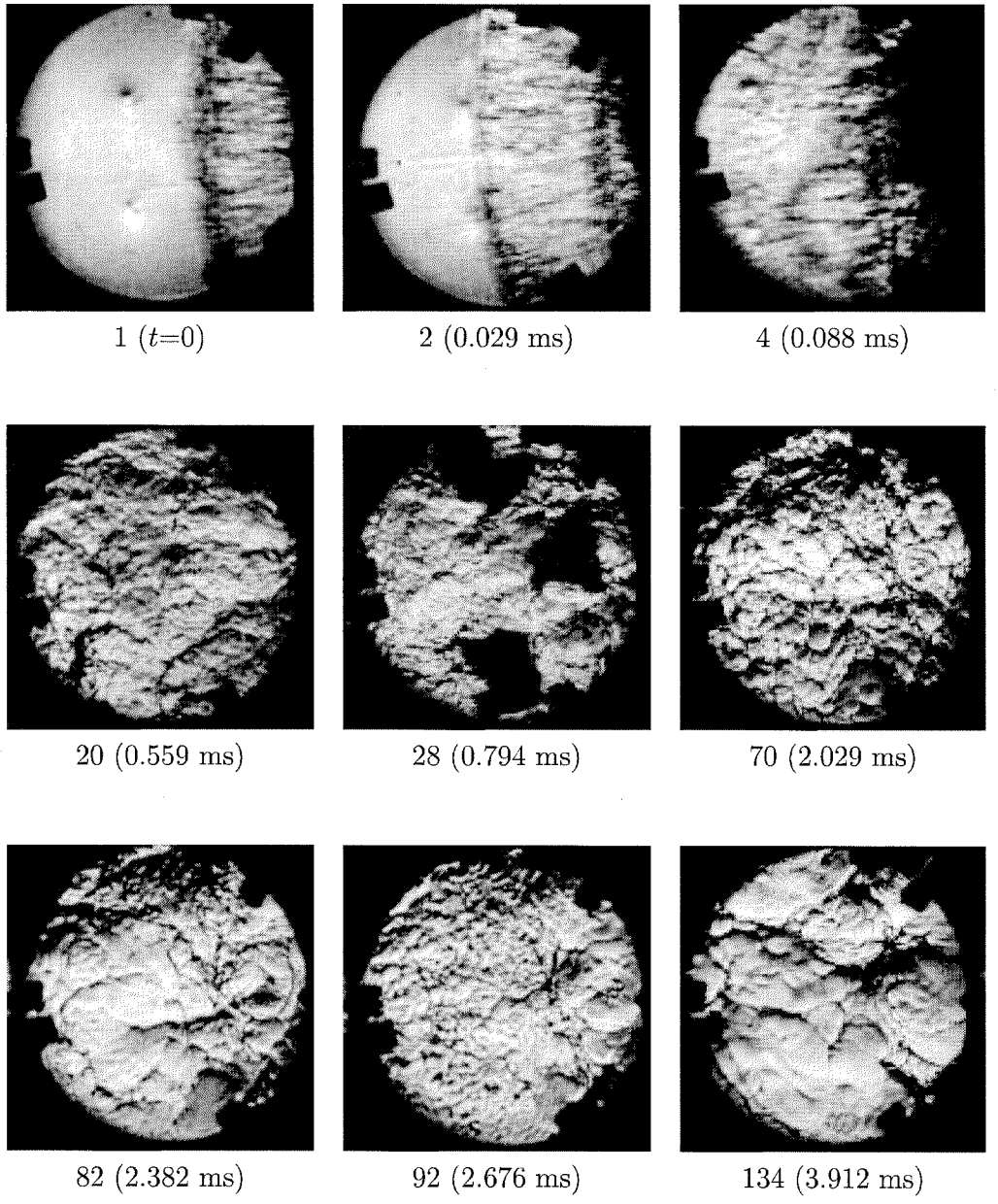

Figure 6.44: Jet initiation of deflagration by 25-mm nozzle, window station 2. Receiver β=3.76. Run 419.

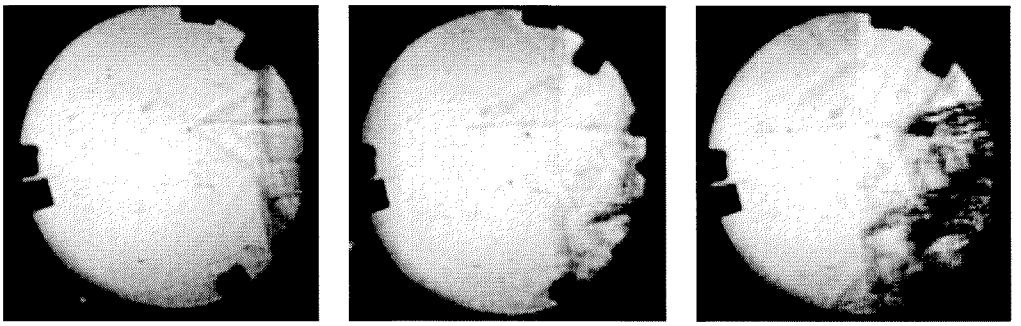

1 (t=0)

2 (0.029 ms)

3 (0.059 ms)

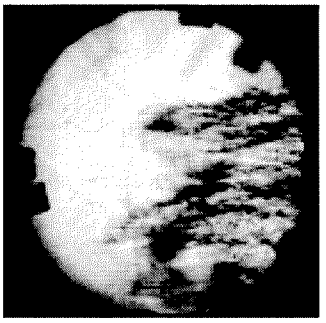

4 (0.088 ms)

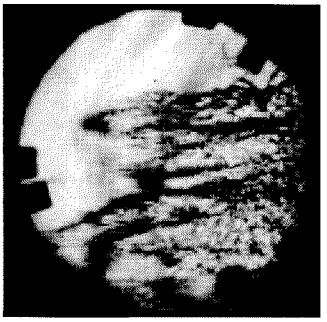

5 (0.118 ms)

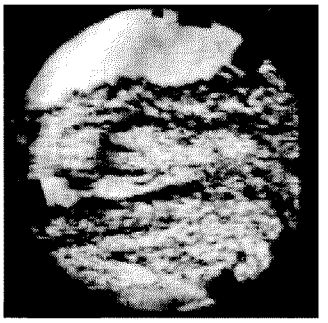

6 (0.147 ms)

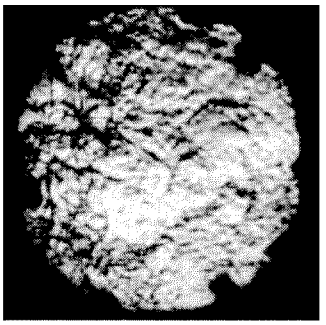

20 (0.559 ms)

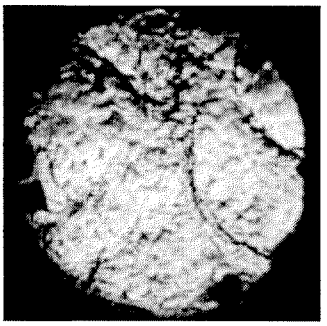

60 (1.735 ms)

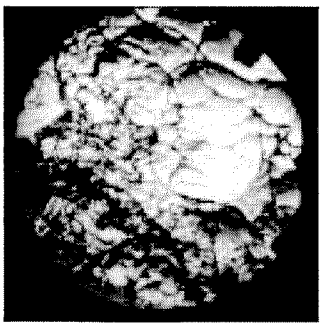

120 (3.500 ms)

Figure 6.45: Jet initiation of deflagration by 25-mm nozzle, window station 3. Receiver β=3.76. Run 425.

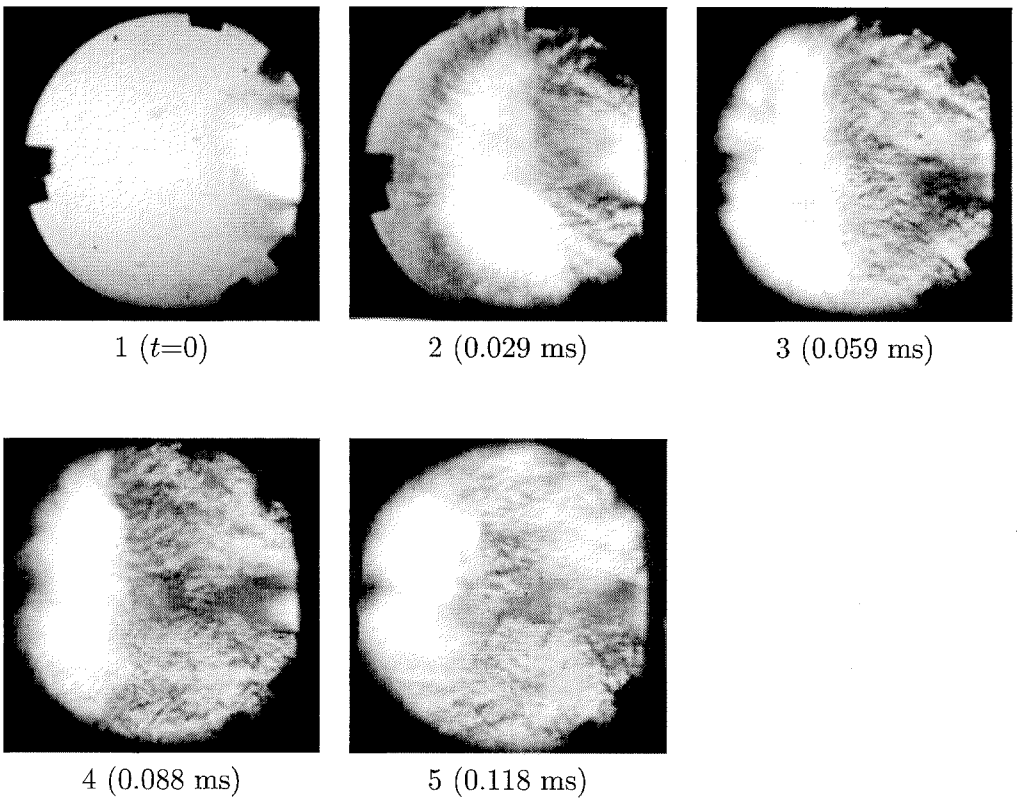

Figure 6.46: Jet initiation of detonation by 25-mm nozzle, window station 1. Receiver β=2.6. Run 407.

1 (t=0) 2 (0.029 ms) 3 (0.059 ms)

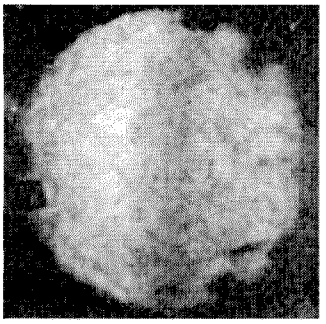

4 (0.088 ms)

Figure 6.47: Jet initiation of detonation by 25-mm nozzle, window station 2. Receiver β=2.4. Run 424.

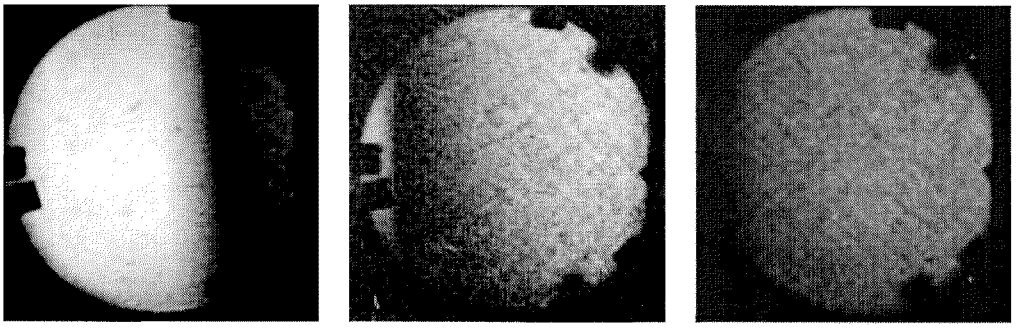

1 (t=0)

2 (0.029 ms)

3 (0.059 ms)

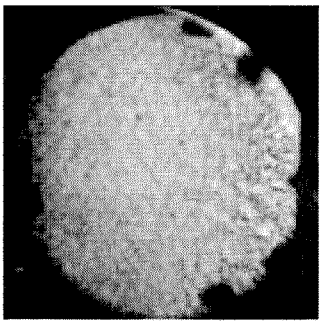

5 (0.118 ms)

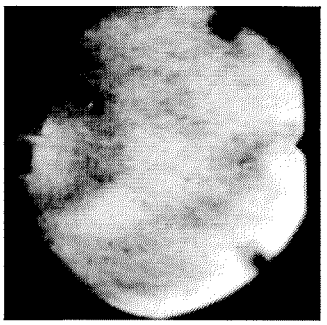

7 (0.176 ms)

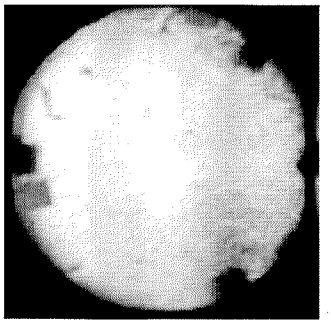

54 (1.559 ms)

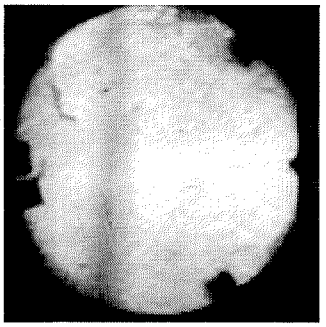

55 (1.588 ms)

Figure 6.48: Jet initiation of detonation by 25-mm nozzle, window station 3. Receiver β=2.4. Run 430.

6.3.2 Tests With No Diaphragm

Figures 6.49–6.55 are from runs with no diaphragm between the vessels. The lack of a diaphragm allows a flow field to start before the flame exits the driver. The venting also decreases the peak pressure in the driver. Figures 6.49–6.51 show the initiation of a deflagration. In Figure 6.49, the first frame is from run 412, which failed to catch the deflagration because the shutter timing was still being adjusted. We see the shock structure typical of underexpanded jets. (The nozzle is a simple orifice, so we expect choked flow.) In frame 0, we see that the pre-jet flow has nearly died out by the time the product jet arrives in frame 1. The leading edge of the jet is moving at 2000 m/s in the photo, but this mixture has a higher hydrogen fraction and hence a higher sound speed. Flame structure is beginning to form in frame 4, and by frame 11 the field is filled by a turbulent flame front. This goes on to hit the windows at frame 111.

Moving to station 2 in Figure 6.50, we see that the lead shock has pulled away from the jet head. The lead shock was photographically measured at 840 m/s, while the jet head has a velocity of 700 m/s. The field remains filled with jet flow structure through frame 5, and a flame structure is formed by frame 11. As the flame progresses, the structure goes from fine to coarse until the flame hits the window at frame 111. Figure 6.51, at station 3, is essentially the same. The lead shock is further separated from the jet (velocities of 590 and 500 m/s, respectively), and the flame front is well-established by frame 22. One interesting feature is seen in frame 120, where a wrinkled band about 1 cm thick is seen. This band is just right of center, and arcs in a way that connects the shadows of the mirror retention tabs. The nature of this form is unknown. In the adjacent frames on the negative, it doesn't appear to be moving, but simply fades in and fades out over 6–10 frames.

Figures 6.52–6.55 show the initiation of a detonation with no diaphragm. Station 1, Figure 6.52, is basically the same as in the diaphragm case, Figure 6.46. No distinct wave is seen at startup, but there is a region of intense self-light at the jet head that is not seen in the deflagration cases. Oddly, no precursor flow was seen in this case, as there was in the deflagration. Either the flame is quick enough to stay close to the shock, or the mixture has transitioned to detonation inside the driver. The nozzle diameter is less than one-third of the critical tube diameter for this mixture, so it is unlikely that a detonation would pass through the nozzle without failing. The driver pressure trace (β=1.7, Figure 6.53) is similar to that of the standard driver (β=2.6), except the peak pressure is reached about 4 ms sooner in this case. Since the Kulite doesn't respond quickly enough to show a detonation, it is not possible to discern transition in the driver. The jet head in this case (leading edge of the self-light) is moving at 1300 m/s. In frames 11–13, we see a round wave developing. This may be the detonation reflecting off of the windows. This phenomena was seen at all three window stations.

At station 2, Figure 6.54, the capping shutter opened just as the detonation was passing, so vignetting occurred in the early frames. However, in frame 1 we can see the distinct dark front seen in Figure 6.48. There is some cellular structure visible in the original print, but the cell size is much smaller due to the decreased dilution, so it is not visible in reproduction. In frame 10, we again see the circular wave pattern. Figure 6.55

is from station 3, and here we see the wave passing in the first two frames. The velocity here is 2200 m/s, which compares well with the CJ value of 2280 m/s. Cellular structure is visible in the originals, but the cell size for this mixture is only 6 mm, so the pattern is hard to see. The circular form is again seen in frame 7.

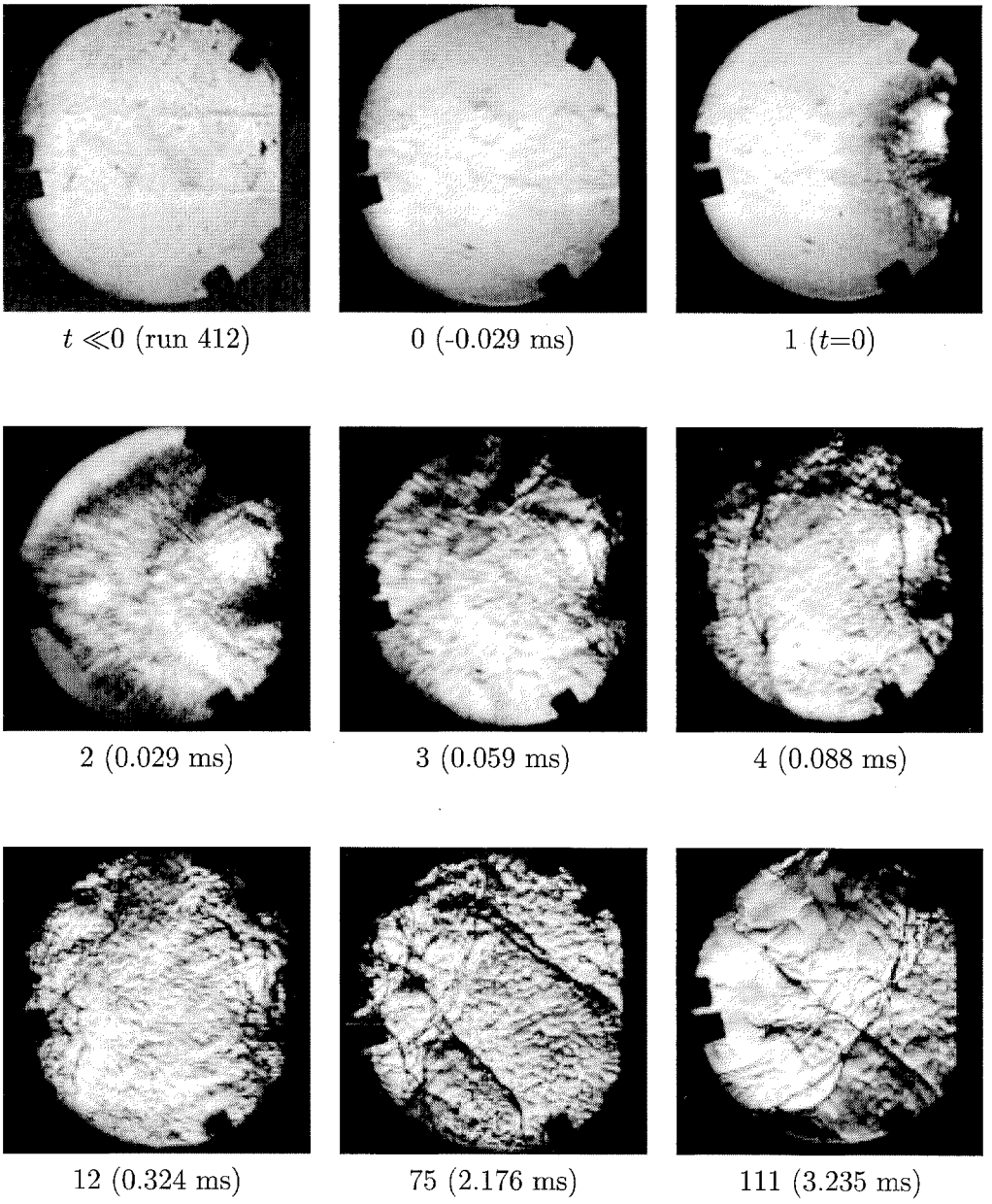

Figure 6.49: Jet initiation of deflagration by 25-mm nozzle, no diaphragm, window station 1. In both vessels, β=3.76. First frame, showing jet, is from run 412, which was a camera timing test using the same mixture. Run 417.

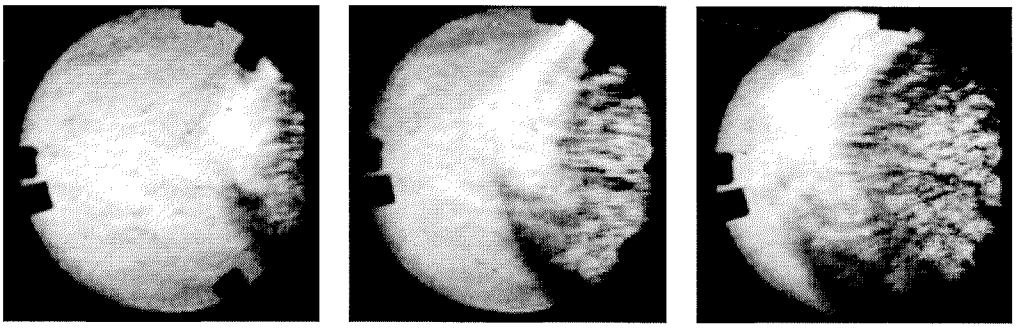

1 (t=0) 2 (0.029 ms) 3 (0.059 ms)

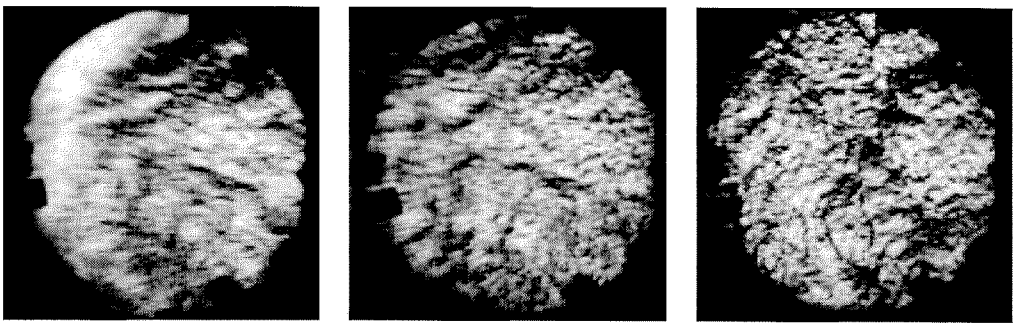

4 (0.088 ms) 5 (0.118 ms) 11 (0.294 ms)

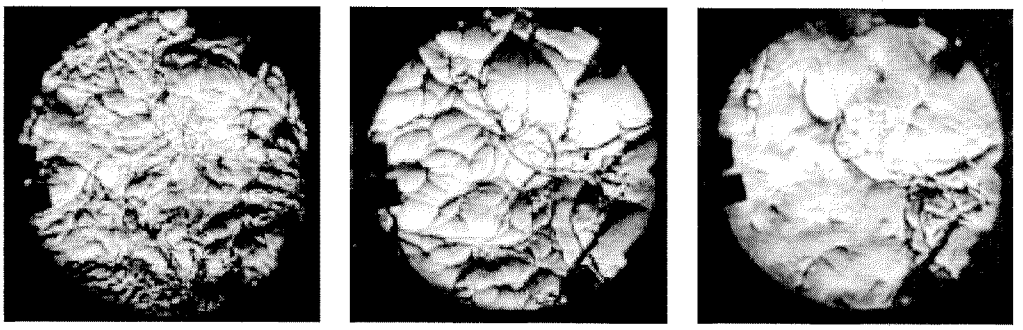

41 (1.176 ms) 91 (2.647 ms) 111 (3.235 ms)

Figure 6.50: Jet initiation of deflagration by 25-mm nozzle, no diaphragm, window station 2. In both vessels, β=3.76. Run 418.

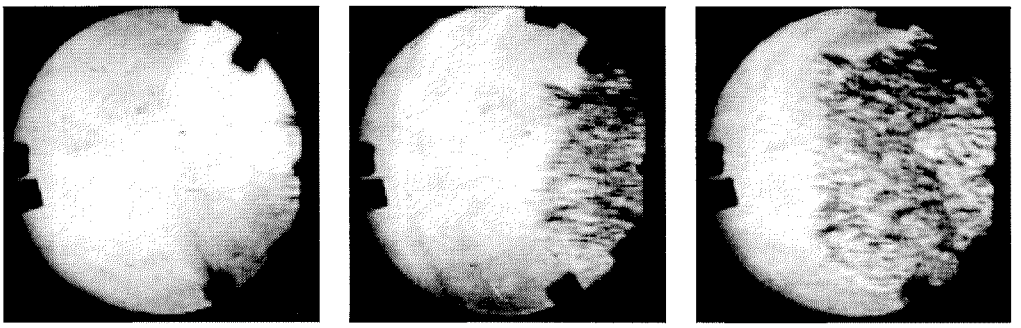

1 (t=0)

3 (0.059 ms)

5 (0.118 ms)

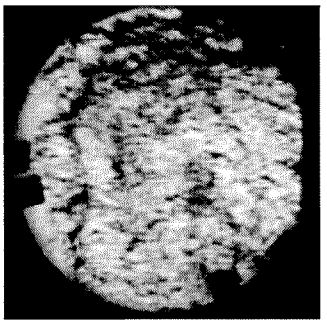

7 (0.176 ms)

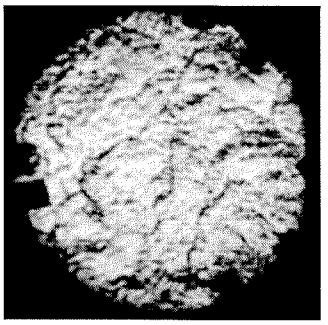

22 (0.618 ms)

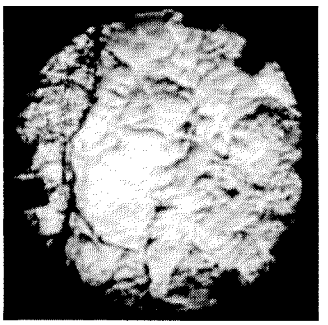

30 (0.853 ms)

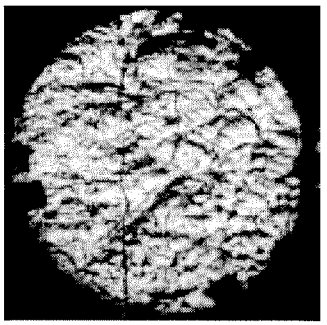

50 (1.441 ms)

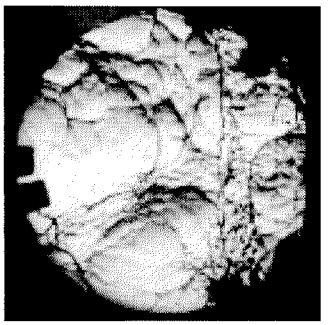

80 (2.324 ms)

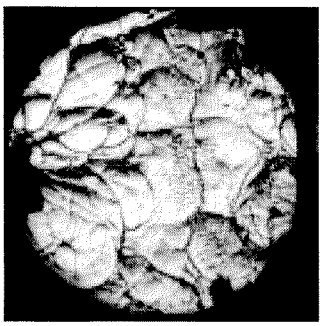

120 (3.500 ms)

Figure 6.51: Jet initiation of deflagration by 25-mm nozzle, no diaphragm, window station 3. In both vessels, β=3.76. Run 426.

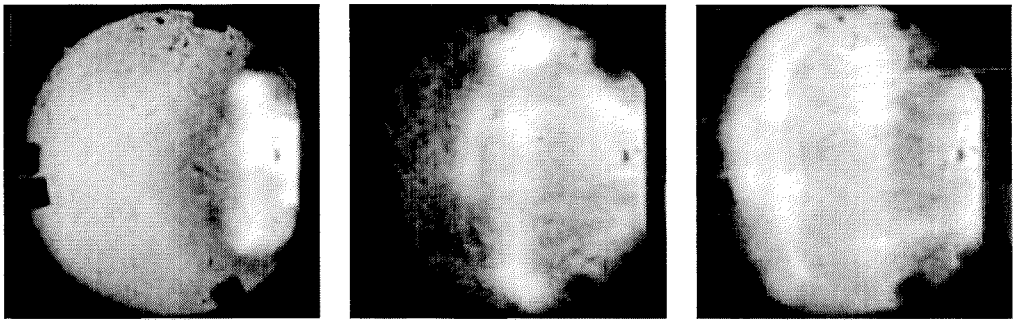

1 (t=0) 2 (0.029 ms) 3 (0.059 ms)

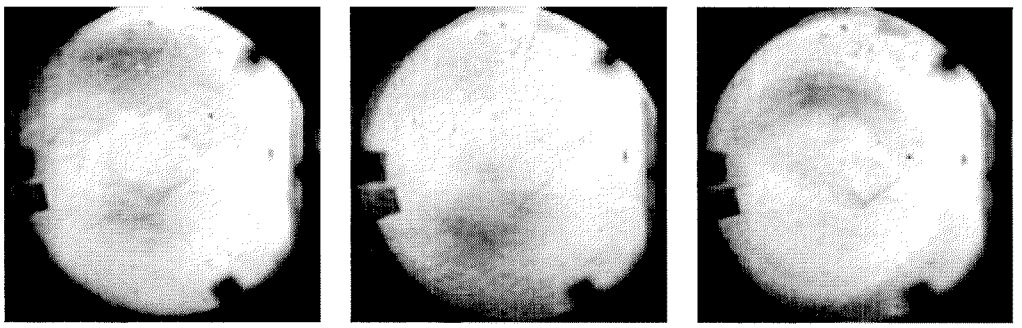

11 (0.294 ms) 12 (0.324 ms) 13 (0.353 ms)

Figure 6.52: Jet initiation of detonation by 25-mm nozzle, no diaphragm, window station 1. In both vessels, β=1.7. Run 411.

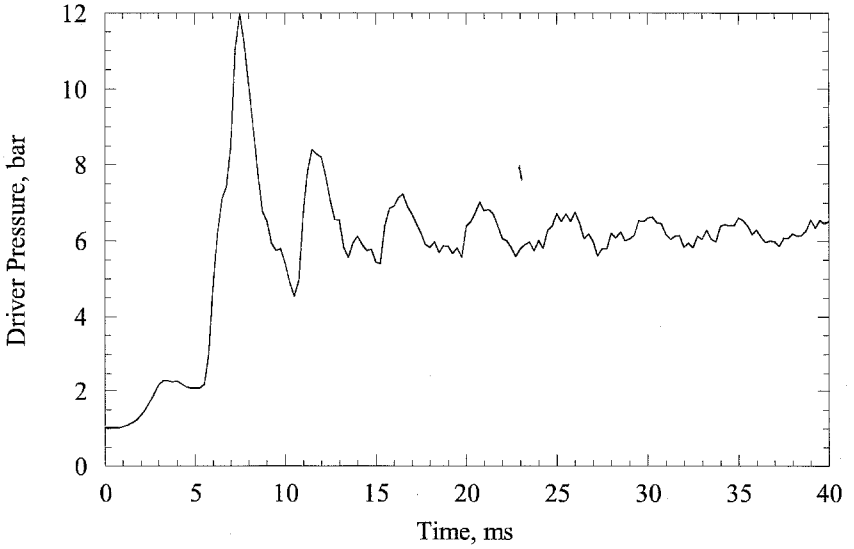

Figure 6.53: Driver pressure trace, β=1.7, no diaphragm.

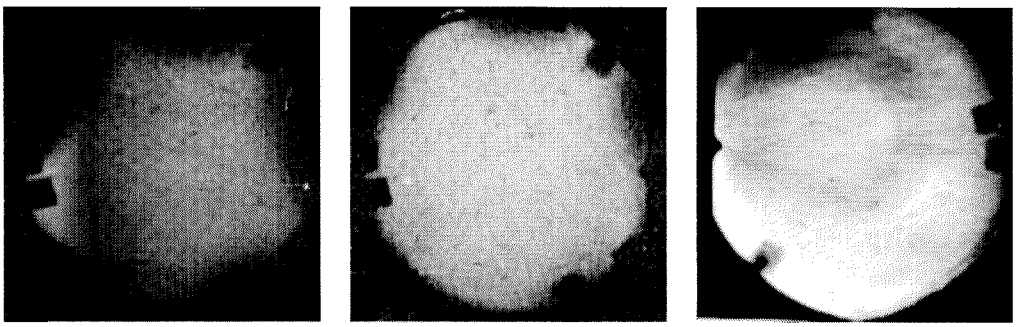

1 (t=0) 3 (0.059 ms) 10 (0.265 ms)

Figure 6.54: Jet initiation of detonation by 25-mm nozzle, no diaphragm, window station 2. In both vessels, β=1.5. Run 423.

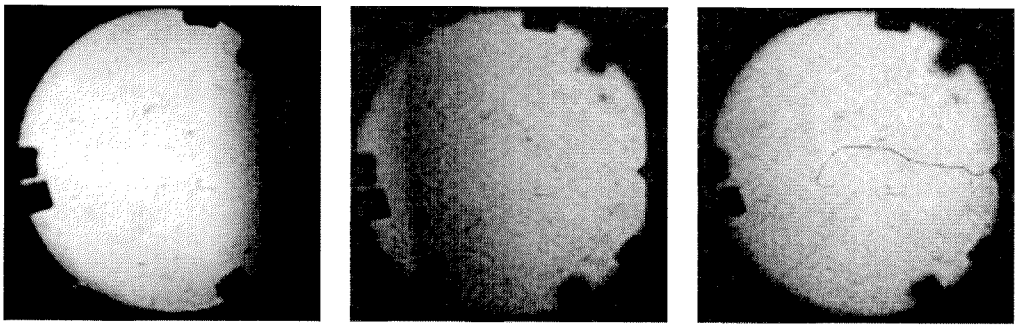

1 (t=0) 2 (0.029 ms) 3 (0.059 ms)

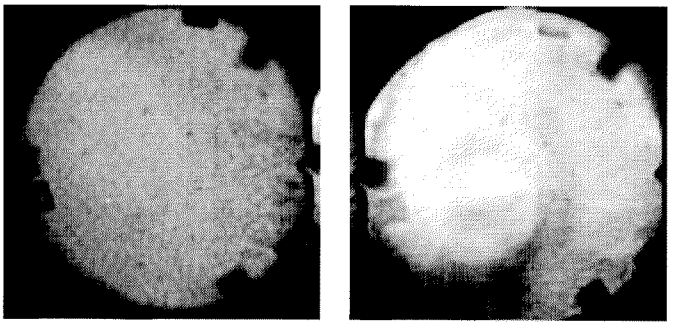

5 (0.118 ms) 7 (0.176 ms)

Figure 6.55: Jet initiation of detonation by 25-mm nozzle, no diaphragm, window station 3. In both vessels, β=1.5. Run 431.

6.3.3 Secondary Phenomena

This section contains photographs that were not part of the main analysis, but showed interesting phenomena nonetheless. Figure 6.57 is from a camera timing run that used air as the driver diluent instead of nitrogen. The change in stoichiometry increased the flame speed, so the peak driver pressure occurred 2 ms earlier than usual (Figure 6.56). In the first frame, we see the bow shock and vortex ring produced by the diaphragm. By frame 4, we see a second vortex ring formed by the initial flow of jet gas, indicating that the diaphragm must have already ruptured. In frame 6, the rings have combined, and the jet gas is beginning to run through the vortex. We see fluid entrainment proceed through frame 8, and fast jet material is evident in frame 9. It appears that the diaphragm ruptured before the flame front reached it, as the gas venting before frame 9 is moving slower than it would for a typical jet.

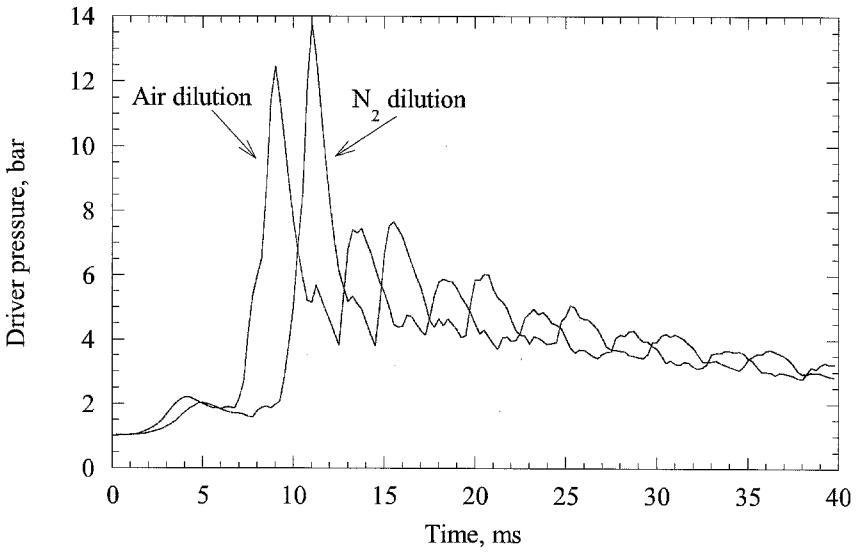

Figure 6.56: Driver pressure traces showing effect of diluent. Data from Kulite (slow) transducer.

Figure 6.58, from station 2, is from a no-diaphragm run that was expected to undergo prompt initiation, but did not. The flame later underwent DDT. Again, we see no precursor flow as we did in the deflagration cases. In the first few frames, we see a shock front, followed by the flame. The shock speed is about 770 m/s, while the flame speed is only 400 m/s. In between the two waves, weak shocks are visible as thin lines. The DDT probably occurs after the lead shock reflects from the downstream end of the vessel, when the flame front hits the twice-shocked reactants. This is similar to run 409; the pressure traces from that run are shown in Figures 6.20 and 6.21 on page 85. The DDT occurs much later than the initial flame, so the capping shutter closes before the returning wave passes. In the remaining frames shown, however, we see the alternating smooth-rough flow field that occurred in the previous deflagration cases. The early images in this

sequence are similar to those seen by Inada et al. (1992) in a failed initiation, although their case was with a diaphragm.

Figure 6.59 is another initiation failure sequence viewed from station 2, but in this run a diaphragm was used. This run resulted in a deflagration only. These photos show the interaction of the flame front with the vortex ring. In the first frame, the lead shock has just passed over the vortex. In frames 2 and 3, note the bubble forming around the lower part of the vortex. This is a flame, and indicates that ignition occurs at the leading edge of the jet. In these photos, the lead shock is moving at 760 m/s, and the flame at 400 m/s, nearly identical to the previous example.

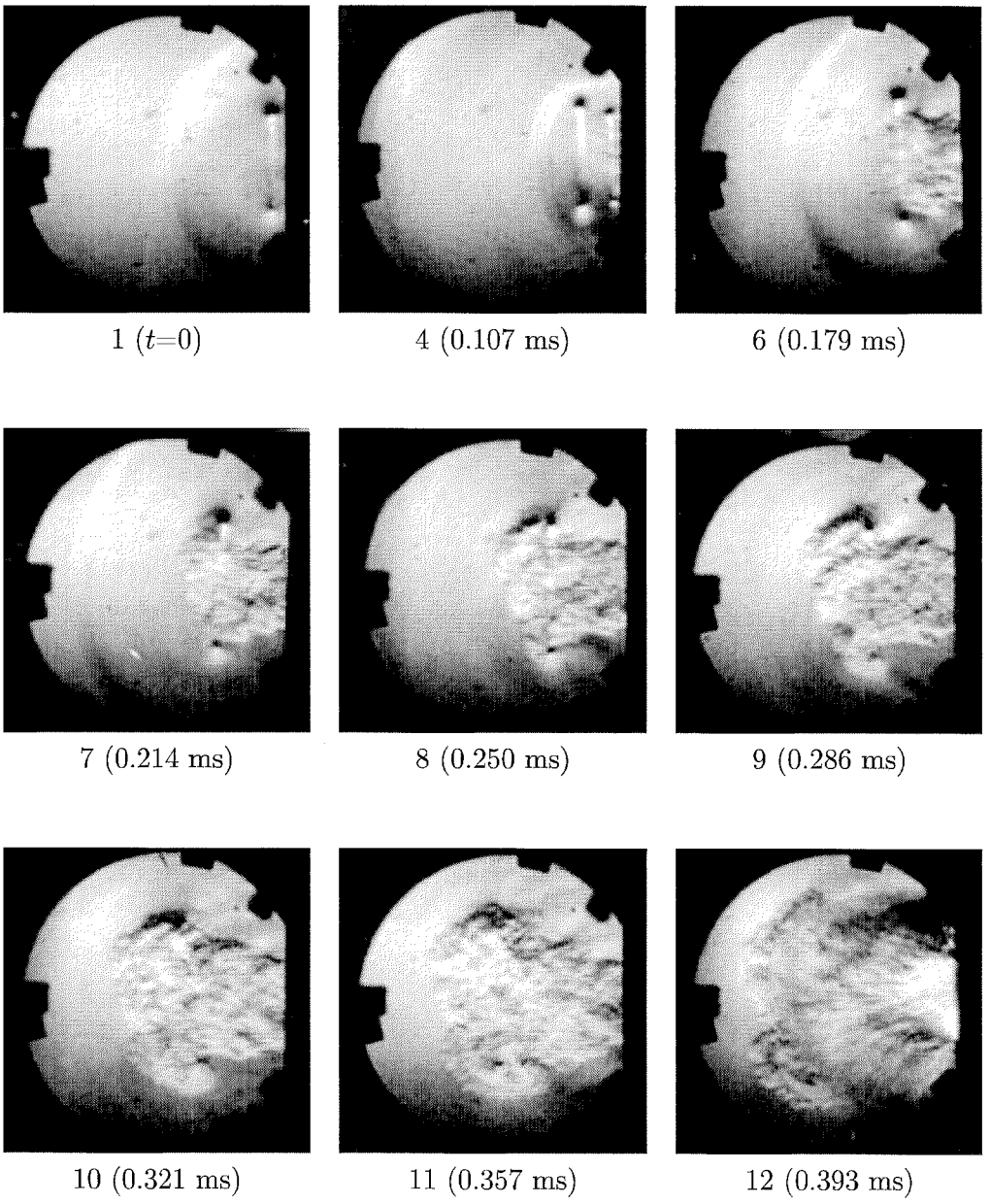

Figure 6.57: Jet startup sequence, with initial vortex rings due to diaphragm-piston action. Driver mixture was diluted with air instead of nitrogen. Camera run at 28 kfps for this sequence. Run 403.

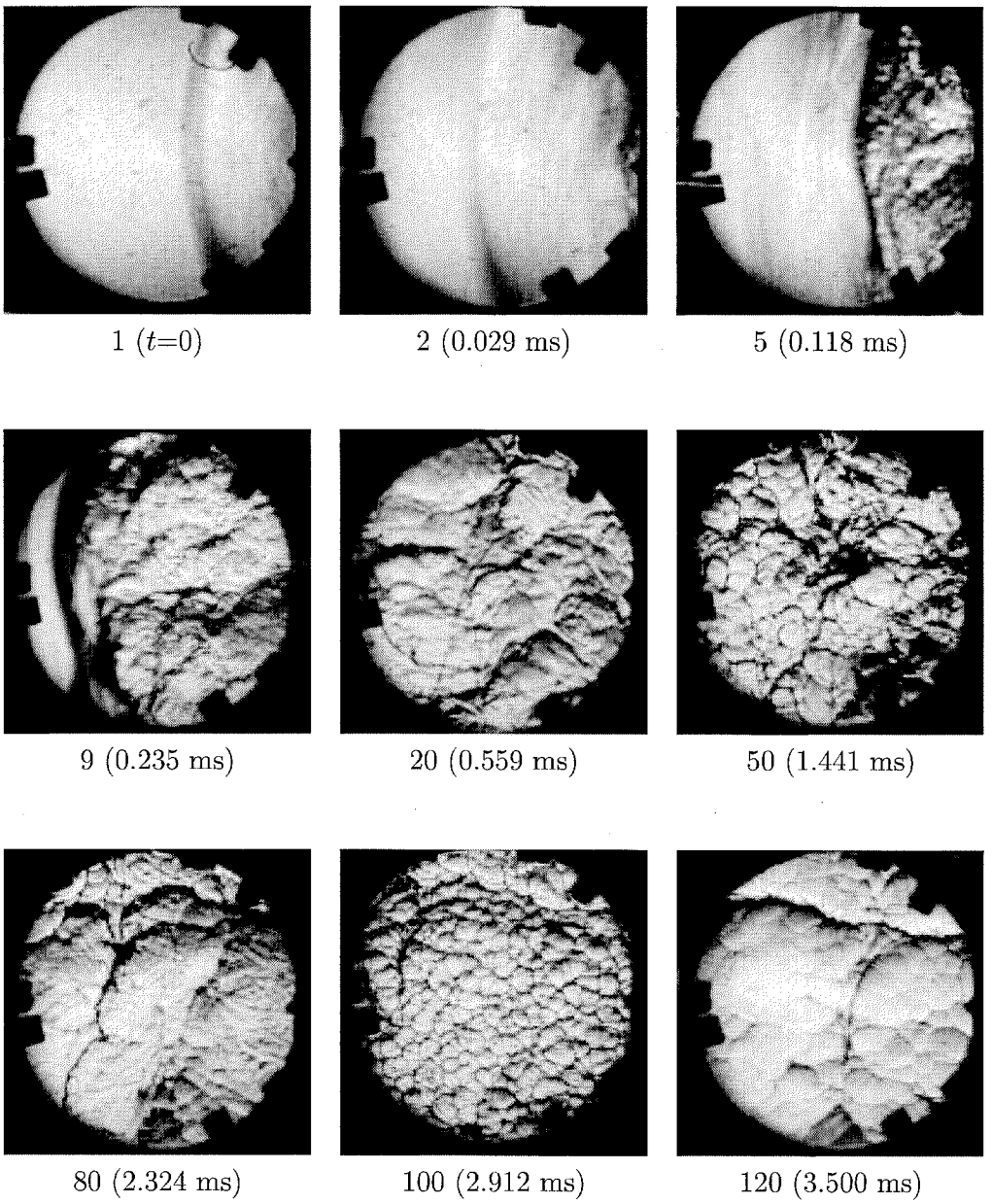

Figure 6.58: Failure to initiate detonation with 25-mm nozzle, no diaphragm, station 2. In both vessels, β=1.7. This flame later transitioned to a detonation. Run 422.

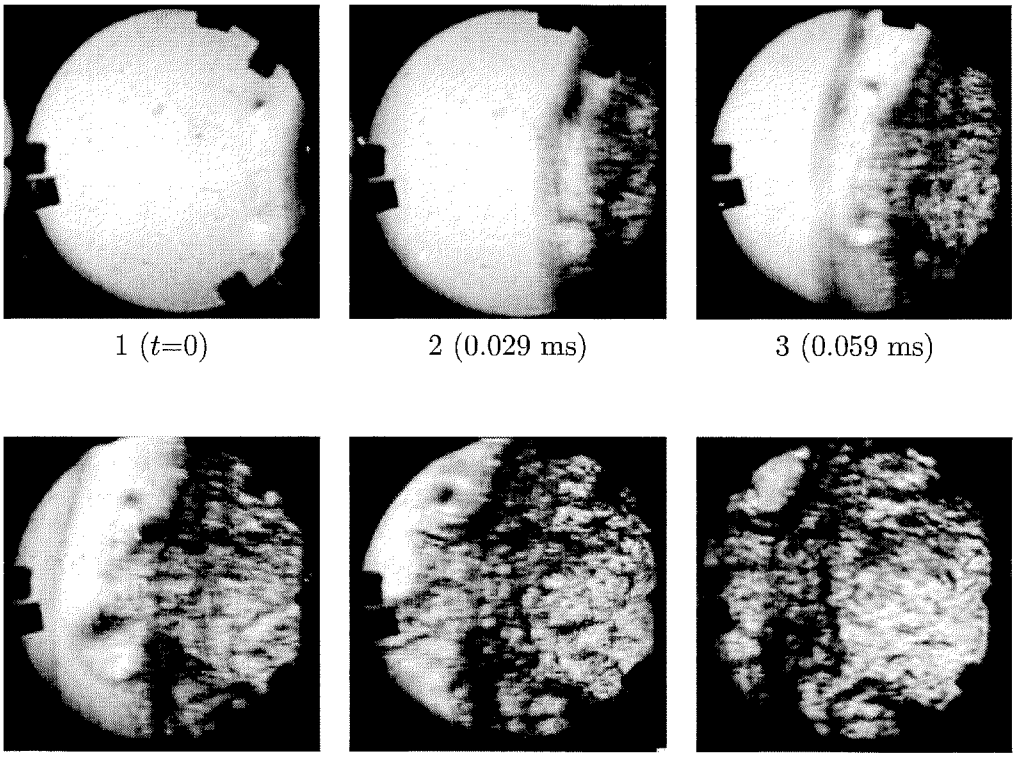

Figure 6.59: Failure to initiate detonation with 25-mm nozzle, using diaphragm, station 2. In the receiver, β=2.6. Note flame/vortex interaction in frames 2 and 3. Run 421.

Chapter 7

Summary

The HYJET facility was constructed to study hydrogen combustion phenomena related to severe accidents in nuclear power plants. Jet-initiated deflagration and detonation have been studied in H_2-air and H_2-O_2 mixtures with N_2 and H_2O dilution. The mixtures are contained in an 1180 ℓ receiver vessel that can be maintained at temperatures up to 383 K. The jet ignition source is supplied by a 28 ℓ driver vessel that is filled with H_2-O_2-N_2 mixtures. These mixtures are spark ignited and the products are vented through nozzles of 12.7–92 mm diameter. The resulting event in the receiver depends on the receiver composition, driver composition, initial temperature, and jet (i.e., nozzle) diameter. The tests were divided into several series, based on objective.

7.1 COMP and S Series

The COMP series compared the HYJET facility to a similar facility previously used at Rensselaer Polytechnic Institute. These tests examined the effect of igniter strength on the lean flammability limit of diluted H_2-air mixtures. The receiver mixtures consisted of nitrogen and air in a 1:1 ratio, with 0–10% hydrogen. The driver was filled with 80% H_2-20% O_2, producing a hot jet of 50% H_2-50% H_2O upon ignition to simulate a DCH jet. The initial conditions in both vessels were 1 bar and 298 K. The driver was vented through the 12.7 and 25-mm nozzles. The results are summarized in Figure 7.1, which compares the peak receiver pressures to P_{AICC}.

Both the RPI and CIT facilities were able to ignite deflagrations in mixtures with at least 6% H_2. Previous studies in the RPI facility found that at least 9% H_2 was required for ignition via glow plug. Initiation of deflagration was easy to detect in HYJET, for either nozzle diameter. In the RPI facility, tests with the 25-mm nozzle were dominated by receiver pressurization and combustion of the jet gas as a diffusion flame. Receiver deflagration would not have been indicated without data from the 12.7-mm nozzle. Finally, a simple mole-balance method was used to estimate completeness of combustion in the HYJET tests. The results indicated that combustion was incomplete for 6% H_2, but complete for 8 and 10%. A reverse-flow period was also seen that had the potential to delay or suppress deflagration with the 25-mm nozzle.

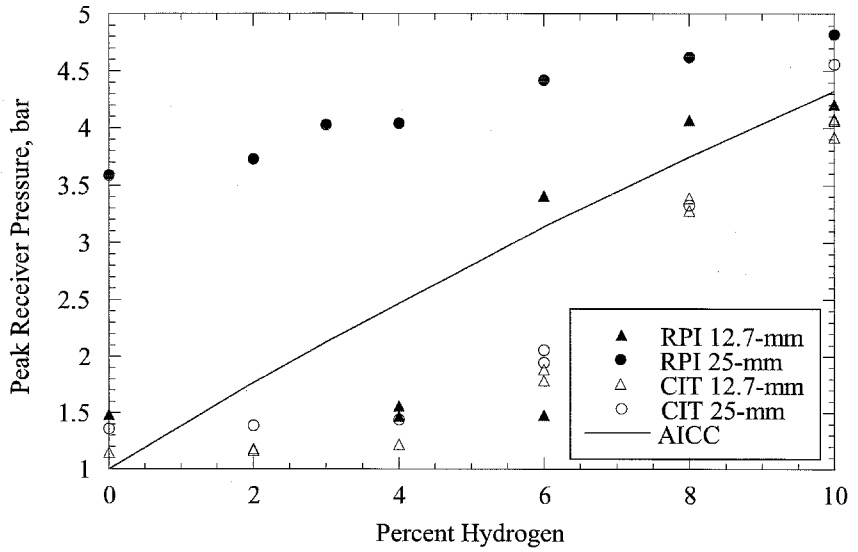

Figure 7.1: Summary of COMP test series.

The S series duplicated the COMP mixtures, using water vapor for dilution instead of nitrogen. The initial receiver temperature for these tests was 373 K, and only the 12.7-mm nozzle was used. The tests showed that H_2O is a more effective suppressant than N_2, owing to its higher heat capacity. With H_2O dilution, the H_2 concentration had to be increased to 8% for a deflagration to occur. The pressure traces for 8% H_2 with N_2 and H_2O dilution are shown in Figure 7.2.

7.2 SA Series

While the previous series examined deflagration at the lean limit, the SA series fixes the stoichiometry and varies the fraction of water vapor to study deflagration suppression. In this series, the hydrogen-air ratio in the receiver was kept constant at 20% H_2 in air (dry). The mixture was diluted with 0–60% water vapor. Initial conditions in the receiver were 1 bar and 373 K. The driver mixture was 80% H_2-20% O_2 at 1 bar and 298 K, as in the previous series. The 12.7, 25 and 92-mm nozzles were used for receiver ignition. The results are shown in Figure 7.3, which plots the peak receiver pressures against P_{AICC}.

The 12.7 and 92-mm nozzles were able to initiate deflagrations in mixtures with up to 60% water vapor. Previous studies, using glow plug ignition, were only able to ignite mixtures with 55% H_2O. Reverse flow with the 25-mm nozzle may have extinguished the flame kernel before it could propagate in the 60% mixture. It was able to initiate a deflagration in mixtures with 50% H_2O.

As nozzle diameter was increased, receiver pressure traces became increasingly noisy, owing to shock oscillations. With the 92-mm nozzle, jet effects dominate. In the 60% mixture, deflagration with the 92-mm nozzle was evident when the long-term pressure trace was compared to that of the 12.7-mm nozzle.

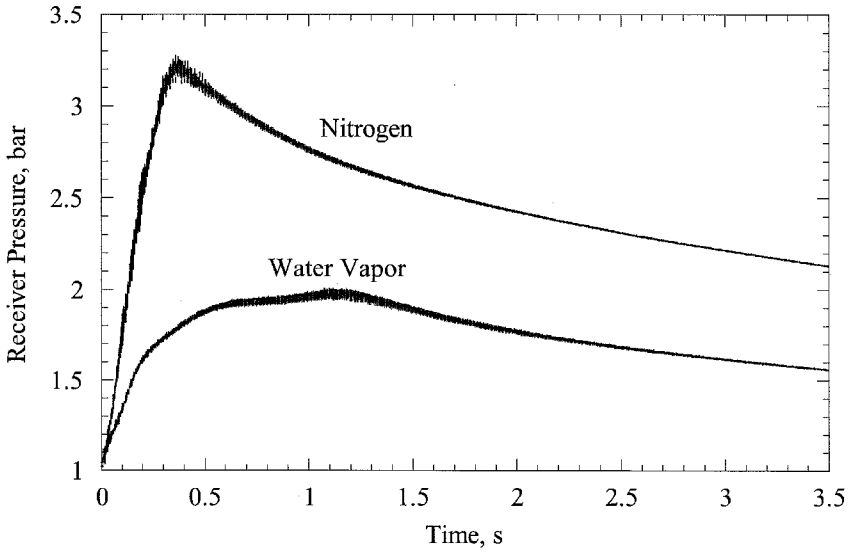

Figure 7.2: Comparison of water vapor and nitrogen as diluents.

7.3 NITRO Series

The NITRO series studied jet initiation of detonation, and the effects of driver strength. The receiver was filled with 0–30% H_2 in air, at 1 bar and 298 K. The driver used a fixed ratio of 80% H_2-20% O_2, which was diluted with 0–50% N_2 to reduce the flame speed. To compensate for the displaced reactants, the initial pressure was increased to keep the peak pressure constant at approximately 9.7 bar. Unforeseen dynamic effects raised the peak pressure to nearly 13 bar for 20–35% N_2. The flame speed was successfully reduced, as indicated by the burn time. Peak driver pressures for a plugged driver are shown in Figure 7.4.

The results for jet initiation are shown in Table 7.1. Drivers with 30% or more N_2 were unable to initiate a detonation in any H_2-air mixture. Drivers with less dilution were able to initiate detonations in mixtures containing at least 26% H_2. The driver with 25% N_2 was the most effective, requiring only 24% H_2 for detonation in the receiver. It appears that, although the peak pressures were similar for 30% nitrogen, the decrease in flame speed subdued the driver.

Table 7.1: Results of NITRO tests.

% N_2	Minimum % H_2 for Detonation	% N_2	Minimum % H_2 for Detonation
0	26	25	24
10	25	30	No detonation
20	26		

Previous studies by other researchers indicated that a minimum jet diameter-cell size ratio of $D/\lambda \approx 11$–13 was required for direct initiation of detonation. With the 92-mm

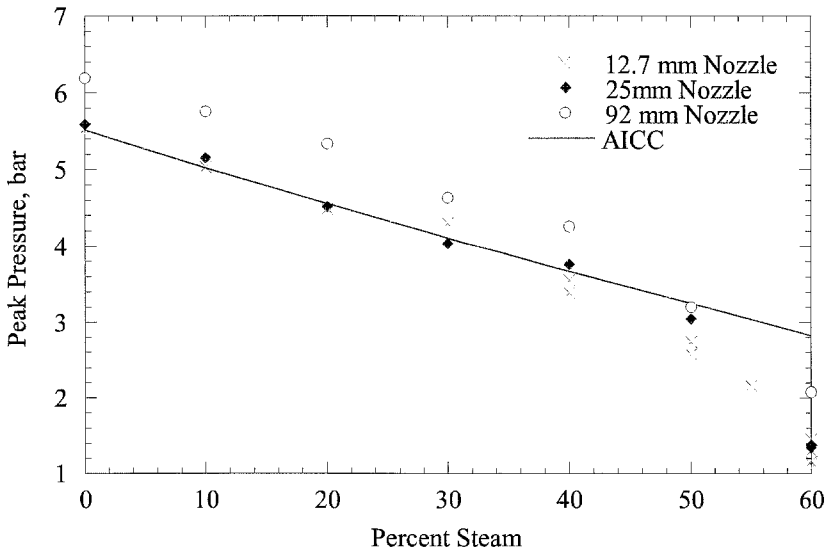

Figure 7.3: Summary of SA test series.

nozzle, HYJET has a $D/\lambda \approx 8$ for 30% H_2-air, so we thought that our "detonations" were actually the result of DDT between the nozzle exit and the transducers. Additional instrumentation in the BETA series showed that these detonations were initiated promptly at the jet exit. Since the D/λ criteria does not take into account the energy in the driver, its usefulness in jet initiation is questionable. Other research has shown that jet initiation is dependent on both large and small-scale turbulence, for entrainment and mixing, respectively.

Effects of confinement were also evident in the NITRO tests. When the receiver hydrogen concentration was just below the detonation threshold, strong secondary explosions were seen. Secondary explosions were also seen following the detonations. Many of these occurred approximately 0.3 ms after the lead wave reflection. We found that the secondary explosions were the result of shock focusing from the elliptical head of the vessel. An attempt to experimentally map the focus zone showed strong focusing, but was unable to clearly determine the shape of the region. Acoustic simulations indicated the presence of two focusing regions, one in the flange extension and one at the focus of the elliptical head.

7.4 BETA Series

The BETA series continued our study of jet initiation. The receiver was filled with stoichiometric H_2-O_2 mixtures of the form $H_2 + 0.5(O_2 + \beta X)$, where X represents N_2 or H_2O dilution. The initial conditions were 1 bar at 298 and 373 K for N_2, and 373 K for H_2O. The objective was to find the maximum value of β (β_{CRIT}) for which a detonation could be initiated. The driver used this mixture with N_2 and β=2.6, at 1 bar and 298 K. The 25, 38, 64 and 92-mm nozzles were used. Combustion regimes were determined by

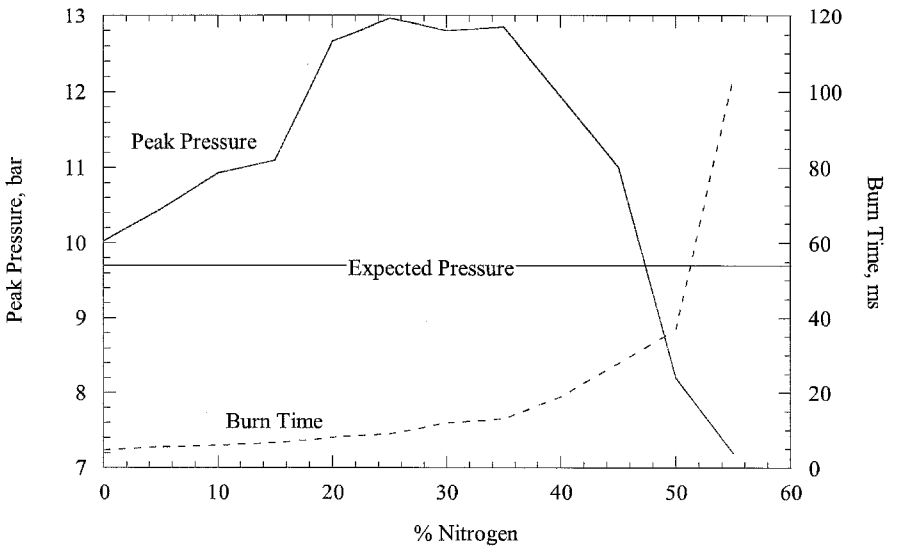

Figure 7.4: Results of constant-volume driver tests.

examination of pressure traces.

The results are summarized in Table 7.2. Earlier research with these mixtures required $D/\lambda \geq 11$ for detonation to occur. In the BETA series, we found $2 < D/\lambda < 7$ (with one exception at 10.7). Again, it appears that D/λ is of limited use in jet initiation experiments. We propose that a critical energy model may be more suitable. The results correlate well when plotted as β_{CRIT} vs. nozzle area, shown in Figure 7.5. We see that β_{CRIT} decreases with nozzle area for all systems. For the 298 K N_2 case, which used all of the nozzles, we see β_{CRIT} approaching an asymptote as nozzle size is increased. This indicates a physical limit for the HYJET facility. As nozzle size is decreased, we expect a sharp drop below 25 mm, as a nozzle size must exist for which no detonation will occur with $\beta = 0$. The effect of jet turbulence is also seen, as adding the diaphragm cutter to the 25-mm nozzle increases its effectiveness by a small amount.

Other trends can be seen by fixing the nozzle size at 92-mm. Mixtures become more sensitive as temperature is increased, and we see that β_{CRIT} is higher for N_2 at 373 K than at 298 K. Water vapor is a more effective suppressant, and β_{CRIT} is much lower for H_2O at 373 K. The tests with no diaphragm are not directly comparable to the others, but we still see the change in β_{CRIT} with nozzle size.

Analysis of the peak pressures recorded at each transducer indicated that the detonation initiation was spherical in nature, with the 92-mm nozzle initiating a detonation further into the vessel than the smaller ones. Even direct initiation must take place downstream of the nozzle exit, as the jet fluid is displacing the reactants. Initiation will also be delayed by the induction time, which will vary as β is changed.

For each run, the velocity of the lead wave was calculated near the end of the vessel. The difference between initiation and failure was clearly indicated. If a detonation occurred, the wave velocity was slightly above the CJ value, indicating either overdrive or

Table 7.2: Summary of D/λ results. (w/c, with cutter; ND, no diaphragm.)

D, mm	Diluent	T	β_{CRIT}	% Diluent	ZND Δ, mm	D/λ
92	N_2	298 K	4.3	58.9	0.222	6.6
64	N_2	298 K	4.2	58.3	0.213	4.7
38	N_2	298 K	3.0	50.0	0.133	3.8
25	N_2	298 K	2.6	46.4	0.114	2.8
25, w/c	N_2	298 K	2.9	49.2	0.128	2.6
92, ND	N_2	298 K	3.3	52.4	0.149	10.7
25, w/c, ND	N_2	298 K	1.8	37.5	0.088	3.3
92	N_2	373 K	5.2	63.4	0.293	5.4
92	H_2O	373 K	1.1	26.8	0.479	3.9
38	H_2O	373 K	0.55	15.5	0.114	4.3

an oblique incidence. If the jet failed to initiate a detonation, the lead wave typically corresponded to a shock of M=1.33, although shocks from the 92-mm nozzle were slightly stronger. The degree of wave curvature was also calculated, but the vessel geometry affects the wave structure at the end of the vessel. The bow leads for detonations fell in the range $1<L<$ 12 cm. One "correct" measurement was taken with a sting installed, indicating a lead of 9 cm.

A photographic analysis of the 25-mm nozzle showed that the detonations were initiated downstream of the nozzle exit, by the second or third window station. Deflagrations were highly turbulent, as expected. We also found that wave action in the driver "thumps" the diaphragm like a drum, generating a small ring vortex at the exit. This travels nearly 100 mm before the diaphragm ruptures and the main jet flow begins. The vortex does not appear to have any effect on detonation initiation.

7.5 Conclusion

The HYJET facility has proved useful in studying jet-initiated combustion phenomena. Combustion-generated jets with radicals were more effective igniters than shock-generated hot jets of air or hydrogen. Lean-limit ignition tests found a 6% hydrogen-air limit for combustion to occur, with 8% required for complete combustion. This agrees with previous tests using sparks and glow plugs. Tests with steam dilution of a 20% H_2-air mixture achieved ignition with 60% H_2O, while previous tests with glow plugs found a limit of 50–55%.

In detonation tests, we found that shock focusing is very important in mixtures immediately below the detonability limit. If a mixture is not detonated promptly, focusing, DDT and shock reflection can generate pressures up to and even over 100 bar. This is over twice the reflected CJ pressure ($\approx 2.5 P_{CJ}$), which can no longer be considered an upper limit for design considerations. DDT was also much more likely in mixtures containing H_2O than in those with N_2 dilution.

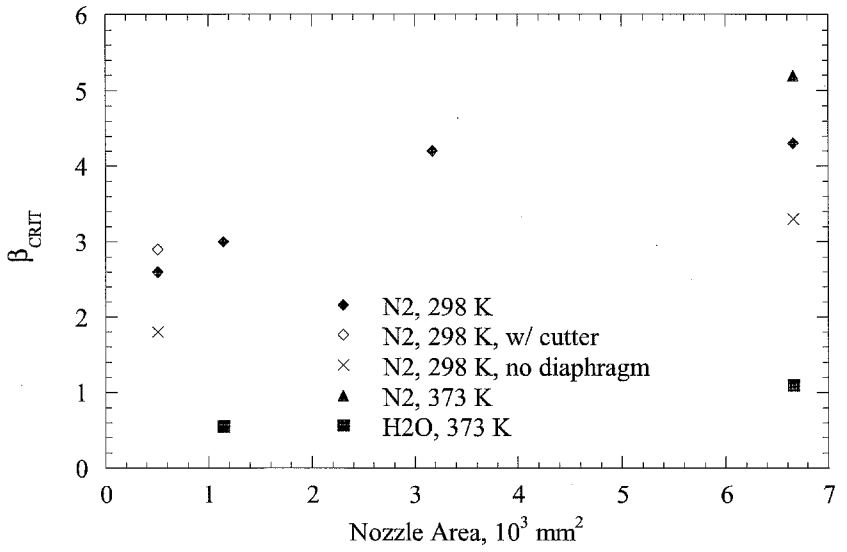

Figure 7.5: Summary of critical beta values.

The tests also found that detonation limits (in jet initiation) are strongly dependent on driver strength and geometry. While previous studies required a minimum jet diameter of 11–13λ for initiation, we were able to initiate detonation with $2<D/\lambda<7$. The results indicate that jet energy is a more meaningful parameter than D/λ.

Future experiments in this facility will continue to study jet initiation of detonation. To suppress transition in the driver, we will add more spark plugs, or move the existing one to the middle of the vessel. We will then vary driver parameters, such as dilution (i.e., P_{AICC} and flame speed) and length, in an attempt to model the initiation process. Ideally, "unconfined" tests would be useful to remove receiver size effects, but this is not feasible with the HYJET facility. The final tests will study detonation initiation with particles in the jet gas. These particles, simulating molten core material in a DCH event, will enhance heat transfer to the reactants and accelerate the onset of detonation.

Bibliography

Anon. (1984, September). *Military Explosives.* Department of the Army. TM 9-1300-214.

Benedick, W. B., J. C. Cummings, and P. G. Prassinos (1984). Combustion of hydrogen:air mixtures in the VGES cylindrical tank. Report NUREG/CR-3273 SAND83-1022, Sandia National Laboratories.

Berman, M. (1985, august). A critical review of recent large-scale experiments on hydrogen-air detonation. In *23rd ASME/AIChE/ANS National Heat Transfer Conference*, Denver, Colorado.

Bezmelnitsin, A. V., S. B. Dorofeev, and Y. G. Yankin (1997). Direct comparison of detonation initiation by turbulent jet under confined and unconfined conditions. Russian Research Centre Kurchatov Institute, Moscow, Russia.

Bezmelnitsyn, A. V., S. B. Dorofeev, and V. P. Sidorov (1995, June). Large scale turbulent jet initiation experiments in KOPER facility, test series 4. Technical report, Russian Research Center Kurchatov Institute, Moscow, Russia.

Boyack, K. W., S. R. Tieszen, and D. W. Stamps (1992). Loads from the detonation of hydrogen-air-steam mixtures. Technical Report SAND92-0541, UC-741, Sandia National Laboratories.

Breitung, W. (1993). Conservative estimates for dynamic containment loads from hydrogen combustions. *Nuclear Engineering and Design 140*, 95–109.

Bull, D. C., J. E. Elsworth, P. J. Shuff, and E. Metcalfe (1982). Detonation cell structures in fuel/air mixtures. *Combustion and Flame 45*(1), 7–22.

Camp, A. L., J. C. Cummings, M. P. Sherman, C. F. Kupiec, R. J. Healy, J. S. Caplan, J. R. Sandhop, and J. H. Saunders (1983). Light water reactor hydrogen manual. Report SAND82-1137 (NUREG/CR-2726), Sandia National Laboratories.

Carnasciali, F., J. H. S. Lee, R. Knystautas, and F. Fineschi (1991). Turbulent jet initiation of detonation. *Combustion and Flame 84*, 170–180.

Cates, J. and D. Howard (1993). Ray tracing program. Documentation for Ae 237 class project.

Chan, C. K. (1995). Collision of a shock wave with obstacles in a combustible mixture. *Combustion and Flame 100*, 341–348.

Chan, C. K., D. Lau, and D. Radford (1990). Transition to detonation resulting from burning in a confined vortex. In *Twenty-Third Symposium (International) on Combustion*, pp. 1797–1804. The Combustion Institute.

Ciccarelli, G., T. Ginsburg, J. Boccio, C. Economos, C. Finfrock, L. Gerlach, K. Sato, and M. Kinoshita (1994). High-temperature hydrogen-air-steam detonation experiments in the bnl small-scale development apparatus. Report NUREG/CR-6213 BNL-NUREG-52414, Brookhaven National Laboratory.

Coward, H. F. and G. W. Jones (1952). Limits of flammability of gases and vapors. Bulletin 503, United States Bureau of Mines.

Djebaili, N., R. Lisbet, C. Paillard, and G. Dupre (1994). Comparison between the ignition of H_2-air-CO_2 and H_2-air-H_2O mixtures by hot gas jet. In *Twenty-Fifth Symposium (International) on Combustion*, pp. 1539–1545. The Combustion Institute.

Dorofeev, S. B., A. V. Bezmelnitsyn, A. A. Efimenko, A. S. Kochurko, V. P. Sidorov, J. G. Yankin, and I. D. Matsukov (1993, June). Experimental study on the combustion behavior of hydrogen- air mixtures with turbulent jet ignition at large scale. Technical Report RRCKI-80-05/3, NUGEG/CR–6072, Russian Research Center Kurchatov Institute.

Dorofeev, S. B., A. V. Bezmelnitsyn, and V. P. Sidorov (1995, December). Large scale turbulent jet initiation experiments in KOPER facility, test series 4 and 5. Technical report, Russian Research Center Kurchatov Institute.

Fickett, W. and W. C. Davis (1979). *Detonation.* Berkeley: University of California Press.

Glasstone, S. and P. J. Dolan (1977). *The Effects of Nuclear Weapons* (third ed.). United States Department of Defense.

Guirao, C. H., R. Knystautas, J. Lee, W. Benedick, and M. Berman (1982). Hydrogen-air detonations. In *19th Symposium (International) on Combustion*, pp. 583–590. The Combustion Institute.

Inada, M., J. H. Lee, and R. Knystautas (1992). Photographic study of the direct initiation of detonation by a turbulent jet. In A. R. Seebass (Ed.), *Dynamic Aspects of Detonations*, Volume 153 of *Progress in Astronautics and Aeronautics*, pp. 253–269. American Institute of Aeronautics and Astronautics.

Knystautas, R., J. H. Lee, and C. M. Guirao (1982). The critical tube diameter for detonation failure in hydrocarbon-air mixtures. *Combustion and Flame 48*(1), 63–83.

Knystautas, R., J. H. Lee, I. Moen, and H. G. Wagner (1979). Direct initiation fo spherical detonation by a hot turbulent gas jet. In *Seventeenth Symposium (International) on Combustion*, pp. 1235–1244. The Combustion Institute.

Krok, J. C. (1992). Hydrogen combustion facility and experiments. Master's thesis, Rensselaer Polytechnic Institute, Troy, New York, USA.

Kuchta, J. M. (1985). Investigation of fire and explosion accidents in the chemical, mining, and fuel-related industries—a manual. Bulletin 680, United States Bureau of Mines.

Lacerda, N. L. (1986). *On the Start Up of Supersonic Underexpanded Jets.* Ph. D. thesis, California Institute of Technology.

Lee, J. H., R. Knystautas, and N. Yoshikawa (1978). Photochemical initiation of gaseous detonations. *Acta Astronautica 5*, 971–982.

Liu, D. D. S., L. J. Clegg, D. Bell, and D. C. Marek (1980). The effect of steam on the combustion of hydrogen-air mixtures near the lower flammability limit. Technical Report CONT-H-7, Whiteshell Nuclear Research Establishment, Pinawa, Manitoba, Canada.

Liu, D. D. S. and R. MacFarlane (1983). Laminar burning velocities of hydrogen-air and hydrogen-air-steam flames. *Combustion and Flame 49*, 59–71.

MacKay, D. J., S. B. Murray, I. O. Moen, and P. A. Thibault (1988). Flame-jet ignition of large fuel-air clouds. In *22nd Symposium (International) on Combustion*, pp. 1339–1353. The Combustion Institute.

Marshall, Jr., B. W. (1986). Hydrogen:air:steam flammability limits and combustion characteristics in the FITS vessel. Report SAND84-0383 (NUREG/CR-3468), Sandia National Laboratories.

McCormack, P. D., K. Sheller, G. Mueller, and R. Tisher (1972). Flame propagation in a vortex core. *Combustion and Flame 19*, 297.

Moen, I. O., D. Bjerketvedt, T. Engerbretsen, A. Jenssen, B. H. Hjertager, and J. R. Bakke (1989). Transition to detonation in a flame jet. *Combustion and Flame 75*, 297–308.

Moen, I. O., D. Bjerketvedt, A. Jenssen, and P. A. Thibault (1985). Transition to detonation in a large fuel-air cloud. *Combustion and Flame 61*, 285–291.

Nettleton, M. A. (1987). *Gaseous Detonations: Their Nature, Effects and Control.* Chapman and Hall.

Quirk, J. J. (1996). An introduction to Amrita. Technical report, California Institute of Technology. For information, see http://www.galcit.caltech.edu/~jjq/.

Reynolds, W. C. (1986, January). The element potential method for chemical equilibrium analysis: Implementation in the interactive program STANJAN, version 3. Technical report, Dept. Mechanical Engineering, Stanford, CA.

Ross, M. C. (1994). Transient jet diffusion flames in hydrogen-air-nitrogen atmospheres. Master's thesis, Rensselaer Polytechnic Institute, Troy, New York, USA.

Shchelkin, K. I. and Y. K. Troshin (1965). *Gasdynamics of Combustion.* Mono Book Corp.

Shepherd, J. E. (1986). Chemical kinetics of hydrogen-air-diluent detonations. In J. Bowen, J.-C. Leyer, and R. Soloukhin (Eds.), *Dynamics of Explosions*, Volume 106 of *Progress in Astronautics and Aeronautics*, pp. 263–293. American Institute of Aeronautics and Astronautics.

Shepherd, J. E. (1992, September). Pressure loads and structural response of the BNL high-temperature detonation tube. Prepared for Brookhaven National Laboratory.

Shepherd, J. E., A. Teodorczyk, R. Knystautas, and J. H. S. Lee (1991). Shock waves produced by reflected detonations. In *Progress in Astronautics and Aeronautics*, Volume 134, pp. 244–264.

Stamps, D. W., W. B. Benedick, and S. R. Tiezen (1991). Hydrogen-air-diluent detonation study for nuclear reactor safety analyses. Report NUREG/CR-5525, SAND89-2398, Sandia National Laboratories.

Stamps, D. W. and S. R. Tieszen (1991). The influence of initial pressure and temperature on hydrogen-air-diluent detonations. *Combustion and Flame 83*(3), 353–364.

Sturtevant, B. and V. A. Kulkarny (1976). The focusing of weak shock waves. *J. Fluid Mech. 73*, 651–671.

Thompson, P. A. (1972). *Compressible-Fluid Dynamics*, pp. 347–358. McGraw-Hill.

Tieszen, S. R., M. P. Sherman, W. B. Benedick, J. E. Shepherd, R. Knystautas, and J. H. S. Lee (1986). Detonation cell size measurements in hydrogen-air-steam mixtures. *Progress in Astronautics and Aeronautics 106*, 205–219.

Üngüt, A. and P. Shuff (1989). Deflagration to detonation transition from a venting pipe. *Combustion Science and Technology 63*, 75–87.

Urtiew, P. A. and C. M. Tarver (1979). Effects of cellular structure on the behavior of gaseous detonation waves under transient conditions. In *Progress in Astronautics and Aeronautics*, Volume 75, pp. 370–384. Proceedings of the 7th International Colloquium on Gas Dynamics of Explosions and Reactive Systems.

Völkl, T. and S. Schlamp (1996). Ignition of a hydrogen-air mixture by a hot air jet. Ae104 Final Report.

White, D. R. (1961). Turbulent structure of gaseous detonations. *Physics of Fluids 4*(4), 465.

Yip, T. W. G., R. A. Strehlow, and A. I. Ormsbee (1985). An experimental investigation of two dimensional flame-vortex interactions. In *20th Symposium (International) on Combustion*, pp. 1655. The Combustion Institute.

Appendix A

Safety Assessment

This Appendix contains a duplicate of the GALCIT Laboratory Safety Assessment filed at GALCIT. It describes the facility, potential hazards, and steps taken to mitigate them.

GALCIT Laboratory Safety Assessment

Facility or Experiment	Explosion Dynamics Laboratory Hydrogen Jet Combustion Facility
Location	Guggenheim 14/14A, bottle farm on the SE corner of Guggenheim
Responsible Faculty or Staff	Joseph Shepherd
Research Associates or Students	J. Christopher Krok

Introduction

The Hydrogen Jet Combustion Facility is designed to examine the transient combustion and explosion processes that occur when a high-temperature jet of hydrogen and steam is injected into a combustible atmosphere of air, steam and hydrogen. The facility constructed at Caltech is a second-generation experiment based on a facility and experiments carried out at the Rensselaer Polytechnic Institute (RPI) in Troy, NY, from 1990 to 1993. In that facility, design and operational issues were studied and over 125 experiments were completed in a two-year period of operation (Krok 1992, Ross 1993).

The design philosophy for our explosion test facilities is to insure complete containment and control over the experiment at all times. Although these experiments are designed to examine explosive events with uncertain outcomes, the initial conditions are always well defined and peak conditions can be bounded. The facility is designed as a pressure vessel to contain any possible event that can occur within the test envelope (with the exception of the schlieren windows; see later discussion). When appropriate, these events include detonations and transition to detonation.

These tests will result in a transient and spatially nonuniform load on the containment system. Although these loads are outside the scope of the existing design guides (Harvey 1974), it is possible (Shepherd 1992) to define an equivalent maximum working pressure using gasdynamic estimates of the pressure transients and elastic response of the vessel structure to dynamic loads. The pressure vessel is then designed using available standards such as the ASME Boiler and Pressure Vessel Code. Standard mechanical engineering practice was used to compute the moments and forces on all other components. The calculations are realistic as possible using hand computations and include the reduction in strength due to potential material flaws, stress concentrations and fastener limitations. The design goal is to specify a containment system that will operate within the limits of the materials with a factor of safety for design basis events and without catastrophic failure (within the ultimate strength of the material) for exceptional events. We have used these techniques to design a number of explosive facilities, including a detonation tube at BNL, the previous jet combustion facility at RPI and the detonation test section currently in use on the T5 free-piston shock tunnel at GALCIT.

In addition, safety features have been designed into the facility to minimize this exposure of the operators and building occupants to potential hazards, and to control and mitigate accidental gas releases. We have solicited the advice of the Safety Office of Caltech, pressure vessel manufacturers and the gas supply vendors in developing and implementing these safety features. The facility and these safety-related features are described in this document.

Lessons learned from RPI The facility at RPI was operated without any significant safety-related incidents, i.e., events which had the potential to injure the operators or bystanders. There were two events that were not part of the normal operating regime, but did no damage. These were two incidents of accidental ignition with the mixing system open, due to ignition system triggering by electrical interference. To prevent this in the GALCIT facility, the ignition system now has remote power and arming control, as well as a logic circuit that blocks power to the ignition modules unless all valves are closed.

Brief Description

After reviewing operation of the original facility at RPI, the new facility was designed to better simulate the desired test conditions, and made stronger to expand the experimental envelope and incorporate more safety features. The new facility is built around two pressure vessels: (1) the driver, a 6-inch diam. tube 4-ft. long; (2) the receiver, a 36-inch diam., 64-inch long pressure vessel. The total volume (driver and receiver) of the CIT facility is about 1.3 m^3. The driver and pressure vessel are connected with a special hydraulic closure of a design similar to that used in the 6-inch GALCIT shock tube. Figure 1 shows a schematic layout of the experiment.

The new facility has a 20% greater total volume over the old one, and the distribution of volume between driver and receiver is much different. The RPI facility had a 1:1 volume ratio, while the GALCIT version has a 1:40 ratio. The MAWP of the receiver has been increased by 25% to allow for combustion of more energetic mixtures. Some of the original support hardware has been reused, such as the gas fill panels and the ignition systems. Safety improvements have been added to this equipment wherever possible. The pressure vessels are new, and design and safety considerations were made at CIT. Other new systems include the electro-pneumatic valves, ignition safety and lockout system, and outside bottle farm. Although experience gained at RPI was used in the design of the GALCIT facility, the design calculations for new fixtures were done from scratch at CIT. Previous computations were re-examined for the RPI components that were reused. Every aspect of the facility was reconsidered from the standpoint of operations and safety.

A typical experiment begins with both the driver and receiver evacuated to less than 1 mbar. The driver is then filled to 1 bar with a rich mixture of hydrogen and oxygen, and the receiver is filled to 1 bar with a mixture of 50/50 air/diluent (nitrogen or steam), and some small percentage (0 to 10%) of hydrogen. The driver mixture is ignited by the discharge of a 15 kV pulse from an EG&G TM-11 trigger generator through an automobile spark plug. The diaphragm separating the driver and receiver is ruptured by the pressure rise, and a hot jet of hydrogen and steam enters into the receiver. If

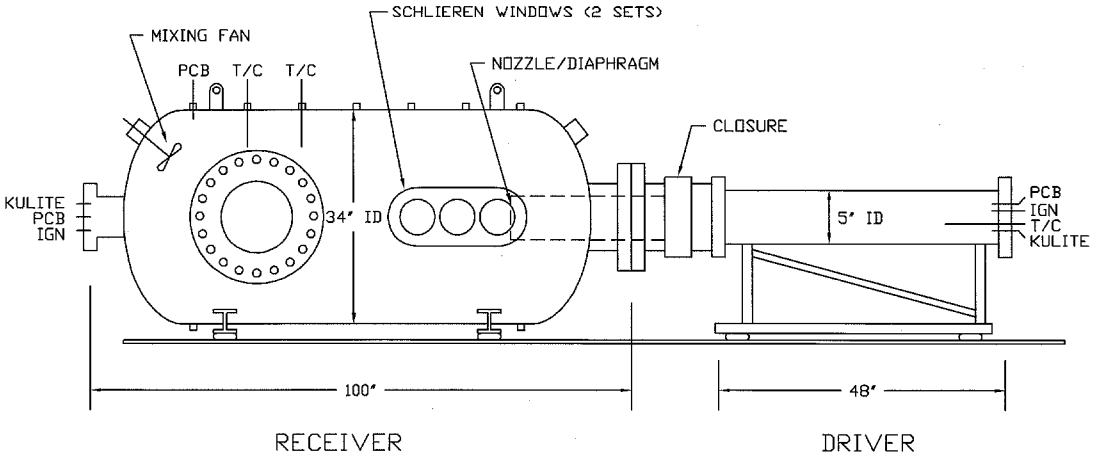

Figure A.1: Basic layout of experiment, showing both vessels.

critical conditions (sufficiently large jet diameter/or high enough hydrogen concentration in receiver) for jet combustion or deflagration exist, a combustion event will occur in the receiver.

With 10% hydrogen in the initial receiver mixture, this results in a peak pressure of approximately 4.1 bar (60 psi) in the receiver. The most commonly used driver mixture is 80% hydrogen and 20% oxygen; combustion of this mixture results in a peak pressure of 9.7 bar (140 psi) in the driver. Figure 2 shows a typical driver pressure history from the experiments done at RPI. A typical receiver pressure history is presented in Figure 5. Both of these traces illustrate the transient nature of the experiment and the short duration for which the vessels actually experience high pressures.

The experiment concludes by venting the combustion products (water, nitrogen and oxygen) through the vacuum pumps into the exhaust system and then into the atmosphere outside the laboratory. The exhaust system is a continuously-operating, high-velocity vent that is installed on the roof of the 2nd floor of "new" Guggenheim. Typically, the combustion products are diluted with air and the steam is condensed out prior to or during the venting process. If a combustion event does not occur, then the mixture is either diluted until it is nonflammable (less than 4% hydrogen) or else fuel and/or oxygen is added until a flammable condition is reached and the mixture is burned. If the receiver mixture doesn't burn initially, then it is already very close to the flammability limit. Thus, if dilution is chosen, no more than 40% nitrogen (400 mbar partial pressure) needs to be added to insure an inert mixture. This is added through the gas handling panel. The gas system can measure up to 2 bar absolute, and the standard starting condition is 1 bar, so the system can handle the additional pressure from dilution. Mixtures are always tested for flammability by several firings of the ignitors before the gasses are pumped out. This technique was used successfully at RPI so that combustible mixtures were never pumped through the vacuum lines or exhaust system.

The driver will always burn unless the mixture is grossly incorrect, e.g., nitrogen is added instead of oxygen, or if both ignition systems fail. Both of these events are

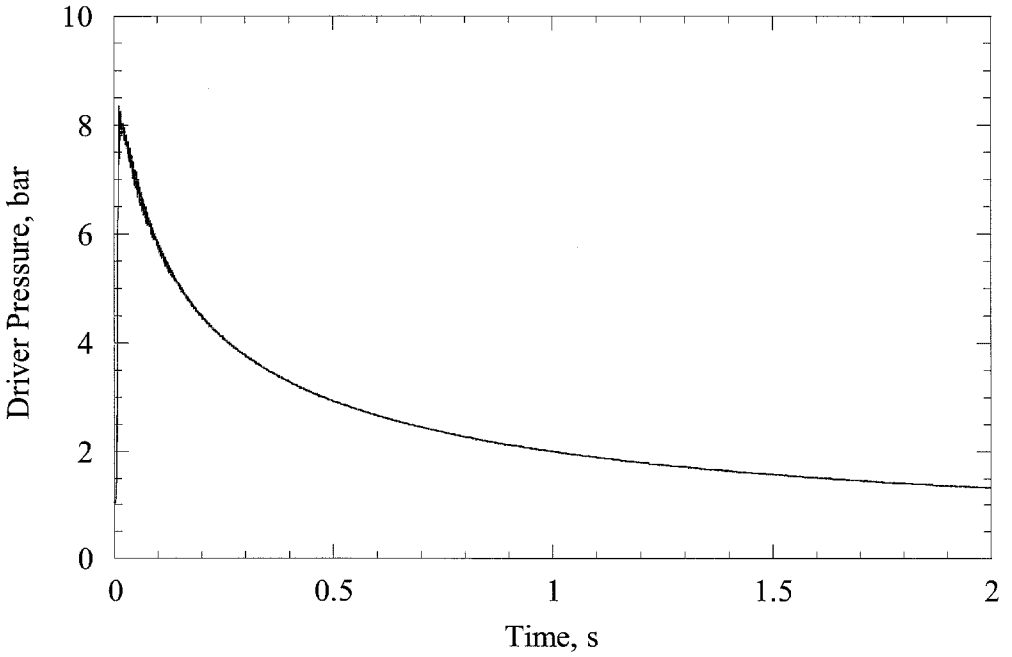

Figure A.2: Typical driver pressure trace from experiments at RPI.

considered to be highly unlikely.

Experimental Procedure

The main steps of the procedure to be followed during each experiment are listed below. The actual checklist to be used in operating the experiment is given at the end of this document.

1. Test emergency ventilation system.
2. Attach diaphragm and appropriate nozzle to end of hydraulic closure.
3. Close, clamp, and pressurize closure.
4. If needed, heat receiver vessel with steam and turn on electrical heaters. (Heaters are controlled by two Omega CN6071A proportional controllers connected to SCR73Z-230 power controllers. The vessel temperature is monitored in the control room and kept below the maximum design temperature of the vessel.)
5. Evacuate vessels with appropriate vacuum pump: liquid ring pump if water vapor is present, main rotary pump if tanks are dry.
6. Close both vacuum valves and wait 15 minutes. If pressure rises more than 1 mbar, find and fix leak. (Prior experience has indicated that if O-rings and Swagelok fittings function under vacuum, they will do so under pressure if properly installed. O-ring grooves have been designed so that they seal preferentially under internal

pressure. Moreover, the system has been hydrotested and helium leak tested under pressure.)

7. Open gas feed valve on receiver, and isolation valves 1 and 2 on driver.
8. Fill both vessels with desired mixtures using method of partial pressures. Monitor pressure gauges for leakage. Close receiver gas feed valve.
9. Run mixers for ten minutes.
10. Close driver isolation valves, and ensure that all other valves are closed.
11. Run data acquisition software, entering appropriate data on screen.
12. Turn on master ignition power key switch. Arm and fire driver when ready.
13. Save data, and safe firing system.
14. Open receiver gas feed and driver isolation valves. Add enough air/oxygen to burn remaining hydrogen. Follow mixing and firing procedure from above, without data acquisition.
15. Evacuate water vapor with liquid ring pump, or vent tank up to atmospheric pressure with air, depressurize closure, and separate tanks.

Design Considerations

The design considerations and safety related features of the key components of the facility are described below.

Compressed Gas Supply Design

Gases are supplied to the experiment from a bottle farm located outside Guggenheim, along the east wall of the addition (see Figure 3). There are four high-pressure manifolds; one for hydrogen (5 DOT-3A class cylinders), one for oxygen (3 DOT-3A class cylinders), one for nitrogen (4 DOT-3A class cylinders) and one for argon (2 DOT-3A class cylinders). The cylinders are connected to the manifolds by flexible, braid-armored pigtails. The manifolds are connected to two-stage regulators (0-1 bar) and shut-off valves. The gases can only enter the building at a maximum pressure of 1 bar gage, minimizing any potential leak rate within the building if a line or valve failure occurs.

The gas bottles are restrained by seismically-rated brackets, which use a chain and screw tightener to hold the bottles firmly against the wall at the top and the bottom. The oxidizer and fuel cylinders will be separated by a rated firewall and a canopy will be placed over the cylinders later this fall. The tubing between the bottle farm and the control system is 0.5-in diameter seamless 316 stainless steel, with an 0.049-in wall thickness. This tubing has a working pressure of 240 bar (3500 psi), so it can withstand full bottle pressure in the event of regulator failure. The tubing is securely mounted to the building and interior walls via Unistrut brackets.

Precautions with compressed gases

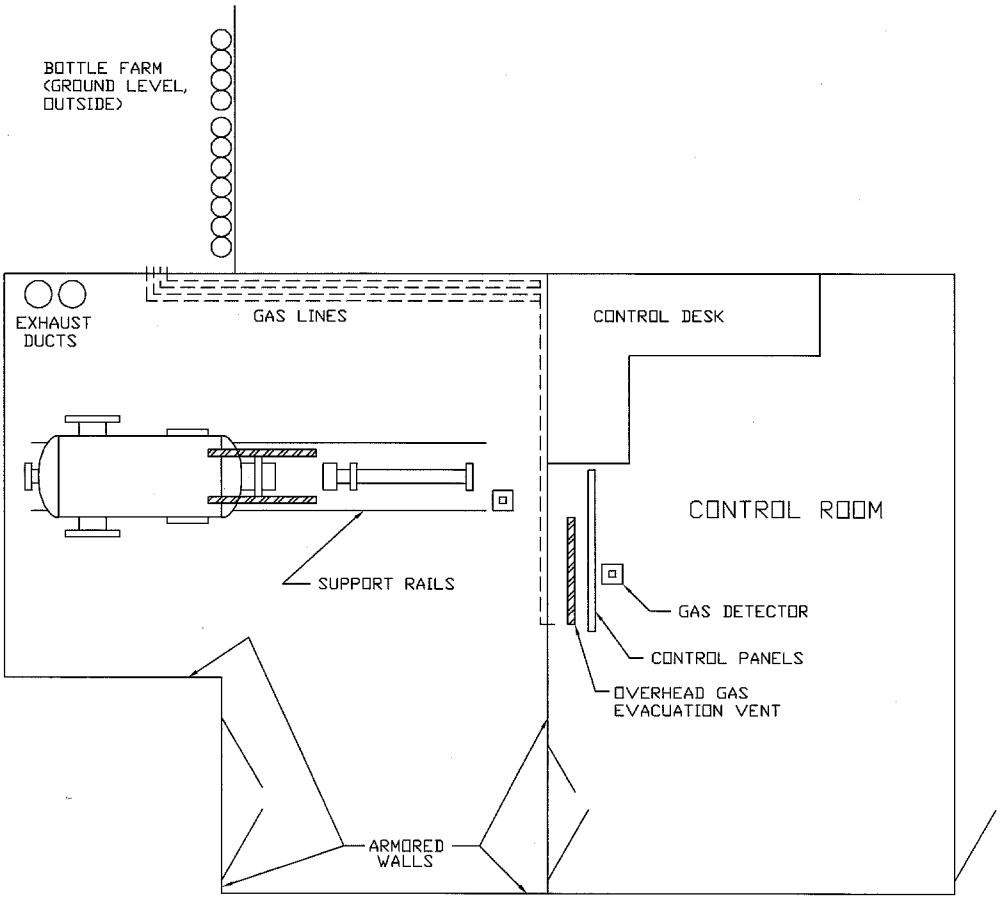

Figure A.3: Floor plan of the Explosion Dynamics Laboratory, 14/14A Guggenheim and bottle farm outside on the upper level.

The gases used in this experiment are argon, nitrogen, oxygen, and hydrogen. There are obvious potential hazards (CGA 1990) when using such gases in a confined space such as our laboratory. The amount of gas present in the lab is minimized by locating the high pressure gas outside of the building, and by not using any secondary mixing reservoirs. There are three types of potential hazards that we have specifically considered:

1. Suffocation (nitrogen, argon and hydrogen).

   The argon and nitrogen are inert, and could be a hazard through displacement of oxygen in the lab. This would be difficult to detect, but unlikely, since fresh air is continually forced into the lab via the building HVAC system. Should the HVAC or emergency purge systems fail, the experiment will not be continued. Failure of these systems would likely be due to a general electrical power outage, which would close the valves and isolate the vessels. Manual gas supply closure would follow.

2. Increased fire hazard (oxygen).

   Enriched oxygen in the lab atmosphere would enhance flammability of items in the lab. This threat will also be reduced by the influx of fresh air from the building HVAC system.

3. Explosion hazard (hydrogen).

The hydrogen gas is the main cause for concern, due to its flammability. Hydrogen is combustible between 4 and 70% by volume in air. A number of design and operational procedures have been included to minimize the potential hazard. These are:

1. All plumbing is heavy wall stainless steel with Swagelok-type fittings.

2. Pressure and quantities of gas within the building are minimized.

3. The gas supply lines are shut off externally (at the bottle farm level) when not in use and internally at the gas supply panel at all other times except when filling with that gas. At the bottle farm, the gas is shut off via a valve between the manifold and the regulator. If the system will be down for an extended period, the bottle valves will be closed as well. In the lab, the procedure is to have all gas supply and metering valves closed except when in use.

4. Plumbing system is pressurized and leak-tested using a helium leak detector purchased specifically for that purpose.

5. The laboratory is equipped with an emergency air ventilation system.

   This system provides for an intake of 500 cfm from the makeup air system and the exhaust of a somewhat larger (800 cfm) amount through a high-velocity exhaust fan mounted on the roof of "new" Guggenheim. The exhaust motor and fan assembly are of explosion proof construction.

The four ceiling intakes for this exhaust system are directly over the gas supply control panels, the driver tube, and the other explosion vessel located in the experimental area (see Figure 3). The vents are located at "high-points" in the ceilings. The ceilings are designed with a slope toward these points and are sealed except for some minor penetrations, the air intakes and the emergency exhaust systems. In case of a major leak into the region above the ceiling, there are three exhaust vents (100 cfm each) located within the space between the ceiling and the concrete floor. This ceiling space is separated between the experimental and control areas. Two of the vents are located in the experimental area and one in the control area. In the case of the experimental area, the ceiling is taped wallboard; in the case of the control room, the ceiling is lift-out acoustical tiles with seals. These acoustical tiles are sealed with a plastic coating to reduce gas penetration. The vent system is either actuated automatically due to gas detection or manually by a switch in the control room.

6. The hydrogen supply is equipped with an emergency shut-off valve.

   A electro-pneumatic valve is located in the hydrogen supply line (outside of building). This valve is opened by remote control only when gas is needed for the experiment. At all other times, it shall be closed. The valve requires both electrical power and air pressure to operate; if one of these is lost due to an accident (i.e., earthquake), the valve will automatically close. The valve is rated to 345 bar, so it can withstand full bottle pressure if the regulator fails.

7. The laboratory is equipped with a flammable gas detection system that is interlocked to the gas supply and the ventilation system.

   There are two flammable gas detectors (Sierra Monitors model 2001) that will actuate when hydrogen is detected at the 400 ppm level (a factor of 100 below the flammability limit). The shut-off valve described above will be closed automatically if either of the detectors are actuated. At the same time, a warning light and an audible alarm is sounded and the emergency venting system is actuated. The detector locations are shown in Figure 3. Further description of this system is provided below.

8. The only exhaust system from the test vessel or the supply system is through a continuously-operated high-velocity vent to the exterior of the building.

9. The operators are physically separated from the test vessels by a wall covered with a steel shrapnel barrier (see Figure 3). The experiment is remotely operated by a mimic panel using electro-pneumatic valves.

When the facility is not in use, it is left either under vacuum or at atmospheric pressure. There is no provision for purging the supply lines, as these gasses are non-reactive with stainless steel under these conditions. To prevent contamination, the gas supply lines are closed and left at or above ambient pressure (0-15 psig) when not in use.

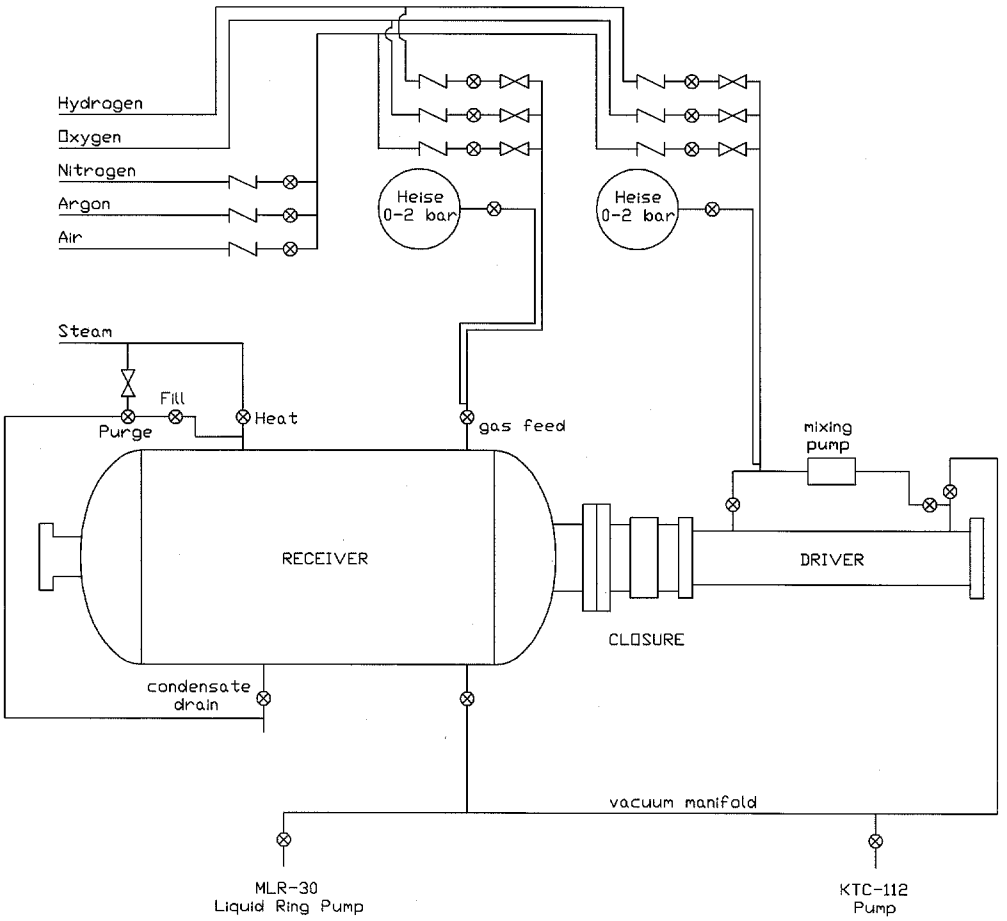

Figure A.4: Gas Supply system for the Hydrogen Jet Combustion Facility.

Driver Design Considerations

The design load for the driver is a detonation of a stoichiometric mixture of hydrogen and oxygen. The CJ pressure for this mixture is 19 bar (initial conditions of 1 bar and 300 K) and the peak reflected pressure is 45 bar. Allowing for the maximum dynamic load factor of 2 (Shepherd 1992), the equivalent maximum average working pressure the vessel should be designed for is 90 bar. This factor of 2 is the upper bound of the response of an undamped elastic system to a step load. It is a general result, not specific to any geometry (Biggs 1965), and used in both the driver and receiver design. In addition to pressure considerations, the driver should be designed from a ductile material with a high ultimate strength in order to accommodate any potential pressure transients that might result from DDT events.

The driver is constructed of a four-foot length of six-inch-diameter, seamless stainless steel (316) tubing with a half-inch wall thickness. Stainless steel (316) flanges 2.0-inch thick and 11-inch diameter are welded to each end of the tubing. Eight 7/8-inch SAE grade 8 bolts are used to connect the flanges to the end plate and the closure assembly. Using an allowable stress of 16.7 kpsi, the corresponding hoop stress would limit the maximum allowable working pressure to 2780 psi (189 bar).

The end flanges are double-welded, and are estimated (using the allowable stress) to take a pressure load of 350 bar. The bolts retaining the blind flange are 7/8-in grade 5, and capable of retaining the end flange under a pressure of nearly 760 bar, so even with preload they will be able to readily withstand 189 bar. The plumbing fittings are all 3000-lb class, and the connecting nipples are schedule 80 stainless steel. These are the same fittings that were used on the RPI apparatus.

Derating this for the stress concentrations at the penetrations, we conclude that the maximum working pressure of this assembly is at least 90 bar. Since the allowable stress used in making this computation includes a substantial factor of safety already, this design can safety accommodate the design load without any safety implications.

Hydrogen embrittlement may be an issue when pressure vessels are used with hydrogen. Three conditions (Harvey 1974, Nelson 1951) are required for hydrogen embrittlement to occur:

1. A high hardness microstructure.
2. Penetration of hydrogen into the metal or pre-existing hydrogen within the metal.
3. Stress, either residual or imposed.

None of these conditions exist in the driver. In general, hydrogen embrittlement in type 316 stainless is never a problem (Harvey 1974) unless the material is used at very high temperatures to contain hydrogen at high pressures (greater than 1000 bar). Data from the U.S. Air Force Metals Handbooks indicate that 304 SS only suffers a 4% loss in strength when exposed to pure hydrogen at 345 bar for 24 hours.

Type 316 stainless steel has a low hardness microstructure and is formulated to resist stress corrosion by hydrogen. There will be extremely limited penetration of hydrogen

in the vessel due to low pressures and temperatures in comparison to typical hydrogen embrittlement conditions. For most of the test, the hydrogen and the vessel will be at room temperature and the hydrogen partial pressure will be less than one atmosphere. After ignition, the pressure and temperature rise to their peak values within milliseconds, but heat transfer to the tube walls cools the gas rapidly and the pressure reaches subatmospheric values within 5 to 10 seconds, as shown in the driver pressure plot. The burn also reduces the hydrogen concentration to 50%.

Cumulative exposure is not considered to be a problem with this facility, as the hydrogen embrittlement process requires a threshold in pressure-temperature conditions before it will even occur. This threshold is not approached in this facility. Both the driver and receiver vessels were designed for hydrogen service. Per the references stated above, there are no restrictions on the lifetime of the vessel for our pressure-time history. The pressure exceeds one bar for approximately 4 seconds per test, and at 100 tests per year, this yields about 7 minutes of cumulative operation with a hydrogen partial pressure of 1 to 3 bar at most.

The facility is expected to be used for at least 10 years. For this duration, fatigue life will not be an issue for this facility. At 100 tests per year, this yields a total of 1000 cycles which places the facility in the low cycle regime of fatigue (Shigley 1990). In this regime, the fatigue strength approaches the tensile strength. Since the facility design incorporates a substantial safety factor (four in the receiver design), the operational stresses are substantially lower than the fatigue limit. Fatigue failure of the components is thus not an issue for the projected lifetime. If the maximum stress incurred in operation is less than the endurance limit (typically one-half of the tensile strength for carbon and alloy steels), the lifetime is effectively infinite. This is most likely the case in our facility.

Closure Design Considerations

A specialized closure assembly design originally developed at GALCIT for the 6-inch shock tube is used to connect the driver to the receiver. This closure is made of forged stainless steel (303 and 304) components and a forged steel (1040) clamp ring that carries the load. Estimates of the axial stress and stress produced by the moment load on the clamp indicate that the performance will be within the allowable stress even with a pressure as high as 136 bar (2000 psi) within the driver section. Radial loads are carried by the main structure of the closure, which is hydraulically sealed when in operation. The hydraulic action provides an axial clamping force of 120,000 lbs on the diaphragm. This closure was successfully used in the previous experiment at RPI.

After the closure was partially modified and installed on the GALCIT facility, it was hydrotested in-situ with the driver at 1500 psi. Pre-shot checkout includes visual inspection of seals, O-rings, closure position, and for hydraulic fluid leaks. When the closure is pressurized, a gage on the pump indicates hydraulic pressure. This gage also has a pressure switch, which is connected to the firing interlock. If the pressure drops below 2000 psi, the firing system will be locked out, and the green light on the control panel will extinguish.

Receiver Design Considerations

Conditions in the receiver vessel are generally much more benign than in the driver.

However, it has been designed to withstand higher pressures than before. In the worst case, we would have a detonation in stoichiometric hydrogen-air at one atmosphere initial pressure. The equivalent pressure produced by a reflected wave with a dynamic load factor of two is 76 bar. The vessel is designed for a maximum average working pressure of 51.7 (750 psi) bar, and was hydrotested to 73 bar (1100 psi). In most cases, the vessel will be filled with more dilute mixtures, and operated at higher initial temperatures, so that the reflected and compensated pressure will not exceed 56 bar. The highest pressure generated in the receiver in the RPI experiments was about 7 bar (Figure 5).

The receiver is a mild carbon steel (ASTM A516-70) pressure vessel 36 inches in diameter, 64 inches seam-to-seam. There are four 600-lb class nozzles and flanges welded to the tank and a number of smaller penetrations. All flange closures are also rated to 600-lb class and are attached with grade 8 (ASTM A574) fasteners. A specially designed flange is used to attach 6-inch diameter windows to each side of the test section. These windows are used for flow visualization of the jet and combustion events within the receiver. There are three axial window locations but only one of these is used at a time. The others are filled with steel blanks when not in use.

The vessel was built and certified to the standards of Section VIII of the ASME Boiler and Pressure Vessel Code. This includes a full X-ray inspection of all welds, and a corrosion allowance of 0.0625 inches. The preliminary design of the vessel, including size and location of flanges and ports, was done at Caltech. Final design and material selection and sizing was done by R. L. Morton Welding Inc., Valley Acres, CA, fabricator of the vessel. All of the materials used in the tank were accompanied by mill reports on chemical composition, yield strength and elongation testing. Discussions with the metallurgist at R. L. Morton identified fracture toughness as being a material issue for an explosive test vessel. This is one of the key reasons for the material choice. To insure material quality, material samples were also impact tested for toughness. The Charpy impact tests were carried out at -40 and -50 degrees Fahrenheit, and the material specimens required at least twice the minimum allowable energy to fracture. The final report on the vessel fabrication and the material certifications is available on file in 14A Guggenheim.

The design pressure (MAWP) of the tank is 750 psi at 250 °F. The pressure was chosen on the basis of the calculated peak pressures in the event of a hydrogen-air detonation within the receiver. Previous tests have all been with deflagrations and the observed peak pressure has always been less than 6 bar (90 psi) in the receiver. The vessels used at RPI had a design pressure of 600 psi, and the peak pressure measured in the driver was 9 bar (125 psi).

This was a case with a very large orifice between the two tanks, and the identical size of the two vessels caused a high level of pressurization in the receiver. If an over-pressure event does occur that exceeds the hydrotest rating of the vessel, then it will be mechanically inspected and retested if necessary.

Hydrogen embrittlement is not an issue in this vessel either. None of the key factors mentioned above are satisfied for the receiver vessel. Tests (Nelson 1953) with mild carbon steel vessels indicate that embrittlement does not occur at hydrogen partial pressures less than 1500 psi when the vessel temperature is less than 500 °F.

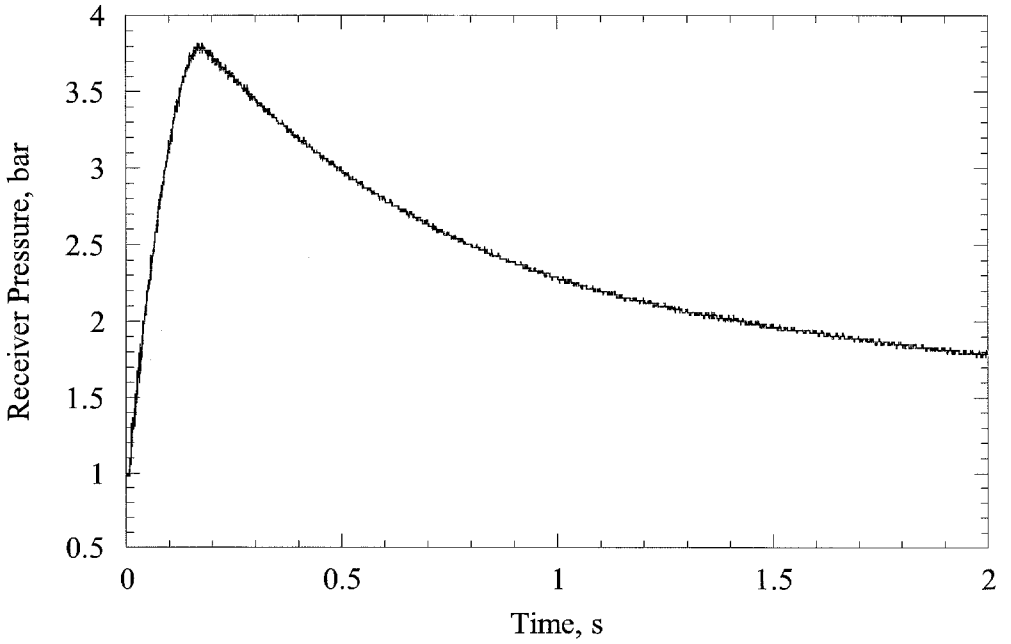

Figure A.5: Highest receiver pressure trace recorded in experiments at RPI. Note that experimental setup was different than it is now.

Operational Safety Precautions

There are several measures incorporated into the check list to ensure the facility integrity and that the safety systems are operating properly.

Key checks before each test include: visual inspection of the facility and bottle farm, measuring the leak rate after pump down; and checking the operation of the remotely operated valves.

The emergency gas evacuation system will normally remain idle, so it is important to test it regularly to ensure correct function in case of a release. The detectors can be tested before each run by releasing flammable gas near the sensor, or waving an acetone-soaked rag nearby. This will also activate the evacuation blower, which can be tested by smoke or tell tales. We plan to equip the vents (in the winter of 1995) with positive flow indicators to ensure that the system is operating at the correct flow rate.

After any seismic events, the entire facility will be visually inspected, the lines and vessels will be tests under vacuum, and the gas lines pressurized with helium and leak checked with a helium detector.

Potential Hazards

We have considered a number of potential hazards and discuss each below.

1. *Hydrogen Leak Into Laboratory Area.* Since the pressure vessels are filled with gas at or below atmospheric pressure, a hydrogen (or inert gas) leak into the room is unlikely. The gas bottles and regulators are located outside the building, so that the gases are only at 1 bar in the feed lines that run to the experiment. However, the

possibility exists that an open valve, a leak in one of the pressure vessel connections, or a leak in one of the Swagelok fittings could release hydrogen into the laboratory environment. To protect against this, we have hydrogen / combustible gas detectors strategically located in each room (SMC model 2001-10, calibrated to activate at 400 ppm hydrogen). In the control room, the detector is located above the gas panels, the only source of hydrogen in that room (see Figure 3). The ceiling in that room is sloped upward towards the detector, as the hydrogen gas will rise and seek the highest point in the room. In the experiment area, the ceiling is sloped upwards to an inverted "trough" over the experiment. This trough contains another combustible gas detector and intakes for the hydrogen exhaust system.

If the detector goes into alarm mode, it activates a latching relay which has several functions. First, it activates a warning light and buzzer in the lab. Second, it shuts off the hydrogen supply valve at the bottle farm, preventing further hydrogen from entering the lab. Third, it is connected to the ventilation system to turn off the air handler and turn on the evacuation system (this is a 1200 cfm exhaust fan located on the roof). This system can not be reset until the detector returns to "safe" mode. There is no way to turn off the detector system unless the power is removed. This would then remove power from the supply valve, stopping the gas supply anyway.

Another situation that could introduce hydrogen into the lab area would be accidental, manual opening of the tanks when they are filled with a combustible mixture and if they were pressurized to greater than atmospheric pressures. Normal operation is to only pressurize the tanks to 1 bar (absolute) initial pressure prior to the test. Therefore in normal operating conditions, opening the vessels to the atmosphere would not constiute a hazard unless the gas supply system was left on.

However, it is possible for the operator to fill the tanks to higher pressures and excessive hydrogen concentrations since the supply manifolds operate at pressure of 1 bar gauge. This would require gross negligence on the part of the operator since the valves used to introduce and control the flow rates of the various gases are manually operated. To reduce the possibility of such negligence, we plan to modify the facility to require continuous operator action (holding down a push button) in order to fill with hydrogen gas. This requirement will force the operator to be physically at the control panel and able to monitor the pressure at all times during the fill process.

A typical experimental condition would be 10% hydrogen in the receiver, and 80% hydrogen in the driver. The volume of the receiver is 1.4 cubic meters, and that of the driver is 0.026 cu m. These fractions would yield a total volume of 0.16 cu m of hydrogen at atmospheric pressure. The volume of the room is 96 cu m, so the fraction of hydrogen in the room would only be 0.2%. Since 4% hydrogen is required to have any type of combustion at all, this would be a non-flammable mixture. It is possible for flammable concentrations of hydrogen to exist locally,

but the HVAC circulation and hydrogen buoyancy would quickly disperse and mix these local concentrations.

2. *Vessel Breach Due To Overpressure.* The peak pressure that could occur in this system is 76 bar, based on a reflected detonation of a stoichiometric mixture of hydrogen and oxygen (including a factor of 2 for dynamic loading). The tank is designed to withstand 51.7 bar, and ASME code incorporates a substantial factor safety is determining the allowable stress. In the case of the receiver, the allowable stress used in the design is 1/4 of the ultimate tensile strength of the material. The welds and penetrations have been designed with a similar factor of safety in this vessel resulting in an ultimate capacity of about 200 bar. Thus, we have a safety factor of 2 for the worst possible case. We conclude that catastrophic failure of this vessel is not a credible failure mode.

   However, as discussed below, the windows or other secondary components may fail under extreme loads. As additional protection, the walls of the experimental area are lined with 1/8-in steel plate to protect the surroundings from any fragments that may be ejected from the tank. These could include transducers, igniter plugs, or window fragments. Note that the 76 bar pressure quoted above can not be obtained within the present operating envelope. This value is used to provide an extreme upper bound on the maximum pressure that might be encountered under abnormal conditions. As mentioned earlier, the highest pressures encountered at RPI were 9 bar. We have considered the strength of the transducer and ignitor mounts, and determined that these will not fail even at the 76 bar level. The force on the transducer will only be 31 lbs, and that on the spark plug will be 216 lbs. These loads produce acceptable stress levels. Therefore, only the windows are subject to failure at 76 bar. These are discussed in the next section.

   The 1/8-inch steel wall will provide useful protection from glass and small metal fragments. Peak fragment velocities are difficult to estimate, but a useful rule of thumb is that the upper limit will be the sound speed in the emerging gas, which will be between 300 and 1000 m/s. Typically, much lower velocities are obtained from ruptured or bursting vessels due to the inertia of fragments and rapid decrease in gas velocity in the jet flow outside the vessel. It is possible to get higher values in an underexpanded jet. Using the estimation techniques discussed in Baker et al. 1985 a 1/8"-thick 1020 CRS plate will withstand (50m/s (normal impact). The penetration velocity varies inversely with particle size and density so that smaller, higher velocity fragments would also be stopped.

3. *Schlieren Window Failure Due To Overpressure.* The 150 mm dia. by 25 mm thick windows used for the schlieren can withstand a pressure of 31-38 bar, much greater than the typical pressures of 4 bar. This estimate was calculated from elastic theory for a simply-supported circular plate. The key parameter in this calculation is the maximum tensile strength of the window material (BK7). Unlike most materials, there are no reliable values of yield strength for glass, as it depends strongly on the surface condition and mounting technique. A value of 5 ksi was used in the

maximum pressure calculation, based on a range of values given by Melles Griot. Glass suppliers commonly quote values up to 10 ksi. We have exposed glass disks of similar aspect ratio to detonation waves resulting in stresses up to twice this value without failure.

In this facility, if a detonation occurs, the peak pressure may exceed the estimated load capacity of the windows, resulting in window failure. As mentioned in item (2), operators and bystanders are protected from this by controlling the experiment from a separate room, and the steel plate on the walls surrounding the apparatus. In addition, the boxes containing the schlieren system will always be in front of the windows, and will help to contain any glass fragments that may be produced.

To eliminate the possibility of window failure, we will only operate the facility with less than 20% hydrogen in air; a reflected detonation in this mixture would result in acceptable peak pressures. If we go to richer mixtures, the window frames can be modified to accept 1.5-inch thick windows, which would increase the failure pressure by a factor of about 2.25. Additional failure protection could be provided by a 3/8 inch thick aluminum plate on the schlieren system opposite the windows.

Failure of the windows could also result in a blast wave, but it is difficult to make an accurate estimate of its strength. The source term is highly transient and analogous to the muzzle blast from a gun. The effective driving pressure will be time dependent but will initially be much closer to the constant-volume explosion pressure, about 8 bar for stoichiometric hydrogen-air, than the detonation pressure. With the above precautions, we consider window failure to be a highly unlikely event. If the operating envelope is enlarged to include near-stoichiometric hydrogen concentrations, then an appropriate blast and consequence analysis will be considered.

4. *Misfire.* A misfire occurs when there is a combustible mixture in either vessel and the ignition system fails to ignite it. This can occur if the electrodes on the spark plugs become fouled or there is an electrical system failure. If the amount of hydrogen in the system is small enough, the mixtures can be inerted by addition of nitrogen, and then pumped out of the vessels. Or, extra oxygen or hydrogen can be added to sensitize the mixture, and the glow plugs can be used to ignite it.

5. *Mixture Ignition With Containment Valves Open.* All of the valves on the driver and receiver vessels are remotely operated with positive indication of the valve position in the control room. The ignition system is interlocked with the valve indicator switches so that ignition can not occur unless the valves are closed.

   If an accidental mixture ignition occurs with the gas supply / tank containment valves open, a pressure wave will travel through the gas supply tubing. This pressure will not exceed the 90 bar mentioned in item (1), and all of the plumbing can safely handle this pressure. The tubing components have a minimum pressure rating of 241 bar, and the weakest valve in the system can withstand 103 bar.

The only weak point in the system is the Heise gage located on each gas supply panel. These are only rated for 2 bar and will be damaged if overpressurized. The gages are quite robust, constructed with a heavy, cast metal body and blowout backs. The manufacturer does not have data on failure pressure available for these gages, but from similar models, they suggest that the failure pressure would be at least 40% greater than full scale.

The gages have their own isolation valves which will be closed after the vessels are filled with the proper mixtures. If the gage is pressurized to failure, the operator will be protected by a 1/4-in thick sheet of Lexan mounted over the face of the gage. Lexan is a very tough material, which can withstand a large amount of plastic deformation without fracturing. The gage faces are constructed of 1/8 inch Plexiglas, so the Lexan shields should be able to safely deflect any fragments.

Failure of these gages would require multiple failures in the operating procedure. Two possible scenarios are: 1) regulator fails, operator doesn't follow checklist, opens supply and metering valves with vessel valve closed, and fails to take corrective action; 2) Operator does not follow checklist, gage valve left open, vessel valves open, interlock system fails to function, and ignition occurs.

6. *High Voltage Ignition System.* Two TM-11A high voltage trigger modules are used to ignite the mixtures in the tanks. These modules generate a 15 kV pulse, and this voltage is considered to be lethal regardless of the current supplied. The wiring for these modules will be protected, and they are connected to AC power such that they can only be turned on from the control room, with a key.

7. *Seismic Damage To Vessels.* The vessels are both mounted on linear bearings which allow them to translate in one direction. Safety brackets are mounted on these rails to prevent the vessels from jumping the track. Also, the gas lines connected to the tank are flexible, minimizing the possibility of damage or breakage.

8. *Miscellaneous.* In addition to the built-in safety devices, the laboratory also contains emergency equipment such as fire extinguishers, first aid kits, and personal protective equipment (safety glasses, dust masks, ear muffs, etc.) to be used while working.

References

1. Baker et al. **Explosion Hazards and Evaluation**, Elsevier, 1983.

2. Biggs, J. M. **Introduction to Structural Dynamics**, McGraw-Hill 1965.

3. GGA 1990 **Handbook of Compressed Gases**, Third Edition, Compressed Gas Association, Inc., Chapman and Hall, NY.

4. Harvey, J. F. 1974 **Theory and Design of Modern Pressure Vessels**, Van Nostrand Reinhold, NY.

5. Krok, J. C., 1992, *Hydrogen Combustion Facility and Experiments*, Master of Science Thesis, Rensselaer Polytechnic Institute, Troy, NY.

6. Nelson, G. A., 1951, "Metals for High-Pressure Hydrogenation Plants," Trans. ASME **73**, 205-213.

7. Ross, M. C., 1993, *Transient Jet Diffusion Flames in Hydrogen-Air-Nitrogen Atmospheres*, Master of Science Thesis, Rensselaer Polytechnic Institute, Troy, NY.

8. Shepherd, J. E., 1992, *Pressure Loads and Structural Response of the BNL High Temperature Detonation Tube*, BNL Technical Report A-3991, Brookhaven National Laboratory.

9. Shigley, J. E. and Mischke, C. R. *Mechanical Engineering Design*, McGraw-Hill, 1989.

Appendix B

System Drawings

This appendix contains AUTOCAD drawings from the HYJET facility for reference purposes.

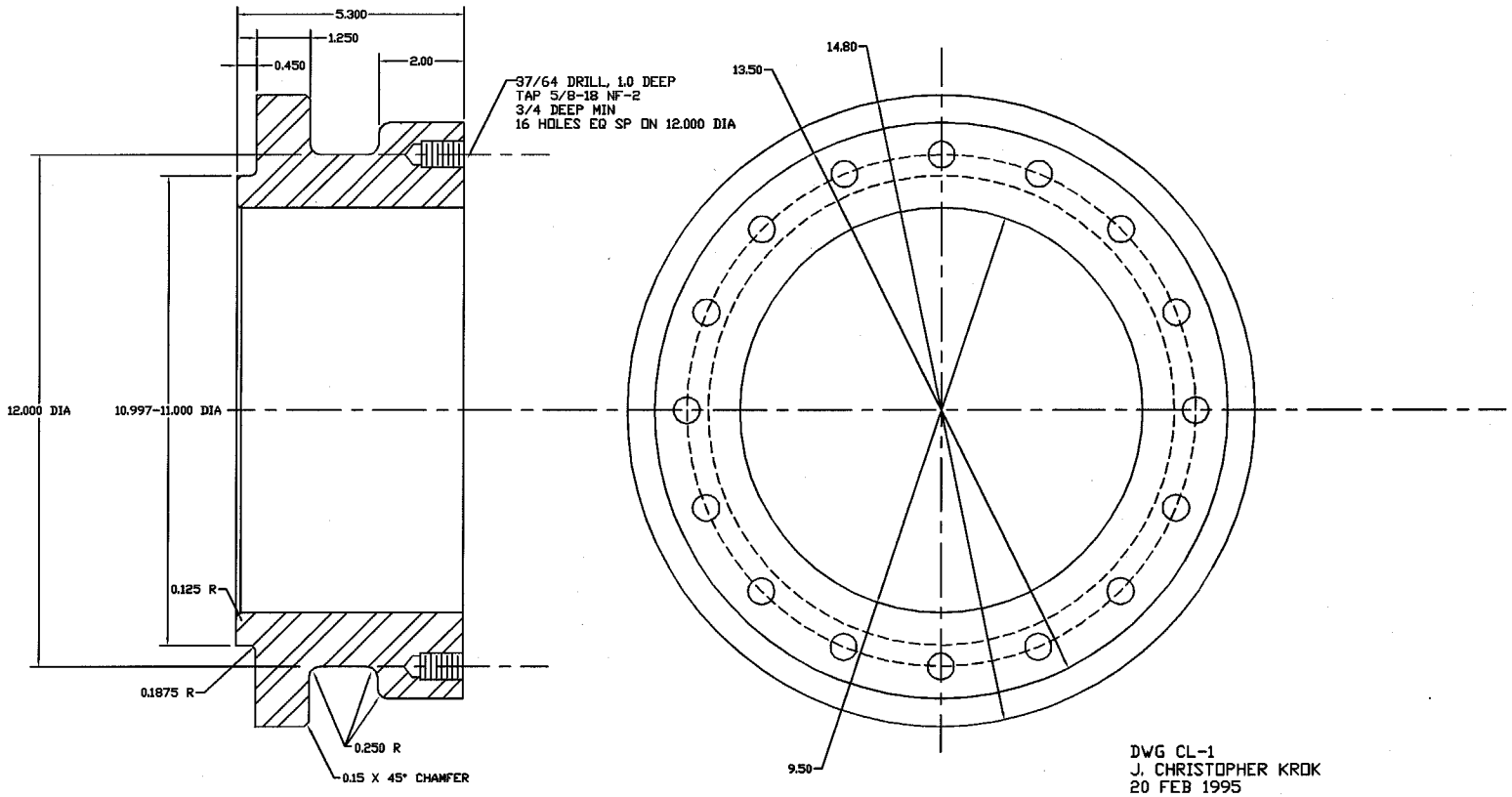

CLOSURE ADAPTER

MAT'L: 304 SS ALL DIMENSIONS INCHES ±0.005 UNLESS NOTED

DWG CL-1
J. CHRISTOPHER KROK
20 FEB 1995

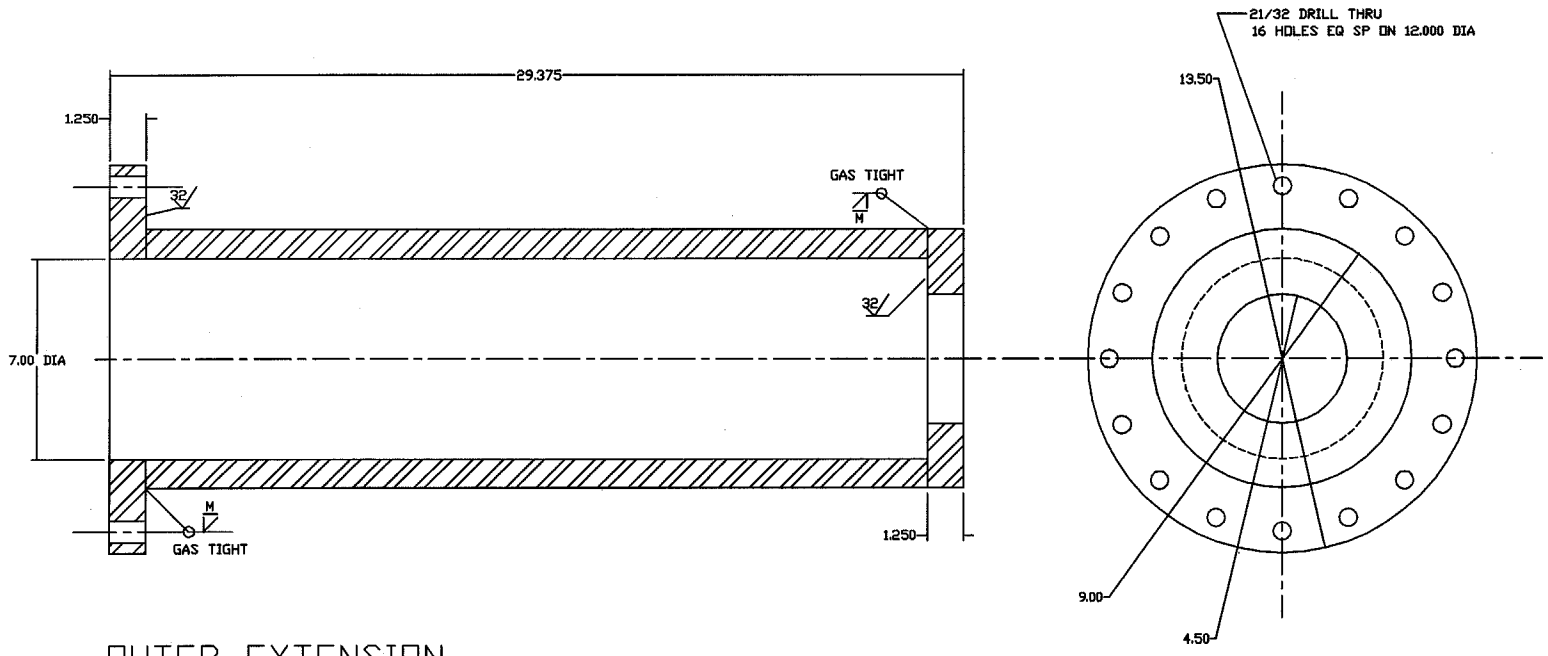

OUTER EXTENSION

MAT'L: 304 SS
ALL DIMENSIONS INCHES ±0.005 UNLES NOTED

J. CHRISTOPHER KROK
2 MARCH 1995
DWG OE-1

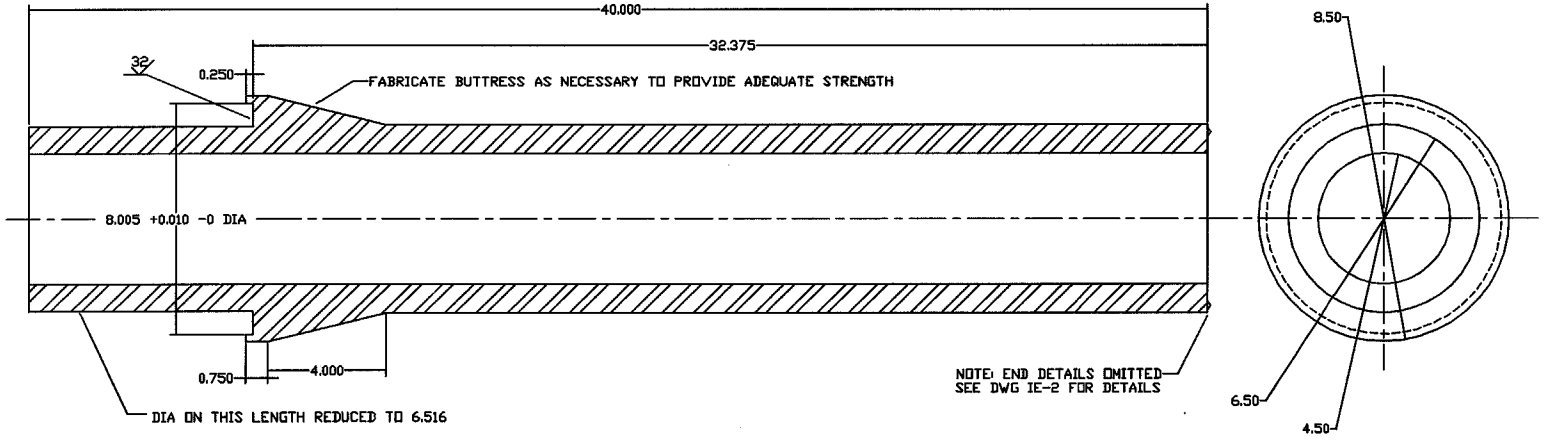

INNER EXTENSION

MAT'L: 304 SS
ALL DIMENSIONS INCHES ±0.005 UNLESS NOTED

J. CHRISTOPHER KROK
8 MARCH 1995
DWG IE-1

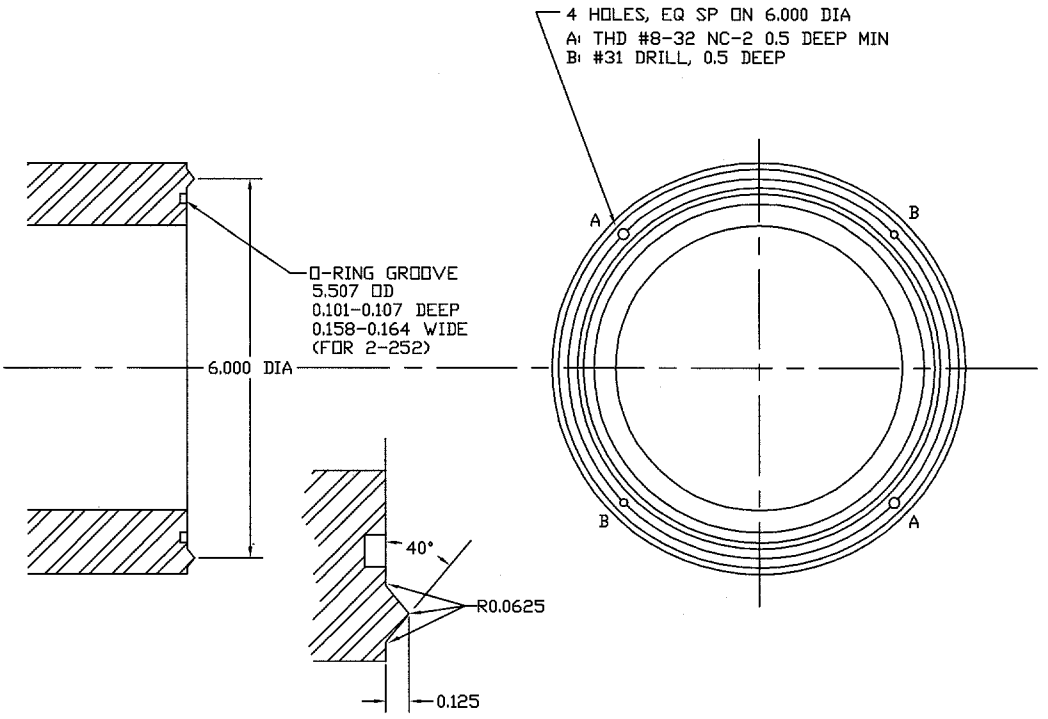

INNER EXTENSION END DETAIL

ALL DIMENSIONS INCHES ±0.005 UNLESS NOTED
FINISH BOTTOM OF O-RING GROOVES TO 32

J. CHRISTOPHER KROK
7 MARCH 1995
DWG IE-2

NOTE: MOST HIDDEN LINES OMITTED

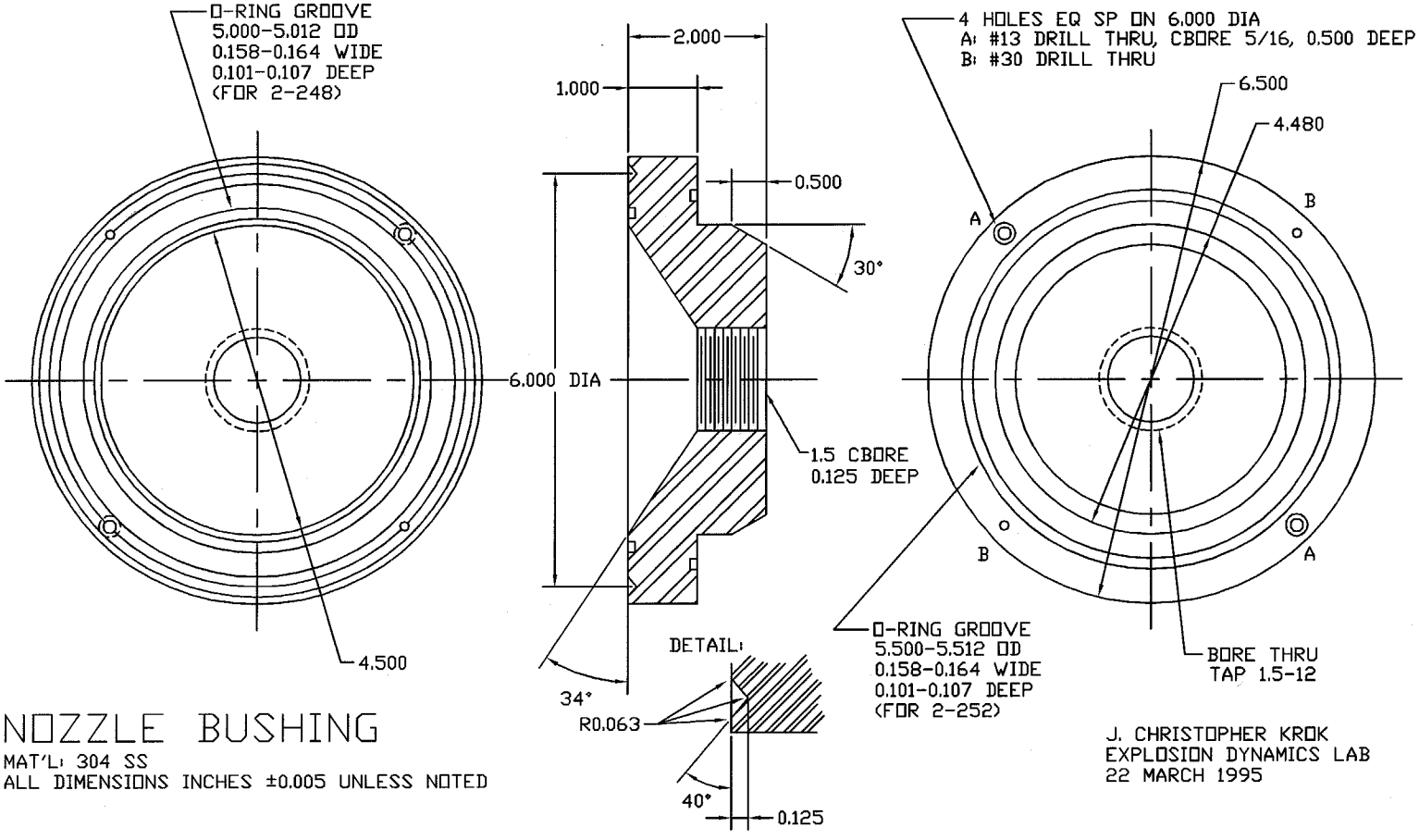

NOZZLE BUSHING

MAT'L: 304 SS
ALL DIMENSIONS INCHES ±0.005 UNLESS NOTED

J. CHRISTOPHER KROK
EXPLOSION DYNAMICS LAB
22 MARCH 1995

NOTE: MOST HIDDEN LINES OMITTED

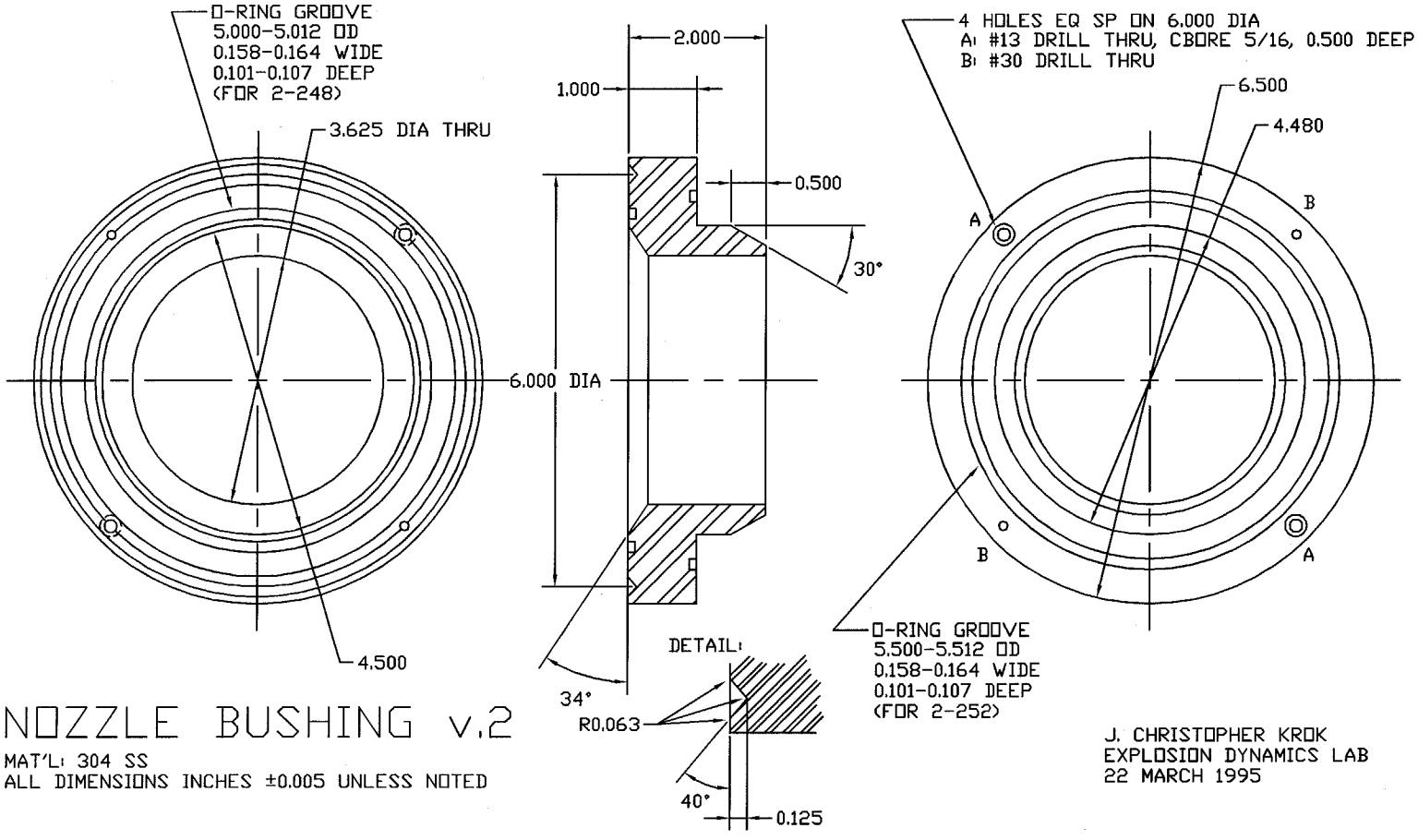

NOZZLE BUSHING v.2

MAT'L: 304 SS
ALL DIMENSIONS INCHES ±0.005 UNLESS NOTED

J. CHRISTOPHER KROK
EXPLOSION DYNAMICS LAB
22 MARCH 1995

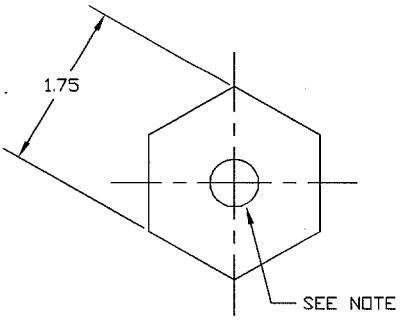

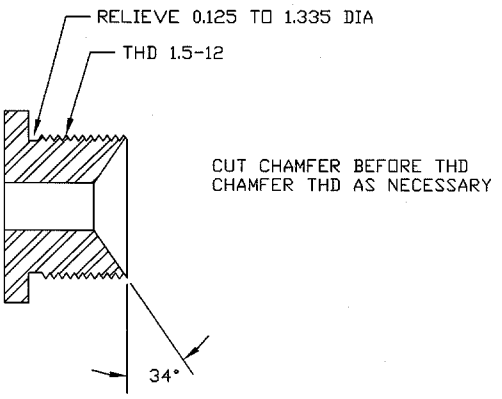

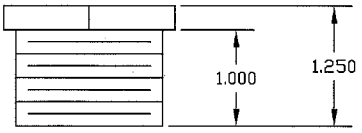

NOTE: ONE EACH OF 1/4, 1/2, 1 DIA REQ'D

NOZZLE

MAT'L: 304SS 1-3/4 HEX BAR
ALL DIMENSIONS INCHES ±0.005 UNLESS NOTED
USE 2-125 O-RING

J. CHRISTOPHER KROK
EXPLOSION DYNAMICS
23 MARCH 1995

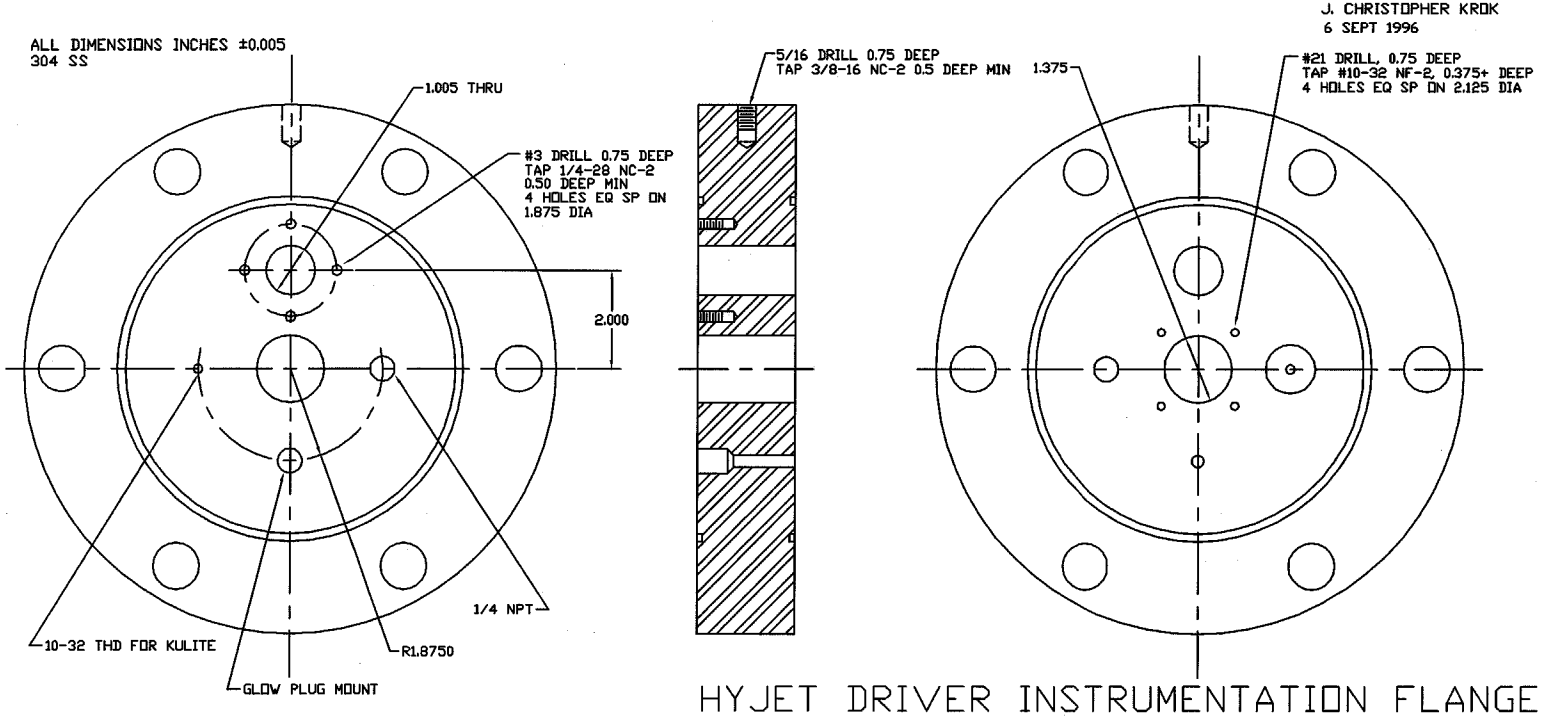

HYJET DRIVER INSTRUMENTATION FLANGE

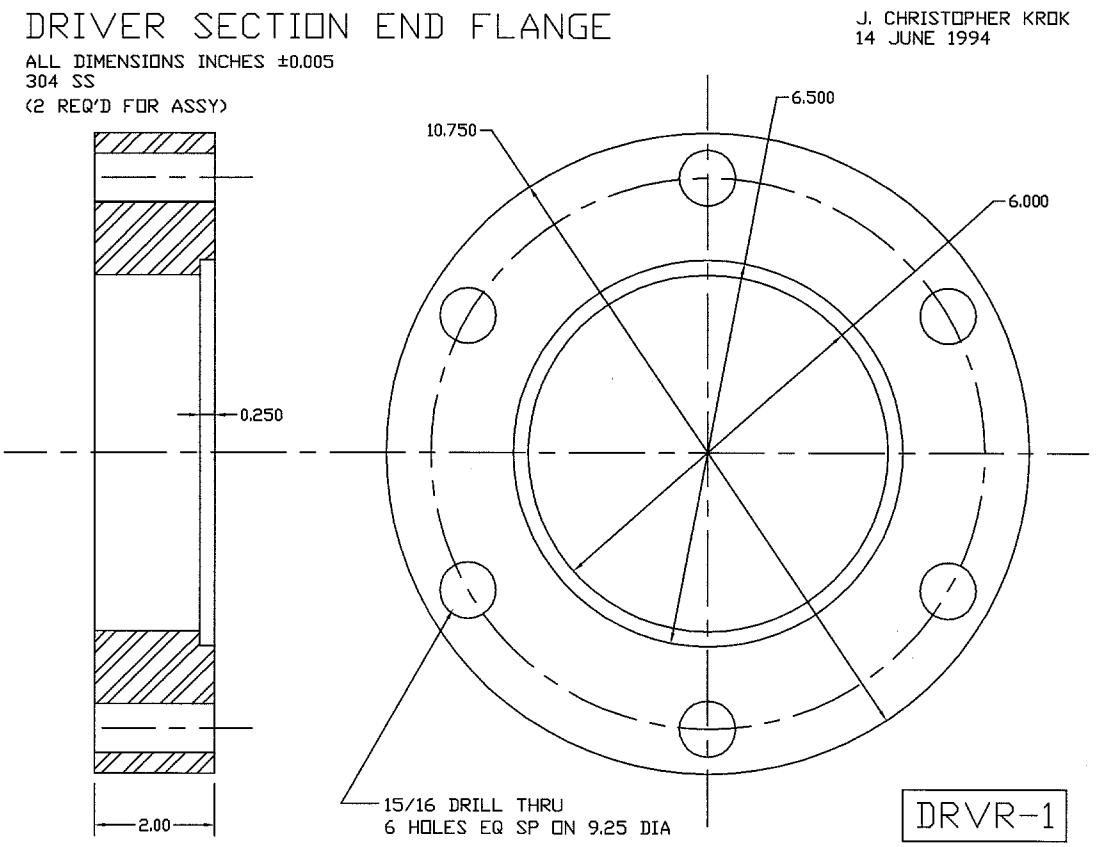
DRIVER SECTION END FLANGE
J. CHRISTOPHER KROK
14 JUNE 1994
ALL DIMENSIONS INCHES ±0.005
304 SS
(2 REQ'D FOR ASSY)
10.750
6.500
6.000
0.250
2.00
15/16 DRILL THRU
6 HOLES EQ SP ON 9.25 DIA
DRVR-1

DRIVER SECTION ASSEMBLY

J. CHRISTOPHER KROK
14 JUNE 1994

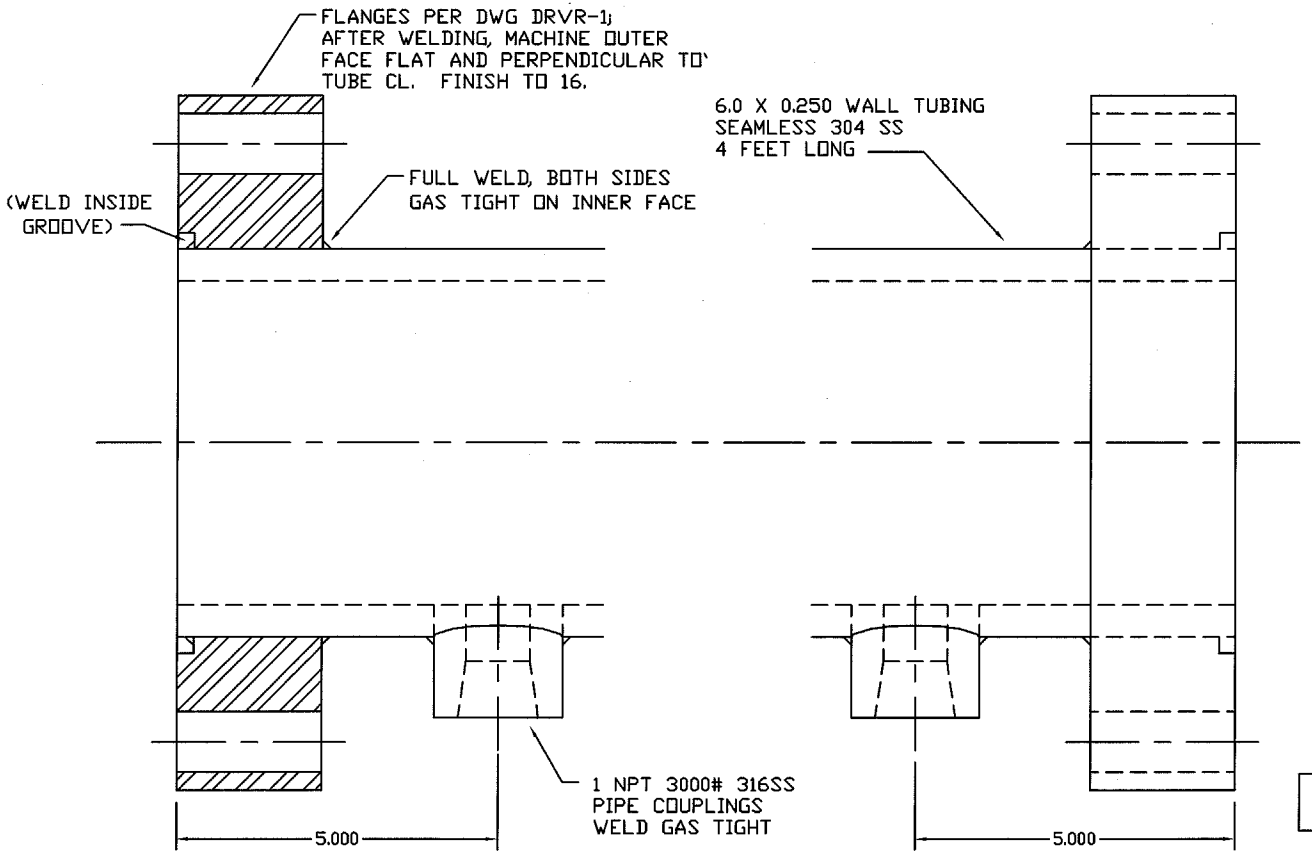

DRVR-4

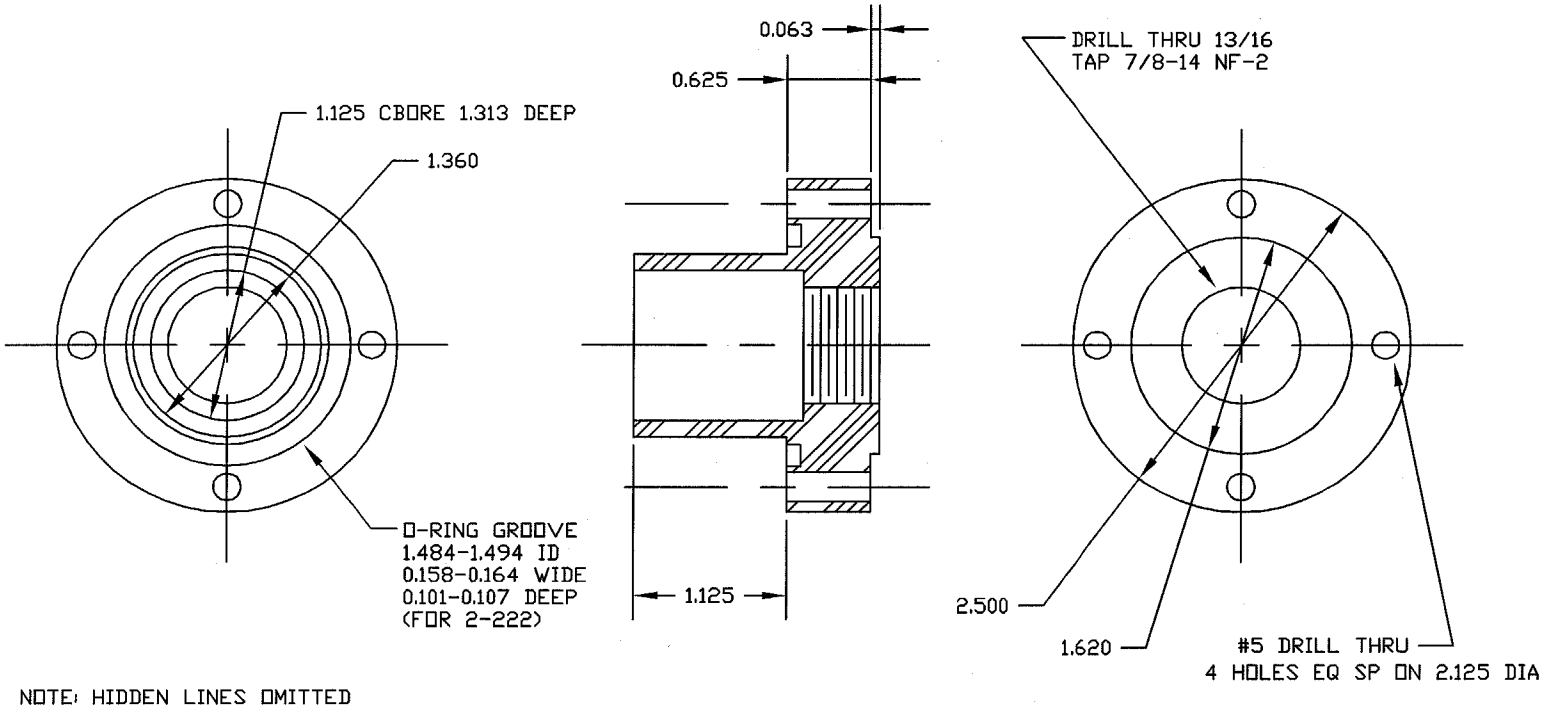

NOTE: HIDDEN LINES OMITTED

SPARK PLUG ISOLATOR

MAT'L: 2.5 DIA TFE BAR STOCK
ALL DIMENSIONS ±0.005 UNLESS NOTED

J. CHRISTOPHER KROK
EXPLOSION DYNAMICS LAB
20 MARCH 1995

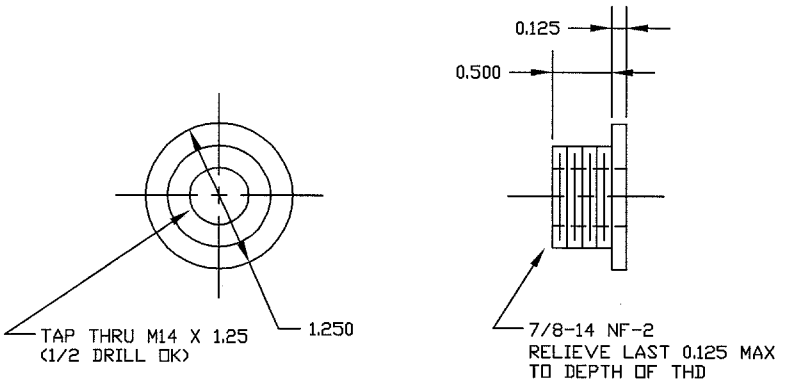

SPARK PLUG BUSHING

MAT'L: 1.25 DIA CRS BAR
ALL DIMENSIONS INCHES ±0.005 UNLESS NOTED

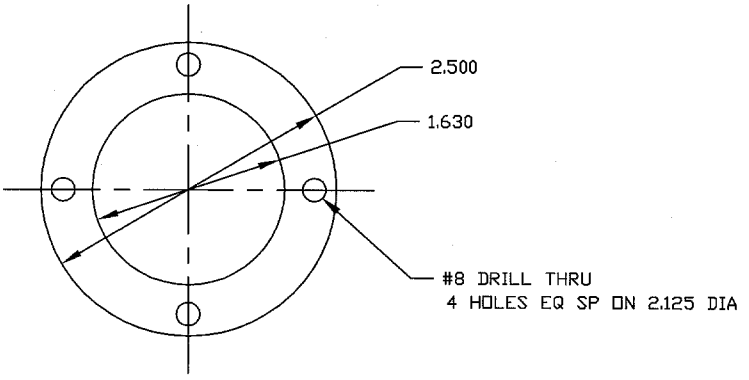

ISOLATOR RETAINING RING

MAT'L: 1/16 STEEL PLATE
ALL DIMENSIONS INCHES ±0.005 UNLESS NOTED

J. CHRISTOPHER KROK
EXPLOSION DYNAMICS LAB
20 MARCH 1995

Window Retainer

ALL DIMENSIONS ± .005 UNLESS NOTED

Explosion Dynamics Laboratory
Drawn By: J. Christopher Krok
18 May 1994

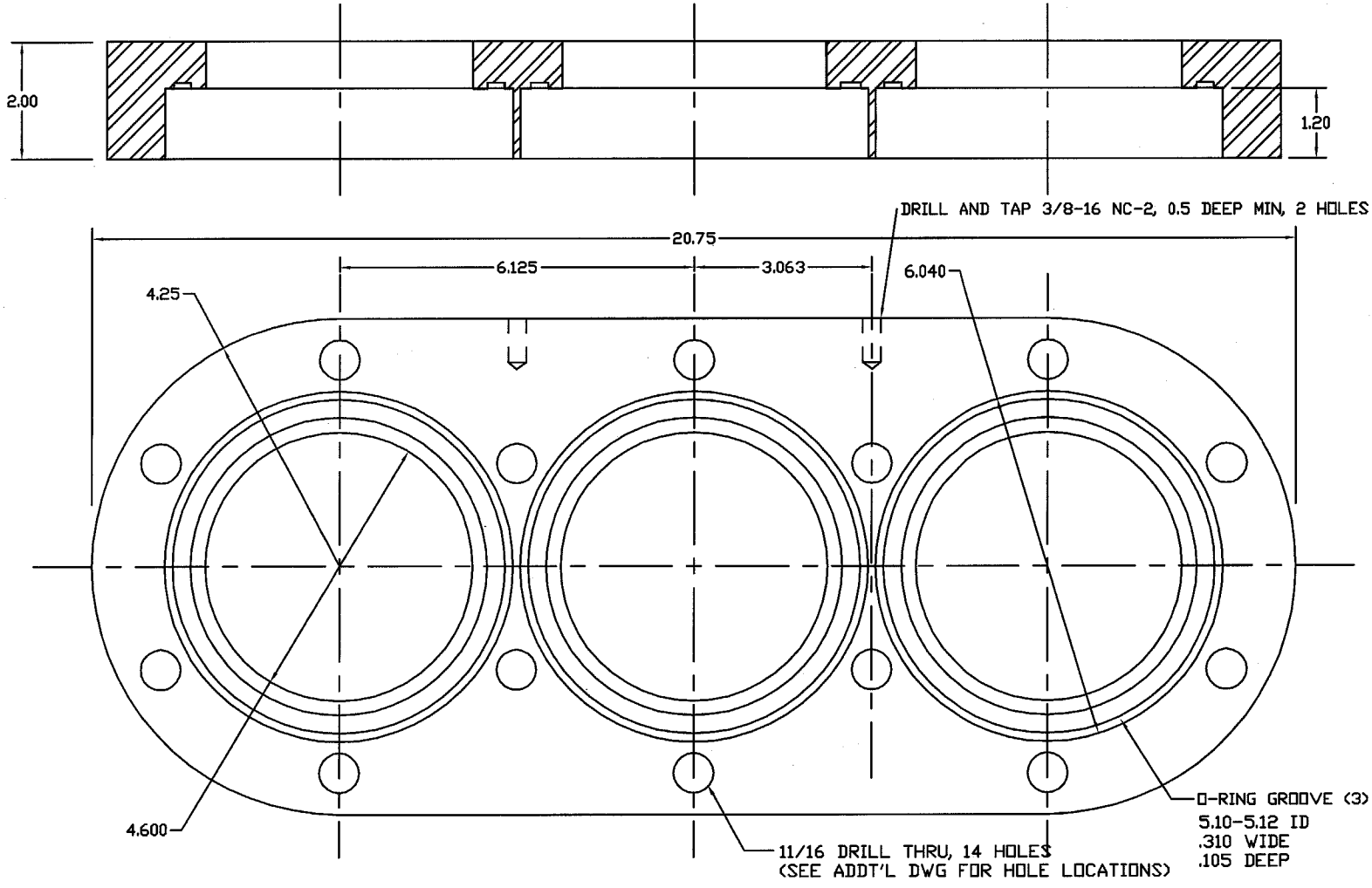

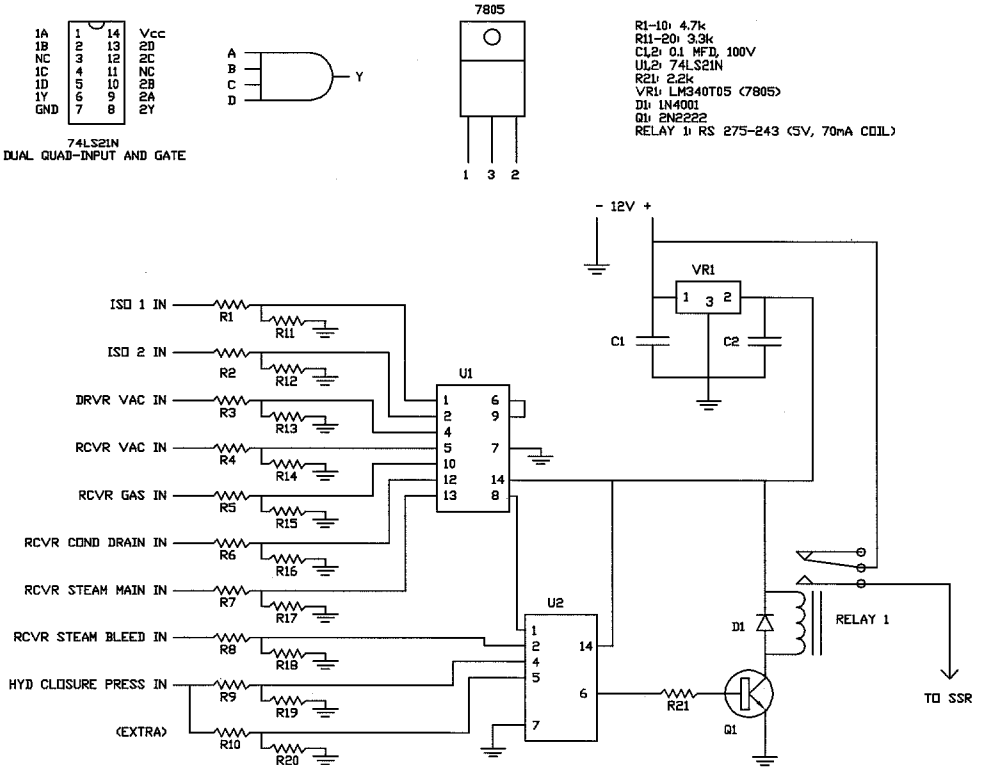

HYJET LOGIC CONTROL SAFETY INTERLOCK CIRCUIT

J. C. KROK 11 SEPT 1995

Appendix C

Run Summary

This appendix contains a table summarizing all of the runs performed in this research. The column headings are as follows:

1. **Run Number**: Sequential numbers used to identify each run, as a serial number.
2. **Date**
3. **Time**
4. **Series**: Indicates the series that each run was part of, as described in the text. The CHA and HHA series, not described in the text, are generic terms for Cold Hydrogen-Air (298 K) and Hot Hydrogen-Air (373 K), respectively. These were used as test runs. Other test runs are listed here as well.
5. **DRVR**: Gas mixture in driver, as percentages. A, air; H, hydrogen; N, nitrogen; O, oxygen; S, steam (gaseous H_2O).
6. **Nozz**: Nozzle diameter, in mm. Additional codes are: NC, no cutter (nozzle diameters 25 mm and smaller use a diaphragm cutter by default); CV, constant volume test (nozzle plugged); ND, no diaphragm.
7. **RCVR**: Gas mixture in receiver, format same as DRVR.
8. **T1, DR**: Initial temperature in driver, in °C.
9. **T1, RC**: Initial temperature in receiver, in °C.
10. **P_p, DR**: Peak pressure measured by driver Kulite, bars.
11. **P_p, RC**: Peak pressure measured by receiver Kulite, bars.
12. **P_p, T3**: Peak pressure measured by PCB in T3 position, bars.
13. **P_p, E**: Peak pressure measured by PCB in E position, bars.

14. **REC**: Receiver Event Code. Describes resulting event in receiver vessel. B, burn (deflagration); D, detonation (prompt initiation); T, transition to detonation (DDT); LE, late or secondary explosion. If blank, receiver was inert, a fault occurred, or run was a systems test.

Run #	Date	Time	Series	DRVR	Nozz	RCVR	T1, DR	T1, RC	Pp, DR	Pp, RC	Pp, T3	Pp, E	REC
18	2-Feb-96	1530	COMP	80H/20O	12.7	50N/50A	19.5	20.5	11.41	1.15			
19	2-Feb-96	1650	COMP	80H/20O	12.7	2H/49N/49/A	20.7	20.7	10.94	1.18			NB
20	5-Feb-96	1030	COMP	80H/20O	12.7	ABORT							
21	5-Feb-96	1150	COMP	80H/20O	12.7	4H/48N/48A	20.6	22.1	10.86	1.22			NB
22	5-Feb-96	1545	COMP	80H/20O	12.7	6H/47N/47A	21.2	22.6	10.63	1.89			B
23	6-Feb-96	0948	COMP	80H/20O	12.7	8H/46N/46A	19.5	21.9	10.98	3.39			B
24	6-Feb-96	1123	COMP	80H/20O	12.7	10H/45N/45A	20.8	22.4	10.78	3.92			B
25	6-Feb-96	1400	COMP	80H/20O	25	50N/50A	20.0	23.0	10.66	1.36			
26	6-Feb-96	1618	COMP	80H/20O	25	2H/49N/49A	21.7	22.8	10.39	1.39			NB
27	12-Feb-96	0918	COMP	80H/20O	25	4H/48N/48A	19.3	20.8	11.01	1.44			NB
28	13-Feb-96	1341	COMP	80H/20O	25	TRIG FAIL							
29	27-Feb-96	1605	COMP	80H/20O	25	CLIPPED							B
30	28-Feb-96	1042	COMP	80H/20O	25	CLIPPED							B
31	28-Feb-96	1305	COMP	80H/20O	25	6H/47N/47A	20.0	21.2	11.07	1.95			B
32	28-Feb-96	1436	COMP	80H/20O	25	6H/47N/47A	22.0	22.0	NR	2.06			B
33	1-Mar-96	1050	COMP	80H/20O	25	8H/46N/46A	19.2	20.0	10.91	3.33			B
34	1-Mar-96	1400	COMP	80H/20O	25	100N	19.7	21.6	10.35	1.18			
35	1-Mar-96	1645	COMP	80H/20O	25	100A	19.5	22.0	10.74	1.39			
36	7-Mar-96	1433	COMP	80H/20O	25	10H/45N/45A	20.0	20.0	10.51	4.56			B
37	7-Mar-96	1609	COMP	80H/20O	12.7	50N/50A	20.3	21.6	10.45	1.15			
38	8-Mar-96	1110	COMP	80H/20O	12.7	100A	19.0	20.6	10.28	1.15			
39	8-Mar-96	1203	COMP	80H/20O	12.7	100A	21.3	21.2	11.65	1.16			
40	13-Mar-96	1530	COMP	80H/20O	12.7	100N	19.3	20.6	10.06	1.05			
41	13-Mar-96	1633	COMP	80H/20O	12.7	100N	20.7	21.2	11.25	1.08			
42	13-Mar-96	1730	COMP	80H/20O	25	100A	21.4	21.2	11.09	1.37			
43	14-Mar-96		COMP	80H/20O	25	100N	18.9	20.4	10.79	1.18			
44	14-Mar-96	1135	COMP	80H/20O	12.7	50N/50A	20.3	20.4	NR	NR			
45	14-Mar-96	1435	COMP	80H/20O	12.7	2H/49N/49A	20.3	20.6	10.16	1.17			NB
46	29-Mar-96	1524	COMP	80H/20O	12.7	6H/47N/47A	19.6	20.4	10.23	1.79			B
47	29-Mar-96	1658	COMP	80H/20O	12.7	8H/46N/46A	20.9	21.1	10.35	3.28			B
48	1-Apr-96	1511	COMP	80H/20O	6.4	10H/45N/45A	19.5	20.2	10.84	3.92			B
49	1-Apr-96	1729	COMP	80H/20O	6.4	CLOG							B
50	2-Apr-96	1340	COMP	80H/20O	6.4	CLOG							B
51	2-Apr-96	1455	COMP	80H/20O	6.4	CLOG TEST							
52	15-Apr-96		S	80H/20O	12.7	ABORT							B
53	16-Apr-96	1523	S	80H/20O	12.7	10H/45S/45A	23.6	98.0	10.59	2.95			B
54	16-Apr-96	1648	S	80H/20O	12.7	8H/46S/46A	23.8	97.7	9.68	2.01			B
55	16-Apr-96	1818	S	80H/20O	12.7	6H/47S/47A	24.7	96.6	10.52	1.16			NB
56	16-Apr-96	1938	S	80H/20O	12.7	4H/48S/48A	25.4	95.8	10.22	1.09			NB

Run #	Date	Time	Series	DRVR	Nozz	RCVR	T1, DR	T1, RC	Pp, DR	Pp, RC	Pp, T3	Pp, E	REC
57	17-Apr-96	1038	S	80H/20O	12.7	2H/49S/49A	22.2	102.9	10.58	1.17			NB
58	17-Apr-96	1206	S	80H/20O	12.7	50S/50A	23.6	102.2	10.32	1.09			
59	17-Apr-96	1334	S	80H/20O	25	8H/46S/46A	24.0	101.0	10.09	1.99			B
60	17-Apr-96	1521	S	80H/20O	25	8H/46S/46A	24.2	100.4	10.22	1.93			B
61	21-Apr-96	1504	COMP	80H/20O	25	10H/45N/45A	22.4	24.3	10.77	4.33			B
62	22-Apr-96	1605	COMP	80H/20O	12.7	10H/45N/45A	22.0	26.0	10.35	4.07			B
63	23-Apr-96	1610	COMP	80H/20O	12.7	10H/45N/45A	23.3	20.4	10.41	4.08			B
64	24-Apr-96		SA	80H/20O	12.7	ABORT							B
65	24-Apr-96	1344	SA	80H/20O	12.7	60S/8H/32A	24.2	102.8	10.21	1.13			NB
66	24-Apr-96	1502	SA	80H/20O	12.7	50S/10H/40A	24.0	102.0	NR	2.58			B
67	24-Apr-96	1648	SA	80H/20O	12.7	40S/12H/48A	25.3	100.2	10.26	3.39			B
68	25-Apr-96	0914	SA	80H/20O	12.7	60S/8H/32A	23.4	103.7	10.59	1.45			B
69	25-Apr-96	1017	SA	80H/20O	12.7	50S/10H/40A	24.0	103.0	NR	2.74			B
70	25-Apr-96	1306	SA	80H/20O	12.7	40S/12H/48A	24.4	102.6	10.75	3.56			B
71	29-Apr-96	0900	SA	80H/20O	12.7	30S/14H/56A	23.9	102.2	10.46	4.3			B
72	29-Apr-96	0959	SA	80H/20O	12.7	20S/16H/64A	25.2	103.6	10.24	4.49			B
73	29-Apr-96	1110	SA	80H/20O	12.7	10S/18H/72A	25.7	102.8	10.21	5.03			B
74	29-Apr-96	1230	SA	80H/20O	12.7	0S/20H/80A	26.1	103.6	10.20	5.53			B
75	29-Apr-96	1413	SA	80H/20O	25	0S/20H/80A	25.0	103.0	10.08	5.59			B
76	29-Apr-96	1606	SA	80H/20O	12.7	60S/8H/32A	25.6	104.8	10.15	1.16			NB
77	30-Apr-96	1036	Kg20H		CV	20H/80A							B
78	30-Apr-96	1319	SA	80H/20O	12.7	55S/9H/36A	23.8	103.4	10.07	2.16			B
79	30-Apr-96	1516	SA	80H/20O	12.7	GAINS OFF	24.9	106.2	9.78	1.3			B
80	30-Apr-96	1625	SA	80H/20O	25	60S/8H/32A	25.7	106.1	10.07	1.37			NB
81	30-Apr-96	1802	SA	80H/20O	25	CLIPPED	25.5	105.8	10.10	CLIP			B
82	30-Apr-96	1900	SA	80H/20O	25	50S/10H/40A	26.4	106.0	10.01	3.05			B
83	30-Apr-96	2045	SA	80H/20O	25	40S/12H/48A	25.8	107.7	10.00	3.76			B
84	30-Apr-96	2145	SA	80H/20O	25	30S/14H/56A	26.6	108.3	9.67	4.04			B
85	1-May-96	0945	SA	80H/20O	25	20S/16H/64A	23.7	102.3	10.19	4.52			B
86	1-May-96	1051	SA	80H/20O	25	10S/18H/72A	25.1	103.7	9.94	5.15			B
87	1-May-96	1158	SA	80H/20O	92	60S/8H/32A	26.1	104.6	7.74	2.08			B
88	1-May-96	1316	SA	80H/20O	92	30S/14H/56A	26.3	103.6	7.58	4.64			B
89	1-May-96	1423	SA	80H/20O	92	20H/80A	26.8	103.6	7.60	6.19			B
90	1-May-96	1520	SA	80H/20O	92	100A	27.6	106.0	7.25	2.21			
91	1-May-96	1601	SA	80H/20O	92	100N	28.2	105.6	7.56	1.92			
92	2-May-96	1530	SA	80H/20O	92	100A	23.2	57.3					
93	3-May-96	1152	SA	80H/20O	92	50S/10H/40A	23.7	100.8	7.87	3.2			B
94	3-May-96	1515	SA	80H/20O	92	40S/12H/48A	24.1	106.8	7.58	4.26			B
95	4-May-96	0920	SA	80H/20O	92	20S/16H/64A	23.5	104.1	7.01	5.34			B

Run #	Date	Time	Series	DRVR	Nozz	RCVR	T1, DR	T1, RC	Pp, DR	Pp, RC	Pp, T3	Pp, E	REC
96	4-May-96	1115	SA	80H/20O	92	10S/18H/72A	25.6	103.8	6.94	5.76			B
97	4-May-96	1225	SA	80H/20O	25	60S/8H/32A	26.1	105.5	9.68	1.34			NB
98	10-May-96	1020	HHA	80H/20O	92	22H/78A	23.6	99.3	7.82	7.06			B
99	10-May-96	1425	HHA	80H/20O	92	24H/76A	23.4	99.4	NTRIG				
100	10-May-96	1615	HHA	80H/20O	92	24H/76A	25.2	101.8	8.61	7.05			B
101	10-May-96	1735	HHA	80H/20O	92	26H/74A	26.2	103.6	8.56	7.48			B
102	29-May-96	1120	HHA	80H/20O	92	28H/72A	23.8	95.2	8.34	8.87			B
103	29-May-96	1355	HHA	80H/20O	92	30H/70A	24.7	96.4	8.60	9.05			D?
104	30-May-96	0940	HHA	80H/20O	92	26H/74A	22.0	100.0	8.60	8.6		12.35 M	B
105	30-May-96	1100	HHA	80H/20O	92	28H/72A	25.3	100.5	8.43	8.95		12.35 M	D?
106	21-Jun-96	1300	CAM TEST										
107	21-Jun-96		CAM TEST										
108	21-Jun-96		CAM TEST										
109	21-Jun-96		CAM TEST										
110	21-Jun-96		CAM TEST										
111	22-Jun-96		CAM TEST										
112	22-Jun-96		CAM TEST										
113	24-Jun-96	1400	CHA	80H/20O	6.4	10H/90A	23.3	24.0	9.88	4.15			B
114	24-Jun-96		1N2O	80H/20O	92	8H/8N2O/84A			8.22	4.8			B
115	24-Jun-96		2N2O	80H/20O	92	50N2O/50A			8.14	2.69			
116	25-Jun-96	1045	COMP	80H/20O	92	100A	25.0	25.0	8.74	2.65			
117	25-Jun-96	1200	3N2O	80H/20O	92	4H/48N2O/48A	24.7	25.2	8.18	3.72			
118	26-Jun-96		COMP	80H/20O	6.4	100A	23.2	24.8	9.48	1.04			
119	26-Jun-96		COMP	80H/20O	6.4	100N	24.3	25.1					
120	15-Jul-96	1645	CAM TEST										
121	18-Jul-96	1020	NITRO	80H/20O	92	24H/76A	24.4	24.0	8.58	8.3	12.47	14.4	B
122	18-Jul-96	1145	NITRO	80H/20O	92	26H/74A	25.7	26.8	9.02	8.57	9.89	20	
123	18-Jul-96		NITRO	80H/20O	92	24H/76A	26.1	29.3	8.47	8.33	16.43	20.93	LE
124	18-Jul-96	1500	NITRO	80H/20O	92	26H/74A	26.2	31.1	8.43	9.28	36.92 M	36.62 M	D
125	18-Jul-96		NITRO	80H/20O	92	26H/74A	26.3	33.0	8.36	8.96	37.41	61.28	D
126	19-Jul-96	0845	NITRO	80H/20O	92	100A	23.1	28.7	8.44	2.49	2.79	5.63	
127	19-Jul-96	1030	NITRO	80H/20O	92	25H/75A	24.6	28.3	8.61	8.48	13.09	24.01	LE
128	19-Jul-96	1325	NITRO	80H/20O	92	23H/77A	24.4	30.1	8.42	8.08	10.4	17.53	LE
129	19-Jul-96	1445	NITRO	80H/20O	92	27H/73A	25.7	32.1	8.37	9.28	37.59	61.98	D
130	22-Jul-96	1035	NITRO	10N/72H/18O	92	23H/77A	23.1	24.2	8.81	8.65	41.19	25.22	LE
131	22-Jul-96	1145	NITRO	10N/72H/18O	92	24H/76A	25.2	27.1	8.77	8.69	9.87	35.84	LE
132	22-Jul-96	1315	NITRO	10N/72H/18O	92	25H/75A	25.7	29.3	8.66	9.2	40.49	72.25 M	D
133	22-Jul-96	1440	NITRO	10N/72H/18O	92	26H/74A	26.0	31.4	8.73	8.94	47.77	55.4	D
134	22-Jul-96	1625	NITRO	10N/72H/18O	92	27H/73A	25.7	33.0	8.68	9.35	39.5	72.75 M	D

Run #	Date	Time	Series	DRVR	Nozz	RCVR	T1, DR	T1, RC	Pp, DR	Pp, RC	Pp, T3	Pp, E	REC
135	22-Jul-96	1805	NITRO	20N/64H/16O	92	24H/76A	25.7	34.6	10.19	8.34	8.92	26.23	LE
136	23-Jul-96	1010	NITRO	20N/64H/16O	92	25H/75A	23.4	28.9	10.04	8.4	19.59	22.16	LE
137	23-Jul-96	1225	NITRO	20N/64H/16O	92	26H/74A	24.4	30.9	10.11	9.42	47.75	72.75 M	D
138	23-Jul-96	1445	NITRO	50N/40H/10O	92	25H/75A	25.2	32.5	BURN	TOO	SLOW		B
139	23-Jul-96	1600	NITRO	50N/40H/10O	92	25H/75A	25.9	34.6	8.63	8.04	7.5	17.11	LE
140	24-Jul-96	0940	NITRO	30N/56H/14O	92	CONTAMINATED							D
141	24-Jul-96	1100	NITRO	30N/56H/14O	92	25H/75A	25.3	31.4	8.70	8.45	12.81	21.01	LE
142	24-Jul-96	1520	NITRO	30N/56H/14O	92	24H/76A	25.2	31.8	8.48	8.11	11.36	20.49	LE
143	24-Jul-96	1650	NITRO	30N/56H/14O	92	26H/74A	25.7	33.8	8.94	8.33	14.54	12.31	B
144	25-Jul-96	1035	NITRO	30N/56H/14O	92	27H/73A	23.9	28.4	9.13	8.4	8.88	10.31	B
145	25-Jul-96	1215	NITRO	30N/56H/14O	92	28H/72A	24.8	31.2	9.03	8.76	30.73	13.36	LE
146	25-Jul-96	1355	NITRO	30N/56H/14O	92	30H/70A	25.4	33.3					LE
147	25-Jul-96	1555	NITRO	25N/60H/15O	92	30H/70A	25.2	34.9	10.30	9.41	42.18	85.66	D
148	25-Jul-96	1655	NITRO	25N/60H/15O	92	28H/72A	26.3	37.4	10.35	9.27	38.33	83.23	D
149	26-Jul-96	0940	NITRO	25N/60H/15O	92	26H/74A	23.5	29.8	10.86	9.4	42.29	80.62	D
150	26-Jul-96	1105	NITRO	25N/60H/15O	92	24H/76A	25.0	32.4	10.37	8.88	32.39	64.26	D
151	26-Jul-96	1310	NITRO	25N/60H/15O	92	22H/78A	25.1	33.7	10.56	9.02	34.41	101.67	LE
152	26-Jul-96	1425	NITRO	25N/60H/15O	92	23H/77A	25.8	35.3	10.26	11.05	25.25	100.98	LE
153	26-Jul-96	1605	NITRO	25N/60H/15O	92	100A	27.1	37.2	10.31	1.9	3.19	6.66	
154	29-Jul-96	1335	NITRO	25N/60H/15O	92	23H/77A	23.3	24.4	10.13	8.79	9.8	48.86	LE
155	29-Jul-96	1450	NITRO	80H/20O	92	23H/77A	24.9	27.2	8.35	8.12	14.82	25.62	LE
156	30-Jul-96	1000	NITRO	80H/20O	CV	N/A	23.3		10.03				
157	30-Jul-96	1305	NITRO	5N/76H/19O	CV	N/A	24.2		10.45				
158	30-Jul-96	1335	NITRO	10N/72H/18O	CV	N/A	26.5		10.93				
159	30-Jul-96	1435	NITRO	15N/68H/17O	CV	N/A	30.0		11.10				
160	30-Jul-96	1542	NITRO	20N/64H/16O	CV	N/A	29.1		12.66				
161	30-Jul-96	1633	NITRO	25N/60H/15O	CV	N/A	29.1		12.96				
162	31-Jul-96	1037	NITRO	30N/56H/14O	CV	N/A	23.9		12.80				
163	31-Jul-96	1115	NITRO	35N/52H/13O	CV	N/A	26.2		12.85				
164	31-Jul-96	1235	NITRO	40N/48H/12O	CV	N/A	28.7		11.93				
165	31-Jul-96	1315	NITRO	45N/44H/11O	CV	N/A	29.1		8.36				
166	31-Jul-96	1503	NITRO	50N/40H/10O	CV	N/A	27.1		8.20				
167	31-Jul-96	1540	NITRO	55N/36H/9O	CV	N/A	28.3		7.19				
168	5-Aug-96	1610	NITRO	20N/64H/16O	92	27H/73A	23.5	23.7	9.47	9.65	50.39	97.32	D
169	6-Aug-96	1033	NITRO	20N/64H/16O	92	25H/75A	23.2	24.7	9.86	9.23	23.94	72.96	LE
170	6-Aug-96	1145	NITRO	25N/60H/15O	92	25H/75A	25.3	27.8	10.51	8.87	45.67	51.99	D
171	6-Aug-96	1440	NITRO	67H/33O	92	100A	24.6	29.7	3.20	2.4	2.77	9.46	
172	7-Aug-96	1015	NITRO	25N/60H/15O	92	21H/79A	23.4	25.7	10.53	7.98	11.25	51.03	LE
173	7-Aug-96	1145	NITRO	25N/60H/15O	92	20H/80A	25.1	28.2	10.18	7.87	12.21	20.93	LE

Run #	Date	Time	Series	DRVR	Nozz	RCVR	T1, DR	T1, RC	Pp, DR	Pp, RC	Pp, T3	Pp, E	REC
174	7-Aug-96	1255	NITRO	25N/60H/15O	92	19H/81A	25.8	30.1	10.15	7.47	9.2	20	LE
175	8-Aug-96	1345	NITRO	10N/72H/18O	92	100A	22.2	25.9	8.60	2.24	3.26	5.56	
176	8-Aug-96	1520	NITRO	20N/64H/16O	92	100A	23.3	26.0	9.43	2.11	2.77	4.76	
177	8-Aug-96		NITRO	30N/56H/14O	92	100A	23.6	25.8	7.47	1.92	2.87	6.05	
178	11-Aug-96	1310	NITRO	25N/60H/15O	92	10H/90A	21.6	22.5	9.96	2.93	5.6	9.94	B
179	11-Aug-96	1420	NITRO	25N/60H/15O	92	15H/85A	23.4	24.0	10.17	6.51	10.9	18.85	LE
180	12-Aug-96	1120	NITRO	20N/64H/16O	92	10H/90A	21.6	23.2					B
181	12-Aug-96	1255	NITRO	20N/64H/16O	92	10H/90A	23.3	24.7	9.40	6.62	7.68	20.94	LE
182	12-Aug-96	1433	NITRO	20N/64H/16O	92	10H/90A	23.9	25.7	9.27	5.83	10.15	17.36	LE
183	12-Aug-96	1545	NITRO	20N/64H/16O	92	15H/85A	24.5	26.7	9.25	6.63	9.56	16.28	LE
184	4-Sep-96	1320	NITRO	45N/44H/11O	CV	N/A	21.8		11.95				
185	4-Sep-96	1400	NITRO	50N/40H/10O	CV	N/A	23.3		10.74				
186	4-Sep-96	1520	NITRO	40N/48H/12O	CV	N/A	23.3		11.79				
187	5-Sep-96	1105	NITRO	45N/44H/11O	CV	N/A	21.7		7.94				
188	5-Sep-96	1140	NITRO	45N/44H/11O	CV	N/A	22.9		8.75				
189	5-Sep-96	1400	NITRO	50N/40H/10O	CV	N/A	23.1		10.07				
190	5-Sep-96	1443	NITRO	45N/44H/11O	CV	N/A	23.8		8.41				
191	6-Sep-96	1215	NITRO	45N/44H/11O	CV	N/A	22.3		11.01				
192	6-Sep-96	1405	NITRO	45N/44H/11O	CV	N/A	22.9		7.90				
193	27-Sep-96	1020	NITRO	35H/65A	92	100 A	22.2	23.7	5.84	2.92	2.1		
194	27-Sep-96	1515	NITRO	35H/65A	92	100 A	22.3	23.9	6.15	2.65	1.99		
195	27-Sep-96	1635	NITRO	25N/60H/15O	92	100 A	22.8	23.8	13.62	3.02	2.73		
196	18-Oct-96	1600	NITRO	30H/70A	92	10H/90A	20.8	21.2	BAD	TRIG			
206	11-Nov-96	1350	SHOCK-4	30H/70A	92	100A	22.4	23.4					
207	11-Nov-96	1415	SHOCK-4	30H/70A	92	100A							
208	11-Nov-96	1445	SHOCK-4	30H/70A	92	100A	24.3	23.9	6.02	1.6	2.09	2.64	
209	11-Nov-96	1540	SHOCK-5	30H/70A	92	100A	24.3	23.8	5.77	1.52	1.91	3.55	
210	11-Nov-96	1607	SHOCK-6	30H/70A	92	100A	24.7	24.1	5.50	1.61	2.33	2.62	
211	11-Nov-96	1655	SHOCK-7	30H/70A	92	100A	24.6	23.8	4.91	1.65	1.89	3.89	
212	11-Nov-96	1717	SHOCK-8	30H/70A	92	100A	24.9	24.4	1.62	5.71	2.02	5.17	
213	12-Nov-96	1115	SHOCK-9	30H/70A	92	100A	22.3	23.5	5.31	1.61	1.95	3.99	
214	12-Nov-96	1148	SHOCK-10	30H/70A	92	100A	23.3	23.6	6.14	1.58	1.93	3.27	
215	12-Nov-96	1222	SHOCK-11	30H/70A	92	100A	23.9	23.8	7.47	1.7	2.45	4.03	
216	12-Nov-96	1733	SHOCK-12	30H/70A	92	100A	22.9	23.7	5.15	1.68	2.11	3.13	
217	12-Nov-96	1802	SHOCK-13	30H/70A	92	100A	23.6	24.0	4.85	1.62	1.95	4.24	
218	14-Nov-96	1350	SHOCK-14	30H/70A	92	100A	22.7	23.4	5.57	1.62	2.11	3.91	
219	14-Nov-96	1427	SHOCK-15	30H/70A	92	100A	23.4	23.6	6.24	1.61	2.66	3.9	
220	14-Nov-96	1515	SHOCK-16	30H/70A	92	100A	23.9	23.5	6.99	1.7	2.41	4.19	
221	14-Nov-96	1540	SHOCK-17	30H/70A	92	100A	24.3	23.7	6.37	1.57	2.3	4.17	

Run #	Date	Time	Series	DRVR	Nozz	RCVR	T1, DR	T1, RC	Pp, DR	Pp, RC	Pp, T3	Pp, E	REC
222	14-Nov-96	1622	SHOCK-18	30H/70A	92	100A	24.8	23.8	5.13	1.69	2.14	3.76	
223	14-Nov-96	1650	SHOCK-19	30H/70A	92	100A	25.1	23.9	5.37	1.69	1.99	3.1	
224	15-Nov-96	1144	SHOCK-4	30H/70A	92	100A	22.5	23.4	4.92	1.79	2.2	3.43	
225	15-Nov-96	1220	DAS TEST	10H/90A	92	10H/90A	23.4	23.4	3.88	4.1			
226	20-Nov-96	1445	SHOCK-10	100A	92	100A					1.2	1.42	
227	20-Nov-96		SHOCK-10	100A	92	100A					1.29	1.77	
228	3-Dec-96	1710	DAS TEST	10H/90A	92	80H/20O	22.7	22.7	9.43	5.19	12.98	17.55	
229	4-Dec-96	1135	NITRO	80H/20O	92	28H/72O	22.8	23.5	8.85	8.8	34.16	72.72M	D
230	5-Dec-96	1105	SA	80H/20O	12.7	50S/10H/40A	22.7	96.3	11.68	2.7			B
231	11-Dec-96	1110	CHA	80H/20O	12.7	12H/88A	22.6	22.8	13.30	4.67			B
309	3-Feb-97	1440	BETA	β=7.6	CV		22.0		4.19				
311	6-Feb-97	1421	CHA	β=7.6	92	30H/70A	22.6	26.4	4.03				
312	8-Feb-97	1223	BETA-N2	β=2.6	92	β=3.76	21.9	23.6	10.04	8.7	35.82	72.27M	D
313	8-Feb-97	1326	BETA-N2	β=2.6	92	β=4	24.1	26.9	11.23	8.41	35.72	102.31M	D
314	8-Feb-97	1430	BETA-N2	β=2.6	92	β=4.5	25.2	29.9	10.82	7.85	13.69	23.19	LE
315	8-Feb-97	1700	BETA-N2	β=2.6	92	β=4.4	23.9	30.6	11.75	8.03	41.19	102.14	D
316	9-Feb-97	1230	BETA-N2	β=2.6	92	β=4.6	21.9	25.8	11.00	8.12	21.79	16.14	LE
317	9-Feb-97	1336	BETA-N2	β=2.6	92	β=4.3	24.1	28.9	11.05	8.37	33.28	102.48M	D
318	9-Feb-97	1417	BETA-N2	β=2.6	CV		25.7		15.03				
319	10-Feb-97	1722	BETA-N2	β=2.6	92	100A	22.0		9.09	1.6	2.62	4.21	
320	10-Feb-97	1852	BETA-N2	β=2.6	92	100A	23.2	24.8	8.06	1.6	2.54	4.42	
321	11-Feb-97	1157	BETA-N2	β=2.6	92	β=4.6	22.6	99.1	11.09	6.89	21.01	135.03	D
322	11-Feb-97	1337	BETA-N2	β=2.6	92	β=4.8	23.7	99.1	11.44	6.89	26.74	68.44	D
323	11-Feb-97	1432	BETA-N2	β=2.6	92	β=5.5	24.9	100.8	9.03	6.33	10.58	FAULT	LE
324	11-Feb-97	1554	BETA-N2	β=2.6	92	β=5.2	24.4	102.0	10.05	6.8	37.18	135.03M	D
325	11-Feb-97	1751	BETA-N2	β=2.6	92	β=5.3	24.0	102.0	10.45	6.57	9.25	16.71	N
326	11-Feb-97	1856	BETA-N2	β=2.6	92	β=5.4	24.7	100.3	11.39	6.26	9.36	15.73	N
327	11-Feb-97	1945	BETA-N2	β=2.6	92	β=5.3	25.3	102.5	11.23	7.36	28.17	135.03M	LE
328	11-Feb-97	2035	BETA-N2	β=2.6	92	β=5.2	25.8	104.5	8.76	6.29	8.78	13.28	N
329	11-Feb-97	2149	BETA-N2	β=2.6	92	β=5.1	24.0	102.0	11.17	6.66	36.86	193.51M	D
330	12-Feb-97	1007	BETA-H2O	β=2.6	92	β=5.0			10.61	5.37	6.29	5.19	N
331	12-Feb-97	1420	BETA-H2O	β=2.6	92	β=4.0	23.2	103.2	9.13	5.63	7.93	5.78	N
332	12-Feb-97	1521	BETA-H2O	β=2.6	92	β=3.0	25.1	104.7	11.43	KILLED	13.43		N
333	13-Feb-97	1606	NITRO	25N/	92	23H/77A	23.8	43.5	10.24	8.52	23.1	135	LE
334	14-Feb-97	1056	NITRO	25N/	92	23H/77A	22.4	31.4	9.06	9.01	31.47	131.32M	LE
335	20-Feb-97	1354	NITRO	25N/	92	30H/70A	24.7	26.2	9.16	8.44	37.18	55.95	D
336	21-Feb-97	1038	BETA-N2	β=2.6	92	β=4.5	22.1	24.7	10.22	9.1	34.76	132.94M	LE

Run #	Date	Time	Series	DRVR	Nozz	RCVR	T1, DR	T1, RC	Pp, DR	Pp, RC	Pp, T3	Pp, E	REC
337	21-Feb-97	1220	BETA-N2	β=2.6	92	β=4.4	23.6	27.6	10.36	8.3	10.9	18.56	N
338	21-Feb-97	1422	BETA-N2	β=2.6	92	β=4.3	23.6	29.6	11.76	7.99	33.54	44.51	D
339	22-Feb-97	1318	BETA-N2	β=2.6	92	β=4.4	22.1	25.7	9.42	9.22	26.12	130.29	LE
340	22-Feb-97	1432	BETA-N2	β=2.6	92	β=4.2	23.8	28.8	9.73	8.49	3718	60.23	D
341	23-Feb-97	1247	BETA-N2	β=2.6	92	β=5.2	21.9	100.2	9.96	6.56	28.7	35.35	D
342	23-Feb-97	1346	BETA-N2	β=2.6	92	β=5.4	23.7	101.7	8.79	6.4	21.31		N
343	23-Feb-97	1452	BETA-N2	β=2.6	92	β=5.3	24.0	104.0	10.50	6.32	7.82	13.05	N
344	23-Feb-97	1859	BETA-N2	β=2.6	92	β=5.1	22.6	103.4	11.32	6.57	37.18	33.87	D
345	24-Feb-97	1022	BETA-H2O	β=2.6	92	β=3.5	21.7	102.8	11.10	6.12	4.29	7.96	N
346	24-Feb-97	1137	BETA-H2O	β=2.6	92	β=3.0	23.6	102.4	10.70	KILLED	9.61	20.72	N
347	24-Feb-97	1254	BETA-H2O	β=2.6	92	β=2.6	24.5	103.8	9.64		16.73	25.04	LE
348	24-Feb-97	1605	BETA-H2O	β=2.6	92	β=2.0	22.9	103.8	10.97		13.92	30	LE
349	24-Feb-97	1735	BETA-H2O	β=2.6	92	β=1.8	24.1	102.8	9.56		22.02	26.01	T
350	24-Feb-97	1840	BETA-H2O	β=2.6	92	β=1.4	25.3	102.6	10.57		25.15	78.15	T
351	24-Feb-97	1944	BETA-H2O	β=2.6	92	β=1.6	25.9	102.1	10.04		28.66	55.66	T
352	24-Feb-97	2043	BETA-H2O	β=2.6	92	β=1.0	26.5	102.3	10.38		37.18	50.5	D
353	1-Mar-97	1136	BETA-N2	β=2.6	92	β=2.6	20.4	21.3	10.44		36.49	78.54	D
354	18-Mar-97	1234	BETA-N2	β=2.6	92	β=4.3	24.4	26.4					LE
355	18-Mar-97	1549	BETA-N2	β=2.6	92	β=4.2	23.4	27.8	11.46		30.06	56.08	D
356	18-Mar-97	1756	BETA-N2	β=2.6	92	β=2.6	23.8	29.8	11.50		25.75	74.15	D
357	19-Mar-97	0926	BETA-N2	β=2.6	64	β=3.76	22.4	26.4	11.12		25.62	66.97M	D
358	19-Mar-97	1036	BETA-N2	β=2.6	64	β=4.2	24.3	29.6	12.80		23.48	48.63	D
359	19-Mar-97	1325	BETA-N2	β=2.6	64	β=4.3	23.6	30.5	11.43				B
360	19-Mar-97	1922	BETA-N2	β=2.6	64	β=4.1	22.5	29.3	12.08			64.23	D
361	20-Mar-97	0818	BETA-N2	β=2.6	38	β=3.76	22.0	26.3	12.86				B
362	20-Mar-97	1243	BETA-N2	β=2.6	38	β=3.0	22.8	27.8	13.62		24.69	81.31	D
363	20-Mar-97	1624	BETA-N2	β=2.6	38	β=3.4	22.8	28.9	11.94			3.13	B
364	21-Mar-97	0936	BETA-N2	β=2.6	38	β=3.2	22.5	25.7	13.78				B
365	21-Mar-97	1301	BETA-N2	β=2.6	38	β=3.1	22.5	27.5	12.33				B
366	21-Mar-97	1718	BETA-N2	β=2.6	38	β=2.9	22.1	28.3	13.90		24.63	66.97M	D
367	21-Mar-97	2102	BETA-N2	β=2.6	25	β=2.8	22.1	28.7	13.05		27.11	66.97M	D
368	22-Mar-97	0910	BETA-N2	β=2.6	25	β=3.0	21.4	26.2	13.76				B
369	22-Mar-97	1811	BETA-N2	β=2.6	25	β=2.9	21.9	26.2	13.41		25.11	65.68	D
370	23-Mar-97	1241	BETA-N2	β=2.6	25NC	β=2.9	22.6	26.8	12.67			67	LE
371	23-Mar-97	1458	BETA-N2	β=2.6	25NC	β=2.8	22.0	29.0	13.69				B
372	23-Mar-97	1705	BETA-N2	β=2.6	25NC	β=2.6	22.4	30.4	13.85		25.85	66.97M	D
373	24-Mar-97	0829	BETA-N2	β=2.6	25NC	β=2.7	22.2	26.5	13.41				B

Run #	Date	Time	Series	DRVR	Nozz	RCVR	T1, DR	T1, RC	Pp, DR	Pp, RC	Pp, T3	Pp, E	REC
374	24-Mar-97	1157	BETA-N2	β=2.6	25NC	β=2.5	22.1	27.9	13.04				B
375	24-Mar-97	1410	BETA-N2	β=2.6	25NC	β=2.4	22.6	30.1	14.14		26.36	66.97M	D
376	24-Mar-97	1907	BETA-N2	β=2.6	25NC	β=2.5	21.4	28.8	13.04			66.97M	D
377	25-Mar-97	1055	BETA-N2	β=2.6	25	β=2.9	22.2	25.9	14.32			52.53	D
378	25-Mar-97	1338	BETA-N2	β=2.6	25	β=3.1	22.5	28.3	13.53				B
379	25-Mar-97	1729	BETA-N2	β=2.6	64	β=4.5	22.0	28.8	12.42			8.78	B
380	26-Mar-97	0913	BETA-H2O	β=2.6	92	β=1.1	24.2	100.7	10.45		19.88	43.93	D
381	26-Mar-97	1030	BETA-H2O	β=2.6	92	β=1.3	25.8	100.8					T
382	26-Mar-97	1202	BETA-H2O	β=2.6	92	β=1.2	26.3	102.2					T
383	26-Mar-97	1316	BETA-H2O	β=2.6	38	β=1.0	26.9	101.2	12.58				B
384	26-Mar-97	1431	BETA-H2O	β=2.6	38	β=0.86	27.1	103.6					LE
385	26-Mar-97	1549	BETA-H2O	β=2.6	38	β=0.7	26.9	100.4	12.96			61.2	T
386	26-Mar-97	1709	BETA-H2O	β=2.6	38	β=0.66	26.9	103.7	12.63			16.89	T
387	26-Mar-97	1805	MISFILL	β=2.6	38	β=??	27.4	102.6	13.11				T
388	27-Mar-97	0845	BETA-H2O	β=2.6	38	β=0.5	21.7	104.6	13.27		19.91	52.88	D
389	27-Mar-97	0941	BETA-H2O	β=2.6	38	β=0.55	24.6	104.5	12.89		20.62	58.27	D
390	27-Mar-97	1040	BETA-H2O	β=2.6	38	β=0.6	26.2	104.2	12.91			45.57	T
391	27-Mar-97	1212	BETA-H2O	β=2.6	38	β=0.8	26.1	104.2	13.23				B
392	28-Mar-97	1330	BETA-N2	β=3.76	92ND	β=3.76		34.0					B
393	28-Mar-97	1440	BETA-N2	β=3.0	92ND	β=3.0	22.8	35.9	9.45		30.01	66.97M	D
394	28-Mar-97	1663	BETA-N2	β=3.3	92ND	β=3.3	23.1	37.4	9.25		28.08	66.97M	D
395	29-Mar-97	1016	BETA-N2	β=4.0	92ND	β=4.0	21.1	27.6	9.48			12.92	B
396	29-Mar-97	1107	BETA-N2	β=3.76	92ND	β=3.76	23.2	31.2	9.44				B
397	29-Mar-97	1550	BETA-N2	β=2.9	25ND	β=2.9	21.7	29.1	14.34				B
398	29-Mar-97	1850	BETA-N2	β=2.6	25ND	β=2.6	21.9	30.0	13.60				B
399	30-Mar-97	1146	BETA-N2	β=2.4	25ND	β=2.4	21.2	26.6					B
400	30-Mar-97	1400	BETA-N2	β=2.0	25ND	β=2.0	22.2	29.1	12.22			10.73	B
401	30-Mar-97	2100	BETA-N2	β=1.8	25ND	β=1.8	21.4	28.9	11.73		25.37	72.22	D
402	31-Mar-97	1629	CAM TEST	β=2.6	25	100A	20.8	25.5	14.11				
403	31-Mar-97	1800	CAM TEST	β=2.6	25	100A	21.9	25.6					
404	31-Mar-97	1916	CAM TEST	β=2.6	25	100A	22.4	25.4					
405	1-Apr-97	0900	CAM TEST	β=2.6	25	100A	22.0		13.68		1.26	1.93	
406	1-Apr-97	1045	CAM TEST	β=2.6	25	100A							
407	1-Apr-97	1332	BETA-N2	β=2.6	25	β=2.6	21.6	23.6	13.85			63.1	D
408	1-Apr-97	1737	BETA-N2	β=2.6	25	β=2.6			14.09		25.27	66.74	D
409	1-Apr-97	1927	BETA-N2	β=1.8	25ND	β=1.8	22.4	29.7					T
410	2-Apr-97	1112	BETA-N2	β=1.8	25ND	β=1.8	21.1	26.6					T

Run #	Date	Time	Series	DRVR	Nozz	RCVR	T1, DR	T1, RC	Pp, DR	Pp, RC	Pp, T3	Pp, E	REC
411	2-Apr-97	1538	BETA-N2	β=1.7	25ND	β=1.7	21.3	28.9	11.97		26.19	73.51	D
412	2-Apr-97	1655	BETA-N2	β=3.76	25ND	β=3.76	22.8	32.9					B
413	3-Apr-97	0835	BETA-N2	β=3.76	25ND	β=3.76	20.8	27.1					B
414	3-Apr-97	1113	BETA-N2	β=3.76	25ND	β=3.76							B
415	4-Apr-97	1740	BETA-N2	β=2.6	25	100A	21.4	24.3					
416	4-Apr-97	1935	BETA-N2	β=2.6	25	β=3.76	22.0	27.0	14.05				B
417	4-Apr-97	2035	BETA-N2	β=3.76	25ND	β=3.76	23.1	27.4	11.45				B
418	5-Apr-97	1055	BETA-N2	β=3.76	25ND	β=3.76	22.2	29.2					B
419	5-Apr-97	1150	BETA-N2	β=2.6	25	β=3.76	23.3	32.2					B
420	5-Apr-97	1308	BETA-N2	β=2.6	25	β=2.6	21.1	27.4					B
421	5-Apr-97	1413	BETA-N2	β=2.6	25	β=2.6	22.4	31.4	13.74				B
422	5-Apr-97	1528	BETA-N2	β=1.7	25ND	β=1.7	23.5	34.2					T
423	5-Apr-97	1737	BETA-N2	β=1.5	25ND	β=1.5							D
424	5-Apr-97	1850	BETA-N2	β=2.6	25	β=2.4	24.1	39.8	13.42		25.11	66.55	D
425	5-Apr-97	2311	BETA-N2	β=2.6	25	β=3.76	22.3	35.3					
426	6-Apr-97	0021	BETA-N2	β=3.76	25ND	β=3.76	23.3	37.7	9.17				
427	6-Apr-97	0130	BETA-N2	β=2.6	92	100A	23.6	40.3					
428	6-Apr-97	1205	BETA-N2	β=2.6	92	15H/85A	21.3	29.9					
429	6-Apr-97	1607	BETA-N2	β=2.6	25	β=2.6	21.4	28.8	13.69				NG
430	6-Apr-97	1722	BETA-N2	β=2.6	25	β=2.4	22.8	32.3	13.89		25.52	64.68	D
431	6-Apr-97	1831	BETA-N2	β=1.5	25ND	β=1.5	23.6	35.4	11.66		25.59	71	D
432	9-Apr-97	2045	BETA-N2	β=1.9	25ND	β=1.9	20.0	21.3					T
433	16-Apr-97	1813	BETA-N2	β=2.6	92	β=2.6	21.4	24.7			25.5		D

Appendix D

RPI Jet Visualization

This Appendix contains photographs of jet startup from the final tests in the RPI facility. In the photographs, the diameter of the jet tube is 0.5" (12.7 mm). The initial driver mixture is 80% H_2-20% O_2. The receiver mixtures are listed in the captions.

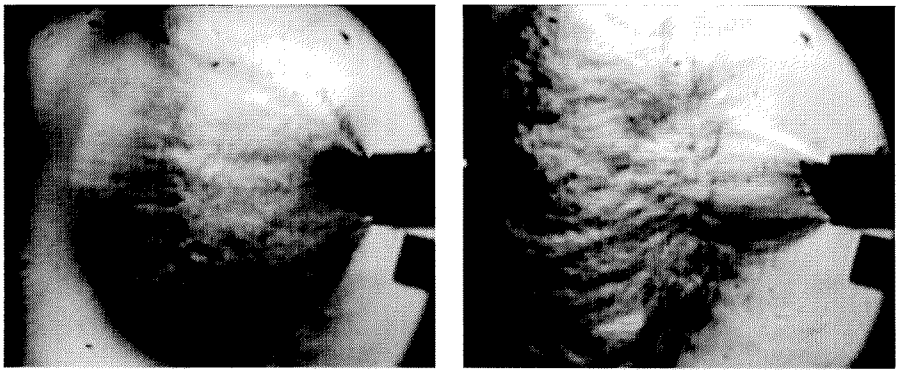

1 (t=0)

2 (0.074 ms)

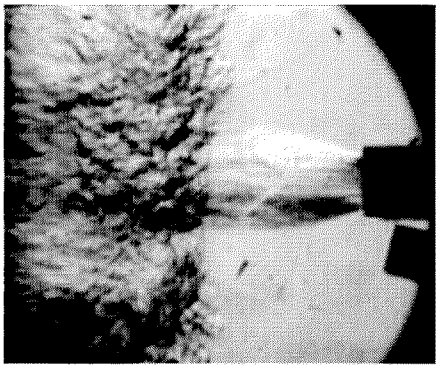

4 (0.223 ms)

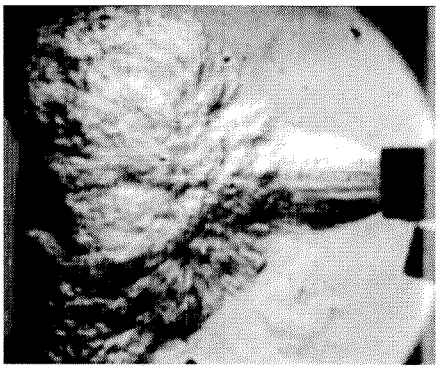

37 (2.678 ms)

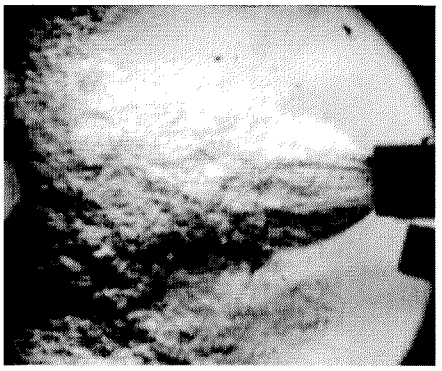

61 (4.464 ms)

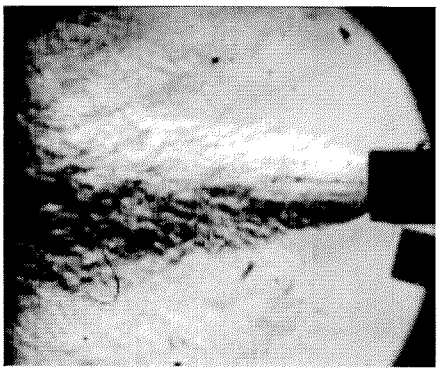

144 (10.639 ms)

Figure D.1: Jet startup, venting into 100% N_2. Note lead shocks and large, turbulent vortex head which convects downstream. Framing rate is 13.44 kfps. RPI run 128.

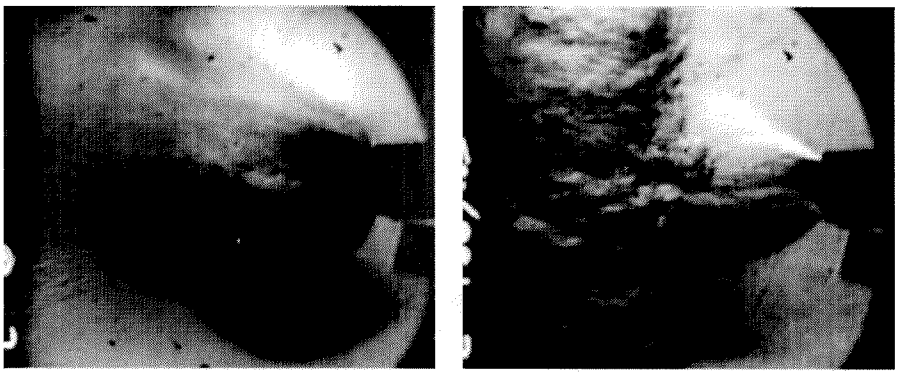

1 (t=0)

2 (0.149 ms)

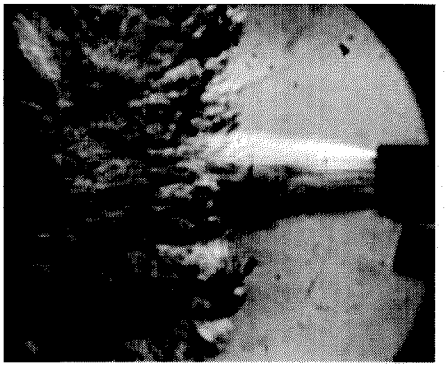

3 (0.298 ms)

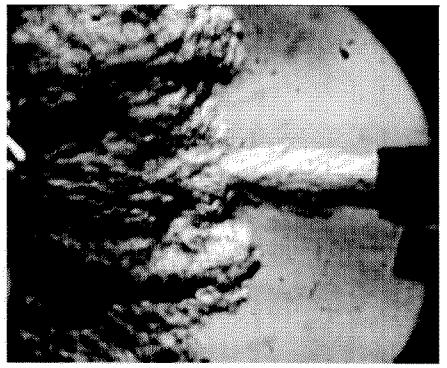

4 (0.447 ms)

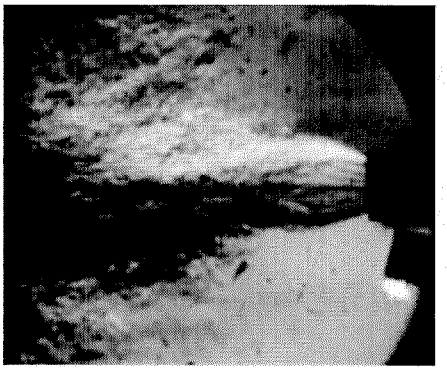

33 (4.768 ms)

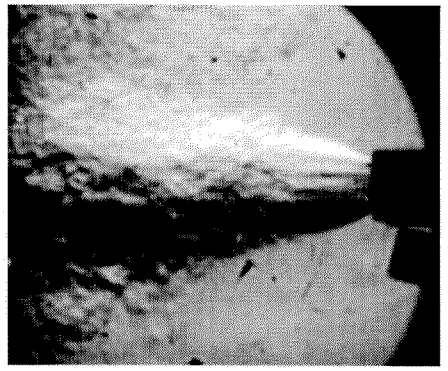

53 (7.748 ms)

Figure D.2: Jet startup, venting into 100% air. The jet is expected to burn as a diffusion flame under these conditions, but no difference is visible between these photos and those of Figure D.1. Reduced flow in frame 4 is due to diaphragm clogging (diaphragm later cleared). Framing rate is 6.72 kfps. RPI run 124.

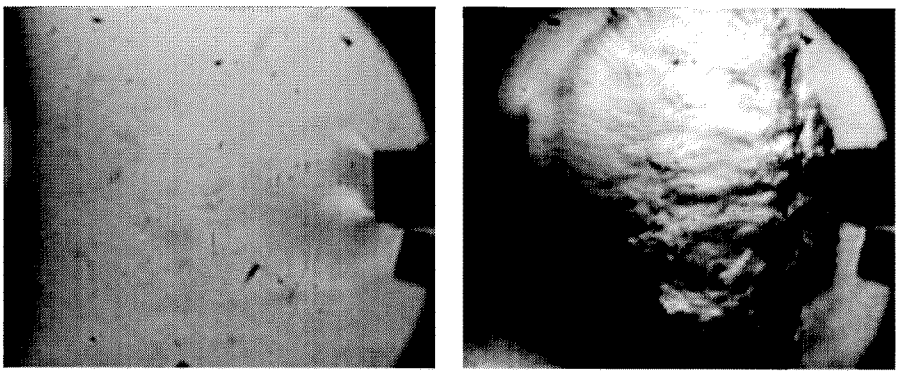

1 (t=0)

2 (0.072 ms)

3 (0.142 ms)

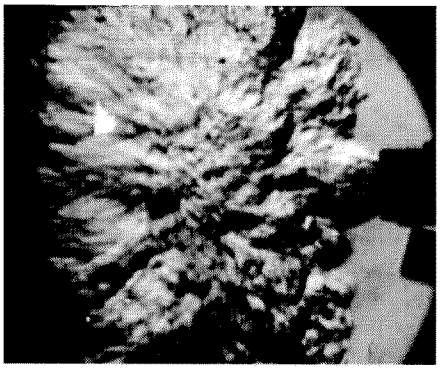

4 (0.215 ms)

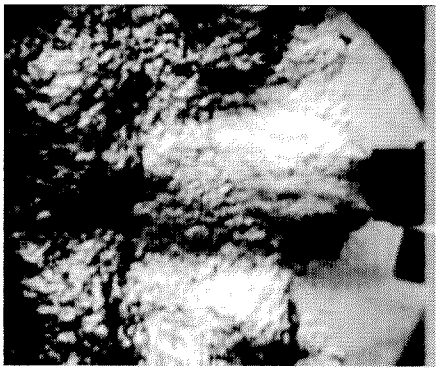

74 (5.220 ms)

124 (8.790 ms)

Figure D.3: Jet initiation of deflagration in 1:1 air:N_2, with 10% H_2. Framing rate is 13.44 kfps. RPI run 127.